Quantification of Cerebral Vascular Hemodynamics Using MRI

Yize Zhao

St Cross College

University of Oxford

A thesis submitted for the degree of

Doctor of Philosophy

Michaelmas 2018

This thesis is dedicated to
my dearest parents

Abstract

Cerebral perfusion is a promising biomarker for the early diagnosis of dementia. Additionally, the change in perfusion in response to vasoactive stimuli, cerebrovascular reactivity (CVR), may also prone to be a valuable dementia biomarker. Arterial spin labeling (ASL) MRI is a non-invasive technique to quantify perfusion and in turn CVR. However, the precise estimation of perfusion using ASL MRI is not only limited by partial volume effects, due to the relatively low resolution of the ASL data, but also affected by confounding factors including arterial transit time (ATT) and blood flow velocity. This thesis investigates the sensitivity of partial volume correction (PVEc) methods for gray matter (GM) perfusion estimation and the impact of confounding factors on CVR measurements.

Linear regression (LR) and spatially regularized PVEc methods were examined using simulated ASL data by comparing the estimation accuracy and the ability to preserve spatial variations in perfusion images. Results indicated that the LR approach was less sensitive to uncertainties in data while the spatially regularized method was superior in preserving spatial details.

The impact of PVEc on the repeatability of GM perfusion was investigated using data from a healthy cohort. The repeatability improved after PVEc using both LR and spatially regularized methods, implying that PVEc is beneficial to increase the reliability of GM perfusion measurements.

CVR quantification was investigated using the standard implementation of ASL (single-PLD PCASL) and a novel ASL technique (Turbo QUASAR ASL). CVR, ATT, and blood flow velocity were estimated before and after acetazolamide administration in healthy volunteers. Regional differences of CVR were found between the two ASL methods. Both PCASL and Turbo QUASAR ASL are limited by the change in blood flow velocity for the use in CVR estimation, while PCASL is also hindered by ATT. Accounting for flow velocity enhanced the CVR estimation for both techniques.

Acknowledgements

I want to give my most sincere gratitude to my parents for their unconditional love, support, and trust while I am pursuing my dreams at Oxford. To my cousin's family in the UK, I am lucky to have your hospitality since day one of my DPhil.

I would like to thank my supervisor Prof Michael Chappell for his supervision, encouragements, and most importantly his patience during the course of my study. Without his vision and inspiration, none of my work would have been possible. Michael has not only enabled me to establish the essential network in the research community but he has also given me tremendous amount of autonomy to explore topics beyond cerebral perfusion. Such professional and wonderful supervisor is rare nowadays.

I would like to express my gratitude to the members of the QuBIC research group: Antoine for the frequent and sometimes transatlantic discussion, Yunus, Paula, and Flora for the encouragement on writing, Yuriko for helping me with the *archeology* project, Martin for his magical skills of making everything work, and all other team members as well as support colleagues.

I am grateful for Esben, who guided me through the complexity of MRI physics while hosting me numerous times at DRCMR. *Tak!* Lena and Aart, I owe you a big *dank je* for the most important data of my work and inviting me to share my research with your group at AMC. Of course. Without the significant input from Dave and Magda, it was impossible to resolve the issues in our project.

Special thanks go to Andy, Tom, Irene, and colleagues of FMRIB for the provision of the test-retest data and the constructive advice on my first journal paper. I want to thank Otto and Egill for sharing the QUASAR ASL data and hosting me at Rigshospitalet.

The ASL community has played a significant role in my professional development. I will always be ready to debate partial volume topics with Henk, Jan, and Andre. To Thijs, Matthias, and Federico, thank you for offering me the opportunity to teach an ESMRMB workshop. To Rik and Xavier, I am grateful for your nomination to moderate at ESMRMB conferences and to participate in COST Action young researchers events. I am impressed by the creativity of fellow ASL PhDs: Joana, Marco, Isaac, Rebecca, Esther, and Sophie. To Patricia of Ghent, I owe you a big favor for proofreading my thesis while looking after your priceless baby. Of course,

I am better prepared for ASL in Spanish with Alexandra, Oriol, and Juan-Antonio. Thanks Janine for giving the opportunity to tutor the FSL course. Thanks Audrey and Greg for inviting me to speak and live stream my presentation at Stanford.

I am lucky to have received critical feedbacks from my DPhil examiners Prof Mark Jenkinson and Dr Iris Asllani as well as my transfer and confirmation examiner Prof Mark Woolrich.

I have enjoyed every aspect of my life at St Cross during the course of my DPhil. Thank you Dan for the frequent lunchtime discussions and your advice on building a successful career. Thank you John, Ella, and Victoria for giving me the opportunities to connect with our alumni. I am also grateful for the advice from Rachel of Oxford's Careers Service.

To all my friends and previous supervisors in Hong Kong, I am grateful for your long-distance support and encouragements. Thank you Clement and William for the career advice. Natalie, I shall continue to explore the idea of treating dementia with scents and sounds. Thank you Jacky for the endless *technical support* to my research.

Finally, my study would not have been possible without the financial support of these organizations: EPSRC, EU COST Action, Gurantors of Brain, Dutch foundation "Fonds Nuts Ohra", St Cross College, Mr K T Soo Bursary, ESMRMB, and ISMRM.

من علمنی حرفا فقد صیرنی عبدا

"I am eternally indebted to whoever teaches me as much as a single letter."

Publications Arising from This Thesis

Journal Articles

- **Moss Y. Zhao**, Lena Václavů, Esben T Petersen, Bart J. Biemond, Magdalena J Sokolska, Yuriko Suzuki, David L Thomas, Aart J Nederveen, Michael A Chappell. Quantification of Cerebral Perfusion and Cerebrovascular Reserve Using Turbo-QUASAR Arterial Spin Labeling MRI, Magnetic Resonance in Medicine, Under review

- **Moss Y. Zhao**, Melvin Mezue, Andrew R. Segerdahl, Thomas W. Okell, Irene Tracey, Yingyi Xiao, Michael A. Chappell. A Systematic Study of the Sensitivity of Partial Volume Correction Methods for the Quantification of Perfusion from Pseudo-continuous Arterial Spin Labeling MRI, NeuroImage, Volume 162, 2017, Pages 384-397

Conference Proceedings

- **Moss Y. Zhao**, Michael A. Chappell. Investigating Different Arterial Spin Labeling Strategies For Measuring Gray Matter Perfusion and Arterial Transit Time, The British Chapter of ISMRM Annual Meeting 2018, Oxford, United Kingdom

- Paula Croal, Kevin Ray, Ruichong Ma, **Moss Y. Zhao**, Benjamin Harris, Nicola Sibson, Michael A. Chappell, Puneet Plaha, Simon Lord. Imaging pH in Glioblastoma Multiforme with CEST MRI (IMAGO Trial): Preliminary Findings, The British Chapter of ISMRM Annual Meeting 2018, Oxford, United Kingdom

- **Moss Y. Zhao**, Lena Václavů, Esben T Petersen, Henk-Jan Mutsaerts, Bart J Biemond, Ed T van Bavel, Charles B. Majoie, Aart J Nederveen, Michael A. Chappell. Investigating Cerebrovascular Reactivity Using Pseudo-continuous ASL and Turbo QUASAR ASL at Varying Blood Flow Conditions, ISMRM 2018 Annual Meeting and Congress, Paris, France

- Lena Václavů, **Moss Y. Zhao**, Esben T Petersen, John C Wood, Charles BLM Majoie, Ed T van Bavel, Bart J Biemond, Michael A Chappell, Aart

J Nederveen. Adaptations of Cerebral Physiology Due to Life-long Chronic Anaemia Measured with Turbo-QUASAR ASL, ISMRM 2018 Annual Meeting and Congress, Paris, France

- **Moss Y. Zhao**, Melvin Mezue, Andrew R. Segerdahl, Thomas W. Okell, Irene Tracey, Yingyi Xiao, Michael A. Chappell. The Impact of Partial Volume Correction on the Repeatability of Perfusion Quantification from Multi-PLD PCASL MRI, ESMRMB 2017 Congress, Barcelona Spain

- **Moss Y. Zhao**, Egill Rostrup, Otto M. Henriksen, Yingyi Xiao, Michael A. Chappell. Investigating the Sensitivity to Partial Volume Estimates of Partial Volume Correction for Single Postlabeling Delay Pseudo-continuous ASL, ISMRM 2017 Annual Meeting and Congress, Honolulu, HI, USA

- **Moss Y. Zhao**, Egill Rostrup, Otto M. Henriksen, Michael A. Chappell. Partial Volume Effects Correction for QUASAR ASL: Investigating the Sensitivity to Partial Volume Estimates, ESMRMB 2016 Congress, Vienna, Austria

- **Moss Y. Zhao**, Esben T. Petersen, Michael A. Chappell. Cerebral Perfusion Quantification Using Turbo-QUASAR Arterial Spin Labelling MRI: A Model-based Approach, MEIbioeng16, Oxford, United Kingdom

- **Moss Y. Zhao**, Egill Rostrup, Otto M. Henriksen, Michael A. Chappell. Partial Volume Effects Correction for QUASAR ASL: A Spatially Regularised Approach, ISMRM 2016 Annual Meeting and Congress, Singapore

- **Moss Y. Zhao**, Egill Rostrup, Otto M. Henriksen, Michael A. Chappell. Partial Volume Correction on QUASAR ASL: Comparing Linear Regression Method Before and After Model-based and Model-free Perfusion Estimation, ESMRMB 2015 Congress, Edinburgh, United Kingdom

Contents

List of Figures **xii**

List of Tables **xvi**

List of Abbreviations **xvii**

1 Introduction **1**
1.1 Motivation . . . 1
1.2 Cerebral Vascular Hemodynamics . . . 2
1.3 Measuring Perfusion . . . 2
1.4 Repeatability of Perfusion Measurements . . . 4
1.5 Cerebrovascular Reactivity . . . 4
1.6 Thesis Objectives . . . 5
1.7 Thesis Outline . . . 5

2 Literature Review **7**
2.1 Perfusion and Cerebral Blood Flow . . . 8
2.1.1 Definitions . . . 8
2.1.2 Neural Activity and Control of Cerebral Blood Flow . . . 8
2.1.3 Cerebral Blood Flow and Diseases . . . 9
2.1.4 Measuring Cerebral Blood Flow . . . 10
2.2 Principles of Magnetic Resonance Imaging . . . 11
2.2.1 Radiofrequency Pulse and B_1 . . . 12
2.2.2 MRI Real and Imaginary Signal . . . 14
2.2.3 Magnetic Resonance Imaging . . . 15
2.3 Arterial Spin Labeling MRI . . . 26
2.3.1 Labeling Pulse . . . 27
2.3.2 Time Delay Between Labeling and Imaging . . . 28
2.3.3 Continuous Arterial Spin Labeling . . . 30
2.3.4 Pulsed Arterial Spin Labeling . . . 32
2.3.5 Pseudo-continuous Arterial Spin Labeling . . . 36
2.3.6 QUASAR ASL . . . 37
2.3.7 Reproducibility of Arterial Spin Labeling Techniques . . . 42

2.4 Cerebral Blood Flow Quantification 43
2.4.1 Model Based Quantification Method 43
2.4.2 Model Free Quantification Method 47
2.4.3 Evaluation of Perfusion Quantification Techniques 49
2.5 Arterial Transit Time Quantification 50
2.6 Bayesian Methods 51
2.6.1 Bayes' Theorem 51
2.6.2 Variational Bayes 53
2.6.3 Approximate Variational Bayes 54
2.6.4 Spatial Regularization 55
2.6.5 Automatic Relevance Determination 57
2.7 Partial Volume Effects and Correction 58
2.7.1 Linear Regression Method 59
2.7.2 Spatially Regularized Method 61
2.7.3 Tissue Volume As A Covariate Method 62
2.7.4 Partial Volume Estimates 63
2.8 Conclusions 65

3 Investigating Partial Volume Correction Using PCASL 67
3.1 Introduction 68
3.2 Theory 69
3.2.1 Linear Regression 70
3.2.2 Spatially Regularized 71
3.3 Methods 71
3.3.1 Data 71
3.3.2 Partial Volume Estimation 72
3.3.3 Simulated Data 73
3.3.4 Perfusion Estimation and Partial Volume Correction 75
3.3.5 Simulation Study 77
3.3.6 Evaluation Metrics for Partial Volume Correction 79
3.3.7 Repeatability Study 81
3.4 Results 82
3.4.1 Simulation Study: Single-PLD Data (Kernel Size 5×5 for the LR Methods) 82
3.4.2 Healthy Cohort Experiments 89
3.5 Discussion 90
3.5.1 Simulation Study 91
3.5.2 Healthy Cohort Experiments 94
3.5.3 Limitations 96
3.6 Conclusions 97

4 Investigating Partial Volume Correction Using Multi-PLD ASL 98
4.1 Introduction . . . 98
4.2 Theory . . . 99
4.3 Methods . . . 101
4.3.1 Simulated Data . . . 101
4.3.2 Healthy Cohort Data . . . 102
4.3.3 Tissue Perfusion and ATT Estimation . . . 103
4.3.4 Evaluation Metrics . . . 104
4.3.5 Statistical Analysis . . . 104
4.4 Results . . . 105
4.4.1 Simulated Experiments . . . 105
4.4.2 Healthy Cohort Experiments . . . 111
4.5 Discussion . . . 114
4.5.1 Simulated Experiments . . . 115
4.5.2 Healthy Cohort Experiments . . . 117
4.5.3 Limitations . . . 119
4.6 Conclusions . . . 120

5 Investigating Cerebrovascular Reactivity Using PCASL and Turbo QUASAR ASL 122
5.1 Introduction . . . 123
5.2 Theory . . . 125
5.2.1 Turbo QUASAR ASL Sequence . . . 125
5.2.2 Tissue Kinetic Model . . . 131
5.3 Methods . . . 135
5.3.1 Simulations . . . 135
5.3.2 Healthy Cohort Data . . . 137
5.3.3 PCASL Perfusion Quantification . . . 140
5.3.4 Turbo QUASAR ASL Perfusion Quantification . . . 140
5.3.5 Absolute Perfusion Quantification . . . 142
5.3.6 Blood Flow Velocity Quantification . . . 143
5.3.7 Statistical Analysis . . . 143
5.4 Results . . . 145
5.4.1 Simulated Experiments . . . 145
5.4.2 Healthy Cohort Experiments . . . 147
5.5 Discussion . . . 155
5.5.1 Turbo QUASAR ASL Sequence . . . 158
5.5.2 Model Based Method and Simulated Experiments . . . 159
5.5.3 Healthy Cohort Experiments . . . 160

5.5.4 CVR Quantification Using PCASL 161
5.5.5 CVR Quantification Using Turbo QUASAR ASL 164
5.5.6 Implications for CVR Studies for SCD Patients 165
5.5.7 Impacts of Resolution and Motion 167
5.5.8 Limitations 167
5.6 Conclusions 169

6 Conclusions and Future Work **171**
6.1 Conclusions 171
6.1.1 Sensitivity of PVEc Methods on Single-PLD ASL 172
6.1.2 Impact of PVEc on Repeatability of GM CBF Estimation . 172
6.1.3 Sensitivity of PVEc Methods on Multi-PLD ASL 173
6.1.4 Impact of PVEc Methods on QUASAR ASL 173
6.1.5 Turbo QUASAR ASL and Model Based Quantification Method 174
6.1.6 Investigating CVR Measurements Using PCASL and Turbo QUASAR ASL 174
6.2 Future Work 175
6.2.1 Partial Volume Correction For ASL Data of Brain Activation 175
6.2.2 Partial Volume Correction For ASL Data of Patients 175
6.2.3 Improving Turbo QUASAR ASL 175
6.2.4 Investigating CVR In Patients 176

Appendices

A Supplementary Data For Investigating Partial Volume Correction Using PCASL **179**
A.1 Simulation Study: Multi-PLD Data (Kernel Size 5×5 for the LR Methods) 179
A.2 Simulation Study: Single-PLD Data (Kernel Size 3×3 for the LR Methods) 179
A.3 Simulation Study: Multi-PLD Data (Kernel Size 3×3 for the LR Methods) 179

References **191**

List of Figures

2.1 Tipping over magnetization by RF pulse. 13
2.2 Free induction decay. 14
2.3 Frequency and phase encoding. 17
2.4 Spin echo MRI. 18
2.5 Gradient echo MRI. 19
2.6 Pulse sequence diagram of 2D EPI and k-space of single and multi shot EPI. 21
2.7 Pulse sequence diagram of GRASE acquisition and its k-space. . . . 22
2.8 Changes in phase and phase contrast MRI. 25
2.9 Example of the transverse plane of PC MRI of a healthy adult. . . . 26
2.10 Process of a typical ASL experiment. 27
2.11 Adiabatic excitation. 29
2.12 Single and multiple slices CASL. 31
2.13 Single and multiple slices PASL. 33
2.14 QUASAR ASL. 40
2.15 Generative model and priors for ASL. 52
2.16 CBF and ATT maps estimated using different techniques. 56
2.17 Transforming PV estimates from high resolution to low resolution for PVEc. 65

3.1 Schematic of the process of generating data for the simulation based experiments. 75
3.2 Perfusion estimation and partial volume correction. 76
3.3 M_{0a} data before and after correcting PVE. 77
3.4 Biased PV Estimates. 80
3.5 Estimated GM CBF map for single-PLD simulated data from a single subject. 83
3.6 RMSE between estimated and simulated GM CBF using noise-free simulated single-PLD data. 84
3.7 Example ROI curves for all experiments using single-PLD data. . . 85
3.8 Estimated slope values of the extended ROI analysis using single-PLD data. 86

3.9 Estimated GM CBF maps of two example subjects using different PVEc methods. . . . 89
3.10 Estimated slope values of the extended ROI analysis on healthy cohort data. . . . 90
3.11 Within-subject coefficient of variation of the PVEc methods in three ROIs. . . . 91

4.1 RMSE between estimated and simulated CBF in multi-PLD PCASL and PASL. . . . 106
4.2 Estimated slope values of the extended ROI analysis for the simulated multi-PLD PCASL and PASL data. . . . 107
4.3 RMSE between estimated and simulated GM ATT for the simulated multi-PLD PCASL and PASL data. . . . 108
4.4 RMSE between estimated and simulated GM CBF for the simulated multi-PLD PCASL and PASL data SNR = 5. . . . 110
4.5 Estimated slope values of the extended ROI analysis for the simulated multi-PLD PCASL and PASL data SNR = 5. . . . 111
4.6 RMSE between estimated and simulated GM ATT for the simulated multi-PLD PCASL and PASL data SNR = 5. . . . 112
4.7 Estimated GM CBF and ATT of an example subject before and after PVEc using LR and spatially regularized method. . . . 113
4.8 Estimated mean GM CBF and ATT of the six subjects before and after PVEc. . . . 114
4.9 ROI plot of an example subject and estimated slope values for all the subjects in the group. . . . 115

5.1 QUASAR and Turbo QUASAR ASL labeling and imaging scheme. 127
5.2 AIF and tissue signal of QUASAR and Turbo QUASAR ASL. . . . 128
5.3 Slice shifting strategy in Turbo QUASAR ASL. . . . 129
5.4 Label and control RF pulses in QUASAR ASL. . . . 131
5.5 Label and control RF pulses in Turbo QUASAR. . . . 132
5.6 Components of a single repeat of Turbo QUASAR ASL. . . . 133
5.7 Experimental design. . . . 138
5.8 2D PC MRI images in a healthy control subject. . . . 144
5.9 Estimated CBF values using model based and model free approach for different boluses at SNR=INF and 10. . . . 146
5.10 Estimated CBF, ATT, and bolus duration using the two-step model based approach at different SNRs of simulated data with different true bolus duration. . . . 148

5.11 Estimated CBF of an example subject using PCASL without and with ATT correction and Turbo QUASAR ASL at both baseline and acetazolamide conditions. 150
5.12 Mean CBF of all subjects before and after acetazolamide administration and non-parametric test results. 151
5.13 Estimated mean CVR map of the three methods. 152
5.14 Mean CVR of the group using three ASL methods. 153
5.15 Results of the paired t-test comparing the CBF before and after acetazolamide administration. 154
5.16 Corrected p-value and CBF differences of t-tests comparing CBF estimated by PCASL and Turbo QUASAR ASL in the baseline condition. 155
5.17 Corrected p-value and CBF differences of t-tests on comparing CBF estimated by PCASL and Turbo QUASAR ASL after acetazolamide administration. 156
5.18 Estimated ATT of an example subject using Turbo QUASAR ASL before and after acetazolamide administration. 157
5.19 Changes in mean ATT of the group after acetazolamide administration and non-parametric test results. 157
5.20 Changes in the mean arterial blood velocity in the carotid artery. . 158
5.21 Mean blood flow velocity of the carotid artery of SCD patients. . . 166
5.22 Estimated CBF from Turbo QUASAR ASL data using different calibration techniques. 169

A.1 Estimated GM CBF map for multi-PLD simulated data using PV estimates of subject 1 as the reference PV estimates (kernel size 5×5 for the LR methods). 180
A.2 RMSE between estimated and simulated GM CBF using noise-free simulated multi-PLD data (kernel size 5×5 for the LR methods). . . 181
A.3 ROI curve for all experiments using multi-PLD data (kernel size 5×5 for the LR methods). 182
A.4 Estimated slope values of the extended ROI analysis using multi-PLD data (kernel size 5×5 for the LR methods). 183
A.5 Estimated GM CBF map for single-PLD simulated data using PV estimates of subject 1 as the reference PV estimates (kernel size 3×3 for the LR methods). 184
A.6 RMSE between estimated and simulated GM CBF using noise-free simulated single-PLD data (kernel size 3×3 for the LR methods). . 185
A.7 ROI curve for all experiments using single-PLD data (kernel size 3×3 for the LR methods). 186

A.8 Estimated slope values of the extended ROI analysis using single-PLD data (kernel size 3×3 for the LR methods). 187
A.9 RMSE between estimated and simulated GM CBF using noise-free simulated multi-PLD data (kernel size 3×3 for the LR methods). . . 188
A.10 ROI curve for all experiments using multi-PLD data (kernel size 3×3 for the LR methods). 189
A.11 Estimated slope values of the extended ROI analysis using multi-PLD data (kernel size 3×3 for the LR methods). 190

List of Tables

3.1 List of simulation parameters 73
3.2 Experimental parameters 78

4.1 Crushing gradients in each dynamics of QUASAR ASL 101
4.2 List of simulation parameters for PASL data 102
4.3 Parameter values used in healthy cohort experiment 104

5.1 Parameter Values in Simulations 136
5.2 Experimental parameter values for PCASL 140
5.3 Experimental parameter values for Turbo QUASAR ASL 142

List of Abbreviations

ABV . . . . . Arterial blood volume

AIF . . . . . Arterial input function

ARD . . . . . Automatic relevance determination

ASL . . . . . Arterial spin labeling

ATT . . . . . Arterial transit time

BBR . . . . . Boundary-based registration

BOLD . . . . . Blood oxygenation level dependent

CASL . . . . . Continuous ASL

CBF . . . . . Cerebral blood flow

CSF . . . . . Cerebrospinal fluid

CVR . . . . . Cerebrovascular reactivity

DSC . . . . . Dynamic susceptibility contrast

EM . . . . . Expectation–maximization

EPI . . . . . Echo-planar imaging

EPISTAR . . Echo-planar imaging and Signal targeting with alternating radiofrequency

FA . . . . . Flip angle

FAIR . . . . . Flow-sensitive alternating inversion recovery

FID . . . . . Free induction decay

FLAIR . . . . Fluid attenuated inversion recovery

FLASH . . . . Fast low angle shot

FOV . . . . . Field of view

FWHM . . . . Full width at half maximum

FT . . . . . Fourier transform

GM . . . . . Gray matter

GRASE . . . . Gradient and spin echo

LR . . . . . Linear regression

MCMC . . . . Markov chain Monte Carlo

mLTS . . . . . Modified least trimmed squares

MPRAGE . . Magnetization prepared rapid gradient echo

MR . . . . . Magnetic resonance

MT . . . . . Magnetization transfer

NMR . . . . . Nuclear magnetic resonance

PASL . . . . . Pulsed ASL

PC . . . . . Phase contrast

PCASL . . . . Pseudo-continuous ASL

PD . . . . . Proton density

PET . . . . . Positron emission tomography

PLD . . . . . Post-labeling delay

PSF . . . . . Point spread function

PV . . . . . Partial volume

PVE . . . . . Partial volume effects

PVEc . . . . . Partial volume correction

PULSAR . . . Pulsed signal targeting by alternating radiofrequency pulses labeling of arterial regions

QUASAR . . . Quantitative STAR labeling of arterial regions

QUIPSS . . . . Quantitative imaging of perfusion using a single subtraction

RF . . . . . Radiofrequency

RMSE . . . . . Root-mean-square error

ROI . . . . . Region of interest

SCD . . . . . Sickle cell disease

SENSE . . . . Sensitivity encoding

SCD . . . . . Sickle cell disease

SNR . . . . . Signal-to-noise ratio

SPECT . . . . Single-photon emission computed tomography

STAR . . . . . Signal targeting with alternating radiofrequency

SVD . . . . . Singular value decomposition

TE . . . . . Echo time

TI . . . . . Inversion time

TR . . . . . Repetition time

VB . . . . . Variational Bayesian

VENC . . . . . Velocity encoding

WET . . . . . Water suppression enhanced through T_1 effects

WM . . . . . White matter

wsCV . . . . . Within-subject coefficient of variation

Les sanglots longs des violons de l'automne, blessent mon cœur d'une langueur monotone.

The long sobs of autumn's violins wound my heart with a monotonous languor...

— Paul Verlaine's *Chanson d'Automne*

1 Introduction

Contents

1.1 Motivation **1**
1.2 Cerebral Vascular Hemodynamics **2**
1.3 Measuring Perfusion **2**
1.4 Repeatability of Perfusion Measurements **4**
1.5 Cerebrovascular Reactivity **4**
1.6 Thesis Objectives **5**
1.7 Thesis Outline **5**

1.1 Motivation

Dementia is the decline of cognitive functions that induces memory loss and difficulties with thinking, problem-solving or language. The disease not only deteriorates an individual's well-being but is also causing a drastic impact on the social and economic development of the world. According to the World Health Organization, there were around 35.6 million people worldwide living with dementia in 2012. The figure is projected to double by 2030 and triple by 2050 [1]. It is estimated that care cost for dementia accounts for nearly 1% of the global GDP each year, and the figure is increasing at an unprecedented pace. Despite the awareness of dementia among the general public, our understanding of the disease is very

limited. In particular, scientists have been searching for ways to detect the early onset of dementia to ensure a more successful treatment, as studies have shown that delaying disease onset by 5 years would reduce its prevalence by 50%. On the positive side, cerebral perfusion has been identified as a potential biomarker for dementia. Several studies have demonstrated that the decrease in perfusion is linked with the onset of dementia [2][3]. Therefore, capturing the subtle changes in perfusion might be a potential diagnostic tool to detect the early onset of dementia.

1.2 Cerebral Vascular Hemodynamics

Cerebral vascular hemodynamics can reflect the overall health of brain tissue. Perfusion is one of the most important hemodynamic parameters due to its role in regulating the nutritive supply to the brain tissues. The process of perfusion is realized by cerebral blood flow (CBF) which delivers nutrients to tissues for cell metabolism. Therefore, CBF is often used as an indirect measurement of perfusion. Since perfusion is an indication of brain tissue health and its variation has been correlated with the prognosis of diseases (such as dementia), a number of perfusion quantification methods have been developed for different medical imaging modalities. An ideal method should include these characteristics: (1) accurate to reflect the genuine value of perfusion in vivo; (2) sensitive to detect the changes in CBF and other hemodynamic parameters; (3) non-invasive to be applied to a wide range of healthy subjects and patients; (4) reliable and repeatable to avoid the impact from confounding factors.

1.3 Measuring Perfusion

Perfusion quantification has been a challenge since its first description by the Nobel laureate August Krogh in his ground-breaking work on the exchange of water between muscles and blood vessels in the 1920s [4]. In 1948, Kety and Schmidt developed a novel tracer kinetic model that allowed the quantitative measurement of CBF in vivo [5]. In this experiment, the researchers estimated the CBF as a

measurement as the area between the arterial and venous washout signal of nitrous oxide (a freely-diffusible tracer in the human body) with respect to time. It was the first time that quantitative CBF measurement was achieved to reflect the physiologic functions of the brain. Subsequently, a number of studies have been conducted to quantify perfusion in different tissues using PET or MRI [6][7]. Apart from CBF, the Kety and Schmidt model also enabled the quantification of oxygen extraction and metabolism rate from the arterial and venous signals [8]. The nitrous oxide used in the original experiment has been replaced by radioactive tracer (such as isotopes of Xenon and Gadolinium) for different medical imaging modalities [9][10]. Despite the availability of this technique, its utility has been very low due to its invasive nature and side effects from using the radioactive substance. The challenge was resolved in the early 1990s by an engineering breakthrough based on magnetic resonance imaging (MRI). The new technique, dubbed arterial spin labeling (ASL) MRI, took advantage of the properties of water molecules in a magnetic field and creates a tracer of the blood water itself [11]. ASL MRI has become an increasingly popular approach to study perfusion not only because the method is non-invasive but also repeatable. Ever since the creation of ASL MRI, a variety of ASL techniques have emerged to improve the accuracy and the efficiency of cerebral perfusion measurement. In addition to CBF, the time required for the labeled bolus to move to the brain tissues, also known as the arterial transit time (ATT), can be calculated from ASL experiments. ATT has been demonstrated to be a unique biomarker for patients with carotid artery occlusion or stenosis [12]. Despite the progress on data acquisition and post-processing techniques in ASL MRI, the precise quantification of CBF is limited by partial volume effects (PVE), which are caused by the mismatch between the resolution of ASL data and thickness of the tissue of interest. In the context of perfusion MRI, it is often the GM that is of primary interest due to its major role in the central nervous system [13]. However, a subtle change in GM CBF might be masked by PVE due to the low resolution of the ASL data, causing the genuine change in GM CBF to be misinterpreted. A number of partial volume correction (PVEc) methods have been developed such as the linear regression (LR)

and the spatially regularized approach [14][15]. Although these methods have been used to correct GM CBF in ASL studies, the sensitivity of the methods for GM CBF estimation from different types of ASL data remains unknown.

1.4 Repeatability of Perfusion Measurements

The estimated GM CBF must be reliable in order for ASL techniques to be applied to clinical applications. In particular, the variations of repeated GM CBF measurements should be minimized. However, PVE contribute to the variabilities of the repeated GM CBF measurements from different sessions because the estimated GM CBF in a particular region (voxel) of an ASL image collected from one session may not contain the same amount of GM in the data collected from other sessions. The impact of PVEc on the repeatability of GM CBF needs investigating.

1.5 Cerebrovascular Reactivity

Cerebrovascular reactivity (CVR) is another hemodynamic parameter that may be of relevance in the diseases of the brain. CVR is a measure of the maximal change in CBF that can be achieved relative to the baseline CBF in response to a vasoactive stimulus. Since changing the diameter of blood vessels (by dilation or constriction) is the most effective way to regulate the delivery of nutrients by CBF, CVR reflects the capacity of tissue perfusion when the upstream blood flow varies in response to a vasoactive stimulus. Blood oxygenation level dependent (BOLD) MRI techniques applied to hypercapnia-inducing breath-hold tasks have previously been used to quantify CVR [16]. The disadvantage of BOLD MRI is that only the relative levels of oxyhemoglobin can be obtained. On the other hand, ASL MRI has the advantage of providing the absolute perfusion quantification that can be used directly for the CVR measurements. Although ASL MRI is capable of estimating perfusion for CVR measurements in theory, its application is limited by the challenges of confounding factors to CBF measurements at different flow conditions. For example, the currently recommended ASL technique (single-PLD PCASL) is limited by the

confounding factors such as variations of ATT and blood flow velocity [17], both of which would change at different flow conditions in the context of CVR estimation. A quantitative analysis is needed to investigate the impact of these confounding factors on CVR measurement using the recommended ASL technique.

1.6 Thesis Objectives

The primary objectives of the thesis are (1) to investigate the sensitivity of different PVEc methods in ASL and (2) to examine the effectiveness of applying ASL to CVR studies. A systematic study of the sensitivity of PVEc methods is conducted on the recommended implementation of ASL MRI. The aim of this work is to investigate the accuracy and consistency of different PVEc methods on data simulated using the recommended and most widely used parameters. The study also explores the impact of PVEc on the repeatability of GM CBF measurement using ASL MRI. Subsequently, the systematic analysis is extended to different ASL techniques to examine the sensitivity of the PVEc methods to different types of ASL data collected under similar conditions. The novelty of this work also includes the application of different PVEc methods on QUASAR ASL data. Finally, a study on CVR measurements using two different ASL techniques is conducted. The goal is to assess the sensitivity of ASL methods on CVR quantification as well as to investigate how different ASL techniques are limited by the changes in confounding factors due to different blood flow conditions.

1.7 Thesis Outline

Chapter 2 presents the basic principles of MRI and ASL perfusion quantification techniques. The motivation of studying cerebral perfusion is introduced to establish the foundation of the thesis. Various MRI and ASL techniques are explained to illustrate the common data collection process of perfusion MRI experiments. A number of quantification methods are explained to demonstrate how hemodynamic parameters are measured using ASL MRI. Partial volume effects (PVE) are

described to emphasize the importance of PVEc in GM perfusion quantification using ASL MRI.

Chapter 3 investigates the sensitivity of the LR and spatially regularized PVEc methods for CBF quantification from PCASL data. A systematic study is conducted to compare the accuracy of consistency of the two PVEc techniques in simulated and healthy cohort data. The evaluation metrics of the simulated experiments include the ability to preserve spatial variations and the accuracy of GM CBF estimation. For the healthy cohort data, we compare the effectiveness of different PVEc methods. The impacts of PVEc on the repeatability of GM CBF measurement are investigated to establish the importance of performing PVEc in GM CBF estimation.

Chapter 4 compares the impact of PVEc methods for GM CBF and ATT estimation on PCASL and PASL data. A systematic analysis is conducted to compare the estimated CBF and ATT after PVEc using simulated PCASL and PASL data. The PVEc methods are applied to estimating the hemodynamic parameters from QUASAR ASL data of a healthy cohort. In order to separate the signal contribution from GM and WM, a new model is developed to represent the kinetics of both tissues as well as the arterial blood component for QUASAR ASL. PVEc is performed to estimate the GM CBF and ATT from the QUASAR ASL dataset.

Chapter 5 investigates the CVR quantification using single-PLD PCASL and Turbo QUASAR ASL on a healthy cohort. ASL MRI allows the quantification of CVR by estimating CBF under different conditions. Data were collected by PCASL and Turbo QUASAR ASL before and after the administration of acetazolamide, which dilates vessels and increases CBF. A new model is proposed for the Turbo QUASAR ASL data and the various hemodynamic parameters are estimated. Estimated CVR from the two ASL techniques are compared, and regional differences are identified. The influence of transit time and blood flow velocity to CVR measurements are investigated to address the limitations of the chosen ASL techniques.

Chapter 6 summarizes the contributions of the thesis and outlines some future research directions.

Blood very likely may rush to each region of the cortex according as it is most active, but of this we know nothing.

— William James

2 Literature Review

Contents

2.1 Perfusion and Cerebral Blood Flow 8
2.1.1 Definitions 8
2.1.2 Neural Activity and Control of Cerebral Blood Flow . . 8
2.1.3 Cerebral Blood Flow and Diseases 9
2.1.4 Measuring Cerebral Blood Flow 10
2.2 Principles of Magnetic Resonance Imaging 11
2.2.1 Radiofrequency Pulse and B_1 12
2.2.2 MRI Real and Imaginary Signal 14
2.2.3 Magnetic Resonance Imaging 15
2.3 Arterial Spin Labeling MRI 26
2.3.1 Labeling Pulse 27
2.3.2 Time Delay Between Labeling and Imaging 28
2.3.3 Continuous Arterial Spin Labeling 30
2.3.4 Pulsed Arterial Spin Labeling 32
2.3.5 Pseudo-continuous Arterial Spin Labeling 36
2.3.6 QUASAR ASL 37
2.3.7 Reproducibility of Arterial Spin Labeling Techniques . . 42
2.4 Cerebral Blood Flow Quantification 43
2.4.1 Model Based Quantification Method 43
2.4.2 Model Free Quantification Method 47
2.4.3 Evaluation of Perfusion Quantification Techniques . . . 49
2.5 Arterial Transit Time Quantification 50
2.6 Bayesian Methods 51
2.6.1 Bayes' Theorem 51
2.6.2 Variational Bayes 53
2.6.3 Approximate Variational Bayes 54
2.6.4 Spatial Regularization 55
2.6.5 Automatic Relevance Determination 57

2.7 Partial Volume Effects and Correction 58
2.7.1 Linear Regression Method 59
2.7.2 Spatially Regularized Method 61
2.7.3 Tissue Volume As A Covariate Method 62
2.7.4 Partial Volume Estimates 63
2.8 Conclusions 65

2.1 Perfusion and Cerebral Blood Flow

2.1.1 Definitions

Perfusion is a general term that describes the process of nutritive delivery of arterial blood to a capillary bed in the tissue. Cerebral blood flow (CBF) delivers nutrients (such as glucose) and O_2 to tissues for cell metabolism. Since perfusion is realized by the mechanism of CBF through the delivery of nutritive substances, it is natural to use CBF as an indirect measurement to describe perfusion at various conditions, and CBF is a measurement of the delivery of the arterial blood. The physical meaning of CBF is the total volume of blood delivered to a volume of tissue in a period of time. A common unit for CBF is milliliters of blood per 100 grams of tissue per minute (ml/100g/min). Due to the close relationship between CBF and perfusion, these two terms are often used interchangeably in neuroimaging studies. Cerebrovascular reactivity (CVR) is the changes in CBF in response to vessel dilation or constriction, and CVR is defined as the ratio between CBF differences and baseline CBF. Since the level of CVR is an indication of vascular reserve and autoregulatory efficiency [18], it has become an important biomarker to assess cerebrovascular health [19]. Cerebrovascular reserve is the highest amount of increase in CBF from baseline value after stimulation.

2.1.2 Neural Activity and Control of Cerebral Blood Flow

The first observation of the relationship between neural activity and CBF was described by Roy and Sherrington in 1890 [20]. In this work, the researchers discovered a direct relationship between activation of neurons (induced by mechanical

stimulation to the nerve) and changes in blood supply (measured by aorta pressure). In essence, functional activities increased the demand for energy for metabolism, which triggered higher CBF to deliver more nutrients and O_2. Recently, a competing view was proposed by Attwell and Iadecola that challenged the direct relationship between neural activity and CBF [21]. The authors believed that the increase in CBF in functional tasks was not induced by a depletion of nutrients for higher metabolism rate, but rather by the neural activity itself. Although the two views appear to be in opposition, it is important to understand how CBF is regulated and changes in functional activities and diseases. It is commonly believed that the CBF is regulated by dilating or constricting arterioles (upstream of the capillary) which lead to changes in flow. Whilst the primary force to change CBF is the arterioles, several studies suggested the role of pericytes (a type of cell that wrap around the endothelial cells that line inside the capillaries and venules and regulates capillary blood flow) that change CBF at the capillary level. For instance, Peppiatt et al showed that pericytes were responsible for the dilation of capillary due to stimuli in the brain [22].

2.1.3 Cerebral Blood Flow and Diseases

Studying CBF enriches the understanding of diseases and improves diagnostic and treatment procedures. CBF decrease has been identified in various studies of neurodegenerative diseases, in particular at the early stage of dementia. For example, Bron et al identified the reduction of CBF in patients of early stage presenile dementia, making perfusion a potential diagnostic marker for frontotemporal dementia [13]. A recent work based on the data from Alzheimer's Disease Neuroimaging Initiative suggested that perfusion should be treated as the earliest and most predictive biomarker for Alzheimer's disease [23]. Changes in CBF (or CVR) have also been investigated in studying tissue infarction and cortical thickness due to blood disorders. For example, Kim et al demonstrated a regional association between CVR and cortical thickness in children with sickle cell disease (SCD) [24]. In cancer imaging, contrasts of CBF have been used to distinguish malignant from benign brain tumors as well as the grade of tumors [25]. Law et al showed that

relative CBF measurements improved the sensitivity and positive predictive value to determine glioma (a common brain tumor) grade [26].

2.1.4 Measuring Cerebral Blood Flow

Several methods have been developed to measure CBF in vivo. The first quantitative CBF measurement was conducted by injecting a high diffusible radioisotope into the carotid artery [27]. Yang et al demonstrated a technique based on microspheres by labeling different radioactive nuclei and measuring the radioactive decay photons [28]. One of the limitations of this approach is that the microspheres must be carefully designed to be small enough to pass the arterioles but large enough to be trapped by the capillary bed in the tissue. Single Photon Emission Computed Tomography (SPECT) has been employed to exploit gamma-emitted radioisotopes, which are injected into arteries, to produce perfusion images. Studies by Jagust et al demonstrated that SPECT perfusion imaging may provide additional information to the pathological diagnosis of dementia [29]. Positron Emission Tomography (PET) perfusion imaging was proposed as an improvement to SPECT. The radioactivity of inhaled xenon isotope (^{133}Xe) can be detected and displayed on an image with a spatial resolution of 1cm^3 [9]. Studies based on PET reported cortical CBF declines and metabolic abnormalities in Alzheimer's disease [30][10]. $H_2{}^{15}O$ has also been used as a common tracer in the PET method to quantify CBF.

In 1948, Kety and Schmidt developed a novel tracer kinetic model that allowed the quantitative measurement of CBF in vivo [5]. In this experiment, the researchers estimated the CBF as a measurement as the area between the arterial and venous washout signal of nitrous oxide (a freely-diffusible tracer in the human body) with respect to time. It was the first time that quantitative CBF measurement was achieved to reflect the physiologic functions of the brain. Subsequently, a number of studies have been conducted to quantify perfusion in different tissues using PET or MRI [6][7]. Apart from CBF, the Kety and Schmidt model also enabled the quantification of oxygen extraction and metabolism rate from the arterial and venous signals [8]. The nitrous oxide used in the original experiment has been

replaced by radioactive tracer (such as isotopes of Xenon and Gadolinium) for different medical imaging modalities [9][10]. In a simulation study, Boellaard et al showed that estimated CBF from the $H_2{}^{15}O$ method using the one-compartment model gave CBF estimation with greater than 95% accuracy [31]. This metric indicated that the method successfully estimated the simulated values in at least 95% of all the simulated trials. An alternative metric to evaluate the performance of the method would be the errors between the simulated and the estimated values. Since PET involves the exposure to ionizing radiation, it is not advised for repeated measurements [32]. Dynamic Susceptibility Contrast (DSC) MRI uses a time series of T_2-weighted images after the injection of a Gadolinium contrast agent to alter the T_2^* relaxation time of the blood water [33]. When the contrast agent passes through the tissue, it will change the signal intensity on the MR images. Together with the deconvolution of AIF, this method in theory allows CBF to be determined [25]. The major drawback of DSC MRI is the usage of Gadolinium, which poses potential risks to patients with kidney problems. Arterial spin labeling (ASL) is an MR based alternative perfusion quantification technique that uses labeled blood water as an endogenous tracer. It offers flexibility in data acquisition and repeated measurement on a wide range of population. Therefore, ASL MRI is growing in popularity as a means to investigate the quantification of perfusion and other hemodynamic parameters.

2.2 Principles of Magnetic Resonance Imaging

The field of nuclear magnetic resonance (NMR) began with the understanding of the physics of nuclear magnetism. In the 1940s, Edward Purcell and Flex Bloch both performed the first experiments demonstrating the technique of NMR [34][35]. Certain nuclei have a unique magnetic moment in a magnetic field that they rotate (precess) about the direction of the magnetic field with a frequency proportional to the field. The intrinsic angular momentum is called *spin*. In NMR, the term spin can have different meanings including (1) the intrinsic angular momentum and (2) the magnetic properties of a group of similar protons such as the spins of the

hydrogen atoms of water in a biological tissue. The exact precession frequency of a nucleus in the magnetic field is governed by its gyromagnetic ratio γ, an intrinsic property of the nucleus, and the following equation describes the relationship between the magnetic field and the frequency:

$$v_0 = \gamma B_0 \tag{2.1}$$

where v_0 and B_0 are the precession frequency and magnetic field strength respectively.

When a specimen (such as the protons of water) is placed in a magnetic field, its protons will be preferentially aligned with the magnetic field. However, there is no exchange of energy between the protons and the external magnetic field. The magnetization of all the protons can be considered to create a net magnetization M_0, which is proportional to the density of the spins (or proton density, PD) of the specimen.

2.2.1 Radiofrequency Pulse and B_1

The equilibrium magnetization M_0 is difficult to measure due to its magnitude being several order less than B_0. If we apply a second external magnetic field B_1 perpendicular to B_0, M_0 will move towards B_1. If the direction of B_1 rotates about the M_0 at the frequency v_0, all the spins that contribute to M_0 will be tipped by a flip angle (FA, α) and precess about M_0 at the same frequency, causing M_0 to be tipped by the same FA as well. Tipping over the magnetization creates a measurable signal and the process is achieved by the radiofrequency (RF) pulse. Figure 2.1 shows the process of tipping M_0 from B_0 to the transverse plane perpendicular to B_0. The oscillating RF current in the coil creates B_1 perpendicular to B_0. If the frequency of B_1 is different from v_0, it has little effect on M_0. Once the frequency of B_1 matches v_0, M_0 begins to move away from B_0 with each precessional rotation as shown in Figure 2.1. The effect of B_1 or RF pulse is often characterized by the FA, which can be adjusted by changing the amplitude or the duration of B_1.

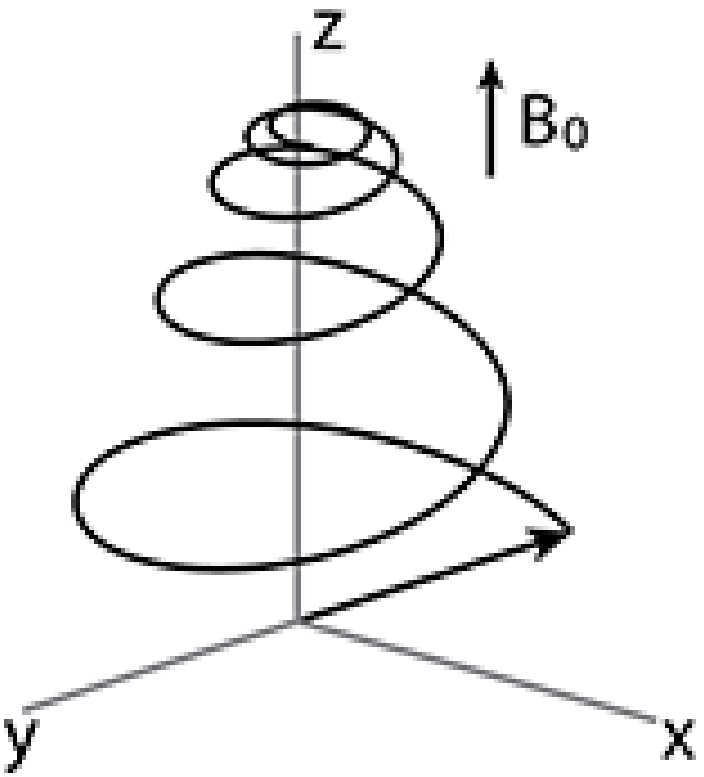

Figure 2.1: Tipping over magnetization by RF pulse. RF pulse of frequency v_0 is applied to tip over the magnetization to the transverse plane.

Once B_1 is turned off, M_0 continues to precess about B_0 and generates a signal called free induction decay (FID), as shown in Figure 2.2. Over time M_0 will move away from the transverse plane and eventually align to B_0 again. The time for M_0 to restore its alignment with B_0 is defined as T_1, and the process is known as spin-lattice relaxation. The value of T_1 refers to the time at which the magnetization reaches 63% of its maximum value. If the contrast of an image is predominately determined by the T_1 properties of tissue, it is known as a T_1-weighted image. The time for the transverse magnetic to vanish is defined as T_2, and the process is known as spin-spin relaxation. The value of T_2 refers to the time required for the transverse magnetization to fall at 37% of the initial magnetization. In reality, however, due to the inhomogeneity of B_0, the spins transverse magnetic relax at a much faster rate at T_2^*, which can be regarded as the observed T_2 and the following equation holds:

$$\frac{1}{T_2^*} = \frac{1}{T_2} + \frac{1}{T_{2i}} \tag{2.2}$$

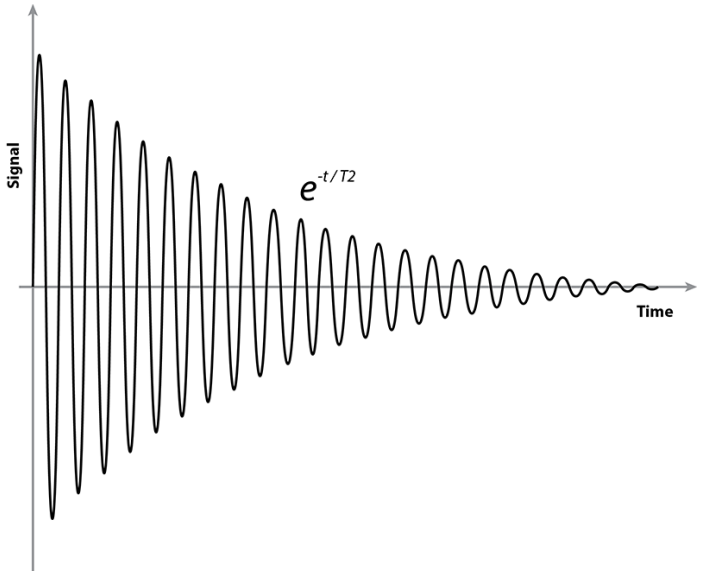

Figure 2.2: Free induction decay. After the 90 degree RF pulse to tip the spins to the transverse plane, an oscillating signal is observed and decay with T_2. In reality, due to field inhomogeneity, the signal decays more quickly under T_2^*.

Where $\frac{1}{T_{2i}} = \gamma \cdot \Delta B_i$ is the relaxation rate contribution attributable to field inhomogeneities ΔB_i of a voxel [36]. This formulation assumes that the T_2 decay curve follows Lorentzian shape and effects of microscopic diffusion have been neglected [36].

2.2.2 MRI Real and Imaginary Signal

The magnetic resonance (MR) signal is detected by two receiver coils orthogonally positioned denoted in phase (I) and quadrature (Q) respectively. In theory, the I and Q channels measure the same precessing magnetization except for a 90 degree phase shift. At the same time, the coils also detect noise, which is independent in the two channels. The quadrature design increases the SNR by a factor of $\sqrt{2}$ from a linear design of receiver coils. Thus, the MR signal of the two channels is represented using a vector with real and imaginary component. The magnitude of the vector is what is often displayed as the MR image. The phase of the vector is represented in the phase image of the signal.

2.2.3 Magnetic Resonance Imaging

An image can be formed by detecting the signal from NMR phenomenon using magnetic field gradients and Fourier transform (FT). By carefully changing the gradients and time to detect the signal, position information and contrast can be formed to reflect the anatomy of the specimen. Typically, an MRI scanner includes three magnetic field gradients in x, y, and z direction to alter the field strength of each direction. Without the change in magnetic field (or gradient), all the spins precess in the same frequency and phase, making it impossible to create a contrast or localize a region of interest (ROI). Instead, applying a gradient of magnetic field of the three dimensions makes it possible to separate the location information with different frequencies. The frequency information can be then transformed to reflect location by FT. Both 2D and 3D acquisition techniques have been developed to form MR images. In 2D acquisition, slice selection is applied followed by frequency and phase encoding. In 3D acquisition, two phase-encoding gradients are applied at the same time to two different dimensions of the imaging volume. Each of the two phase-encoding gradients loops from the maximum and minimum value. In each of the two phase-encoding gradients combinations, a frequency-encoding is applied to acquire the signal. Although 2D acquisition techniques may achieve lower SNR than the 3D techniques, they are still commonly used in perfusion imaging.

Slice Selection

The first step of forming an MR image is slice selection, usually done on the z axis. A magnetic field gradient is applied along the z axis so that the precession frequency of the spins vary along the z direction. Since the RF pulse has a very narrow bandwidth, the gradient will cause only a thin slice of spins to have the same on-resonance frequency with the RF, which makes the spins of this slice to be rotated by an FA to the transverse plane. The frequency of the spins above and below this slice is either above or below the on-resonance frequency (or off-resonance). By adjusting the gradient, different slices can be selected. Thus the combination of magnetic gradient and RF pulse allows the localization of a particular slice along the z axis.

Frequency and Phase Encoding

After a slice is localized by the slice selection technique, the spatial information within the slice needs to be determined to fully represent the specimen on an MR image. Each pixel on the MR image reflects the frequency information on the k-space (to be explained in the next section). Figure 2.3 shows the frequency and phase encoding technique. If we apply a gradient along the frequency encoding direction, the resonance frequency of the spins on the slice selected will vary linearly according to its position along the gradient. We can record the frequency on the k-space, and we are able to separate blue and red pixels as shown in Figure 2.3. However, spins at location A and B still have the same frequency, and we need a phase encoding technique to separate them. The phase encoding gradient dephases the spins of the same frequency, causing different phase shift to each of the spins. In the example of Figure 2.3, we record the aggregated signal of Step 0 and Step 1. Now we are able to separate the signal contribution from A and B using linear algebra. In essence, phase encoding needs to be applied multiple times with each frequency encoding to allow the separation of the contribution of the summed signal from the spins at different locations.

k-space

k-space is an array of numbers representing the spatial frequencies in an MR image. Performing inverse FT transforms the information of k-space into an MR image. Although it is common to divide the k-space using a grid of cells, it should be noted that k-space is continuous and the grid technique merely a way to sample the MR signal. Typically, a 2D k-space is divided into k-x and k-y directions, and data on the k-x and k-y direction represent the frequency of the x and y direction of the image respectively. The center of the k-space represents the low-frequency information such as the overall contrast of the specimen whereas the points toward the edge of the k-space represent the details of the specimen. Therefore, a high-resolution MR image has a much greater k-space than a low-resolution image. Field of view

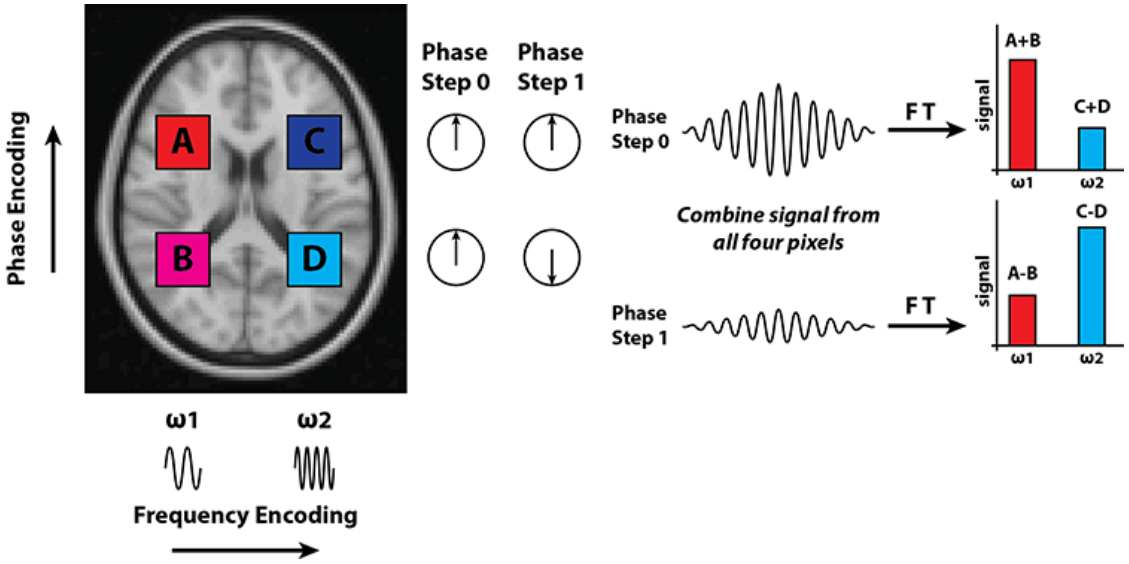

Figure 2.3: Frequency and phase encoding. A gradient is applied in the frequency encoding direction to localize the spins in this direction. Phase encoding gradient is applied repetitively to allow dephasing of the spins at different locations. The aggregated signal is Fourier transformed and the contribution from each individual pixel can be determined.

(FOV) is the spatial extend for an MR image to be displayed, and it is inversely proportional to the distance between each adjacent sample in k-space.

Spin Echo

The spin echo technique takes advantage of the signal loss in the FID to regenerate the spin phase information. Figure 2.4 shows the procedure of a typical spin echo sequence as originally proposed by Hahn [37]. Echo time (TE) is the time between the first RF pulse and the center of the echo. Repetition time (TR) is the time between each successive excitation pulses. After the first RF pulse is applied, the spins will be inverted by 90 degrees to the transverse plane. Immediately, they will undergo signal decays at the rate of T_2^*. Due to the spin-spin relaxation, the phase of the spins will become incoherent. At exactly half of TE, a second pulse is applied to invert all the spins by 180 degrees. Ideally, the spins will become more coherent and eventually refocus to form an echo at TE because they have been inverted by 180 degrees. Due to T_2^* effects, however, not all magnetization is refocused in Spin Echo.

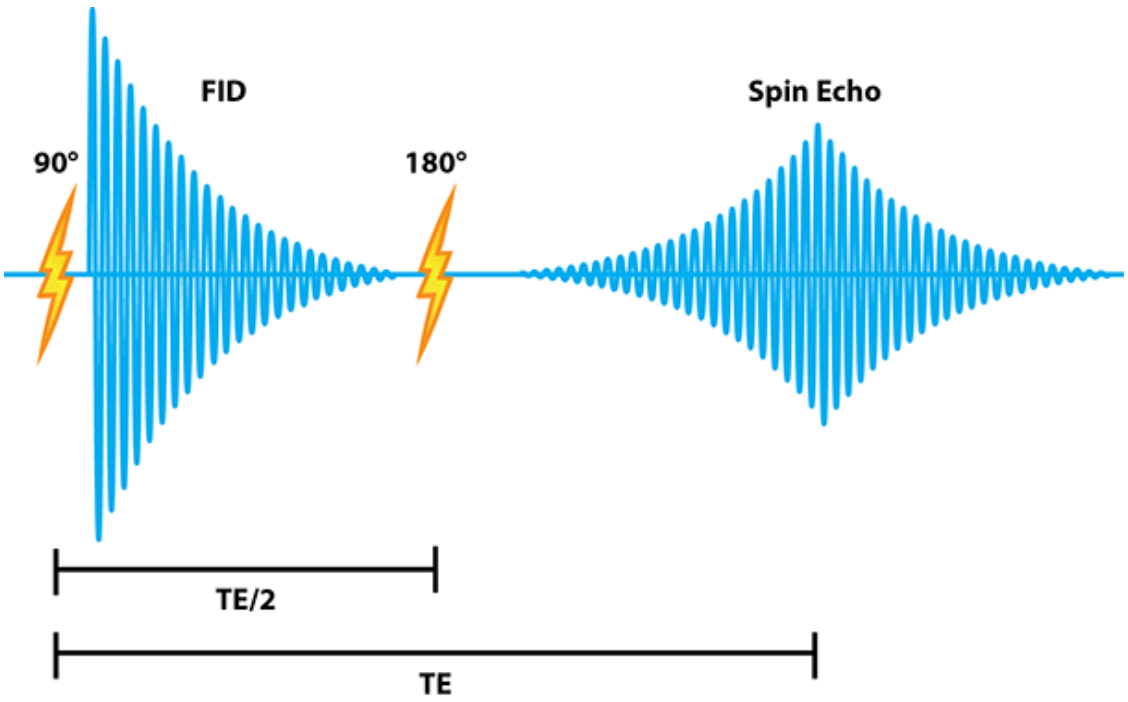

Figure 2.4: Spin echo MRI. Two pulses are used in a spin echo sequence. After the first RF pulse, the spins are inverted to the transverse plane, and the phase of the spins becomes less coherent due to spin-spin relaxation. At TE/2, a second pulse is applied to invert all the spins by 180 degrees. Gradually the spins will refocus and an echo can be formed at TE. In theory, all magnetization is refocused in a spin echo.

Gradient Echo

The gradient echo technique manipulates the FID signal by using a dephasing gradient before forming an echo [38]. Figure 2.5 shows the procedure of creating a gradient echo. After the initial RF excitation to invert the spins by 90 degrees, the spins experience spin-spin relaxation at the rate of T_2^*. A dephasing gradient is then applied, altering the resonance frequencies slightly for all the spins of the specimen and accelerating the dephasing process. Afterward, a rephasing gradient of the same strength is applied in the opposite direction of the previous dephasing gradient. The phases of each individual spin will become more coherent and an echo can be formed. In Figure 2.5, the positive gradient is kept on for twice as long as the negative gradient. As a result, the peak signal of the gradient echo is always placed in the center of k-space to improve SNR.

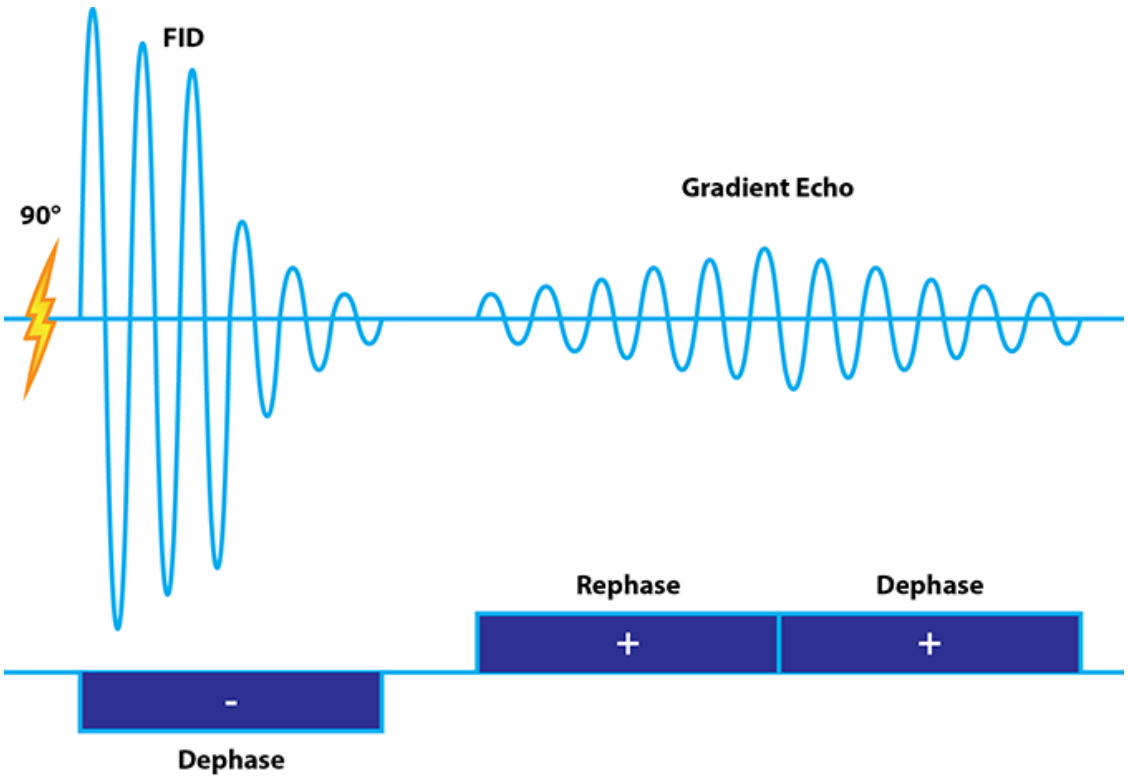

Figure 2.5: Gradient echo MRI. After the initial RF pulse, a dephasing gradient is applied to accelerate the FID of T_2^*. A rephasing gradient of the same strength of opposite polarity is then applied to reverse the phase scramble until an echo is formed.

T_1 and T_2 Weighted Images

The spins in the specimen can be characterized by two different relaxation times: T_1 and T_2. The aim of forming an MR image is to create contrast between different anatomical structures based on the T_1 and T_2 relaxation times in different types of tissues. The MR signal S can be described using the following equation [39]:

$$S \propto \rho \cdot (1 - e^{-TR/T1}) \cdot e^{-TE/T2} \tag{2.3}$$

where ρ is the proton density. In T_1 weighted images, the impact of T_2 effects is minimized by selecting a short TE (TE $\ll$ T_2) in order to allow $e^{-TE/T2} \rightarrow e^0 \rightarrow 1$. Also, a short TR is used to accentuate T_1 effects. In T_2 weighted images, the impact of T_1 effects is minimized by using a long TR to allow the magnetization of the tissues with different T_1 values to fully recover. A relatively long TE (in comparison to the short TE used in T_1 weighted images) is chosen such that the

signal is dominated by the $e^{-TE/T2}$ term and tissues with different T_2 values can be differentiated. For example, the typical TR values are less than 800 ms and TE less than 30 ms for T_1 weighted images, and the typical TR values are greater than 2000 ms and TE greater than 80 ms for T_2 weighted images [40].

Echo Planar Imaging

Echo planar imaging (EPI) is a fast imaging technique developed by Mansfield et al [41]. Figure 2.6A shows the pulse sequence diagram of a generic 2D-EPI sequence. The goal of EPI is to acquire multiple lines in k-space to reduce the acquisition time. First of all, an RF pulse is applied for slice selection. A phase encoding gradient (red) and frequency encoding gradient (purple) are then applied so that the acquisition can start from a corner (bottom left corner in this case) of the k-space. Then the interleaved positive and negative frequency encoding gradients (purple) sweeps the k-space from left-to-right or right-to-left. In the meantime, the phase encoding gradients (red) will gradually increase the phase, causing the acquisition to move step by step toward the opposite side of the k-space. For the process described, a single RF excitation pulse is used and such acquisition is known as single shot EPI (Figure 2.6B). Multi shot EPI is possible when multiple RF excitation pulses are used (Figure 2.6C).

GRASE

Gradient and spin echo (GRASE) is a hybrid technique that creates multiple gradient echoes and spin echoes from multiple RF pulses [42]. Figure 2.7 shows the original implementation of GRASE. In this work, eight spin echoes (each separated by a 180 degree refocusing pulse) were formed after one 90 degree RF pulse. In each spin echo, three gradient echoes were inserted using the EPI process. In essence, GRASE reduces the acquisition time by two factors: the total number of spin echoes and EPI gradient echoes. Figure 2.7B shows how GRASE samples signals in k-space. Instead of reading the information line by line as in single-shot EPI (Figure 2.6B), GRASE acquires multiple lines simultaneously to reduce the total acquisition time. After the first spin echo, multiple refocusing RF pulses are applied to generate

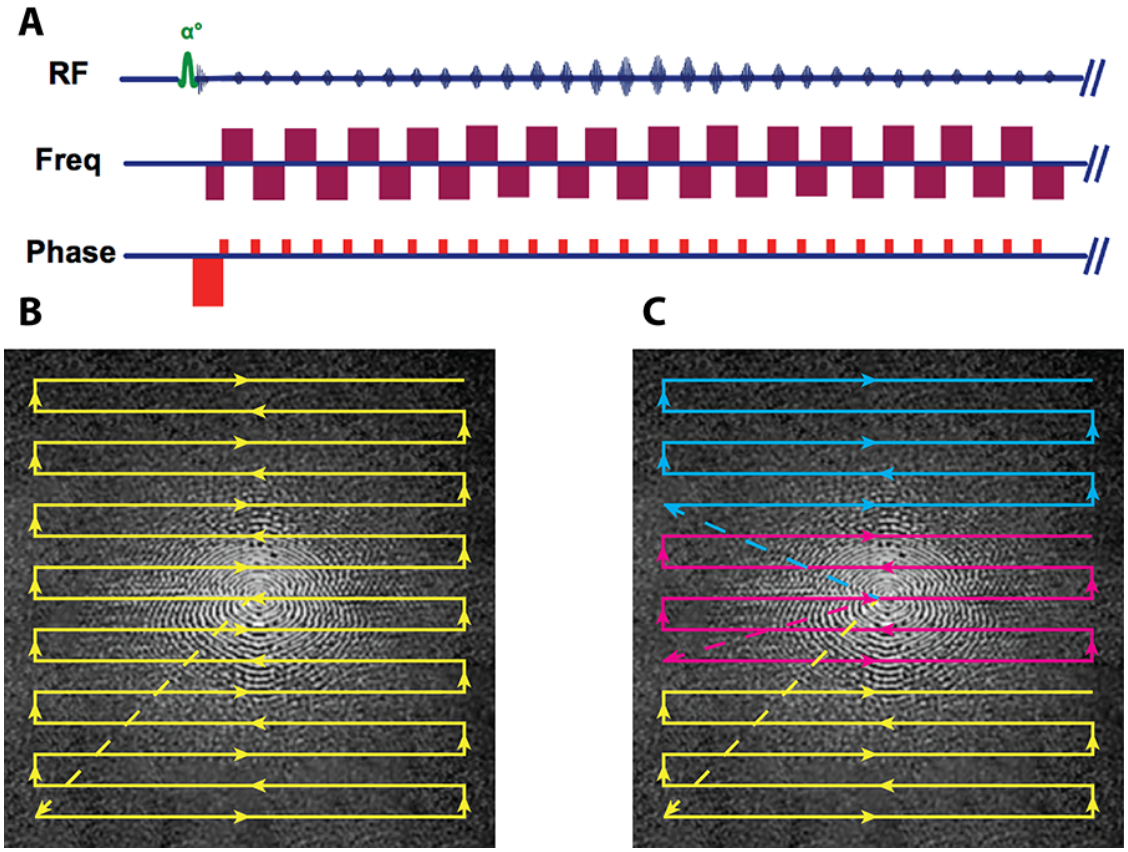

Figure 2.6: Pulse sequence diagram of 2D EPI and k-space of single and multi shot EPI. (A) In 2D EPI, a phase encoding (red) and frequency encoding (purple) lobe are placed after the initial RF pulse to position the readout from the corner of k-space (dash yellow line in B). Signal are collected by sweeping the k-space across the frequency and phase encoding domain. (B) Single shot EPI. (C) Multi shot EPI.

additional spin echoes. Between each of these spin echoes, phase-encoding gradients are employed to prepare spins for different lines of k-space. Thus, multiple lines in k-space can be acquired simultaneously. Günther et al developed a 3D GRASE technique for perfusion MRI to overcome the limited full brain coverage issue in conventional EPI readout [43]. All slices were acquired together using the echo train and later separated by 3D Fourier Transform. In a study that compared 3D GRASE and 2D EPI to achieve the same SNR, 3D GRASE showed a factor of 6-8 times reduction of total scanning time [44].

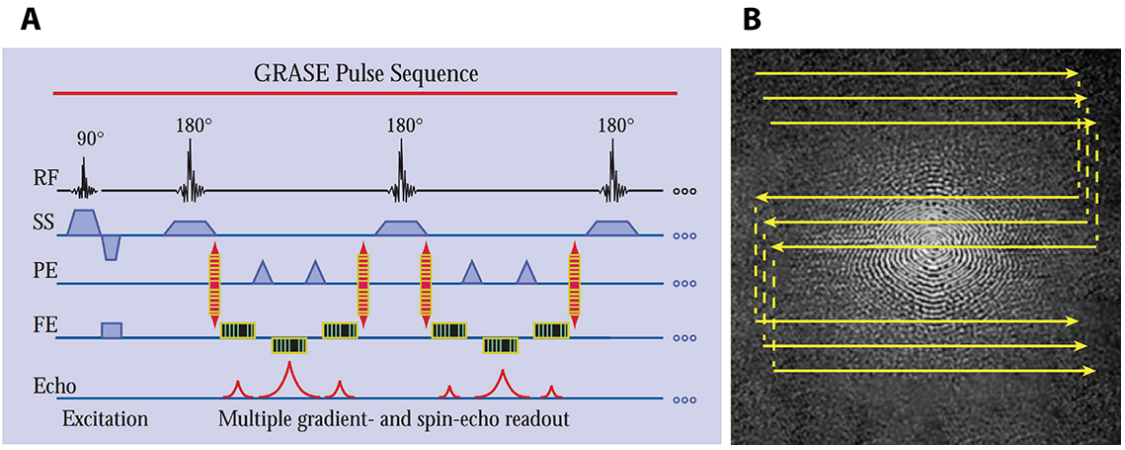

Figure 2.7: Pulse sequence diagram of GRASE acquisition and its k-space. (A) In GRASE readout, multiple gradient echoes are used and each of the gradient echo contains a number of spin echoes to reduce acquisition time [45]. (B) In this example, three spin echoes are included in each gradient echo of GRASE.

MPRAGE

Magnetization prepared rapid gradient echo (MPRAGE) is a fast T_1-weighted MRI technique commonly used for imaging anatomical structures of the brain [46]. A 180 degree inversion pulse is applied followed by a gradient echo imaging sequence. MPRAGE is a rapid T_1 image technique with high SNR and image contrast using Turbo Fast Low Angle Shot (TurboFLASH) with a short TR. A spoiling gradient, which causes incoherence of the transverse magnetization that may remain after each gradient echo sequence, can be added before each inversion pulse to allow sufficient decay of the transverse magnetization.

FLAIR

Fluid attenuated inversion recovery (FLAIR) is a commonly used MRI technique to produce T_2-weighted images developed by Hajnal et al in the early 1990s [47][48]. The characteristic of T_2-FLAIR is the very long TE (300ms) and TR (4800ms) values to minimize T_1-weighting. In the late 1990s, the development of fast spin echo sequences (using multiple 180 degree refocusing pulse in conventional spin echo) reduced the total acquisition time for T_2-FLAIR MRI, making it a standard protocol in neuroimaging studies. The inversion time of FLAIR sequence is adjusted such that the net transverse magnetization of spins in CSF is minimized [49].

Look-Locker Readout

The Look-locker readout technique was originally developed to reduce the scanning time for estimating the T_1 value of tissues [50]. In the classic technique, a single measurement at a particular inversion time was collected in an inversion recovery sequence. The process was then repeated at different inversion times while a single measurement can be taken from each inversion recovery. Model fitting techniques were then applied to estimate the T_1 value from the data collected from the inversion recovery curve. In the Look-locker method, multiple measurements were collected from a single inversion recovery using a periodic train of constant FA pulses. Due to the constant pulses, the longitudinal magnetization of the spins would be driven to a new state (lower than the classic inversion recovery technique), making the observed T_1 value different from the true T_1 to be estimated. A correction procedure is needed to compute the true T_1 from the apparent T_1 estimated from the Look-locker technique [51]. The accuracy of the correction technique can be affected by such factors as flip angle, the efficiency of saturation or inversion, and MT effects. For example, Kellman et al demonstrated that the accuracy of T_1 estimation reduced by 32% if the flip angle increased from 20 to 35 degrees for a simulated T_1 of 1200ms [52].

Parallel Imaging Methods

Sensitivity encoding (SENSE) is a parallel imaging technique to accelerate image formation after reconstruction of data from individual coils. Before acquiring the k-space data, a coil sensitivity map is obtained from each coil. After reading data of k-space from each coil, a partial FOV image is formed by each coil. Only a fraction of the lines in k-space are acquired from each coil. For example, if the acceleration factor is two, half of the lines in k-space are skipped and only half of the FOV of the image is acquired from each coil. Finally, the full FOV image is computed by incorporating the coil sensitivity maps and partial FOV images. Parallel imaging techniques have been widely applied in perfusion MRI sequences to accelerate the acquisition time.

Phase Contrast MR and Velocity Encoding

The principle of using phase contrast (PC) MR to detect velocity is that spins with different velocity undergo different phase changes in the same gradient. Figure 2.8 shows the different changes in phase between stationary and moving spins. In essence, if the spins are static, the change in phase is proportional to the time in which the gradient is applied. If the spins are moving at a constant velocity, the phase change is proportional to the square of time. If the gradient is applied longer than one unit of time as seen in Figure 2.8, then the changes in phase between the static and moving spins will be different. Applying this principle in vivo, it is possible to separate the signal from the moving and stationary spins using a pair of bipolar gradients as shown in the right plot of Figure 2.8. Suppose the imaging region contains both stationary and moving spins, such as in the neck region with the static spins in tissue water and the moving spins in arterial blood water. The first gradient is applied such that the phase of both stationary and moving spins alters but by different amounts. Immediately after the first gradient, a second gradient of the same strength is applied in opposite direction. Now the phase of the stationary spins will shift backward and return to the original phase because of the linear relationship between phase change and time applied. For the moving spins, however, the phase shift induced by the second gradient will be double of the change induced by the first gradient because the current gradient is in opposite direction. In the left plot of the Figure 2.8, it can be observed that the change in phase is proportional to time if the spins are static or proportional to the square of time if the spins are moving in a constant velocity. As a consequence, when the same gradient is applied to both static and moving spins for the same period of time, the change in phase for these two types of spins are different – the moving spins result in a larger phase shift than the static spins. After applying these two gradients, a phase difference occurs between the stationary and moving spins, resulting in contrasts of signal intensities on the MR image. By measuring the phase changes, the velocity of the moving spins can be computed. By designing the amplitude, duration, and gap of the bipolar gradients, it is possible to create different contrast from spins of

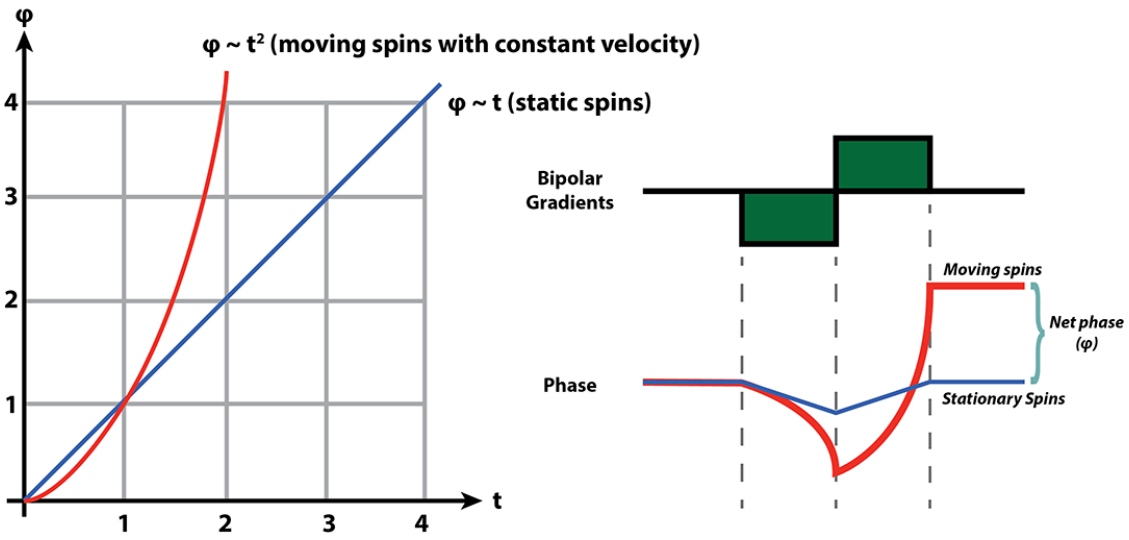

Figure 2.8: Changes in phase and phase contrast MRI. (Left) Phase change is in a linear relationship with time for static spins whereas in a quadratic relationship with time for moving spins with constant velocity. (Right) In phase contrast MRI, bipolar gradients are applied to separate the phase of stationary and moving spins.

different velocity. The velocity encoding (VENC) parameter controls the degree of sensitivity of PC MRI to various flow velocities. For example, if VENC is set to 50cm/s, flows between ±50cm/s can be represented. Figure 2.9 shows an example of PC MRI of the neck. The areas pointed by arrows indicate the carotid and vertebral arteries. The same principle can also be applied to remove (crush) the signals of spins with different velocities. For example, if our aim is to remove the signal from moving spins, it is possible to create a bipolar gradient whose property is to shift the phase of stationary spins while keeping the phase of moving spins the same.

Magnetization Transfer

The protons contributing to the signal of MRI can be characterized into two types: (1) free protons - the hydrogen atoms bonded to water molecules that move freely and have a very small range of resonance frequencies near the Larmor frequency and (2) bound protons – the hydrogen atoms on the surface of the lipid membranes in biological tissues and the hydrogen in bound water molecules associated with macromolecules. The bound protons have a much broader range of resonance frequencies than the free protons. In MRI perfusion studies, only the signal from

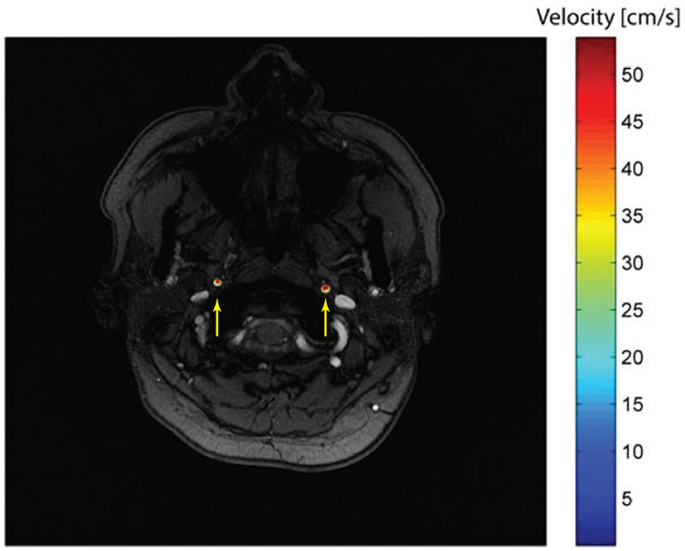

Figure 2.9: Example of the transverse plane of PC MRI of a healthy adult. Carotid arteries are pointed by the arrows, and the blood velocity can be computed from the signal intensity of the PC MRI (VENC=80cm/s).

the free protons is of interest and should be acquired to reflect the hemodynamics of the blood water. The transfer of magnetization between these two types of protons is known as magnetization transfer (MT) [53]. In spin-lattice or T_1 relaxation, the energy transfers from the free protons to the bound protons. Although the energy deposited onto the bound protons is low, some bound protons may still be driven to a higher energy or resonance state. These high energy bound protons may induce a signal if accumulated over time, causing artifacts to the desiring MR images [54]. A possible solution to reduce the artifact is by applying a pulse to saturate the high energy bound protons before acquiring the image.

2.3 Arterial Spin Labeling MRI

ASL MRI is a non-invasive technique to measure perfusion or CBF using an endogenous tracer [55]. A pair of images are obtained in an ASL experiment: label and control as shown in Figure 2.10. To acquire the label image, the magnetization of the blood water proximal to the brain is inverted by one or more RF pulses to create a bolus of tracer. The bolus travels through the vasculature to reach the brain tissue where the labeled blood water exchanges with the tissue water. In

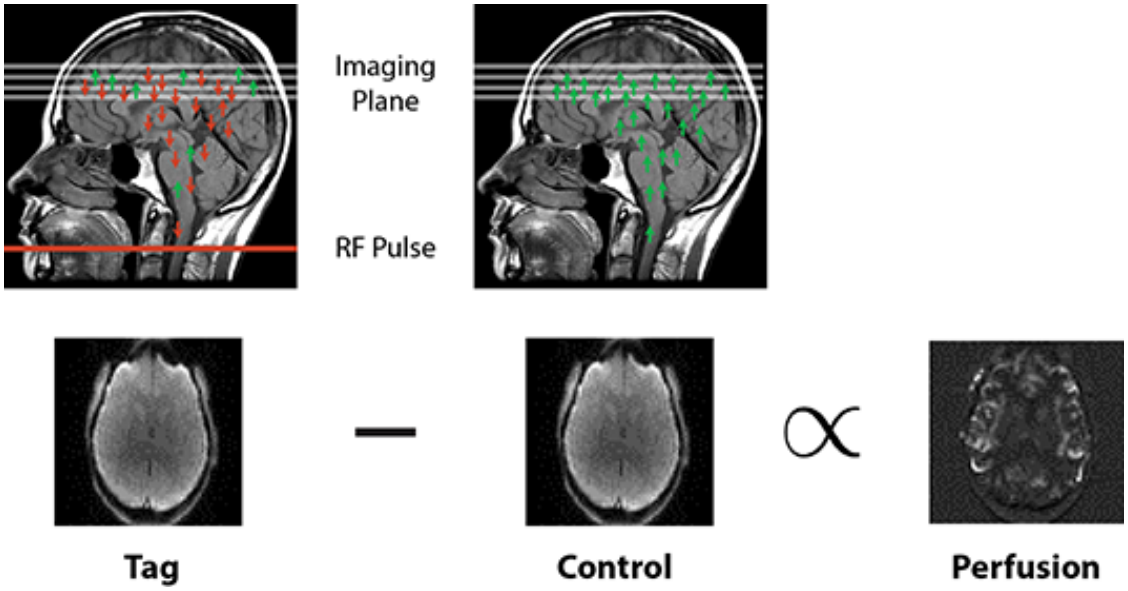

Figure 2.10: Process of a typical ASL experiment. In obtaining the label image, an RF pulse is applied to invert the spins of the inflowing blood water (red arrows) before acquiring an MR image in the imaging plane. In the control experiment, the image is acquired at the same location without applying the RF pulse to the inflowing blood (green arrows) or applying the RF pulse above the head (not shown). The difference between label and control image is proportional to perfusion in the imaging region.

acquiring the control image, the same procedure is performed but without applying the RF pulse or by placing the RF pulse above the head (not shown in Figure 2.10) to reduce MT effects in the imaging region, and no bolus is created. The difference between the label and control image is proportional to the perfusion of the tissue in the imaging region. An important condition must be satisfied in ASL experiments: the magnetization of the stationary spins in the tissue should be identical in the label and control experiments. The time needed for the bolus to reach the tissue is defined as the arterial transit time (ATT). The entire ASL procedure (both label and control experiments) is often repeated multiple times (each time is known as one repeat) to increase the SNR of the acquired image.

2.3.1 Labeling Pulse

In ASL, an adiabatic RF pulse is used to invert the spins of the inflowing blood water. Adiabatic excitation is a special type of RF stimulation that takes advantage of the off-resonance effects. The process of adiabatic excitation is illustrated in

Figure 2.11. Suppose a hydrogen proton is placed in a static magnetic field, it will precess at the resonant frequency f_0. Then a transverse RF field B_1 is applied with a constant magnitude B_1 and varying frequency f_1, where f_1 changes from less than the Larmor frequency f_0 ($f_1 < f_0$) to greater than that ($f_1 > f_0$). As the frequency f_1 varies, a magnetic field with magnitude $(f_1 - f_0)/\gamma$, where γ is the gyromagnetic ratio, is created. The process of RF inversion by the adiabatic pulse can be described in four steps: (1) When f_1 is far less than the Larmor frequency ($f_1 \ll f_0$), the effective magnetization (the net magnetization between B_1 and the magnetization induced by the pulse with the a varying frequency f_1). will precess around B_0, and the spin is not being inverted; (2) When f_1 is slightly greater but still less than f_0 ($f_1 < f_0$), the magnetization will precess around the effective field of B_{eff} because of the off-resonance effect; (3) As the f_1 continues to increase and is equal to f_0 ($f_1 = f_0$), the desired Larmor frequency is reached, and the effective magnetization is identical to B_1; (4) As f_1 keeps increasing ($f_1 > f_0$ and $f_1 \gg f_0$), the effective magnetization will eventually reach $-B_0$, and the adiabatic inversion is achieved. In practice, adiabatic inversion can be implemented in two ways: (1) set the frequency of the RF pulse to be wide enough (from $-f$ to $+f$) to achieve adiabatic inversion and (2) set the frequency of the RF pulse to be constant but altering the resonance frequency of the spins of the specimen by a magnetic gradient. The former technique is commonly applied in more stationary spins whereas the latter in more mobile spins. In essence, both implementations require the relative frequency of the RF pulse to cover a wide range of values to achieve adiabatic inversion of the inflowing spins.

2.3.2 Time Delay Between Labeling and Imaging

The time between the end of the labeling and the start of acquiring the MR image is defined as the post-labeling delay (PLD) [17]. As soon as the spins of the arterial blood water are inverted, they start to experience T_1 decay, which reduces the signal in the ASL images. The PLD must be chosen long enough for sufficient amount of labeled blood water to reach the imaging region from the labeling plane but also

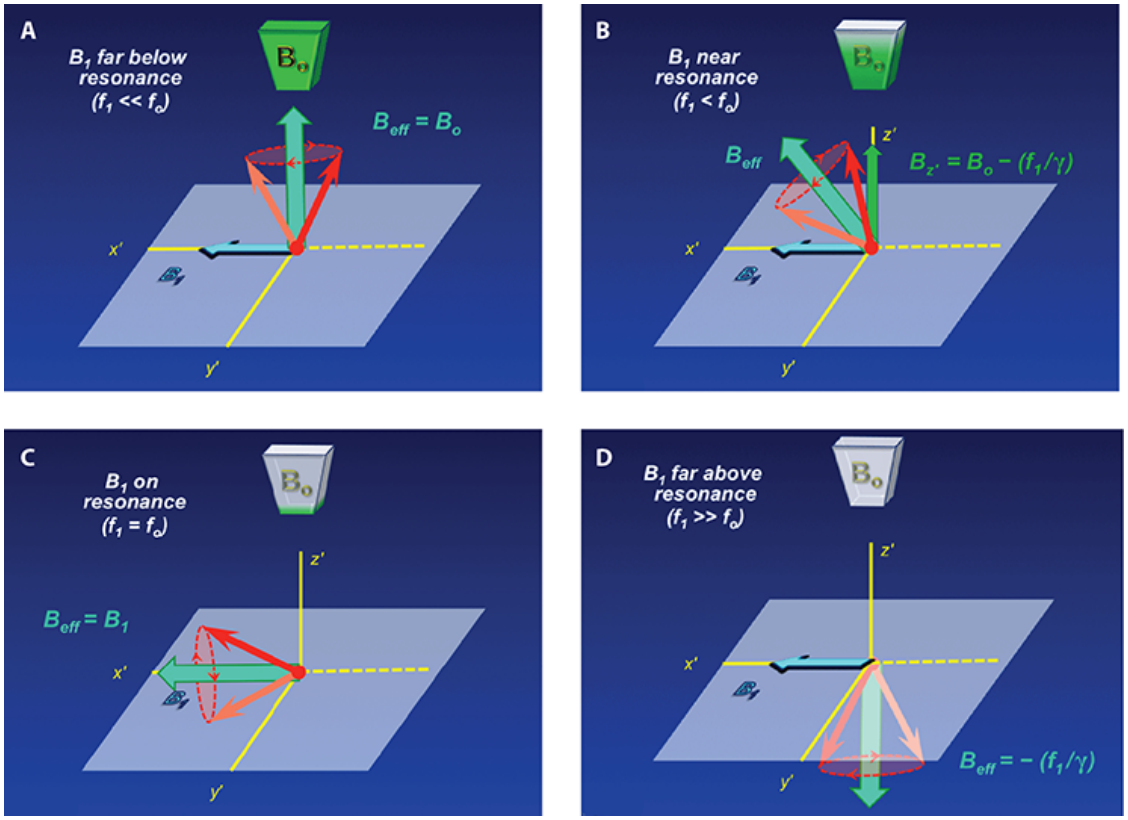

Figure 2.11: Adiabatic excitation. (A) When f_1 is far below f_0, it is off-resonance and B_{eff} is identical to B_0. (B) The increment of f_1 induces the effective magnetization to precess around B_{eff}. (C) When f_1 is equal to f_0 (Larmor frequency), it is on resonance, and the effective magnetization precesses around B_1. (D) As f_1 continues to increase, the effective B_1 will be in the opposite direction to B_0 and eventually inverted by 180 degrees to achieve adiabatic inversion. Figure reproduced with permission. http://mriquestions.com/adiabatic-excitation.html

short enough to ensure that sufficient signal can be preserved from the T_1 decay. The term inversion time (TI) is also frequently used in the ASL literature. TI is defined as the period between the start of the RF pulse and acquiring the ASL image, and it can be computed by adding PLD and the duration of the RF pulse (or bolus duration). In single-PLD ASL, a single image is acquired at a single PLD. In multi-PLD ASL, multiple images are acquired at different PLDs. A recent consensus of the ASL community has recommended a single-PLD ASL sequence with the PLD longer than 1200ms as the standard implementation of ASL in clinical applications [17]. ASL data from multi-PLD sequences have been collected in neuroimaging studies because it provides more knowledge about the physiological state of the

subject by capturing richer information about the dynamics of the tracer in the tissue. For example, the multi-PLD ASL method provides a direct measurement of ATT, which may be employed to study diseases with cerebral artery abnormalities, such as steno-occlusive disease [56]. Both single-PLD and multi-PLD ASL are available as part of the built-in packages on commercial MRI scanners.

2.3.3 Continuous Arterial Spin Labeling

In the label experiment of continuous arterial spin labeling (CASL), the magnetization of the spins of the inflowing blood water are inverted by a continuous RF pulse applied to a narrow plane below the imaging region. In the control experiment, the same RF pulse is applied above the imaging region to ensure that the static spins in the imaging region and the MT effects are identical to the label experiment [57]. The first studies of ASL were conducted using CASL based techniques on rat's brain at 4.7T [11][55]. The first application of CASL for humans was implemented by Detre et al using at 1.5T as shown in Figure 2.12A [58]. In this work, each labeling pulse consisted of four identical rectangular pulses of 18.5ms separated by a 0.16ms gap, and the labeling position was placed 3-5cm from the imaging region to reduce signal loss during arterial transit time. Label and control pulses were applied symmetrically to ensure that MT effects were fully canceled by label and control subtraction, and one slice was acquired. Perfusion was estimated using the Bloch equation method (to be explained in Section 2.4) [35]. Despite the fairly visible contrast between GM and WM, the resulting perfusion map included some severe artifact from arterial blood and lipid.

Alsop et al expanded the spatial coverage of CASL from one slice to eight slices by inverting the labeled spins twice (resulting in 360 degrees rotation) to control the MT effects in the control experiment as shown in Figure 2.12B [59]. While the acquisition and labeling parameters were similar to the work by Detre et al [58], the bolus duration was increased to 2.3s from 0.75s, and PLD was increased to 2.4s from 1.2s. The estimated mean and standard deviation of CBF of eleven

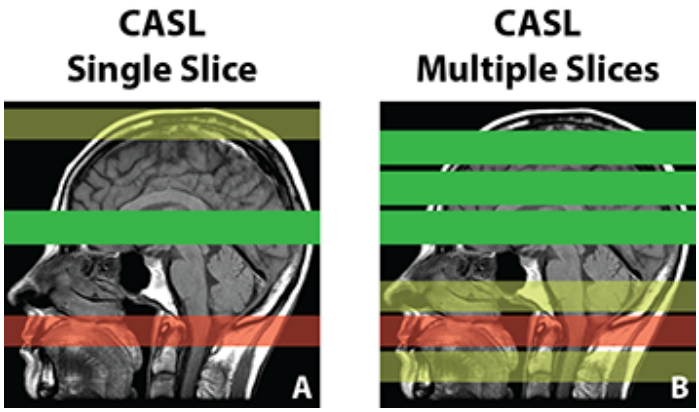

Figure 2.12: Single and multiple slices CASL implemented in vivo. (A) In single slice CASL, RF pulses (red for label and yellow for control) are applied symmetrically (below and above) to the imaging slice (green) to reduce MT effects in the label and control experiment. (B) In multiple slices CASL, RF pulse (yellow) is applied twice in the control experiment to ensure all imaging slices have the same MT effects in label and control experiments.

subjects were 57.7 ± 10 ml/100g/min, which were consistent with the previous single slice approach [58] and PET technique [60].

CASL offers the highest SNR in the acquired image among all ASL techniques due to two main reasons: (1) the bolus duration of CASL is longer than PASL therefore more labeled blood water is created in CASL. For PASL, the width of the labeling slab is typically 10-20cm thick [17] due to the limitation of the spatial coverage of the RF coil. Since the average flow velocity of the arterial blood is about 20cm/s [17], the effective bolus duration is typically less than 1s for PASL. (2) The labeled blood water (bolus) of CASL experiences less T_1 decay than PASL, which also leads to a higher SNR. The implementation of CASL is limited by the availability of hardware and high RF pulse deposition [61][62]. Since a separate RF coil is needed to create the bolus in multiple slice CASL, it must be placed at a further distance from the imaging region and most commercial scanners do not support the additional hardware [63]. At higher field (3T), although the SNR and T_1 relaxation of the labeled arterial blood water increase, the reduced RF penetration and increased power deposition may be harmful to humans, making CASL difficult to apply in vivo.

2.3.4 Pulsed Arterial Spin Labeling

Pulsed arterial spin labeling (PASL) differs from CASL by the labeling technique used to invert the spins of inflowing blood water. In PASL, labeling is conducted by applying the RF pulse in a slab (10 – 15 cm) proximal to the imaging slices as opposed to applying the RF pulse in a period of time in a much thinner region in CASL. In PASL, the time during with the RF pulse is applied to invert the inflowing spins is substantially shorter than CASL. For example in the EPISTAR sequence, the duration of the RF pulse is only 23 ms [64]. As described in the Labeling Pulse section, the frequency of the RF pulse ranges from very low to very high compared with the Larmor Frequency to achieve adiabatic inversion of the spins of the inflowing blood water. The first pulsed labeling technique was proposed by Edelman et al in an MR angiography study using the signal targeting with alternating radiofrequency (STAR) sequence as shown in Figure 2.13A [65]. In this technique, the bolus was created by alternating the phase of the RF pulse in the labeling pulse, which was applied in both label and control experiment. The differences in phase caused the longitudinal magnetization of the inflowing blood water to be inverted, and thus removing the stationary signal in the imaging region when subtraction was performed. Edelman et al created the echo-planar imaging and signal targeting with alternating radio frequency (EPISTAR) sequence for perfusion quantification in vivo using the similar technique employed in STAR at 1.5 T [64]. The inversion pulse was set to be 90mm to invert inflowing blood water, and the pulse in the control experiment was placed symmetrically superior to the imaging region. To reduce MT effects in the tissue region caused by the labeling pulse, a pre-saturation pulse was applied in the imaging plane to saturate the spins of the tissue water before image acquisition. A single slice of the image was acquired in each experiment. An improved version that included multiple slices to improve spatial coverage was developed as shown in Figure 2.13B [66]. By inverting the spins twice (360 degrees) and including a spoiler gradient to saturate the magnetization of the transverse plane in the tissue region, a near perfect cancellation of MT effects

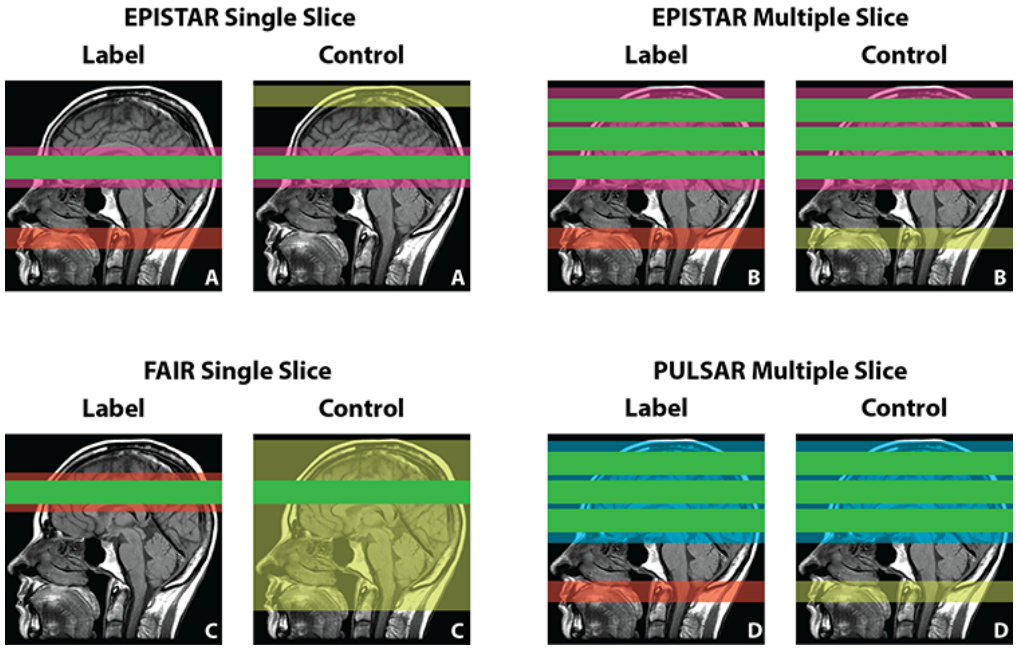

Figure 2.13: Single and multiple slices PASL. (A) In single slice EPISTAR, a saturation pulse (pink) is applied in the imaging region and RF pulses (red for label and yellow for control) are applied symmetrically (below and above) to the imaging slice (green). (B) In multislice EPISTAR, RF pulse (yellow) is applied twice in the control experiment to ensure all imaging slices have the same MT effects in label and control experiments. (C) In FAIR, the labeling plane (red) is slightly broader than the imaging plane (green) whereas the plane for the plane for control image (yellow) occupies the whole brain. (D) In PULSAR, pre and post saturation pulses (blue) are applied in the imaging region to remove the signal from static water and define a clear starting point of the bolus respectively.

was achieved in phantom studies. Perfusion results obtained from multiple slice EPISTAR method were consistent with single slice EPISTAR.

Another PASL experiment for perfusion quantification was performed by Kwong et al and Kim using similar approaches [67][68]. Kwong et al used both selective and non-selective EPI inversion recovery spin echo sequence on a 1.5 T scanner. In the labeling experiment, the selective EPI sequence was employed to invert the spins of the inflowing blood water by 180 degrees with an adiabatic pulse. In the control experiment, the non-selective sequence was applied with the same adiabatic pulse but the slice selective gradient was moved 10 ms after the inversion pulse to ensure no slice selective gradient under the inversion pulse. The combination of selective and non-selective pulse created the same MT effects in the label and control experiments, and they were eliminated after subtraction. Results of healthy control

subjects revealed clear contrast between GM and WM perfusion. Due to the low resolution of the MR images, partial volume effects were problematic in CSF and GM. Kim developed a similar flow-sensitive alternating inversion recovery (FAIR) sequence and extended to functional studies at 4T [68] as shown in Figure 2.13C. In the label experiment of FAIR, a spatially selective RF pulse is applied to invert the spins in an area slightly greater than imaging region. In the control experiment, the same RF pulse is applied but without the spatially selective gradient. As a consequence, the spatial coverage of FAIR is limited by the labeling region in which the slice selective RF pulse is applied. The results from using FAIR sequence not only demonstrated the measured relative perfusion to be consistent with other modalities such as PET with $H_2{}^{15}O$ tracer but also correlated CBF increase with functional activities (bilateral finger opposition movements). Apart from partial volume effects, the spatial coverage was limited in FAIR such that only one slice was acquired.

Golay et al developed pulsed signal targeting by alternating radio-frequency pulses labeling of arterial regions (PULSAR) sequence for quantitative analysis of regional perfusion imaging as shown in Figure 2.13D [62]. This technique was based on the multiple slice version EPISTAR sequence where RF pulses were applied to the same region in both label and control experiments. The PULSAR sequence consisted of three components: (1) water suppression enhanced through T_1 effects (WET) pre-saturation pulse in the imaging region; (2) STAR labeling pulse proximal to the imaging region; (3) post-saturation dephasing pulse in the imaging region. In the WET pre-saturation pulse [69], four pulses of different FA were used to suppress the signal from water in the imaging region. In the STAR labeling pulse, the same RF pulse developed by Edelman et al was used in both label and control experiments to ensure that the MT effects were identical [66]. A post-saturation dephasing pulse with 90 degree FA was applied to the same region with the pre-saturation pulse to ensure that a clear leading edge of the bolus. Without a clear leading edge of the bolus, the estimated CBF may be biased because the bolus is subject to dispersion effects. Perfusion was estimated using the Bloch equation method [57].

A common issue of PASL techniques is the unknown bolus duration. Since the labeling RF pulse is applied to a fixed length of region (10 – 15 mm) and the velocity of the inflowing blood varies among individuals, the exact bolus duration of each PASL experiment becomes uncertain without the precise knowledge of the blood velocity, causing inaccurate perfusion estimation (to be discussed in the perfusion quantification section). Wong et al developed the quantitative imaging of perfusion using a single subtraction (QUIPSS and QUIPSS II) sequence to ensure a well-defined bolus duration for PASL [70]. In QUIPSS, an RF pulse was applied in the label experiment to create a bolus as normal. After a period of time (t_1), during which the front edge of the bolus reaches the imaging region ($t_1 > ATT$), a saturation pulse is applied to the imaging region. Before the end of the bolus reaches the imaging region, another pulse is applied to the imaging region at time t_2 ($t_2 < ATT + \tau$, where τ is the actual but unknown bolus duration). The time difference between t_2 and t_1 is equivalent to the effective bolus duration delivered to the imaging region, which may be less than the bolus duration created by the labeling pulse. In QUIPSS II, the saturation is applied to the labeling slab region instead of the imaging region. After the RF pulse to create the bolus, a saturation pulse is applied in the labeling region at time t_1 ($t_1 < \tau$, where τ is the actual but unknown bolus duration). Similar to QUIPSS, the image is acquired at time t_2 under the condition where t_2 is longer than the ATT after t_1 ($t_2 > t_1 + ATT$). Thus, the time difference between the starting time of the RF pulse and t_1 is equivalent to the effective bolus duration.

The main drawback of PASL is the relatively low SNR and uncertain bolus duration that reduces the precise quantification of perfusion unless QUIPSS is implemented in the sequence to ensure a fixed bolus duration. Despite the fact that increasing the width of the slab may improve the duration of the bolus, several factors have limited this approach: (1) the RF coil has a limited width to produce a homogeneous field that the tagging slab should not exceed; (2) the tail edge of the bolus may be incompletely inverted and requires longer transit time to the imaging plane, increasing TR and lowering efficiency; (3) even if the width of

the slab is large enough, the tail of the bolus will travel through a much longer distance to reach the imaging plane than the front of the bolus, leading to higher signal loss. Despite such issues, the creation of PASL allowed ASL to be applied in vivo to quantify hemodynamic parameters in the early development of ASL. Thus, PASL based techniques have been available in most commercial scanners for clinical use such as single and multi-PLD PULSAR sequences on Philips and FAIR based sequences on Siemens.

2.3.5 Pseudo-continuous Arterial Spin Labeling

Pseudo-continuous arterial spin labeling (PCASL) combines the features of CASL and PASL by creating a CASL-like labeling pulse using pulsed RF and gradient fields [61]. PCASL has been developed to replace the continuous RF pulse by hundreds of short RF pulses at the rate of approximately one pulse per millisecond, and both single and multi-PLD PCASL sequences are available for perfusion quantification. In PCASL, the adiabatic inversion is performed by keeping the frequency of the RF pulse constant while changing the resonance frequency of the moving spins by applying a magnetic gradient simultaneously. As the inflowing spins moved through the gradient, the resonant frequency alters according to the location of the gradient, allowing the relative frequency of the RF pulse to vary with respect to the moving spins. Thus, the spins can undergo adiabatic inversion if the velocity v of the spins satisfies the following condition [71]:

$$\frac{1}{T_2} \ll \frac{G \cdot v}{B_1} \ll \gamma \cdot B_1 \tag{2.4}$$

where T_2 is the T_2 relaxation of the spins, G is the strength of the gradient, γ is the gyromagnetic ratio of the spins, and B_1 is the field strength of the B_1 field. The velocity term is not a constant value. Instead it indicates the mean velocity of the inflowing arterial blood. In a simulation study that investigated the inversion efficiency and the flow velocity, Utting et al demonstrated that at least 75% inversion efficiency can be achieved for velocities ranging between 9 to 20 cm/s [72].

A recent review (known as the ASL White Paper) by the ISMRM Perfusion Study Group and the European ASL in Dementia consortium has recommended single-PLD PCASL as the standard implementation of ASL in clinical applications due to its robustness and simplicity in clinical settings [17]. One of the advantages of PCASL is the higher SNR. As mentioned in the previous section, one of the drawbacks of PASL is reduced signal due to the T_1 decay of the bolus between labeling and imaging, in particular the tail of the bolus as it travels a longer distance. For PCASL, however, the spins of the inflowing blood water is inverted continuously as it passes through the labeling region, leading to less T_1 decay and stronger ASL signal. The velocity of the inflowing blood affects the labeling efficiency, which describes the fraction of spins fully inverted by the RF pulse. As seen in Equation 2.4, if the velocity of the moving spins becomes too large or small, the formulation breaks down, causing adiabatic inversion to fail.

2.3.6 QUASAR ASL

Quantitative STAR labeling of arterial regions (QUASAR) ASL has been developed to offer PASL style labeling scheme and multi-PLD acquisition using Look-locker read-out to enable the quantification of perfusion and ATT [73]. QUASAR ASL allows the quantification of the arterial input function (AIF), which measures the dynamics of the labeled blood water being delivered to the tissue region and is critical for CBF to be estimated using the deconvolution method. In order to overcome the issue of the poor temporal resolution of multi-PLD ASL methods where only one image can be acquired in each TR, QUASAR ASL uses Look-locker readout scheme that samples the ASL signals at multiple inversion times with a low flip angle in a single TR. Although the low flip angle affects the apparent T_1 relaxation of the bolus, solutions have been proposed to correct the value, making the Look-locker technique an efficient acquisition scheme [51]. Since multiple images were acquired in each Look-locker readout, a potential issue was when the first image (or the first PLD) should be taken. If the time to acquire the first image was shorter than the actual ATT to the tissue, the labeled spins would

still reside in the macrovasculature rather than the tissue, making the acquired signal a measurement of the magnetization of the arterial blood component. The signal acquired from this component is proportional to the arterial blood volume (ABV), or the percentage of signal from the macrovasculature in a certain voxel. If the signal from the arterial blood component was misinterpreted as from the tissue component, overestimation of tissue CBF would occur. Thus, the precise quantification of CBF requires the elimination of macrovasculature signals, and the exact amount of AIF and ABV must be determined.

The velocity encoding principle of MRI was applied in this case to remove the signal from the arterial blood. As discussed, the signal from the tissue is desired whereas the signal from the arterial blood is considered an artifact. By applying the bipolar gradient with specific VENC values, the signal from the spins of the moving blood can be removed (crushed) and the signal from the more stationary spins of the tissue can be preserved. Schepers et al applied this technique in a perfusion MRI study and the crushing gradients successfully removed the signal from fast-flowing spins in phantom scans [74]. QUASAR ASL employed a series of bipolar crushing gradients, which may be turned off and on in image acquisition [75]. When the crushing gradient is turned off, the measured signal includes both arterial (macrovasculature) and tissue components. When the crushing gradient is on, the signal from arterial blood was removed (crushed), leaving the tissue component. By subtracting the signal obtained without the crushing gradients from that with the gradients, the amount of magnetization from the macrovasculature can be determined. In computing the shape of AIF and the value of ABV, the exact bolus duration was needed to determine the end point of the delivery of the labeled blood. QUASAR ASL resolved this issue by including a PULSAR and QUIPSS II style pulse to identify a clear start and end of the bolus, and thus ensuring a well-defined bolus duration [62][70]. Once the AIF became available, CBF was computed by the deconvolution or model-fitting techniques (to be discussed in the next section) using the data from the tissue component. QUASAR ASL offers a number of advantages to improve the perfusion quantification including: (1) shape

of the AIF derived from the macrovasculature component to facilitate deconvolution; (2) the measurement of ABV as an auxiliary parameter from ASL experiments; (3) estimation of ATT from the tissue component. Figure 2.14 shows the schema of QUASAR ASL. The order and the purpose of the different pulses applied in QUASAR ASL is the following: (1) pre-saturation pulse (red) applied in the imaging region to remove the signal from the static water; (2) pulsed label (one 180 degrees, dark green) pulse to invert the spins of the inflowing arterial blood water or the control pulse (two 180 degrees to minimize MT effects, yellow); (3) post-saturation pulse applied in the imaging region to define a clear starting point of the bolus (dark blue); (4) bolus-saturation pulse in the labeling region to define a clear end of the bolus using the QUIPPS II technique (purple); (5) slice selective excitation pulse in the imaging region (pink); (6) bipolar crushing gradient turned on (in four out of seven dynamics of one complete QUASAR acquisition cycle) in the imaging region to saturate signal from arterial blood or turned off (in three out of seven dynamics) to include the arterial signal (light blue); (7) dual flip angle Look-locker readout sequence in the imaging region (light green).

ASL Data Quality

The effective ASL signal for perfusion estimation is the difference between the label and control signal. Typically only less than 1% of the signal change between the label and control data is retained after subtraction [76], and this signal change is governed by the number of labeled spins (or tracer). Thus, a longer bolus duration would lead to a higher SNR in an ASL experiment. For CASL and PASL data collected at 1.5T, the SNR of CASL was about 1.5 while that of PASL was less than 1 [77]. Increasing the field strength resulted in an improved SNR of 2.28 for PASL [77]. In a test-retest study using all PCASL, CASL, and PASL techniques at 3T, Chen et al reported that the SNR of PCASL and CASL is about twice as high as PASL [78]. CASL and PCASL have a higher SNR not only because of the longer bolus duration but also because the labeled spins experience less T_1 decay than PASL as the labeling plane of CASL and PCASL is much narrower than PASL.

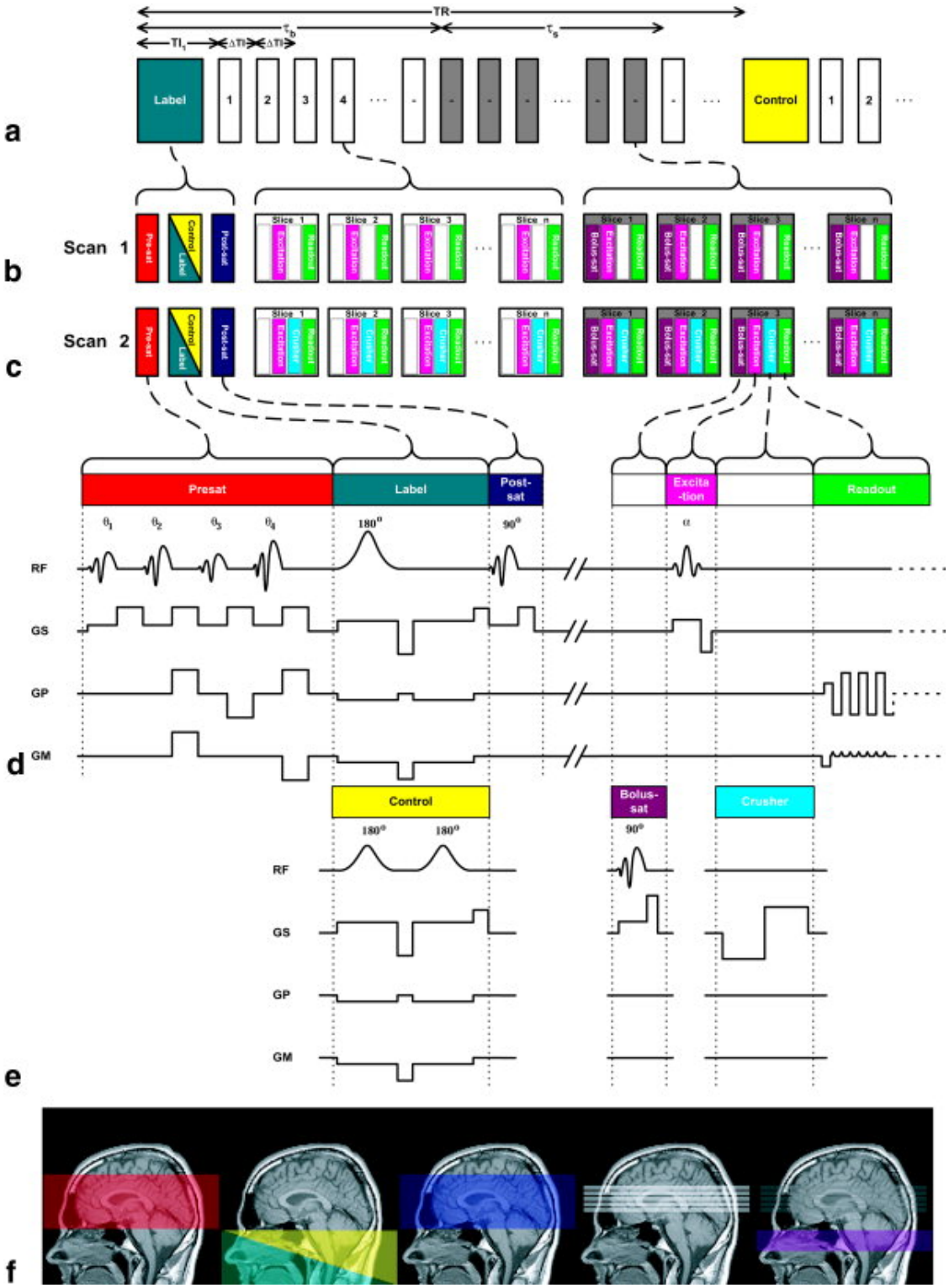

Figure 2.14: QUASAR ASL. a: PULSAR sequence to produce label and control ASL images. b: Scans without flow-suppression gradients. c: Scans with flow-suppression gradients. d: Presaturation and Look-Locker readout scheme. e: Bolus saturation to ensure well-defined bolus shape. f: positions to apply various scans [73]. Order of pulses: (1) Presaturation (red) pulse; (2) label (dark green) or control (yellow) RF pulse; (3) post-saturation pulse (dark blue); (4) bolus saturation (purple); (5) excitation pulse (pink); (6) bipolar crushing gradients on or off (light blue); (7) Look-locker readout (light green). Reproduced with permission from John Wiley and Sons.

Since all ASL techniques assume identical signal from the static tissues in the label and control experiments, the SNR of ASL data can also be improved by minimizing the static signal using background suppression techniques (to be explained).

Background Suppression

Background suppression is an MRI technique commonly used in ASL to minimize the signal of static tissue by applying pulses before each acquisition [79]. Since the label/control difference signal of ASL is less than 1% of the static tissue signal, suppressing the background signal can make the signal from static spins more consistent by reducing the unwanted signal contributions such as motion artifact, thus improving the overall SNR of the ASL difference data [76]. Including background suppression in single-PLD PCASL experiments has been recommended by the consensus paper of the ASL community [17]. Since a single inversion pulse is able to suppress the signal from spins of a particular T_1, in practice several inversion pulses are applied together to suppress signals from spins of a wide range of T_1 values [80]. However, the inclusion of several inversion pulses must be carefully designed such that the timing of these pulses can be optimized to the maximum suppression of the static signal. On the contrary, a number of studies have indicated that suboptimal use of background suppression may lead to a signal loss in the ASL difference data and reduction of the inversion efficiency. For example, Duyn et al demonstrated a 9% perfusion signal reduction with the application of a single background suppression pulse [81]. Ye et al showed that the inversion efficiency of the background suppression pulses was only 91% when a pair of background suppression pulses were employed in a FAIR sequence [82]. Therefore, the trade-off between the gain in temporal SNR of the ASL data and the signal loss due to multiple background suppression pulses must be evaluated before implementing background suppression in ASL experiments.

2.3.7 Reproducibility of Arterial Spin Labeling Techniques

In order for ASL MRI to be applied in clinical applications, the estimated CBF must be reliable and repeatable. Several reproducibility studies have been performed to evaluate the reliability of the various ASL techniques. In a study that compared PASL, CASL, and PCASL on healthy adults, Chen et al demonstrated that CBF derived from PCASL was the most repeatable followed by CASL and PASL [78]. In terms of the reproducibility of GM CBF, PCASL also achieved the highest intraclass correlation coefficientof 0.911 [78]. In investigating the longitudinal (2-4 weeks apart) reproducibility of PCASL on developing children, Varsha et al showed moderate repeatability of PCASL in the whole brain and GM CBF [83]. Mezue et al demonstrated the high sensitivity and repeatability of multi-PLD PCASL in functional tasks (within subject coefficient of variation of GM CBF was 3.32, 5.33, and 9.95 for session, week, and month repeat respectively) [84]. Inter-vendor and inter-site reproducibility of ASL have been studied to demonstrate the reliability of particular ASL techniques. For example, Mutsaerts et al compared the intra-vender and inter-vendor CBF of two slightly different single-PLD PCASL sequences [85]. Apart from the fairly consistent CBF measurements, the authors also demonstrated that small differences in ASL sequence parameters can cause greater impacts on reproducibility than vendor-specific hardware or software differences. In terms of the inter-site reproducibility, Petersen et al investigated the reproducibility of QUASAR ASL implemented on the same hardware in different locations, and the average repeatability was 12.9 for all sites [86]. As expected, the session repeat repeatability metric without subject repositioning was the highest in all experiments, and the scan planning software reduced the variability of CBF after subject repositioning.

2.4 Cerebral Blood Flow Quantification

2.4.1 Model Based Quantification Method

Bloch Equation

A Bloch equation based method was used to estimate CBF in the early development of ASL [35][39]. Assuming the exchange between blood and tissue water occurs in a well-mixed single compartment, the model describes the exchange of the longitudinal magnetization of the blood and tissue water using the formulation by William et al [11] as:

$$\begin{aligned} \frac{dM_T(t)}{dt} &= \frac{M_{0T} - M_a(t)}{T_1} + F \cdot M_a(t) - F \cdot M_v(t) \\ M_v(t) &= \frac{M_T(t)}{\lambda} \end{aligned} \tag{2.5}$$

where F is perfusion, T_1 is the T_1 relaxation of tissue, M_T, M_a, and M_v are the longitudinal magnetization of tissue, blood, and venous water respectively, M_{0T} is the longitudinal relaxation of tissue water in fully relaxed state, t is the time since the bolus is created, and λ is the blood-tissue water partition coefficient that indicates the fraction of the labeled blood water that can exchange with tissue water freely. In this equation, the rate of change in the longitudinal relaxation of the tissue $\frac{dM_T(t)}{dt}$ is modeled as the summation of the rate of change in tissue water $\frac{M_{0T}-M_a(t)}{T_1}$ and the change in magnetization of the blood water entering the brain tissue $F \cdot M_{0a}(t)$ minus the change in the magnetization of the labeled water removed by the venous blood $F \cdot M_v(t)$.

General Kinetic Model

A more general kinetic model was developed by Buxton et al for both PASL and CASL (or PCASL) techniques [87], and it is suitable for both single and multi-PLD ASL data. ASL signal is proportional to the longitudinal magnetization difference $\Delta M(t)$ between the label and control images. The amount of longitudinal magnetization in the imaging region at time t consists of three parts: the delivery of the magnetization by labeled arterial blood water, labeled tissue water washed

out by venous blood, and longitudinal relaxation of the labeled water in the tissue. These processes can be expressed by three functions of time respectively: (1) the delivery function $c(t)$ describes the magnetization arrived at the tissue at time t; (2) the residue function $r(t, t')$ is the fraction of labeled blood that arrived at time t' and remaining at time t; (3) the magnetization relaxation function $m(t, t')$ is the longitudinal magnetization of labeled blood that arrived at time t' and remains at time t. The longitudinal magnetization of the inflowing blood water in the imaging region at a given time t can be considered as the accumulation of the delivered blood water that arrives at time t' weighted by the fraction of the labeled water remaining in the imaging region. This can be represented $\int_0^t f \cdot \alpha \cdot M_{0a} \cdot c(t') \cdot r(t-t') \cdot m(t-t')dt'$, where α is the inversion efficiency, M_{0a} is equilibrium magnetization of arterial blood, f is perfusion, and the integral represents the accumulation of the labeled blood water from time zero to t. Since the spins of the inflowing blood water are inverted by 180 degrees in the label experiment, the difference between the magnetization in the label and control experiment is $\alpha \cdot M_{0a} - (-\alpha \cdot M_{0a})$ or $2 \cdot \alpha \cdot M_{0a}$. Therefore, the difference of the longitudinal magnetization between the label and control experiment can be expressed in the following:

$$\Delta M(t) = 2 \cdot \alpha \cdot M_{0a} \cdot f \cdot \int_0^t c(t') \cdot r(t - t') \cdot m(t - t')dt' \tag{2.6}$$

The integration can be replaced by convolution in the following:

$$\Delta M(t) = 2 \cdot \alpha \cdot M_{0a} \cdot f \cdot \Big\{ c(t) \otimes [r(t) \cdot m(t)] \Big\} \tag{2.7}$$

where $\otimes$ denotes the convolution operation.

If the bolus duration is τ and blood flow follows a uniform plug flow profile, no blood arrives at the imaging region before the initial transit delay Δt, also known as the ATT. Thus, the delivery function is zero during this period $c(t) = 0$. After Δt, the blood arrives and has decayed by the longitudinal relaxation time of the arterial blood T_{1b}. The delivery function $c(t)$ is different between PASL and CASL (including PCASL) techniques. In PASL, the spins of the inflowing blood water are inverted all at the same time to create a bolus of tracer, and the

spins of the bolus experience signal decay due to the T_1 relaxation immediately after labeling pulse. The bolus duration of PASL depends on the length of the slice selective inversion pulse (in EPISTAR). In CASL or PCASL however, the blood water continues to be labeled in the labeling region while the RF pulse is on. The bolus duration of CASL and PCASL depends on the total time in which the RF pulse is on. In PASL, the spins of the blood water is only labeled at $t = 0$. Then the magnetization of the labeled blood water to be delivered decreases in the exponential form $c(t) = e^{\frac{-t}{T_{1b}}}$. For CASL and PCASL, the amount of labeled blood water to be delivered is constant $c(t) = e^{\frac{-\Delta t}{T_{1b}}}$ because of the continuous labeling by the RF pulse. After the entire bolus has entered the imaging region (at time $\Delta t + \tau$), the delivery function becomes zero $c(t) = 0$. Therefore, the delivery function $c(t)$ for PASL is expressed in the following:

$$c(t) = \begin{cases} 0 & 0 < t < \Delta t \\ e^{-t/T_{1b}} & \Delta t \leq t < \Delta t + \tau \\ 0 & \Delta t + \tau \leq t \end{cases} \tag{2.8}$$

For CASL and PCASL, the delivery function is in the following form:

$$c(t) = \begin{cases} 0 & 0 < t < \Delta t \\ e^{-\Delta t/T_{1b}} & \Delta t \leq t < \Delta t + \tau \\ 0 & \Delta t + \tau \leq t \end{cases} \tag{2.9}$$

For the residue function $r(t)$ that describes the clearance of the labeled blood water by venous flow, we assume that the concentration of the tracer in the venous blood is always identical to the concentration of the remaining tracer in the tissue or $C_V = \frac{C_T}{\lambda}$ where C_V is the venous concentration and C_T is the tissue concentration respectively, and λ is the tissue/blood partition coefficient that indicates the fraction of the labeled blood water that can exchange with tissue water freely. In each short time ΔT the amount of tracer removed by the venous blood is $f \cdot C_V \cdot \Delta T$. Replacing C_V with $\frac{C_T}{\lambda}$, the formulation becomes $f \cdot \Delta T \cdot \frac{C_T}{\lambda}$. Therefore, the fraction of tissue concentration removed by the venous blood is $f \cdot \frac{\Delta T}{\lambda}$. Applying the exponential decay of the tissue concentration, the residue function can be expressed in the following:

$$r(t) = e^{-ft/\lambda} \tag{2.10}$$

Under the assumption of a single well mixed compartment where there is a full exchange of labeled blood water between the tissue and the vasculature, the bolus decays with the relaxation of tissue T_{1t}. Therefore, the magnetization relaxation function is expressed in the following:

$$m(t) = e^{-t/T_{1t}} \tag{2.11}$$

Analytical Solutions to the General Kinetic Model

Hrabe et al proposed an analytical solution for PASL based on the general kinetic model [88]. If the arterial input function is modeled as a boxcar input, where dispersion is neglected, the analytical solution of the convolution equation is:

$$\Delta M(t) = \begin{cases} 0 & 0 < t < \Delta t \\ \frac{F}{R} \cdot (e^{R \cdot t} - e^{R \cdot (t+\Delta t)} & \Delta t \leq t < \Delta t + \tau \\ \frac{F}{R} \cdot (e^{R \cdot (\Delta t+\tau)} - e^{R \cdot (t+\Delta t)} & \Delta t + \tau \leq t \end{cases} \tag{2.12}$$

where $F = 2 \cdot \alpha \cdot M_{0a} \cdot f \cdot e^{\frac{-t}{T_{1t}}}$ and $R = \frac{1}{T_{1t}} - \frac{1}{T_{1b}}$. For CASL and PCASL, the analytical solution of convolution is the following:

$$\Delta M(t) = \begin{cases} 0 & 0 < t < \Delta t \\ \frac{F}{R} \cdot e^{-R \cdot t}(1 - e^{-R \cdot (t-\Delta t)} & \Delta t \leq t < \Delta t + \tau \\ \frac{F}{R} \cdot e^{-R \cdot t} \cdot e^{-R \cdot (t-\Delta t-\tau)} \cdot (1 - e^{-R \cdot t}) & \Delta t + \tau \leq t \end{cases} \tag{2.13}$$

where $F = 2 \cdot \alpha \cdot M_{0a} \cdot f$ and $R = \frac{1}{T_{1t}} - \frac{1}{T_{1b}}$.

Direct Quantification Method from Single-PLD Data

A direct CBF quantification method was derived from the general kinetic model if specific values for the ASL MRI sequence were used [17]. The formulation has been recommended in the ASL white paper to estimate CBF in the absolute units from a single-PLD PCASL or PASL sequence when the ASL data was collected using the parameter values from the white paper [17]. The assumptions of this technique

include: (1) the bolus is completely delivered to the tissue (PLD is longer than arterial transit time); (2) the tissue compartment is sufficiently large in comparison to the arterial blood component so that no outflow of the labeled blood water occurs and water exchange between arterial blood and tissue is rapid. This assumption may become weakened if the CBF is larger than 150ml/100g/min and higher field strength (4.7T) is used in the ASL experiment [89]; (3) the decay of labeled spins is governed by the T_1 relaxation of the labeled blood. With these assumptions, PCASL CBF can be computed according to the following equation:

$$CBF = \frac{6000 \cdot \lambda \cdot (SI_c - SI_t) \cdot e^{PLD/T_{1,b}}}{2 \cdot \alpha \cdot T_{1,b} \cdot SI_{PD} \cdot (1 - e^{-\tau/T_{1,b}})}[ml/100g/min] \tag{2.14}$$

In PASL, CBF is calculated by the following [70]:

$$CBF = \frac{6000 \cdot \lambda \cdot (SI_c - SI_t) \cdot e^{TI/T_{1,b}}}{2 \cdot \alpha \cdot TI_1 \cdot SI_{PD}}[ml/100g/min] \tag{2.15}$$

where λ is the tissue/blood partition coefficient, SI_c and SI_t are the measured control and label signal intensity, PLD is the post labeling delay, $T_{1,b}$ is the T_1 relaxation of arterial blood, α is inversion efficiency, τ is the bolus duration, TI is the time point of image acquisition, and TI_1 is the bolus duration for QUIPSS II PASL, SI_{PD} is the signal intensity of a PD-weighted image acquired using a long TR that ensures the signal intensity of each voxel representing the fully relaxed spins.

2.4.2 Model Free Quantification Method

A model free method has been developed to compute the numerical solution to the convolution operation of Equation 2.7. This technique has been used frequently in perfusion quantification of DSC MRI [90][91], and it was first demonstrated on ASL using the QUASAR technique [73]. This technique was expressed as a 'model free' method for two purposes: (1) in order to be consistent with the original paper in which the technique was described [73]; (2) to reflect the fact that the AIF and residue functions of this approach were directly derived from the data instead of 'modeled' using equations. The AIF is the delivery function $c(t)$ of Equation

2.6 weighted by the inversion efficiency α and the equilibrium magnetization of the arterial blood M_{0a} in the following:

$$AIF(t) = 2 \cdot \alpha \cdot M_{0a} \cdot c(t) \tag{2.16}$$

where $c(t)$ is the term that describes the exponential decay of the signal due to the T_1 relaxation of the arterial blood. Numerical deconvolution requires the knowledge of the shape of AIF, which can be determined from the signal of the arterial blood component of QUASAR ASL because the delivery function $c(t)$ is identical in the tissue and arterial blood components. The signal of the arterial blood component is modeled using the following equation:

$$\Delta M_a(t) = 2 \cdot \alpha \cdot M_{0a} \cdot ABV \cdot c(t) \tag{2.17}$$

where ABV is the arterial blood volume, α is the inversion efficiency, M_{0a} is the equilibrium magnetization of the arterial blood, and $c(t)$ follows the same formulation in Equation 2.16. When sampling the ASL signal with the same time interval ΔTI after the bolus arrival time Δt, the discrete form of convolution of Equation 2.6 can be written as

$$\begin{aligned} \Delta M_t(t) &= 2 \cdot \alpha \cdot M_{0a} \cdot f \cdot \sum_{i=1}^{j} \Delta TI \cdot c(t_i) \cdot r(t_j - t_i) \cdot m(t_j - t_i) \\ &= \Delta TI \cdot f \cdot \sum_{i=1}^{j} AIF(t_j) \cdot R(t_j - t_i) \end{aligned} \tag{2.18}$$

where $R(t_j - t_i) = r(t_j - t_i) \cdot m(t_j - t_i)$ [92]. Since Equation 2.18 is the discrete form of the convolution operation in Equation 2.6, a numerical deconvolution method is needed to obtain the solution for CBF. Equation 2.18 can be simplified into the form of $c = A \cdot b$, where b contains the $R(t)$ vector scaled by f. By decomposing A using SVD, the inverse of A can be found to solve the linear system in Equation 2.18 [93]. At the presence of noise, this numerical deconvolution is ill-conditioned. Regularization was needed to approximate the solution by truncating certain singular values below a threshold and thus reducing the rank of the matrix. Since CBF

was obtained by the maximum of the residue signal, it became underestimated after the removal of certain singular values [94].

2.4.3 Evaluation of Perfusion Quantification Techniques

The Bloch equation model was the foundation for the early ASL studies that allowed noninvasive measurement of perfusion. However, the model neglected the inversion efficiency of the adiabatic pulse in creating the tracer. In the study by William et al that utilized the Block equation method, the inversion efficiency was assumed to be 0.9 in both humans and rats [11]. As discussed in the previous section, the changes in the velocity of the inflowing blood affect the inversion efficiency of the RF pulse. Moreover, the development of more complex labeling methods (such as pseudo-continuous labeling) decreased the labeling efficiency.

The advantages of using model based methods to estimate perfusion are twofold. First, the method is more robust to different types of ASL techniques of both PASL and CASL (PCASL). Second, the inclusion of additional parameters to be estimated provides clinicians richer information about the physiological state of the subject, which extends the application of ASL beyond perfusion estimation. For example, the estimation and mapping of ATT can be an important physiological parameter used to correlate cognitive performance in subjects with coronary artery disease due to the propensity for developing small-vessel disease [95]. In a study that investigated the ATT during functional tasks, Ho et al showed significant changes in ATT (estimated from QUASAR ASL data) during visual stimulation [96]. On the other hand, the increasing amount of parameters to be estimated (such as arterial transit time and bolus duration) complicates the perfusion quantification process.

The direct quantification approach for single-PLD PCASL has been applied by a number of studies due to its simplicity in acquisition as well as post-processing quantification [97][98]. It has also been implemented by major MRI vendors in their commercial software package such as Philip's Magnetic Resonance Imaging Connectivity release version R5.3® [99]. Despite its prevalence, this technique has numerous drawbacks because of the strict parameter values in the data collection

and an oversimplified description of the quantification model. For example, the model assumed the T_1 relaxation of tissue to be equal to arterial blood at 1650 ms for data collected by 3.0T scanners and 1350 ms for 1.5T. In most healthy subjects, however, the T_1 relaxation of tissue varies between these values [100]. The variations of these parameters values need to be considered to ensure a more accurate quantification of CBF.

The numerical deconvolution approach allows more freedom than the model based method in terms of the dissipation of the bolus, known as dispersion, making the model free method fairly robust. On the other hand, the estimated perfusion values are 10% less than those obtained by the model based approach, which has been confirmed by simulations and in vivo studies [94][101]. This problem arises from the formulation of numerical deconvolution that is known to underestimate the true results. In the numerical deconvolution method, the CBF was obtained by the maximum value of the residue signal after performing SVD. Due to the delay in arterial transit time, however, the maximum value of the observed residue signal was consistently lower than the true CBF value, leading the underestimation of CBF using the numerical deconvolution method.

2.5 Arterial Transit Time Quantification

In ASL, ATT is the period of time between the creation of the labeled bolus and the time that the arrival of the bolus at the tissue region. The distance between the labeling plane and the tissue and the velocity of the arterial blood affect the variability of ATT. The chosen ASL technique and the ROI are two important factors to determine the distance between labeling and tissue. For example, the distance is often longer in PCASL than PASL and longer in WM than GM. Blood velocity can be derived by the ratio of blood volume and the cross-sectional area of the vessel, and PC MRI is often performed. In the human body, altering the cross-sectional area is the most effective way to regulate blood velocity, which can be achieved by dilating or constricting the smooth muscle cells on the vessel walls. As a result, the cross-sectional area of the vessel is an important factor to induce changes in ATT.

For example, studies have found the ATT of cerebrovascular disease patients to be significantly longer than healthy controls due to the changes in the cross-sectional area of the vessel in the patients [102][103]. In a study that compared the gender related differences of ATT in healthy subjects, Maclntosh et al demonstrated a model-fitting technique to estimate ATT by fitting the general kinetic model [104]. Results showed that the temporal lobe had the shortest ATT whilst the occipital lobe the longest and that the mean GM ATT of male (814 ms) was found to be 15% longer than female (694 ms). Results showed that the temporal lobe had the shortest ATT whilst the occipital lobe the longest and that the mean GM ATT of male was found to be 15% shorter than female. Edge detection has been also used to estimate ATT of both arterial and tissue components from QUASAR ASL [94].

2.6 Bayesian Methods

In ASL, a generative model incorporates the physiological parameters, such as perfusion, ATT, and noise, to generate neuroimaging data. Figure 2.15 shows the generative model for ASL [105]. In reality, the aim is to extract meaningful physiological information from the data, which is an inference problem. Least square fitting methods have been developed to estimate the parameters assuming the noise to be in a Gaussian distribution [106]. The limitation of these techniques, however, includes failing to incorporate biophysical information about the unknown parameters and ignoring the uncertainty of the estimated parameters. On the contrary, Bayesian inference takes these factors into account by modeling the unknown parameters in a probability distribution.

2.6.1 Bayes' Theorem

The objective of Bayes' theorem is to infer the distribution of certain parameters subject to an established model based on the data observed [107]. Applying the theory to the ASL model M, the prior distribution (our existing knowledge) of the parameters Θ, $p(\Theta|M)$ is updated to a posterior distribution $p(\Theta|Y, M)$ by the data Y collected using the following equation:

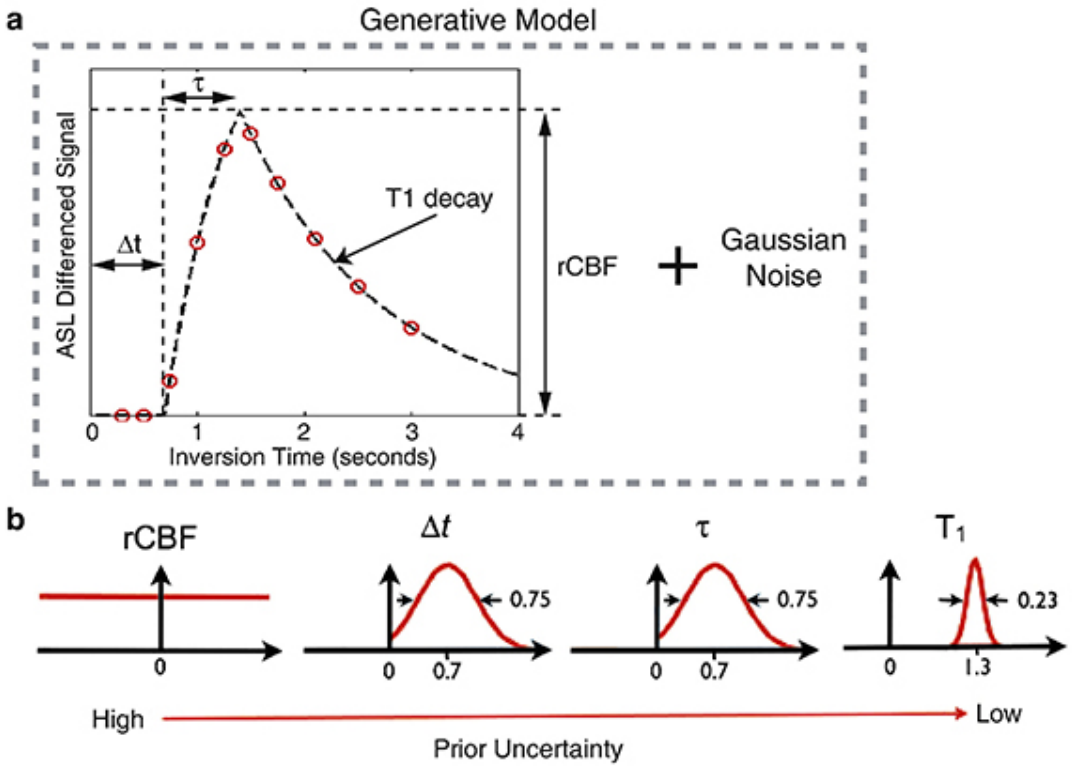

Figure 2.15: Generative model and priors for ASL. (A) The generative model consists of the tissue kinetic curve and noise. (B) Priors of the unknown parameters have different uncertainties [105]. Reproduced with permission from Elsevier.

$$p(\Theta|Y,M) = \frac{p(\Theta,Y|M)}{p(Y|M)} = \frac{p(Y|\Theta,M)\cdot p(\Theta|M)}{p(Y|M)} \tag{2.19}$$

where $p(Y|\Theta,M)$ is the likelihood that contains the generative model. It should be noted that both the prior and posterior are joint probability distributions of all the parameters to be inferred [108]. The priors can incorporate biophysical information into the analysis. For example, we are aware that the T_1 relaxation of tissue at 3T is 1.3s on average so the prior for T_1 has a mean of 1.3 and a fairly small variance. On the other hand, we have little knowledge about CBF so the prior for CBF is non-informative with zero mean and infinitive variance. The advantage of representing each parameter by a probability density function is that the biophysically plausible values of these parameters are into account while allowing the estimated parameters to differ from the existing knowledge. For example, the measured T_1 of tissue may not always be exactly 1.3s at 3T in practice.

The denominator of Equation 2.19 (or evidence term) can be represented by the distribution of the observed data marginalized over all the parameters in the following:

$$p(Y|M) = \int_{\Theta} p(Y|\Theta, M) \cdot p(\Theta|M) d\Theta \tag{2.20}$$

The integral is often not tractable and that the number of parameters can be large, both of which lead to the situation where the integration must be evaluated numerically with a large number of dimensions (parameters). A number of methods have been proposed to obtain the solution numerically. For example, Markov chain Monte Carlo (MCMC) is a numerical method that searches in the space of the posterior and draws samples from the posterior to create the posterior distribution [109]. However, MCMC is time consuming and not computationally efficient. Laplace approximation is an alternative approach that applies Taylor's expansion to approximate the posterior distribution [110]. Although it is mostly accurate and fast to compute, the posterior distribution is restricted to be a normal distribution.

2.6.2 Variational Bayes

Variational Bayes (VB) approximates the posterior distribution by estimating it using an approximated form of the posterior consisting of factorizations over subsets of model parameters. Since the denominator of Equation 2.19 indicates the evidence for the data based on the selected model, it is possible to neglect this term to derive the following:

$$p(\Theta|Y) \propto p(\Theta, Y|M) \propto p(Y|\Theta) \cdot p(\Theta) \tag{2.21}$$

The posterior probability distribution can be approximated by replacing it with a new term $q(\Theta)$, which is parameterized by several hyper-parameters, and maximizing the free energy F in the following [111]:

$$F = \int q(\Theta) \cdot log[\frac{p(Y|\Theta) \cdot p(\Theta)}{q(\Theta)}] d\Theta \tag{2.22}$$

The integral of Equation 2.22 can be factorized to be the product of each individual parameters using a variational approach:

$$q(\Theta) = \prod_i q_{\Theta_i}(\Theta_i) \tag{2.23}$$

The parameters Θ_i are grouped with their own posterior distribution $q_{\Theta_i}(\Theta_i)$, and each group must be independent. For example, the parameters of the model and noise are often separated into different groups. Each of the factors in Equation 2.23 must be simple enough such that it can be integrated to produce a tractable solution for the next update. The purpose of the variational approach was to approximate the true posterior distribution by minimizing the Kullback-Liebler distance, which was defined between the true and approximate posterior. Minimizing the Kullback-Liebler distance was equivalent to maximizing the free energy in order to find the approximate posterior [108]. For the factors to be tractable, the prior must be conjugate such that the posterior has the same distribution with the prior. The computation of each term $q_{\Theta_i}(\Theta_i)$ in the factorization can be done by maximizing $q_{\Theta_i}(\Theta_i)$ over F, and we have:

$$log[q_{\Theta_i}(\Theta_i)] = \int q_{\Theta_{i'}}(\Theta_{i'}) \cdot log[p(Y|\Theta) \cdot p(\Theta)] d\Theta_{i'} \tag{2.24}$$

where $_{i'}$ refers to the parameters not in the ith group. Since the posterior $q_{\Theta_i}(\Theta_i)$ depends on the parameters not in its group, the VB procedure follows an expectation–maximization (EM) update process where current values are used to compute for the next iteration until convergence.

2.6.3 Approximate Variational Bayes

In estimating the parameters in ASL, we consider a nonlinear forward model for each independent measurement y in the following:

$$y = g(\Theta) + \epsilon \tag{2.25}$$

where $g(\Theta)$ is the kinetic model with parameters Θ and ϵ is the Gaussian noise with precision ϕ. To use VB updates for this formulation, Θ is modeled using a

multivariate normal (MVN) distribution and ϕ using a Gamma distribution with its own hyperparameters [108]. The distributions were chosen such that they satisfy the conjugate exponential requirement of VB. In the case of ASL, this formulation is not conjugate due to the nonlinear property of the generative model, which violates the requirement of the VB method and makes the integral term analytically non-tractable. Approximate Variational Bayes method approximate the posterior to be multivariate Gaussian. Chappell et al demonstrated that using the first Taylor expansion of $g(\Theta)$ as approximation may resolve the non-tractable issue of the log-posterior in the updating process for nonlinear models [108].

2.6.4 Spatial Regularization

In perfusion quantification using ASL, the raw ASL difference data are often smoothed by a Gaussian spatial filter before quantifying perfusion and other parameters [85][106]. The purposes of the smoothing are: (1) to reduce the noise in the raw data; (2) to incorporate the assumption that parameter values in one voxel are likely to be similar to its neighbors. However, the drawback of applying the spatial smoothing is that if a single kernel size of the filter is used for the whole data, it may not be suitable for all the parameters to be estimated. Spatial priors not only resolve this issue by assigning different smoothness hyper-parameters for each parameter to be estimated, but also determines the smoothness adaptively from the raw data. Hyper-parameters are some parameters that do not affect the data but influence the prior of the model. Penny et al proposed the concept of spatial priors in the form of a MVN distribution across voxels, and the new parameter was introduced to correlate the similarity between the values of a parameter and its neighbors [112]. Groves et al modified the Gaussian process prior, which was developed for stimulus-response functions in neural recordings, to capture both biophysical knowledge of the unknown parameter and adaptive spatial regularization, thus combining the spatial and non-spatial prior in the form of a Gaussian process prior [113]. This was implemented by creating a covariance matrix whose elements

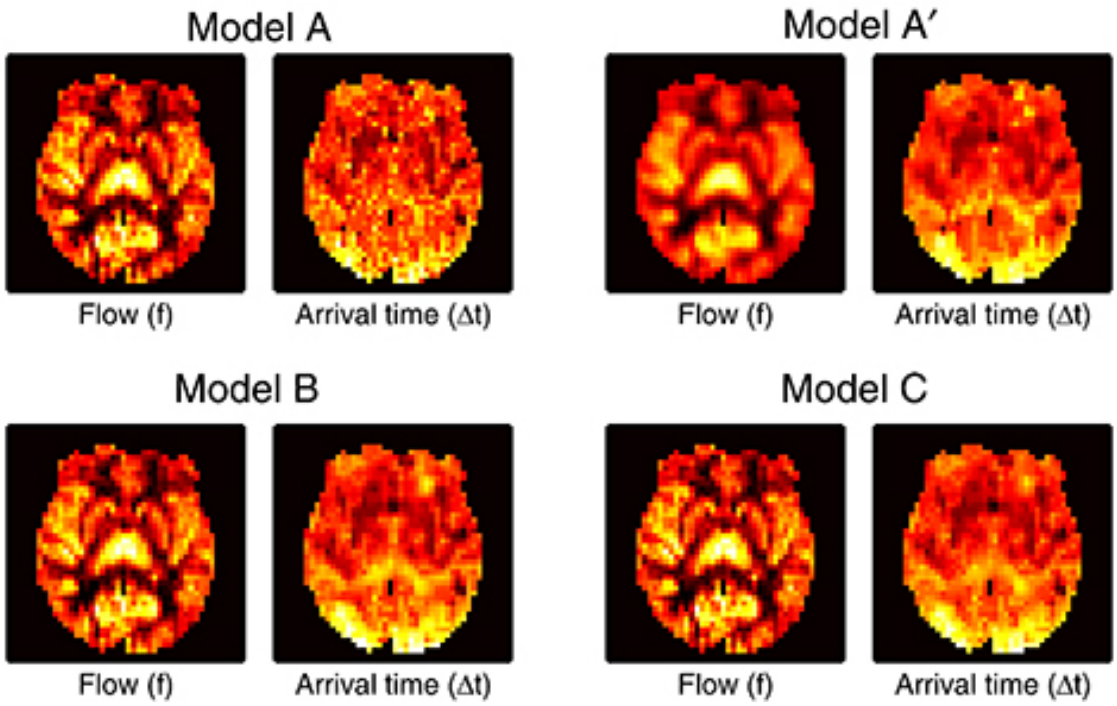

Figure 2.16: CBF and ATT maps estimated using different techniques. Spatial smoothness prior was used in all models. The smoothing techniques used to estimate ATT are non-spatial priors (Model A); Gaussian spatial filter with 6mm FWHM (Model A'); spatial smoothness only prior (Model B); Gaussian process prior (Model C) [113]. Reproduced with permission from Elsevier.

served two purposes: (1) the diagonal elements control the variance of the non-spatial prior in the VB inference; (2) the other elements control the between-voxel correlation which decreases with the Euclidean distance. CBF and ATT maps in Figure 2.16 demonstrate the different degree of smoothness using non-spatial priors (Model A), a Gaussian spatial filter (Model A'), spatial smoothness priors without the informative non-spatial prior (Model B), and Gaussian process priors (Model C) [113]. The application of spatial priors (Model B and C) achieved similar results with spatial smoothing (Model A') in artifact reduction compared with Model A. However, the spatial smoothness on CBF was different between Model A' and Model B and C due to spatial priors that allowed a different degree of smoothness for different parameters.

2.6.5 Automatic Relevance Determination

In multi-PLD ASL, it is common to capture signals from both the arterial blood and the tissue component in the first few PLDs. Since only the signal from tissue contains the true perfusion that we are interested in, the signal of the arterial blood must be excluded (such as multi-PLD ASL methods) or modeled separately. In practice, it is possible to combine both arterial blood and tissue kinetic models to create a more complicated model. Since the signal from the arterial blood only appears in certain regions of the brain such as voxels at the circle of Willis, we must make a choice on which model (tissue only or tissue plus arterial blood) to use for each voxel in our analysis. Automatic relevance determination (ARD) resolves this issue by reducing the complexity of the model. It was implemented by assigning a special prior to the parameter (such as arterial blood volume) subjected to ARD with a zero mean and unknown variance, which can be estimated in the variational Bayesian process.For an ARD parameter $\theta_A|\delta$ in θ, the prior on this parameter is:

$$(\theta_A|\delta) \sim \mathbb{N}(0, 1/\delta) \tag{2.26}$$

where the mean of the $\theta_A|\delta$ is zero and the standard deviation is $1/\delta$. Since the prior of the parameters is multivariate normal, the log-likelihood (Equation 2.24) can be expressed as:

$$L = log[P(Y|\theta, \varphi) \cdot P(\theta|\delta) \cdot P(\theta) \cdot P(\delta)] \tag{2.27}$$

Since the ARD parameter is incorporated into the existing joint distribution of the parameters, the update for θ remained the same. In each iteration, only the precision needs to be updated using the techniques in [108]. A very small estimated variance indicates that the chosen model was too complex to support to data, and a simpler model (tissue component only) to be used instead. Otherwise, the more complex model (both tissue and arterial blood components) can be used.

2.7 Partial Volume Effects and Correction

As a simplification, the brain consists of three components: gray matter (GM), white matter (WM) and cerebrospinal fluid (CSF). In the context of perfusion MRI, GM is of primary interest due to its major role in the central nervous system. Partial volume effects (PVE) refer to the loss of contrast when the signal of more than one type of tissue is being encoded in a voxel. Since ASL has a low spatial resolution with a voxel size of 3-5mm, it is unlikely for a particular voxel to encode a single type of tissue in cortical regions, where the tissue thickness is between 2 to 4 millimetres [114]. As a consequence, the estimated perfusion of each tissue type is affected by PVE. Although the PV artifact can be reduced by decreasing the size of voxels or the thickness of the imaging slice, this will reduce the SNR in the image. Since the decrease in GM CBF has been identified in the early development of dementia [13][115], it may be used as a piece of clinical evidence to diagnose dementia at an earlier stage before tissue atrophy occurs, making ASL MRI a potential diagnostic tool. However, PVE may mask the subtle changes in GM CBF. Therefore, it is important to correct PVE to improve the accuracy of GM CBF estimation and reflect the true GM CBF changes in ASL MRI.

A general description of ASL signal that incorporates both GM and WM contributions can be written as:

$$\Delta M(t) = \sum_i P_i \cdot \Delta M_i \quad i \in \{GM, WM\} \tag{2.28}$$

where ΔM is the longitudinal magnetization difference between the ASL label and control images, P_i is the PV estimates of each type of tissue, ΔM_i is the magnetization difference of each type of tissue in an ASL experiment, and t is the time since the start of the RF inversion. It has been assumed that the contribution from the CSF is zero since no ASL difference magnetization should be observed in the CSF [71][116]. This formulation holds for both single and multi-PLD ASL data. Independent estimation of either GM and WM magnetization, and hence their perfusion, is ill-posed in any given voxel since only a single

measurement of magnetization ΔM is available. PVEc methods seek to address the issue by using neighboring voxels, differing in the way this information is incorporated into the estimation process such as the linear regression based method where the neighborhood is fixed and the spatially regularized approach where the neighborhood varies.

2.7.1 Linear Regression Method

In the linear regression (LR) model, each voxel intensity, which represents the level of perfusion, is considered as the weighted sum of tissue contribution as described using the formulation of Equation 2.28 by Asllani et al [14]. The LR approach to correct PVE in ASL assumes that the CBF in both GM and WM can be treated as constant values within a 2D regression kernel with size $n \times n$ and centred at a voxel in which both GM and WM values are required. Assuming identical GM and WM CBF values in all the voxels, the ASL difference signal in the voxels within the kernel can be written in matrix form, based on Equation 2.28, as:

$$\Delta M(t) = P\Delta\bar{M} \tag{2.29}$$

Where ΔM is a vector of length n^2 containing all the ASL difference values, P is $n^2 \times 2$ matrix of GM and WM PV estimates and $\Delta\bar{M}$ is a vector with two entries for the GM and WM perfusion in the kernel. The values of matrix P can be obtained from the partial volume estimate of GM or WM transformed to the same resolution of the ASL data. A numerical solution can be obtained by the following equation that minimizes the squared error and is equivalent to linear regression:

$$\Delta\bar{M} = (P^T \cdot P)^{-1} \cdot P^T \cdot \Delta M \tag{2.30}$$

where $(P^T \cdot P)^{-1} \cdot P^T$ is the pseudo-inversion matrix of P. This calculation is repeated at every voxel within the brain to arrive at a map of PV corrected GM and WM ASL difference signal. The method can be equally applied to the final quantified perfusion image [115] and in principle can be used with different shapes of kernels, as long as they can be specified in terms of whole voxels.

Asllani et al demonstrated PVEc by improved GM CBF estimation in simulations and reduced dependency between GM PV estimates and GM CBF in healthy cohort data [14]. In the simulations, the accuracy of GM CBF estimation after PVEc was examined using a number of different kernel sizes (5×5 to 15×15). Results showed that the accuracy was negatively proportional to the kernel size due to the weaker assumption of CBF homogeneity in a larger kernel. The effectiveness of PVEc in healthy cohort data was evaluated by an ROI analysis where the correlation between GM PV estimates (from 0 to 100%) and GM CBF was plotted. Before PVEc, a positive correlation was observed indicating the mean GM CBF increased with the increment of GM tissue fraction. After PVEc, the correlation reduced with GM CBF nearly independent of GM tissue fraction. In the same study, the LR PVEc technique was applied in CBF images from a motor-task ASL data, and the activated regions expanded after PVEc.

The major drawback of the LR based methods is the loss of spatial details in the perfusion image, which is caused by the blurring effects from assuming the signal intensity to be the same within the regression kernel. Asllani et al demonstrated that the effect of spatial smoothness of using a $5^2 \times 1$ regression kernel is similar to a 5mm Gaussian filter [14]. The loss of spatial details may reduce the sensitivity of PVEc to detect subtle changes in GM CBF, and thus lowering the reliability of correcting PVE. The LR method was first demonstrated using single-PLD CASL data and later applied to multi-PLD ASL techniques such as the studies performed by Petr et al [117] and Mutsaerts et al [85]. In these two studies, PVEc was performed on the ASL difference signal of each PLD before CBF estimation, and their results showed increased mean GM CBF after PVEc.

A number of different approaches have emerged to better account for the spatial homogeneity of perfusion signal by varying the kernel shape of the LR method. For example, Ahlgren et al replaced the 2D squared kernel with a circular one for PVEc analysis of QUASAR ASL and DSC MRI data [118][119]. In both studies, the authors not only demonstrated PVEc improved GM perfusion estimation in simulations but also offered higher repeatability of perfusion measurement. A

potential issue that the authors highlighted was the variabilities of PV estimates due to flaws in registration and tissue segmentation. Liang et al proposed a modified least trimmed squares algorithm to perform PVEc on single PLD ASL data [120]. Square shaped regression kernels were used, and the method detected outliers by minimizing the sum of the squared residuals within the regression kernel. The outlier voxel was then excluded in the computing the specific tissue perfusion in PVEc.

2.7.2 Spatially Regularized Method

Chappell et al proposed an alternative spatially regularized PVEc method that adopts the model in Equation 2.28 but subjects both GM and WM CBF to spatial priors in a Bayesian inference framework. The same assumption of locally homogeneous tissue perfusion was adopted in the spatially regularized approach. Although the spatially regularized method used neighboring voxels to realize local homogeneity as in the LR approach (implemented by the regression kernel), the contribution of each of the neighboring voxels to the central voxel was different from the LR approach. This was realized by making a covariance matrix for the prior of the parameter to capture both spatial and non-spatial information of the parameter to be estimated. The matrix was constructed such that its diagonal elements encode the non-spatial information and the remaining elements reflect the spatial information, which was modeled using an exponential decay function with respect to the Euclidian distance between two voxels and regulated by an adaptive correlation-distance term (δ_k in [113]) estimated from the smoothness of the data. Based on Equation 2.28 where the ASL signal was decomposed into GM and WM contributions, the spatially regularized PVEc algorithm attempts to estimate both GM and WM CBF in every voxel, with each being subject to a prior distribution on the value derived from the estimated values in the neighboring voxels using spatial priors [112][113]. As explained in the section of Bayesian inference, the estimation of the tissue perfusion is an iterative scheme whereby the voxel values are updated, followed by an update to the prior and so on. Through Bayes' theorem, the estimated values in any given voxel reflect both the measured data in the voxel

and the prior information, with the balance being determined automatically, hence making the spatial regularization adaptive to the data.

The spatially regularized approach has been demonstrated to perform better than the LR approach in preserving spatial details of the GM CBF image in a study that used multi-PLD PASL [15]. In this work, a number of artificially spatial variations were created on simulated GM CBF maps, which were then used to generate simulated ASL images. Both LR and spatially regularized PVEc methods were applied to estimate the GM CBF from these simulated ASL data. The estimated GM CBF results were evaluated by assessing the spatial variations preserved, as well as the estimation accuracy of each PVEc methods. The simulation results revealed that the spatially regularized method was superior to the LR methods implemented using 5×5 and 9×9 kernel sizes in preserving the edges and sinusoidal variations in the GM CBF maps after PVEc. Results from healthy control data showed that the GM CBF estimated by the spatially regularized PVEc method became less dependent on GM PV estimates, indicating the bias of WM CBF in GM perfusion estimation reduced and thus a successful PVEc.

2.7.3 Tissue Volume As A Covariate Method

In investigating CBF differences between different groups, the impact of partial volume effects has been accounted as a covariate in the analysis of the un-corrected CBF values [121]. The volume of each type of tissue, represented by partial volume estimates, was considered a voxel-wise covariate in comparing the voxel-wise CBF difference in group analysis, thus attempting to reduce the impact on group-wise CBF differences of PV effect. In essence, considering the PV estimates as covariates models the impact of partial volume effects as an extra linear explanatory variable. This is in contrast to the LR and the spatially regularized methods which regard the PV estimates as multiplicative factors in the corresponding tissue signal. Hence, such covariate-based PVEc approach is limited if the absolute tissue perfusion is desired because PV estimates are merely modeled as a confounding factor instead of correcting for the fractional contribution of specific tissue signals to the total signal.

2.7.4 Partial Volume Estimates

In correcting PVE, the exact contribution of each type of tissue on a voxel must be determined. A common practice is to segment the T_1-weighted structural images to compute the fraction of different types of tissues, known as the PV estimates or PV maps, in each voxel. A number of tools have been developed to segment tissue maps such as FSL, SPM, and FRASIER [122][123]. SPM provides tissue probability maps as part of the segmentation results. Instead of using PV estimates, these tissue probability maps have been used as PV estimates in the PVEc process in several studies [115][117]. It should be noted that the PV estimate of each tissue type differs from its probability value, although both have the same range of value between 0 to 100%. The tissue PV estimate indicates how much percentage of the space in a voxel is occupied by a particular type of tissue. On the other hand, tissue probability describes the likelihood of the voxel to be classified to a particular type of tissue. Misusing the tissue probability maps as tissue PV estimates leads to a systematic bias in PVEc, causing the tissue perfusion to be wrongly estimated after partial volume correction because the contribution (true PV estimates) of the total perfusion from each type of tissue in a particular voxel is wrongly represented by the likelihood of classifying this voxel to a specific type of tissue. As a consequence, the uncertainties in PV estimates affected the PVEc, particularly in low tissue PV estimate regions. In FSL FAST, the segmentation algorithm aimed to fit a mixture model representing the combined histogram of GM, WM, and CSF to the intensities of the structural image [124]. The underlying mechanism of the segmentation process is based on a hidden Markov random field model and an associated EM algorithm. Spatial priors were encoded in the tissue classification parameters to incorporate the spatial homogeneity of tissue types to refine the segmentation results [105]. Although using tissue probability maps as priors may enhance the bias field estimation in FAST, it may also cause misalignment of the registration process between the input data and the template, leading to segmentation errors [105].

In order for the PV estimates to be used in PVEc (the P_i term in Equation 2.28), they must be transformed into the same resolution of the ASL data. Chappell

et al demonstrated the registration by using a multi-stage procedure in the FSL tool FLIRT [125] as well as a more recently developed tool ASL_REG that utilized the Boundary-Based Registration (BBR) technique to derive the transformation matrix [126]. In the registration of ASL_REG, the WM contour was aligned to the perfusion weighted ASL image. Samples of the ASL image were taken from a fixed distance of both sides of the contour, and the difference between the intensities in each pair is used to compute the cost function. The resulting transformation matrix was then used to transform the PV estimates to the ASL resolution. A two-step process of transformation was developed by Chappell et al and implemented using the FSL tool APPLY_WARP [15], and they consisted of supersampling and downsampling as shown in Figure 2.17. The high resolution (red squares) PV estimates were first upsampled (supersampled) to an even higher resolution (blue squares) using interpolation techniques. Then the image in the super resolution (blue squares) space was downsampled to the low resolution (black squares) space by taking the mean of the voxel intensities within the low resolution boundary. This technique ensured all the information enclosed within the low resolution voxel was sufficiently used in the image transformation.

Apart from using the high-resolution T_1 weighted image to segment the tissue PV estimates, an alternative approach using an estimated T_1 image at the ASL resolution was proposed by Petr et al [117]. In this work, T_1 of GM and WM were estimated by fitting a saturation recovery model to a multi-PLD PASL data acquired by a Look-locker EPI readout. The T_1 image was then segmented to produce voxel-wise tissue probability maps using an approach based on the FRASIER segmentation method [123]. WM tissue fractions were determined by thresholding the T_1 values between 642 and 814 ms. GM tissue fractions were obtained using an iterative method that minimized the residual between the data and fitted signal. Due to the limitation of some segmentation algorithms, such as FRASIER [123], PV estimates may not be available directly from the segmentation results because these values, represented by fractional volumes in FRASIER, must be converted from the fractional signals using the assumed water density for different types of tissues

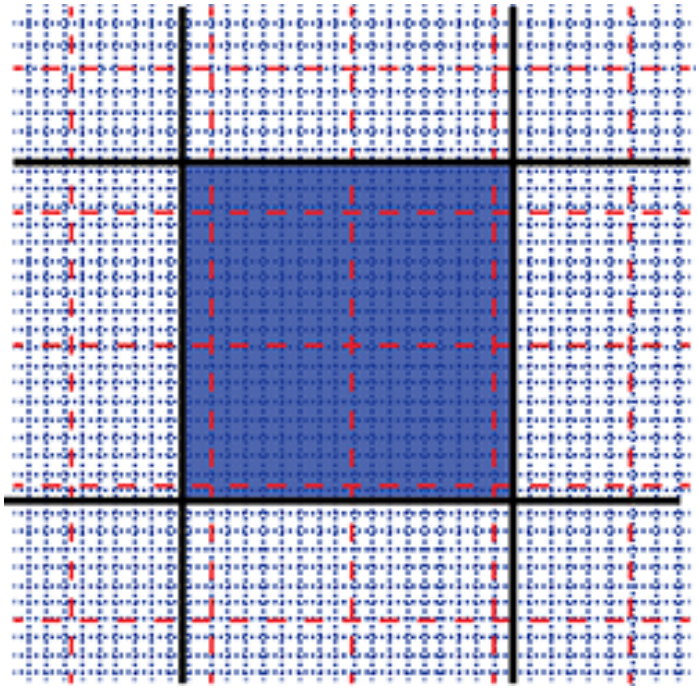

Figure 2.17: Transforming PV estimates from high resolution to low resolution for PVEc. The high resolution (red squares) PV estimates is first upsampled to an even higher resolution (blue squares) before downsampled to the desiring low resolution (black squares).

(0.73, 0.89, and 1.00 for WM, GM, and CSF respectively), and the tissue probability maps were used as PV estimates [85][115][117]. The misinterpretation of tissue probability maps may cause systematic bias in PVEc.

2.8 Conclusions

In conclusion, ASL MRI has become a popular means to investigate perfusion and other hemodynamic parameters. A variety of data acquisition techniques and quantification methods have made ASL MRI a promising tool for clinical applications. Since PVE affects the precise quantification of GM CBF using ASL MRI, it would limit the application of ASL in detecting the subtle changes in GM CBF as a biomarker for diagnosing the early onset of dementia. Despite the various PVEc techniques developed, a systematic study is needed to investigate the sensitivity of these techniques to different variabilities in ASL data as well as the impact of PVEc onto the repeatability of ASL (to be investigated in Chapter

3). Among the various ASL techniques, it is not clear whether a particular type of ASL sequence (PCASL or PASL) is superior in terms of quantifying GM CBF and ATT while correcting the bias of PVE. Hence, it is important to investigate the performance of different ASL methods after PVEc (to be investigated in Chapter 4). Since CVR may be an important biomarker for dementia and that its quantification using ASL MRI has not been established, there is a need to investigate the most suitable ASL technique for the purpose of CVR measurements at different blood flow conditions (to be investigated in Chapter 5).

¿Quien vé correctamente la cara humana: el fotógrafo, el espejo, o el pintor?

Who sees the human face correctly: the photographer, the mirror, or the painter?

— Pablo Ruiz Picasso

3

Investigating Partial Volume Correction Using PCASL

Contents

3.1 Introduction 68
3.2 Theory 69
3.2.1 Linear Regression 70
3.2.2 Spatially Regularized 71
3.3 Methods 71
3.3.1 Data 71
3.3.2 Partial Volume Estimation 72
3.3.3 Simulated Data 73
3.3.4 Perfusion Estimation and Partial Volume Correction . . 75
3.3.5 Simulation Study 77
3.3.6 Evaluation Metrics for Partial Volume Correction 79
3.3.7 Repeatability Study 81
3.4 Results 82
3.4.1 Simulation Study: Single-PLD Data (Kernel Size 5×5 for the LR Methods) 82
3.4.2 Healthy Cohort Experiments 89
3.5 Discussion 90
3.5.1 Simulation Study 91
3.5.2 Healthy Cohort Experiments 94
3.5.3 Limitations 96
3.6 Conclusions 97

3.1 Introduction

The ASL signal obtained from the brain broadly arises from three sources: gray matter (GM), white matter (WM), and cerebrospinal fluid (CSF). The ASL signal from CSF is ideally zero on the basis that no labeled blood water should reach the CSF [71] [116]. In the context of perfusion MRI, it is often the GM that is of primary interest due to its major role in the central nervous system and that subtle changes in GM CBF have been observed in studies of various diseases including dementia [127]. However, ASL data has a low spatial resolution with a voxel size of 3–5 mm that is unlikely to encode a single type of tissue, particularly in cortical regions where the thickness of GM is between 2 and 4 mm [114], leading to partial volume effects (PVE). Whilst all MR imaging in the brain suffers from PVE, it is particularly noticeable in perfusion imaging because of the distinctly different perfusion properties of GM and WM: a perfusion ratios of 3:1 is quite commonly assumed.

It is increasingly being recognized that it may be important to correct PVE to allow GM CBF to be quantified independently of any confounding effects of partial voluming with either WM or CSF. This may be especially relevant for studies involving patients with tissue atrophy [128] where changes in tissue content in voxels could mask or be misinterpreted as changes in perfusion. Several partial volume correction (PVEc) methods have been developed to correct PVE in perfusion estimation from ASL data including linear regression (LR) [14] and a spatially regularized technique that uses spatial priors in a Bayesian inference framework for perfusion quantification [15]. In the LR approach, each voxel intensity is considered as the weighted sum of different tissue contributions. By assuming the perfusion of the central voxel to be equal to its neighbors in a small region, defined by a regression kernel, the perfusion from each type of tissue is estimated by solving a linear system of equations. The spatially regularized method, motivated by the use of spatial information in the LR approach, exploited adaptive spatial priors within an existing Bayesian approach to ASL perfusion quantification, separating the signal into contributions from GM and WM. Studies on multi-PLD PASL have demonstrated the superiority of the spatially regularized method for maintaining

spatial details in the estimated GM CBF image over the LR approach [15]. Both PVEc methods require the knowledge of the exact fraction of tissue in each voxel, known as the PV estimates, which are typically computed by tissue segmentation from a high-resolution T_1-weighted image. However, flaws in the segmentation procedures may introduce error into the PV estimates that could affect the accuracy of PVEc. In addition, PVEc will also be affected by limitations in ASL data acquisition such as background noise and mismatch in the point spread function (PSF) between the ASL acquisition and that of the structural image from which the PV estimates are obtained. The impact of these factors on PVEc methods has not been fully explored, and a comprehensive study is needed to investigate how PVEc methods respond to these factors.

In the present study, we investigate the sensitivity of existing PVEc methods to errors in the PV estimates when applied to PCASL. Two studies were performed: firstly, a simulation study was used to investigate the sensitivity of the methods to a variety of theoretical sources of variability including random error and bias in the PV estimates, along with the effect of noise on the ASL data and differences in the PSF between ASL and structural images. Simulated single-PLD PCASL data were generated using the tissue kinetic model and the parameters in the ASL Consensus Paper [17]. Simulated multi-PLD PCASL data were created using the parameters (PLD and bolus duration) of a previously published reproducibility study of multi-PLD PCASL in neuroimaging studies [84]. Secondly, we performed PVEc on a healthy cohort dataset obtained from this study [84]. The repeatability of CBF images from each PVEc method was assessed by computing the within-subject coefficient of variation (wsCV) under the assumption that PVEc should improve the overall repeatability of perfusion quantification by reducing random variability in measured CBF due to PVE in each subject.

3.2 Theory

A general description of ASL signal that incorporates both GM and WM contributions can be written as:

$$\Delta M(t) = P_{GM} \cdot \Delta M_{GM}(t) + P_{WM} \cdot \Delta M_{WM}(t) \tag{3.1}$$

where ΔM is the longitudinal magnetization difference between ASL label and control images, P is the PV estimates of each type of tissue, and t is the time since the start of RF inversion. It has been assumed that the contribution from CSF is zero since no ASL difference magnetization should be observed in the CSF. This formulation holds for both single and multi-PLD ASL data. Independent estimation of either gray or white matter magnetization, and hence their perfusion, is ill-posed in any given voxel since only a single measurement of magnetization (ΔM) is available. PVEc methods seek to address this by using neighboring voxels, differing in the way this information is incorporated into the estimation process.

3.2.1 Linear Regression

The linear regression approach to correct PVE in ASL assumes that the CBF in both GM and WM can be treated as constant within a 2D regression kernel with size $n \times n$ and centered at a voxel in which both GM and WM values are required. Assuming identical GM and WM CBF values in all the voxels, the ASL difference signal in the voxels within the kernel can be written in matrix form, based on Equation 3.1, as:

$$\Delta M(t) = P\Delta\bar{M} \tag{3.2}$$

where ΔM is a vector of length n^2 containing all the ASL difference values, P is $n^2 \times 2$ matrix of GM and WM PV estimates and $\Delta\bar{M}$ is a vector with two entries for the gray and white matter perfusion in the kernel. A numerical solution can be obtained by the following equation that minimizes the squared error and is equivalent to linear regression:

$$\Delta\bar{M} = (P^T \cdot P)^{-1} \cdot P^T \cdot \Delta M \tag{3.3}$$

where $(P^T \cdot P)^{-1} \cdot P^T$ is the pseudo-inversion matrix of P, ΔM is the vector that contains all the ASL difference values in the regression kernel. This calculation is

repeated at every voxel within the brain to arrive at a map of PV corrected GM and WM ASL difference signal. The method can also equally be applied to the final quantified perfusion image [115] [129] and in principle can be used with different shapes of kernels, as long as they can be specified in terms of whole voxels.

3.2.2 Spatially Regularized

An alternative spatially regularized approach as originally proposed by Chappell et al. [15] adopts the formulation in Equation 3.1, but subjects both the GM and WM to spatial priors within a Variational Bayesian (VB) inference framework. This method was motivated by the same principle as the LR method, in which tissue perfusion is assumed to be homogeneous in a local region, but it relaxes the strict kernel assumption of LR by allowing the spatial regularization to be adaptively determined by the data. In essence, the algorithm attempts to estimate both GM and WM contributions in every voxel by fitting the ASL difference data to Equation 3.1, with the perfusion (as well as other hemodynamic parameters such as transit time) of each type of the tissues being subject to a prior distribution on the value derived from the estimated values in the neighboring voxels, the so-called spatial prior [113] [112]. This is an iterative scheme whereby the voxel values are updated, followed by an update to the prior (both the spatial prior and the priors of the parameters, as discussed in Section 2.6.4). Through Bayes' theorem the estimated values in any given voxel reflect both the measured data in the voxel and the prior information, with the balance being determined automatically, hence making the spatial regularization adaptive to the data. Although it was originally demonstrated on multi-PLD ASL data [15], the approach is also applicable to single-PLD ASL.

3.3 Methods

3.3.1 Data

One hundred high-resolution PV estimates images (GM, WM, and CSF) were randomly extracted from the first release of the UK Biobank Imaging Study to be used in the simulated experiments [130]. These PV estimates were segmented from

the T_1-weighted images of the same study. Scan parameters were: 3D MPRAGE; sagittal; in-plane acceleration factor = 2; TI/TR = 880/2000 ms, voxel size = 1 × 1 × 1 mm; matrix = 208 × 256 × 256; acquisition time = 4min54s.

ASL MRI data from eight subjects were retrospectively analyzed from the reproducibility study on optimization and reliability of multi-PLD PCASL by Mezue et al. [84]. Scan parameters were: PLD = 0.25, 0.5, 0.75, 1, 1.25, 1.5s; bolus duration = 1.4s; TR/TE = 4,000/13 ms; FOV = 220 × 220; matrix = 64 × 64; 24 sequential ascending slices (no slice gap); slice thickness = 4.95 mm; slice acquisition time = 45.2 ms; 12 consecutive label and control images; total scanning time: 6.4min. Two additional proton density (PD) weighted images with TR = 6000 ms (one using the head and the other the body coil) were acquired to calibrate estimated CBF into absolute units. The head calibration was collected to compute the equilibrium magnetization of the arterial blood, and the body calibration image of each subject was used to correct the ASL data for the uneven sensitivity profile of the head coil [131]. This dataset was used in the healthy cohort experiments.

3.3.2 Partial Volume Estimation

PV estimates at the resolution of the ASL data were computed from each subject by affine registration and tissue segmentation. First, brain tissue was extracted from high-resolution T_1-weighted structural images to remove the non-brain components using the FSL tool BET [125]. Then they were segmented to produce PV estimates for GM, WM, and CSF using the FSL tool FAST [124]. Affine registration of T_1-weighted structural images and the brain mask of ASL resolution (computed by taking the mean of ASL control images across all PLDs) was performed using the FSL tool FLIRT with 6 degrees of freedom [125]. For use in PVEc of ASL data, the high-resolution PV estimates were transformed to the same (low) resolution as the ASL image space by subsampling and interpolation as described by Chappell et al. using the FSL tool applywarp [15]. PV estimates of CSF were not used in the analysis. Finally, the PV estimates of GM and WM with voxel intensity less than 10% were excluded from the analysis, by replacing values less than 0.1 by 0 in the

Table 3.1: List of simulation parameters

Parameter		Value
Gray Matter		
CBF	(ml/100g/min)	60 (flat), 30 (hypo), 90 (hyper)
Δt	(ms)	700
T_1	(ms)	1300
λ		0.98
White Matter		
CBF	(ml/100g/min)	20
Δt	(ms)	1000
T_1	(ms)	1100
λ		0.82
Arterial Blood		
T_1	(ms)	1600
Sequence		
τ	(ms)	1800
PLD	(ms)	1800 (Single-PLD)
		300, 600, $\cdots$ 1800 (Multi-PLD)
α		0.91
Repeat		10 (Single-PLD)
		5 (Multi-PLD)

relevant PV estimates. The 10% threshold was chosen in the original work of the spatially regularized method [15]. Since the aim of this work was to compare the LR and the spatially regularized method, the author selected this value in order to be consistent with the original implementation of the spatially regularized method. If a different threshold was used, the spatial coverage of the GM mask would become different but the resulting tissue CBF after PVEc would not be affected. After thresholding, the resulting PV estimates were denoted as the reference PV estimates.

3.3.3 Simulated Data

Using the one hundred PV estimates from the individuals extracted from the Biobank data, simulated ASL difference datasets of both single and multi-PLD PCASL were created by applying the general kinetic model proposed by Buxton et al. [87]. For each simulated dataset, four different patterns of GM CBF were applied using the parameters listed in Table 3.1, with variations in the GM CBF map as the following:

Simulated dataset 1 – Flat GM CBF: homogeneous GM CBF of 60 ml/100 g/min throughout the whole brain.

Simulated dataset 2 – Hyper/hypo GM CBF: homogeneous GM CBF of 60 mL/100 g/min with a hypoperfused (30 mL/100 g/min, spherical region of radius 10 voxels) region to the right of the brain and a hyperperfused (90 mL/100 g/min, spherical region eight voxels radius) region to the left of the brain.

Simulated dataset 3 – Slow Sinusoidal GM CBF Variation: GM CBF of 60 mL/100 g/min with superimposed sinusoidal variations in all three spatial dimensions, with a period equal to 30 voxels and an amplitude of 10 mL/100 g/min, resulting in a smoothly varying GM CBF over the approximate range 50–70 mL/100 g/min.

Simulated dataset 4 – Fast Sinusoidal GM CBF Variation: GM CBF of 60 mL/100 g/min with superimposed sinusoidal variations in all three spatial dimensions, with a period equal to 10 voxels and an amplitude of 10 mL/100 g/min resulting in a smoothly varying GM CBF over the approximate range 50–70 mL/100 g/min.

In all cases, the WM CBF was set to 20 mL/100 g/min throughout the whole brain. The ASL difference signal was derived by summing the two kinetic curves after multiplication of each component by the reference PV estimates using the model developed by Buxton et al. as in Equation 3.1. For each simulated dataset of both single and multi-PLD, a TR of 4 s and a total acquisition time of 4 min were assumed based on the ASL Consensus Paper for single-PLD PCASL [17] and the reproducibility study data used in healthy cohort experiments for multi-PLD PCASL [84]. Under such conditions, the single and multi-PLD simulated data include ten and five repeats respectively. White noise was introduced to simulate the MRI background noise using white noise according to $\mathbb{N}(0, SD)$, where SD is defined as the ratio of reference signal intensity to signal-to-noise ratio (SNR), i.e. $SD = ref(\Delta M_t(t))/SNR$. The reference signal intensity $ref(\Delta M_t(t))$ was chosen to be the maximum signal intensity of a kinetic curve at GM CBF = 60

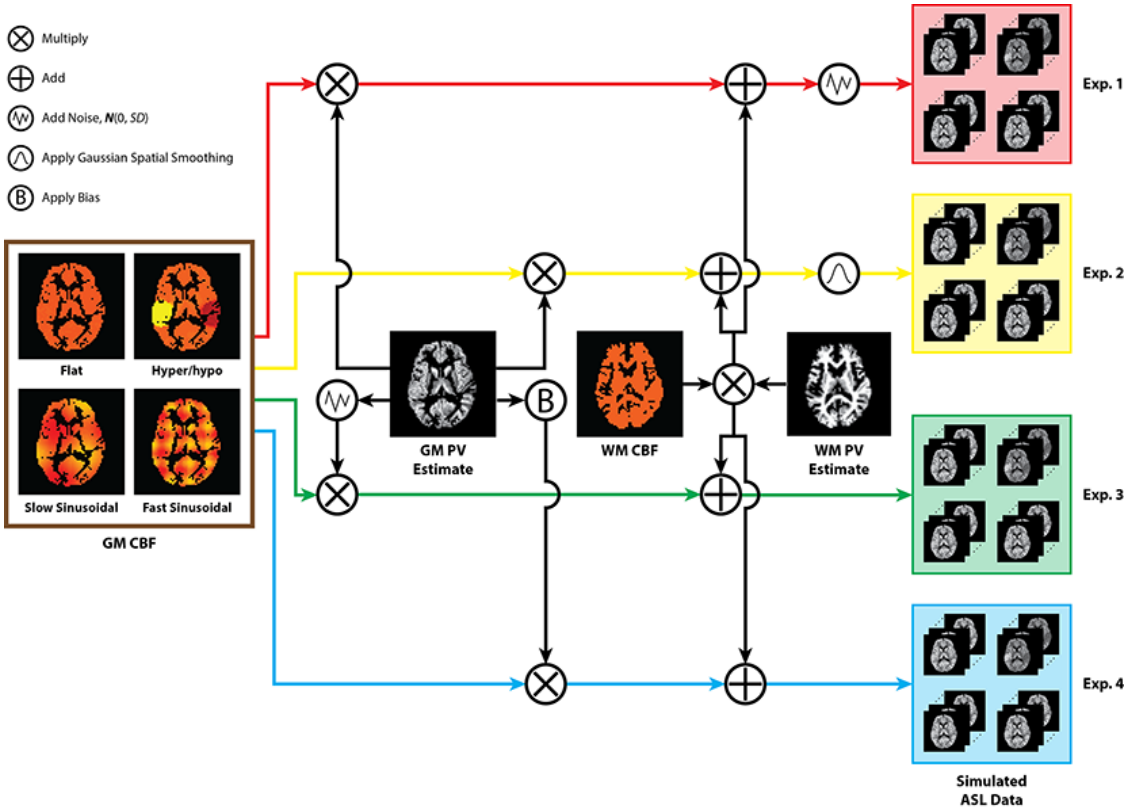

Figure 3.1: Schematic of the process of generating data for the simulation based experiments. Four datasets were created for both single and multi-PLD ASL data based on the CBF maps shown on the left. In each case the GM CBF map was used to generate simulated ASL difference data according to the kinetic model of Buxton et al. [87], and then multiplied by the GM PV estimate from an individual that had already been downsampled to the same space. To this was added a WM ASL difference signal generated using the same model, the WM PV estimates from the same individual and a presumed WM GBF of 20 ml/100 g/min. Data were generated using PV estimates from 100 individuals. In experiment 1 (red), white noise was added to the simulated ASL difference data. In experiment 2 (yellow), Gaussian smoothing was applied to simulated ASL data (no noise was added). In experiment 3 (green), random errors were applied to PV estimates during the generation of the difference data. In experiment 4 (blue), bias was introduced to PV estimates during the generation of the difference data. For the data for both experiments 3 and 4, any adjustment made to the GM PV estimates was mirrored in the WM PV estimates, this process is not shown on the diagram.

mL/100 g/min, $\Delta t = 0.7$s, and $\tau = 1.8$s. Figure 3.1 illustrates the process of creating the simulated data.

3.3.4 Perfusion Estimation and Partial Volume Correction

In both single and multi-PLD ASL datasets, perfusion was estimated by fitting the kinetic curve to ASL difference data using spatial VB method in the FSL tool

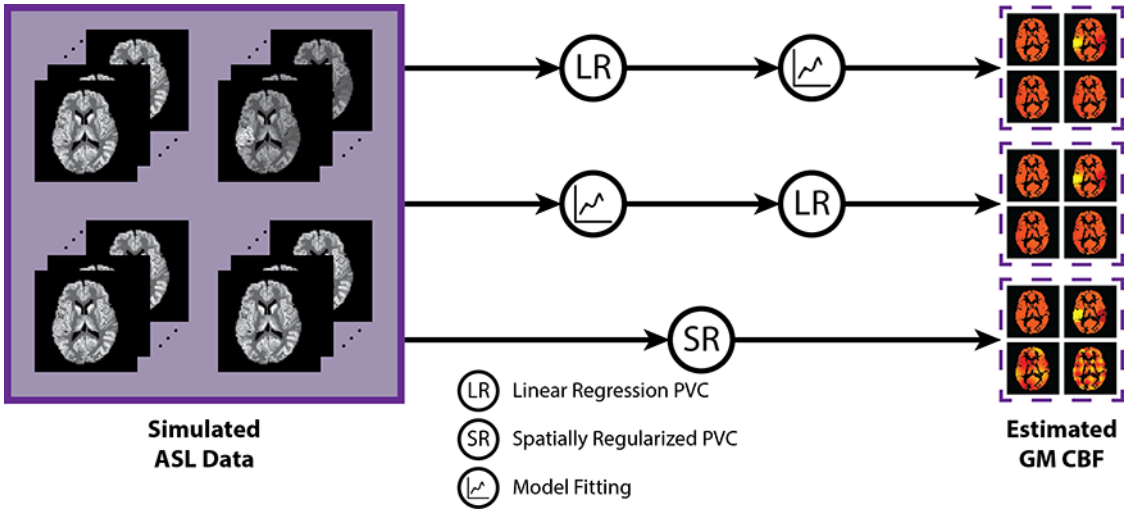

Figure 3.2: Perfusion estimation and partial volume correction. PVEc was performed using three methods – linear regression on ASL data, linear regression on CBF map, and spatially regularized method.

BASIL [108]. PVEc was performed by LR [14] and spatially regularized approaches [15]. The LR method was implemented in two ways: (1) application of LR on ASL difference data before perfusion estimation; (2) application of LR on estimated CBF maps after perfusion estimation. For both implementations, the regression kernel size was set to 3×3 and 5×5. In the spatially regularized approach, 200 iterations were performed in each analysis to ensure convergence. Figure 3.2 shows the CBF estimation and PVEc process.

For the healthy cohort experiments, voxel-wise calibration was performed to compute GM CBF in the absolute unit (ml/100 g/min) using the method proposed by Okell et al. [132]. Specifically, a coil sensitivity map was derived by dividing the head calibration image by the body calibration image. The ASL difference image was corrected using the coil sensitivity map before model-fitting. A PD image was obtained by dividing the head calibration image by the coil sensitivity map. This PD image was then corrected by multiplying by the factor $(\frac{1}{1-e^{-TR/T_{1,tissue}}})$, where $T_{1,tissue}$=1.3s, to compute the M_{0t} image [17]. The M_{0a} image was computed by multiplying the M_{0t} image by the blood-water partition coefficient of 0.9 [84]. Then, a 2-D median filter of kernel size 3 × 3 was applied to the M_{0a} image to reduce noise. Due to the PVE on the edge of the M_{0a} image, the signal intensities of the

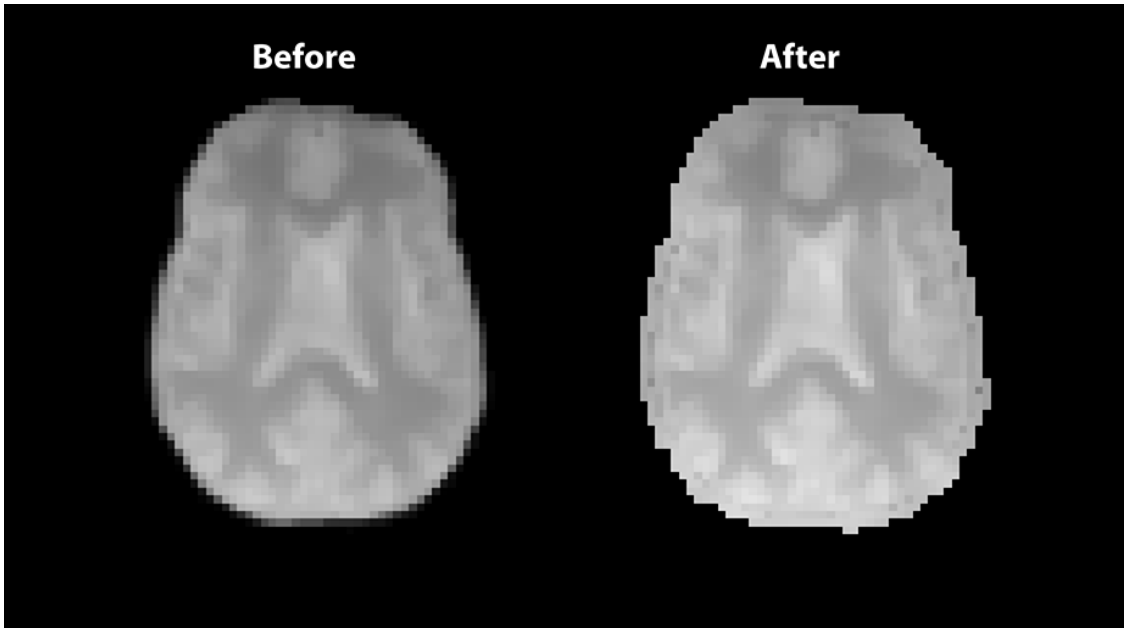

Figure 3.3: M_{0a} data before and after correcting PVE. The voxels on the cortex were eroded and extrapolated to correct the PVE.

voxels on the edge of the brain were substantially less than those inside the cortex, causing overestimation to the absolute CBF values on the edge of the brain. The M_0 data is a measurement of the tissue proton density, which should be largely homogenous for the different types of tissues in the brain. Thus, the voxels on the edge of the cortex affected by PVE should have the similar signal intensity with the voxels not affected. Such issue was resolved by erosion and extrapolation techniques. First the M_{0a} image was eroded by three voxels. Since the resolution of the ASL data was 3×3×4.95mm, eroding by three voxels (10mm) was sufficient to exclude the voxels affected by the partial volume effects on the edge of the brain. The eroded voxels were extrapolated by taking the mean in a 5×5 neighborhood to create the corrected M_{0a} image. Finally, the estimated CBF images were calibrated by the corrected M_{0a} and an assumed inversion efficiency of 0.88 [132]. Figure 3.3 shows an example M_{0a} data before and after correcting the PVE on the cortex.

3.3.5 Simulation Study

Four numerical experiments were conducted to compare the effects on PVEc of variation in the degree of noise in the ASL data and PV estimates. They were

Table 3.2: Experimental parameters

Parameter	Value
Experiment 1	
SNR	5, 10, 15, 20, ∞
Experiment 2	
FWHM	0, 1.5, 3, $\cdots$, 7.5, 9mm
SNR	∞
Experiment 3	
σ	0, 0.025, 0.050, $\cdots$, 0.175, 0.200
SNR	∞
Experiment 4	
b	-0.5, -0.4, $\cdots$, 0, 0.1, $\cdots$, 0.5
SNR	∞

performed using both single-PLD and multi-PLD simulated ASL data. For each experiment, the experimental parameters are listed in Table 3.2, and the results were assessed by root-mean-square error (RMSE) and region of interest (ROI) analysis.

Experiment 1: Impact of Background Noise of ASL Data on PVEc

This experiment investigated the influence of background noise in ASL data on the results of each PVEc method. The same reference PV estimates were used in each PVEc method as were used to create the simulated data for each subject. This experiment provided a baseline for the subsequent experiments under the ideal case where the true PV estimates were known and thus can be used for PVEc.

Experiment 2: Impact of Resolution Mismatch on PVEc

As discussed, one of the limitations of PVEc is an unmatched PSF between structural and ASL images even when differences in matrix size (and thus voxel dimensions) are accounted for. This was modeled by blurring the simulated noise-free ASL data with a 3D isotropic Gaussian blurring kernel defined by a range of standard deviation values θ ($\theta = \sqrt{8ln2}/FWHM$ and $FWHM$ values are listed in Table 3.2). PVEc and CBF estimation were performed on the blurred ASL data using the reference PV estimates.

Experiment 3: Impact of Random Errors in PV Estimates on PVEc

This experiment assessed the sensitivity of each PVEc method to variabilities in the PV estimates. Random errors were added to each of the one hundred reference PV estimates assuming that the errors could be modeled as $\mathbb{N}(0, \sigma)$, and a range of σ were considered as indicated in Table 3.2. The noisy PV estimates were limited between zero and one. A total of one hundred distorted PV estimates were created using the Biobank datasets.

Experiment 4: Impact of bias in PV Estimates on PVEc

This experiment aimed to compare PVEc methods when there is a systematic bias in PV estimates. Biased PV estimates were generated in two steps: (1) altering the reference GM PV estimates using a non-linear transformation to create biased GM estimates; (2) computing the biased WM PV estimates using the reference GM and WM PV estimates and the newly derived biased GM PV estimates in the following:

$$\begin{gathered} \gamma = e^{b} \\ PV_{bias,GM} = (PV_{ref,GM})^{\gamma} \\ PV_{bias,GM} = PV_{ref,GM} + PV_{ref,WM} - PV_{bias,GM} \end{gathered} \tag{3.4}$$

where PV_{ref} and PV_{bias} are the reference and biased PV estimates respectively, b is the bias factor, which is applied to reference GM PV estimates using the range of values given in Table 3.2. Figure 3.4 illustrates the effect of non-linear transformation with different b values. This function exchanges PV in GM for WM, assuming that there is some inherent bias in the PV estimation process between these two tissue types. The biased PV estimates were used in PVEc and CBF estimation using the three methods for noise-free simulated ASL data.

3.3.6 Evaluation Metrics for Partial Volume Correction

RMSE Analysis

In evaluating the accuracy of PV corrected perfusion for the simulated data, RMSE was computed for each PVEc method in the following equation:

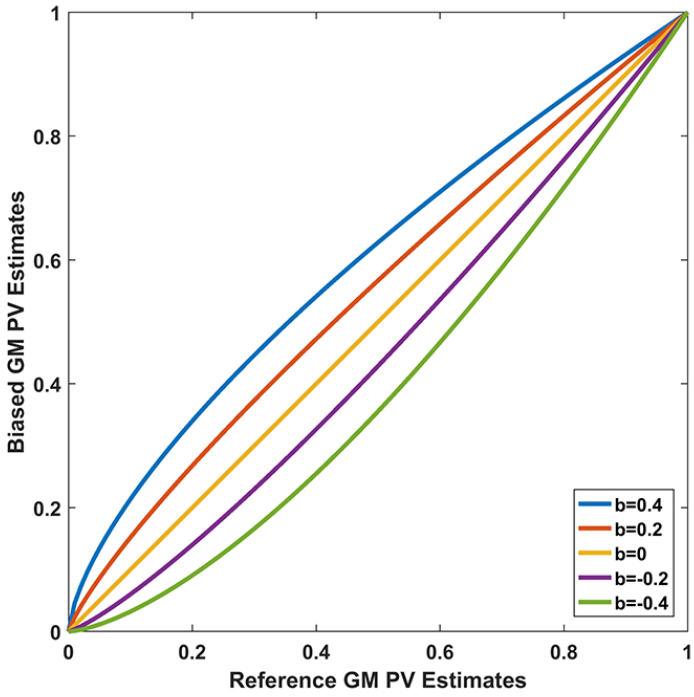

Figure 3.4: Biased PV Estimates. Biased GM PV Estimates were created by applying a non-linear transformation to the reference GM PV estimates.

$$RMSE_{CBF} = \sqrt{\frac{\sum_{j=1}^{N}(\hat{f} - f)^2}{N}} \tag{3.5}$$

where $\hat{f}$ and f are estimated and simulated CBF respectively, N is the total number of voxels within the brain mask in each model-fitting experiment.

ROI Analysis

The ROI based method introduced by Asllani et al. [14] was also used to examine the effects of different PVEc methods. Nine ROIs were defined based on the voxel intensity of estimated PV maps. Each ROI covered a 10% range of the PV estimates, and voxel intensity less than 10% were omitted. The resulting ranges were: 10%–20%, 20%–30%, ... 90%–100%. In each ROI, the mean GM CBF with and without PVEc was computed. The ROI methodology was originally proposed on the basis that pure GM CBF should be independent of the fraction of GM PV estimates because perfusion is an implicit measurement of the density of tissue

CBF at each voxel. For the simulations, this will hold true for the homogeneous GM CBF case. For the two cases of sinusoidal variation, it is still expected to be approximately true over the ensemble of brain voxels, albeit with a larger variability within the ROI. This is based on the assumption that the ROIs defined here are a pseudo-random sampling of the brain and the sinusoidal variations used are applied without any imposed correlation to the brain structure. The ROI analysis is no longer valid for the hyper/hypo perfusion case and thus was not computed.

The ROI method was extended to allow quantitative comparisons of the PVEc performance by considering a linear regression of GM CBF and GM PV estimates for ROI in the range 10%–90% using a least-square fit. The slope of this regression was recorded, a zero slope would be expected to represent good PVEc as it would imply independence of estimated CBF with PV estimates.

3.3.7 Repeatability Study

We assessed the repeatability of the PVEc methods by analyzing the inter-session coefficient of variation of GM CBF calculated from the healthy cohort data collected by Mezue et al. [84]. The hypothesis for the analysis on real data was that the inter-session variability should reduce after PVEc, on the assumption that PVE will introduce between session variability due to the different position of the brain in each scanning session and that PVEc removes this bias from the amount of GM tissue in each voxel. There will in practice be other sources of physiological variability apart from those related to PVE, including those identified by Clement et al. [133]. Thus, although we hypothesize that a reduction might be achieved by an effective PVEc strategy, it could at best only partially improve the repeatability. Ideally, the GM CBF after PVEc would be identical between each session if there are no flaws in registration (and in the absence of noise) and if PVEc removes PVE completely.

A transformation matrix (Matrix 1) from ASL image to high-resolution space was computed by registering the CBF map without PVEc to the structural image of each subject. An initial transformation matrix was obtained using the FSL tool FLIRT between the calibration and structural images. This transformation was then refined

with a boundary-based registration (BBR) cost function that uses the boundary of WM, which was segmented from the structural image [126]. This implementation is available in the *asl_reg* function part of the BASIL toolbox in FSL. For each subject, a second transformation matrix (Matrix 2) was obtained by registering the high-resolution T_1-weighted image to the standard brain (MNI152_T1_2 mm) using the FSL tool FLIRT [134]. Matrix 2 was used to initialize the estimation of the spline coefficients (warp) from structural to standard space using the FSL tool FNIRT [125]. Finally, the GM CBF map was transformed to the standard space using the warp and Matrix 1 with the FSL tool *applywarp*.

We evaluated the repeatability of each PVEc method using within-subject coefficients of variation (wsCV) within three ranges of GM PV estimates ROIs: 10%–40%, 40%–70%, and 70%–100%. Within-subject coefficients of variation were computed as the ratio between the standard deviation of voxel-wise absolute differences of repeated GM CBF estimates and the mean repeated GM CBF estimates in the following equation:

$$wsCV = \frac{SD(|f_1 - f_2|)}{mean(f_1, f_2)} \times 100\% \tag{3.6}$$

where f is the GM CBF. The metric was computed for the three repeated experiments (session, week, and month repeat).

3.4 Results

3.4.1 Simulation Study: Single-PLD Data (Kernel Size 5×5 for the LR Methods)

Figure 3.5 shows the estimated GM CBF maps of an example subject from the simulation of single-PLD PCASL data after applying different PVEc for selected cases within each of the four experiments. Figure 3.6 shows the RMSE between estimated and simulated ground truth GM CBF over all subjects for each experiment. Figure 3.7 shows example ROI curves and the corresponding slope values for each PVEc method for selected cases within each experiment. Figure 3.8 shows the calculated slope values across all the subjects for each experiment.

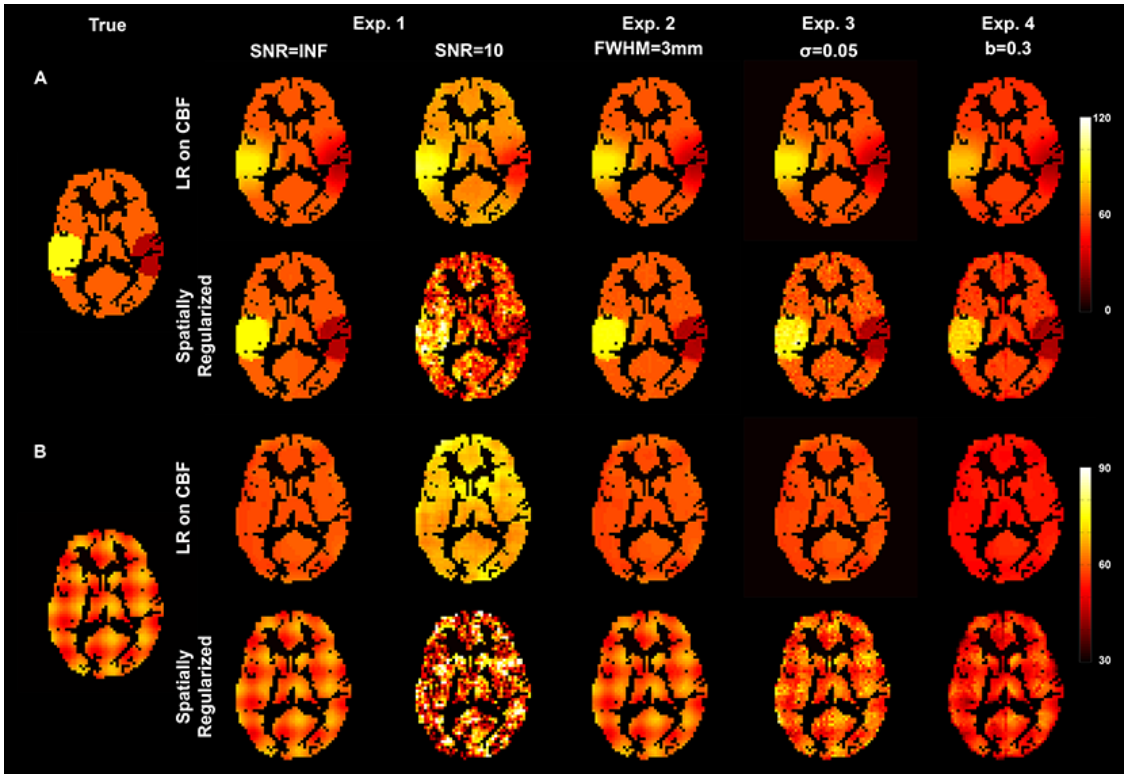

Figure 3.5: Estimated GM CBF map for single-PLD simulated data from a single subject. (A) Hyper/hypo GM CBF; (B) Fast sinusoidal GM CBF variation.

In experiment 1, the reference PV estimates were used within the PVEc to investigate the sensitivity of different PVEc methods to background noise on ASL data. For no noise (SNR=INF), all of the methods were able to correct for PVE, but the spatially regularized method appeared to be more accurate in capturing short scale variations in GM CBF, as can be seen most evidently in the results for hypo/hyper regions in Figure 3.5 and also from the lowest errors when SNR=INF in Figure 3.6A for the two cases with short scale CBF variations: hyper/hypo CBF and fast sinusoidal variation. As the SNR was degraded, all of the methods became less accurate at GM CBF estimation, with LR applied to the ASL data appearing to be least sensitive to noise, followed by LR applied to the CBF map and finally the spatially regularized method. Noticeably in Figure 3.5 as the noise increased the results from the spatially regularized method appeared more 'noisy', whereas the maps from LR remained smooth and errors between true and estimated CBF manifested as global CBF differences, as can be seen for example in Figure 3.7B

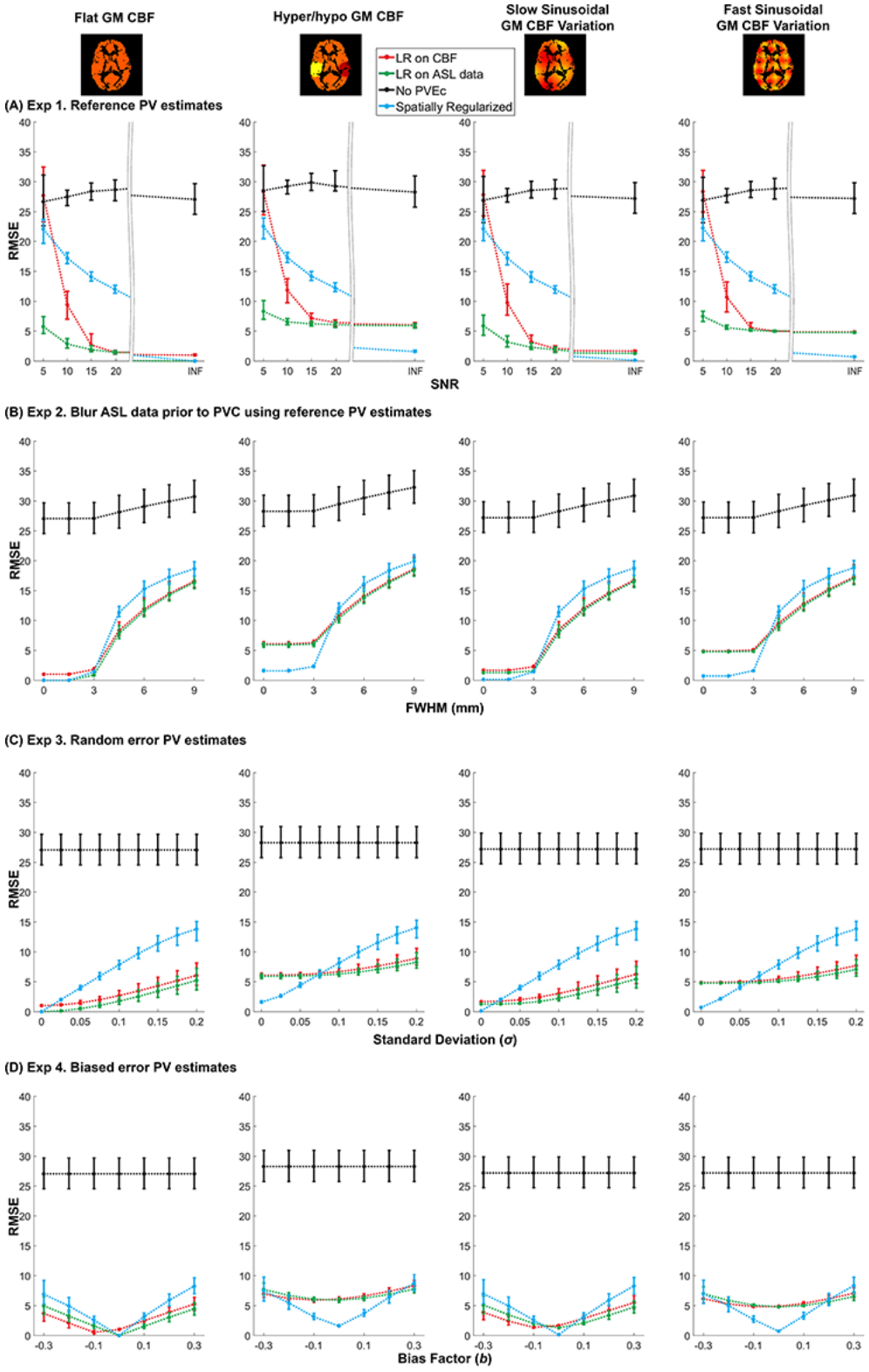

Figure 3.6: RMSE between estimated and simulated GM CBF using noise-free simulated single-PLD data.

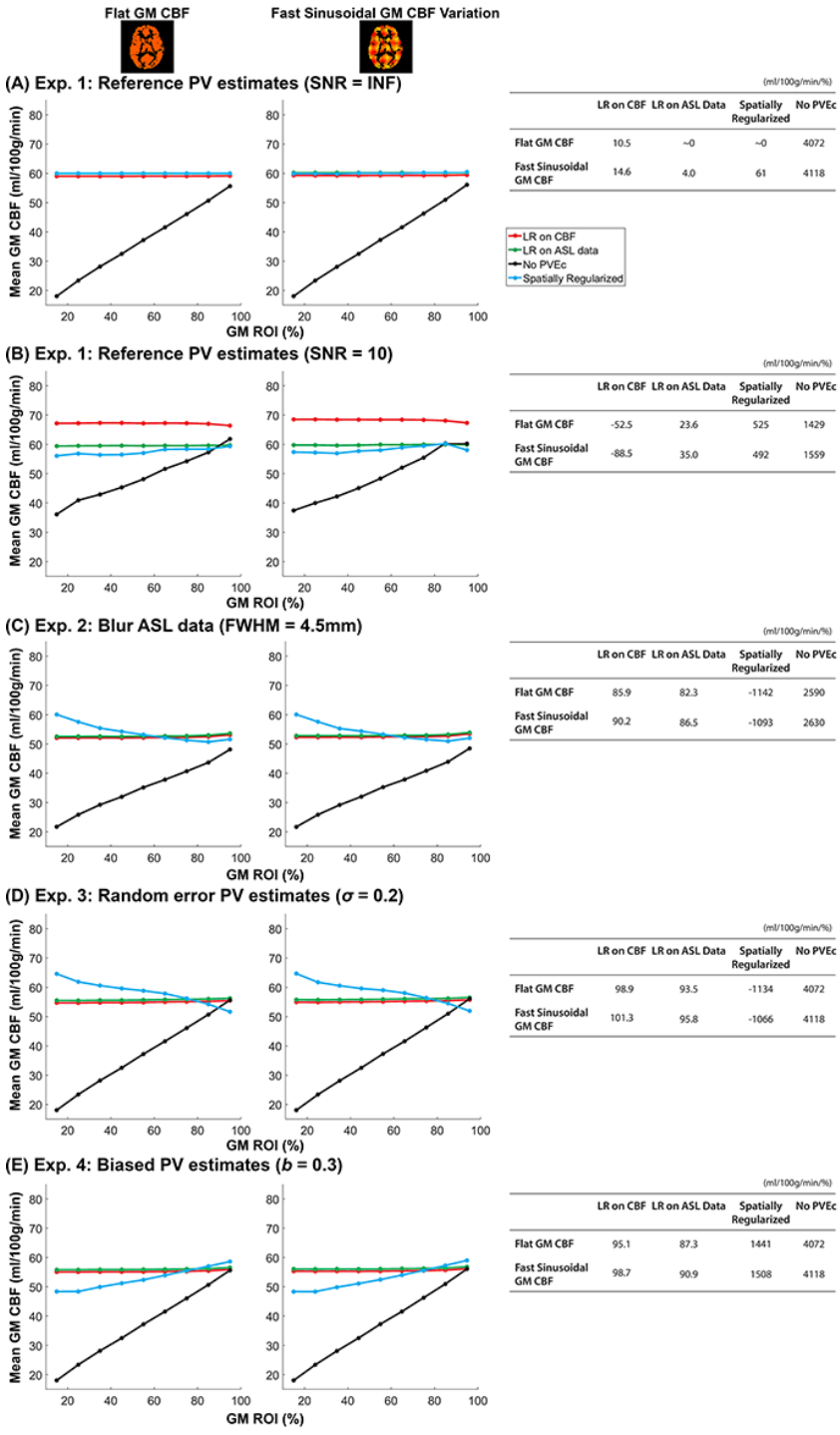

Figure 3.7: Example ROI curves for all experiments using single-PLD data. The first row of curves shows the ROI analysis in a perfect situation (SNR=INF and reference PV estimates). Subsequent plots reveal the changes of mean GM CBF observed in each experiment for a specific choice of experimental parameter. Each adjacent table shows the estimated slope values for the linear regression fitting between estimated GM CBF and GM ROI.

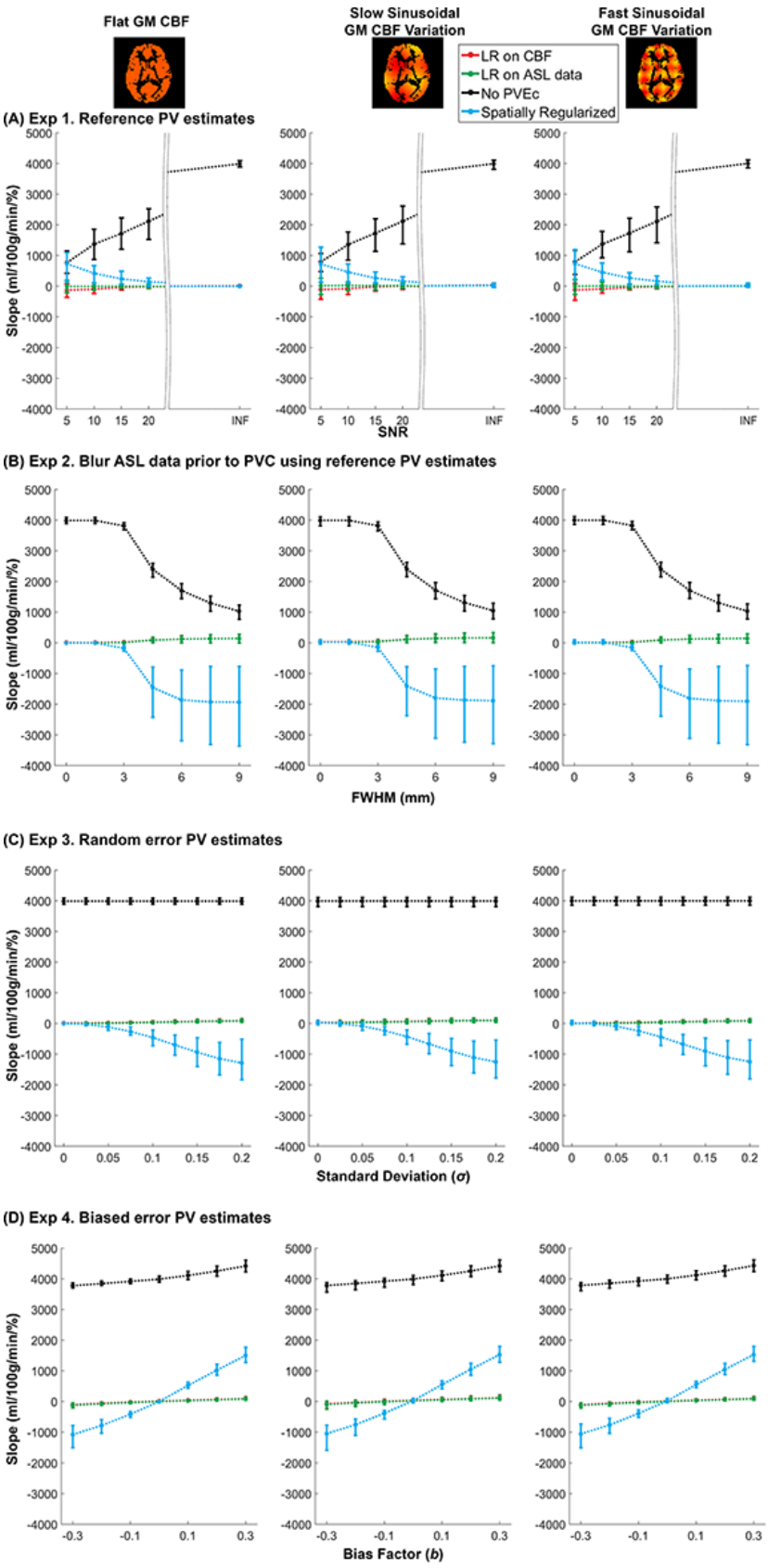

Figure 3.8: Estimated slope values of the extended ROI analysis using single-PLD data.

where the GM CBF in all ROI was greater than the true (mean) value.

The high accuracy of all the PVEc methods for no noise translated to small slope values in the ROI analysis, Figure 3.7A and Figure 3.8A: no correction resulted in a slope of the order of 4,000 ml/100 g/min/%, at least two orders of magnitude larger than the PVEc results. As the noise increased the slope value for no correction became less steep, for example, values around 1,500 ml/100 g/min/% at SNR = 10 in Figure 3.8B. For all of the PVEc methods as noise increased, the absolute value of the slope increased mirroring the reduction of accuracy seen in the RMSE results.

In experiment 2, the impact of mismatch between the PSF of the ASL data and the structural image was examined. Effects on both RMSE and slope were only obvious once the FWHM of the Gaussian kernel applied to the ASL data exceeded the voxel size of the ASL image (3.5 mm). As the FWHM increased beyond this value the RMSE increased to approximately the same degree for all PVEc methods, and it was also associated with a small increase in RMSE for the non-corrected case. For the spatially regularized method, the errors introduced by PSF mismatch were manifested in overestimation at lower PV of GM and underestimation at higher values, as seen in Figure 3.7C (in an example with FWHM of 4.5 mm) and as a negative slope at larger FWHM in Figure 3.8B. However, both LR methods only produced relatively small increases in slope as the PSF FWHM increase, the observed increase in RMSE for these examples being associated with global errors in CBF.

In experiment 3, the impact of random errors in the PV estimates was analyzed for each PVEc method. Similarly to experiment 1, random errors on PV estimates led to an increase in RMSE for all the PVEc methods, as shown in Figure 3.6C, but the increase in error was more marked with the spatial method compared to either LR approach. The slope metric again showed overestimation at low PV GM by the spatial method, as shown in Figure 3.8C, whereas both LR methods estimated the same GM CBF in all ROIs on average even as the error on GM PV estimate increased, thus their slope remained comparatively close to zero. The increase in RMSE seen for the LR methods was due to consistently underestimating GM CBF

in all ROIs, for example in Figure 3.7D both LR methods are underestimating the true (mean) simulated GM CBF (60 ml/100 g/min).

In experiment 4, the impact of bias in the PV estimate on PVEc methods was examined. Bias affected all methods and led to an increase in RMSE with an increase in the degree of bias (bias factor: b), as shown in Figure 3.6D, and the spatial method appeared to be most sensitive to increases in bias. The ROI analysis showed that for increased positive bias the spatial method tended to underestimate in low and overestimate in high GM PV regions, resulting in positive slope values; vice versa for negative bias, as shown in Figure 3.8D. Both LR methods tended to globally underestimate GM CBF at higher bias, but retain slope values relatively close to zero, for example in Figure 3.7E.

Results of simulated experiments using multi-PLD data can be found in Appendix A. Looking at the GM CBF map of multi-PLD ASL data in Figure A.1, the impact of background noise was more substantial than on the single-PLD data for the spatially regularized method. In terms of perfusion quantification accuracy in noisy data, LR when applied to the data or the estimated perfusion map when using multi-PLD data were nearly identical in terms of RMSE (Figure A.2A) as opposed to single-PLD data in Figure 3.6A. Apart from these, the results of simulated experiments using multi-PLD data were similar with the results of single-PLD data.

The results from using LR methods of kernel size of 3×3 are shown in supplementary materials (Figures A.5-A.11). Although the overall trend of the results was similar with using the kernel size of 5×5, the LR methods became more accurate with the smaller kernel size due to less smoothing effects. However, it was still less accurate than the spatially regularized method when reference PV estimates were used in the noise-free simulated data, as shown in Figures A.6A and A.9A. The results from data with infinite SNR and perfect PV estimates served as a baseline to assess the performance of the two PVEc methods, which was the main objective of this work. Although the SNRs of the ASL data are lower in practice, the simulation results can be used as a reference to evaluation PVEc in real data. For

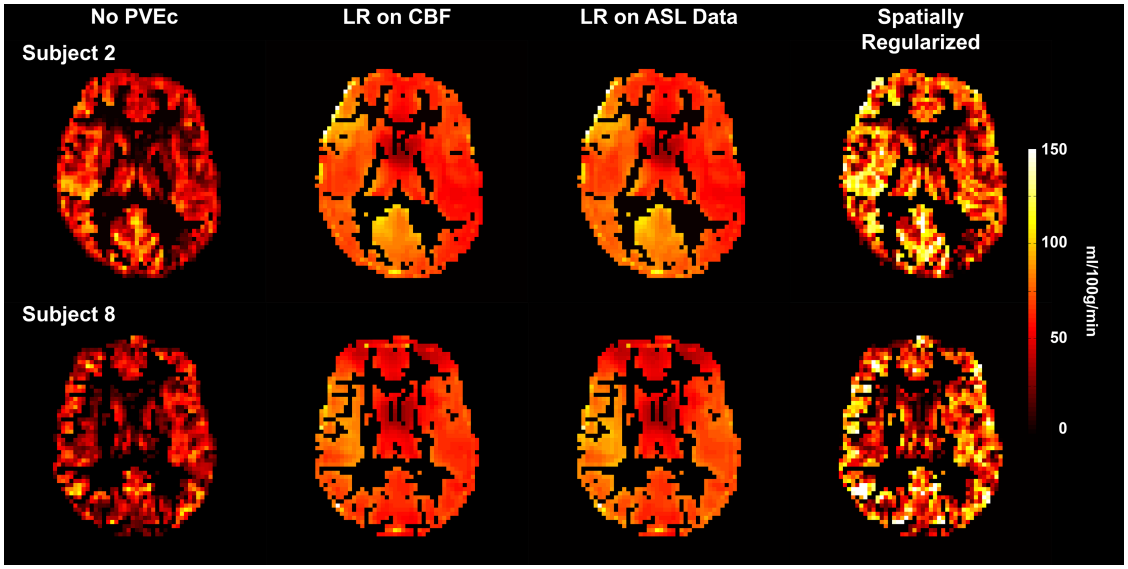

Figure 3.9: Estimated GM CBF maps of two example subjects using different PVEc methods.

example, the slope metric can provide the information on the correlation between the estimated GM CBF and the GM PV estimates, if the SNR of the data is known.

3.4.2 Healthy Cohort Experiments

Figure 3.9 shows the estimated GM CBF before and after PVEc from two subjects within the healthy cohort data. Similar to the simulated experiments, the results of the LR methods are nearly identical, with more spatial variability visible in the maps from the spatially regularized method.

Figure 3.10 shows the estimated slope values of the extended ROI analysis on healthy cohort data. The analysis was performed on data from the first scan session of each subject. Without PVEc, the slope values are positive, in agreement with the simulations. After PVEc, the slope value becomes negative with a median value around $-1{,}000$ ml/100 g/min/% for the LR methods, but more negative for the spatially regularized method. Similarly to the simulations, the two LR methods achieved nearly identical slope results.

Figure 3.11 shows the wsCV of each PVEc method (including no PVEc) for the three ROIs. Overall, the wsCV reduced after performing PVEc. Comparing between each PVEc method, the two LR methods show similar performance in

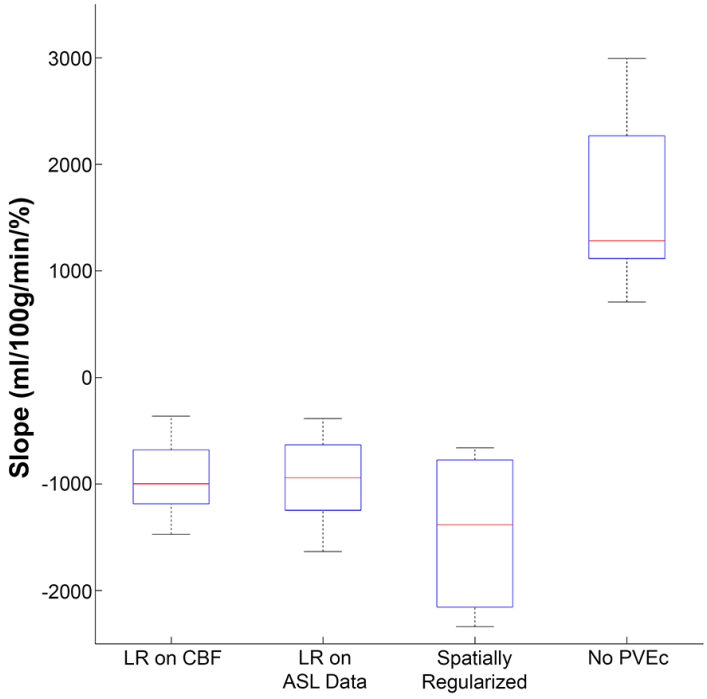

Figure 3.10: Estimated slope values of the extended ROI analysis on healthy cohort data. The slope values of all eight subjects are plotted for each PVEc method.

ROIs containing voxels with less than 70% GM, whereas the LR on ASL data approach appears to be better in reducing variability for ROIs containing voxels with greater than 70% PV GM. The spatially regularized method has similar repeatability to the LR methods for ROIs containing voxels with greater than 40% GM, but not in those ROIs with voxels below this threshold, although it was still more repeatable than no correction.

3.5 Discussion

In this work, we have investigated the sensitivity of two different but similarly motivated PVEc methods for perfusion estimation from ASL on PCASL data. We have simulated different types of variabilities in ASL data acquisition as well as PV estimates including background noise in the ASL data itself, differences in PSF between ASL and structural data, and errors in the PV estimates. A range of artificial spatial distributions was considered in GM CBF, consistent with those

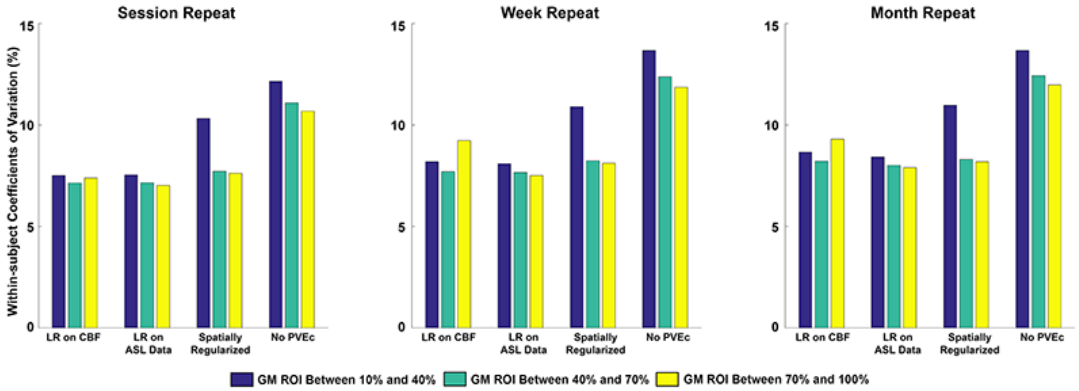

Figure 3.11: Within-subject coefficient of variation of the PVEc methods in three ROIs. All PVEc methods improve repeatability of perfusion quantification, and the repeatability is higher in greater GM ROIs.

that have been used previously by Chappell et al [15], to assess how each PVEc method is able to restore spatial details. Additionally, the impact of PVEc on repeatability was examined using a cohort of healthy individuals previously used to examine the repeatability of PCASL. The findings of the study are threefold: (1) all PVEc methods reduce the bias of PVE in GM CBF quantification substantially regardless of the variabilities in data acquisition and PV estimates; (2) the spatially regularized method has shown superiority to the two LR methods in preserving spatial variations using data with high SNRs, but it is more sensitive to noise and errors in the PV estimates; (3) PVEc improves the repeatability of perfusion quantification using multi-PLD PCASL by reducing the bias from PVE.

3.5.1 Simulation Study

It has already been shown that the spatially regularized method appears to have greater ability to preserve spatial details in the GM CBF image over the LR methods. This was confirmed in this study and was most obvious where GM CBF varies over shorter length scales and in less noisy datasets. This finding was demonstrated qualitatively in the form of estimated GM CBF and quantitatively in the RMSE analysis and the ROI analyses. Specifically, at low noise levels, the RMSE for the spatially regularized method was always lower than LR method for simulations in which the GM CBF map contained short scale variations. Due to the assumption

of the LR method that tissue CBF is homogeneous within the kernel of a fixed size, a substantial degree of 'smoothing' arises after PVEc, which appears to be similar to blurring the data with a Gaussian Filter [14]. Our current analysis not only confirms the previous findings but also give insights on the quality of the preserved spatial variability at different noise levels. In general for data with high SNR, the LR methods appeared to be relatively insensitive to noise in data and errors and bias in the PV estimates; however, this appears to be related to the smoothing effect of the kernel based approach and results in a trade-off in the detail of the final GM CBF image. For example, the LR methods tended to return relatively small slope values (in the range 0–100 ml/100 g/min/%) from the extended ROI analysis, consistent with good correction for PVE. However, this was often associated with a consistent error in GM CBF at all values of GM PVE, see for example Figure 3.7 where the GM CBF values returned by the LR methods were often consistently different from the true (mean) value of 60 ml/100 g/min used in the simulation, and this error was largely invariant with the degree of noise or error in PV estimates used in PVEc. This effect is consistent with what can be seen in Figure 3.5, where the maps from LR are always appearing noticeably smooth implying that errors are being smoothed away, but at the same time so are spatial features.

In studying the impact due to PSF mismatch, we have observed an increase in error with FWHM for both PVEc and non-PVEc methods. The estimation accuracy reduces primarily only when the FWHM imposed became larger than the voxel size as shown in Figure 3.6B. The effect on the non-PVEc results is consistent with the corresponding increase in the influence of PVE that will occur when the true resolution of the data degrades. The more noticeable increase in RMSE for GM CBF estimation under PVEc will then be a combination of greater PVE in the data and the imperfect correction due to the use of a GM PV estimate map that does not match the true effect. Even for relatively modest FWHM beyond the voxel size gave rise to errors of up to 20 ml/100g/min in GM CBF. In practice, the PSF of ASL data is unlikely to be larger than the voxel size and the results here imply that this is not a major concern for PVEc of ASL data. However, there are

notable examples of ASL acquisitions where this could be problematic. For instance, acquisitions using 3D GRASE readouts which tend to have an extended PSF in the slice encoding direction. The original work of Chappell et al did a correction for this effect prior to PVEc using a 'deblurring' method [15]. The present study implies that this should be considered where PSF mismatches might arise. It is also noteworthy that the methodology adopted here to model mismatches in PSF is the same as the spatial smoothing that is sometimes applied to ASL data to improve visualization. The results imply that care should be taken when spatially smoothing ASL data prior to quantification where PVEc is being used. In practice, the added spatial homogeneity introduced by the assumptions of PVEc methods means that smoothing of the data prior to quantification is unlikely to be necessary.

An extended ROI analysis has been developed to compute the slope value of the classic ROI curve proposed by Asllani et al [14]. The purpose was to quantify the observed approximately linear dependency between GM CBF and GM ROI. A positive slope value indicates overestimation in low ROI or underestimation in high ROI, whereas a negative slope value indicates the opposite. For the non-PVEc GM CBF results, the estimated slope value ranged between 2500 to 4000 ml/100g/min/% dependent upon the noise in the data. This matches the already observed positive correlation between estimated GM CBF and PV estimates. These slope values correspond to GM CBF being underestimated between 25 to 40 ml/100g/min in ROIs with the lowest proportion of GM. Notably, the slope value reduced for data without PVEc when the noise increased, implying that care needs to be taken with either the standard ROI analysis or the slope metric calculated here when this is applied for the evaluation of PVEc efficacy on real data.

For the spatially regularized method under the impact of errors and noise, the estimated slope moves away from zero, which indicates a reduced consistency of GM CBF with GM PV. The tendency was for either over- or under-estimation in voxels with low GM PV and the opposite at high GM PV, with the best accuracy in the middle of the range. For the two LR methods, the slope values were comparatively near to zero in all experiments even as the parameters of the experiment were

varied. Whilst this would be consistent with LR being an effective PVEc approach and thus relatively insensitive to the sources of error studies here, it would appear that this arises largely from the smoothing effect of the LR kernel. Even when the slope value was small, implying effective correction, there was global under or over estimation of CBF. Thus the resulting GM CBF images were very smooth and thereby had a fairly consistent value for all voxels irrespective of GM PV estimate. On the contrary, the genuine variations in GM CBF were being suppressed leading to spatially specific errors that are not captured by ROI analysis method. The ROI curve method has previously been used to judge the effectiveness of PVEc on real ASL data. This study implies that this should be interpreted with care, as methods that introduce greater smoothness in the estimated CBF images can appear to be very successful using this approach, despite introducing error into the CBF image.

3.5.2 Healthy Cohort Experiments

Results from the analysis using healthy cohort data have shown an increase of estimated GM CBF in voxels containing low GM PV after PVEc, which is consistent with existing PVEc studies [14][15][118]. The estimated slope values for the non-PVEc method were between 600 to 3000 ml/100g/min/%, indicating a positive correlation with GM PV estimate as shown in Figure 3.10. Cross referencing with the simulation results in Figure 3.8A, such values would be consistent with data containing noise in the range we might expect to observe in ASL data of this duration of acquisition. However, the range would imply there is some variability within the group in either the noise or the degree to which the data from each subject exhibits PVE.

The slope values after LR PVEc were around -1000 ml/100g/min/%, which is more negative than were observed in the simulation study for LR correction. A broader range of slope values (between -2500 to -500 ml/100g/min/%) were observed in results of the spatially regularized method. This latter result could be explained from the simulations by a combination of the different errors simulated. However, the variability in slope value observed and inconsistency with the LR

PVEc method means that care needs to be taken in interpreting these results using the simulations since the simulated scenarios might not be fully capturing variations in GM CBF that are observed in practice.

The repeatability of CBF quantification was improved after PVEc as evidenced by the reduction of wsCV for all repeated experiments. For the results without PVEc, the repeatability decreased with a longer gap between repeated scans, where session repeat was the most repeatable and month repeat the least. This agrees with the findings of the original reproducibility study using the same dataset although the current study used voxelwise calibration instead of CSF-based approach in the original reproducibility study [84]. Together with the results of the ROI analysis, the nearly identical results of the two LR methods imply that it makes no difference whether the LR method is applied before or after CBF quantification. Although wsCV of the spatially regualrized method was over 10% for GM ROI between 10% to 40%, it fell to the same level with the LR method for GM ROI greater than 40%. This confirmed the simulation results that spatially regularized method worked more consistently in medium and high ranges of PV estimates.

The metric of wsCV has been widely used to assess the repeatability of CBF quantification as well as PVEc studies in the past [119][85][86]. Ahlgen et al have reported an improved repeatability after LR applied to single-PLD PCASL data [119]. In particular, the mean within-voxel coefficient of variation for GM reduced from 30% to 25% after correcting PVE by the LR method. Although the present study separated GM ROI into three intervals, we have observed a similar improvement (wsCV reduced by 5%) after the same correction (LR) method were implemented. In addition, Ahlgen et al also investigated the effect of smoothing on CBF images in terms of repeatability, which, as might be expected, was also found to improve repeatability between scans. This implies that the smoothing observed in the GM CBF map after LR PVEc might make a substantial contribution to making the CBF measurements more repeatable apart from correcting for PVE. This was consistent with the observations of Ahlgren at al. that the modified least trimmed squares (mLTS) PVEc method, which introduced less smoothing, was also associated with

lower repeatability, which demonstrated a higher value of within-voxel coefficient of variation [119]. While Ahlgren et al found that the mLTS method for PVEc actually made the ASL measurements less repeatable than no correction, this study has shown the spatially regularized method does offer improvements in repeatability.

3.5.3 Limitations

A limitation of the study is the reliance on PCASL simulated data for the baseline experiments. Despite the four different types of GM CBF patterns created, the simulation does not necessarily capture physiological spatial variations in perfusion. The aim of using the sinusoidal variations of GM CBF in the simulated data was to reflect a more smooth change in GM CBF, compared to the hyper/hypo GM CBF variation. Other alternative spatial variations may be those that simulate a more realistic patterns of CBF, such as more complex and asymmetric spatial variations patterns in the two hemispheres or more subtle GM CBF variations than sinusoidal pattern. However, without a ground truth, the creation of more complex patterns may still not fully capture the possible CBF variations. The patterns chosen in this work allowed us to examine particular features of the PVEc methods and their performance at the presence of both smooth and sharp boundaries in GM CBF. Since both LR and spatially regularized methods assumed local homogeneity of tissue perfusion to separate tissue perfusion from total perfusion, it was a fair comparison between the two. However, the simulations have provided a well-controlled environment in which to systemically study sensitivity to error for different PVEc methods. Unlike previous simulation studies of this kind, here one hundred individual structural images were employed to generate a simulated cohort that captured more natural variation in the population, seeking to avoid any bias in the results from choosing a single subject on which to base the PV estimates.

We have not sought to investigate all possible PVEc methods that have been proposed here and have concentrated on comparing the simplest LR approach to the other major class of methods to use spatial information. A potential extension would be to consider mLTS and a wider range of kernel sizes and shapes for LR.

However, based on the extra exploration found in the supplementary material for a smaller kernel size of 3×3 and existing literature on PVEc [14][15], we believe that the conclusions of this study would hold for other variants on LR. Although we have considered the impact of PVEc on multi-PLD PCASL in this study on CBF estimation, we have not sought to examine how this might affect estimates of arterial transit time, which is of interest in hemodynamic studies in its own right [104]. This is something that could be explored using the same framework in the future.

The current study specifically investigated the influence of variabilities on PVEc for ASL perfusion estimation in individuals and the corresponding repeatability in a cohort of healthy subjects. An open question is the degree to which PVEc might be useful when performing group studies to look for changes in perfusion associated with activation or disease, and whether the different PVEc methods are more of less favorable than each other for this application. This might partially be answered using simulations like those examined here, although further work using different PVEc methods within ASL groups studies would still be valuable to address these questions.

3.6 Conclusions

In this work, we have investigated the impact of different sources of error on PVEc methods when applied to PCASL perfusion images. In simulated experiments, the spatially regularized method demonstrated consistent greater ability to preserve spatial details in CBF maps but was also shown to be sensitive to noise and errors in the PV estimates. The LR method was consistently less sensitive to noise and errors, but this appeared to be largely due to the smoothing effect of the kernel employed, thus the estimated GM CBF was less accurate than the spatially regularized method whenever there were features in the data represented over short length scales. The results from a repeatability study in healthy individuals have shown that both methods reduce intersession variability, the greater reduction coming from LR potentially being another effect of the spatial smoothing associated with the method.

Livet forstås baglæns; men må leves forlæns...

Life can only be understood backwards; but it must be lived forwards...

— Søren Aabye Kierkegaard

4

Investigating Partial Volume Correction Using Multi-PLD ASL

Contents

4.1 Introduction 98
4.2 Theory 99
4.3 Methods 101
4.3.1 Simulated Data 101
4.3.2 Healthy Cohort Data 102
4.3.3 Tissue Perfusion and ATT Estimation 103
4.3.4 Evaluation Metrics 104
4.3.5 Statistical Analysis 104
4.4 Results 105
4.4.1 Simulated Experiments 105
4.4.2 Healthy Cohort Experiments 111
4.5 Discussion 114
4.5.1 Simulated Experiments 115
4.5.2 Healthy Cohort Experiments 117
4.5.3 Limitations 119
4.6 Conclusions 120

4.1 Introduction

Multi-PLD PCASL and PASL are alternative ASL techniques for the combined quantification of CBF and ATT. Although PCASL has the advantage of higher SNR,

PASL has shown to be more sensitive to ATT [135], which might be of assistance for the separation of GM and WM due to the different ATT between GM and WM (0.7s and 1.1s respectively). In most MRI scanners, PASL based sequences (such as Philips' ASL sequence which incorporates the PULSAR labeling technique [62]) are currently the most widely used whereas PCASL based techniques are not always provided. Due to the greater amount of signal collected from multiple numbers of PLDs and the availability of model based quantification methods, the estimation of CBF and ATT can be more accurate than single-PLD ASL techniques [78]. Regardless of the labeling strategy used (PCASL or PASL), PVE remains an issue for the precise quantification of the hemodynamic parameters of multi-PLD ASL techniques. In particular, the influence of PVEc on the performance of multi-PLD PCASL and PASL is unknown. Therefore, a systematic investigation of the effectiveness of PVEc on both PCASL and PASL is needed.

In this work, we compare the sensitivity of the LR and spatially regularized PVEc methods on multi-PLD PCASL and PASL data. Simulated multi-PLD PCASL data were reused from the previous chapter, and simulated multi-PLD PASL data were generated using the parameters of the QUASAR Reproducibility study but excluding the arterial blood component [86]. The simulations were performed in the same conditions as the previous chapter including the SNR of the data, PSF in data acquisition, and random and bias errors of PV estimates. In order to examine the impact of PVEc for GM CBF and ATT estimation on healthy volunteers, we also performed PVEc on a QUASAR ASL dataset extracted from a study that investigated the correlation between the decrease in CBF and the decline of sub-clinical cognitive function [136]. GM CBF and ATT were computed for this population, and the extended ROI analysis was conducted to investigate the correlation between GM CBF and GM PV estimates.

4.2 Theory

QUASAR ASL is a PASL based multi-PLD technique that uses PULSAR labeling and Look-locker readout [73]. Although a tissue kinetic model was developed by

Chappell et al for QUASAR ASL [101], the ASL signal was considered from a single source without taking the bias of PVE into account. A new model is needed to separate the tissue signal of QUASAR ASL into contributions of GM and WM. Since multiple PLDs are used for ASL data collection ranging from 0.04s to 3.64s, the signal from the arterial blood might be sampled in the first few PLDs before the labeled blood water reaches the tissue region. These signals are considered artifact for perfusion estimation and must be excluded in order to estimation CBF accurately. QUASAR ASL employs a number of crushing gradients implemented in different dynamics to separate the tissue signal by removing (or crushing) the signal from the arterial blood component [86]. In order to account for PVE in QUASAR ASL, the ASL difference signal of data collected by the QUASAR sequence is modeled as the summation of the signal from the arterial blood and the tissue components:

$$\Delta M(t) = S_c(\gamma, s) \cdot \Delta M_A(t) + \Delta M_T(t) \tag{4.1}$$

where ΔM_A is the magnetization difference signal in the arterial blood component, $S_c(\gamma, s)$ describes the effect of crushing gradients in QUASAR ASL, ΔM_T is the signal from the tissue component. The description of ΔM_T follows the same formulation in Equation 3.1 (previous chapter) that incorporates both GM and WM contributions. $S_c(\gamma, s)$ is formulated such that its value is equal to 1 when the crushing gradients are off (arterial blood signal included) and less than 1 when the crushing gradients are on (arterial blood signal excluded or crushed):

$$\begin{aligned} S_c(\gamma, s) &= 1 - max(\gamma \cdot s, 0) \\ \gamma &= [sin(\varphi)cos(\theta), sin(\varphi)sin(\theta), cos(\varphi)] \end{aligned} \tag{4.2}$$

where γ is parameterized by the three directions of the crushing gradients and s is a unit vector with values from the different dynamics of QUASAR ASL [101]. In each complete cycle of QUASAR data acquisition, seven dynamics were acquired differing in whether crushing gradient was applied and the degree of flip angle in the Look-Locker acquisition. In dynamic 1, 2, 4, and 5, the crushing gradients were applied to different directions in order to suppress the signal from the arterial

Table 4.1: Crushing gradients in each dynamics of QUASAR ASL

Dynamic	Crushing Direction	s value	Flip angle
1	$+x, +y, +z$	$(+\frac{1}{\sqrt{3}}, +\frac{1}{\sqrt{3}}, +\frac{1}{\sqrt{3}})$	35°
2	$-x, +y, +z$	$(-\frac{1}{\sqrt{3}}, +\frac{1}{\sqrt{3}}, +\frac{1}{\sqrt{3}})$	35°
3	NA	NA	35°
4	$+x, -y, +z$	$(+\frac{1}{\sqrt{3}}, -\frac{1}{\sqrt{3}}, +\frac{1}{\sqrt{3}})$	35°
5	$-x, -y, +z$	$(-\frac{1}{\sqrt{3}}, -\frac{1}{\sqrt{3}}, +\frac{1}{\sqrt{3}})$	35°
6	NA	NA	35°
7	NA	NA	11.7°

blood. In dynamic 3 and 6, no crushing gradients were used. The effects of the crushing gradients is modeled by the s parameter. In terms of the flip angles used in each dynamic, the first six dynamics used a high flip angle of 35 degrees while the dynamic seven used a low flip angle of 11.7 degrees. The values of the s parameter and the crushing direction at different dynamics are shown in Table 4.1.

The signal from the arterial blood component can be described using the following equation:

$$\begin{aligned} \Delta M_A(t) &= 2 \cdot M_a \cdot \alpha \cdot ABV \cdot c(t) \\ c(t) &= e^{-\frac{t}{T_{1a}}} \end{aligned} \tag{4.3}$$

where M_a is the equilibrium magnetization of the arterial blood, α is the inversion efficiency, ABV is the arterial blood volume, T_{1a} is the T_1 relaxation of the arterial blood.

4.3 Methods

4.3.1 Simulated Data

One hundred T_1-weighted structural images and the corresponding PV estimates were randomly extracted from the first release of UK biobank database (identical data to the previous chapter). Simulated multi-PLD PCASL data were reused from the previous chapter. Four simulated multi-PLD PASL datasets were created using the same GM CBF variation patterns as described in the previous chapter (flat, hyper/hypo, and slow and fast sinusoidal) and a homogeneous WM CBF at

Table 4.2: List of simulation parameters for PASL data

Parameter		Value
Gray Matter		
CBF	(ml/100g/min)	60 (flat), 30 (hypo), 90 (hyper)
Δt	(ms)	700
T1	(ms)	1300
White Matter		
CBF	(ml/100g/min)	20
Δt	(ms)	1000
T1	(ms)	1100
Arterial Blood		
T1	(ms)	1600
Sequence		
λ		0.98
τ	(ms)	640
PLD	(ms)	40, 340, $\cdots$ 3640
α		0.91
Repeat		6

20ml/100g/min. The simulated PASL data were effectively the same as QUASAR ASL by using the parameters proposed in the QUASAR Reproducibility study except that only the tissue signal was generated [86]. Table 4.2 shows the parameters used in the simulated data. Noise was added using the same method as in the PCASL data of the previous chapter.

4.3.2 Healthy Cohort Data

MRI data from six healthy volunteers were retrospectively analyzed from a study on the correlation between cognitive performance and CBF [136].[1] Each subject underwent one MRI session of structural and QUASAR ASL scans. All images were acquired at 3.0 Tesla, on a clinical MR system (Philips Ingenia; Philips Healthcare, Best, The Netherlands), and a 32-channel receive head-coil with body-coil transmission was used. ASL MRI data were acquired from six subjects based on the protocol of the QUASAR reproducibility study [86]. Scan parameters were: TR/TE/interval between excitation pulses=4000/22/300ms, 13 inversion

[1]Data were collected by Otto M Henriksen at Copenhagen University Hospital Rigshospitalet Blegdamsvej, Copenhagen, Denmark

times (40–3640ms), matrix=64×64, seven slices, FOV=240×240mm, slice thickness=6mm, slice gap=2mm, flip angle=35°/11.7°, SENSE factor=3.0, inversion slab width=150mm, slice/inversion gap=30mm, 84 averages (48@Venc=4cm/s, 24@Venc=8, 12 low flip-angle), bolus duration=640ms, implemented in single sequence with scan duration 5min52 s. A T_1-weighted structural MR image (TR/TE = 6.9/700ms, flip angle = 9°, voxel size 1×1×1mm) was also obtained in each subject.

4.3.3 Tissue Perfusion and ATT Estimation

For the simulated data, CBF and ATT were estimated using the VB method in the FSL tool BASIL [108]. Similar to the analysis of PCASL, four simulated experiments were conducted to investigate the sensitivity of the PVEc methods to different variabilities of data and PV estimates including (1) background noise of ASL data; (2) resolution mismatch between ASL data and PV estimates; (3) random errors in PV estimates; (4) biased errors in PV estimates.

In the healthy cohort data, tissue perfusion and ATT were estimated by fitting the ASL difference data of all six dynamics to the tissue kinetic model using the spatial VB method [108][113]. ABV was estimated by fitting the arterial blood signal to the model described in Equation 4.1. The equilibrium magnetization of the arterial blood for calibration was estimated from the QUASAR ASL control data. Specifically, the mean control signal across all PLDs was computed before fitted to a saturation recovery model to estimate the equilibrium magnetization of tissue and T_1 relaxation of tissue [101]. An M_0 correction technique (including median filter, erosion and extrapolation) was performed on the tissue M_0 to reduce the PVE on the edge of the brain as demonstrated in Section 3.3.4 of Chapter 3. Finally, the equilibrium magnetization of the arterial blood was computed by dividing the corrected M_0 of tissue by the blood water partition coefficient constant. The priors and sequence parameter values used for the healthy cohort experiment are listed in Table 4.3.

For both simulated and healthy cohort data, PVEc was conducted using both LR and spatially regularized methods. The LR method was implemented on the

Table 4.3: Parameter values used in healthy cohort experiment

Parameter		Value	Spatial Prior
CBF	(ml/100g/min)	(0, 10^{12})*	M
ATT to tissue	(ms)	(0.7, 10^{-1})	
Tissue T_1	(ms)	(voxelwise, 10^{-2})	I
ABV	(%)	(0, 10^{12})*	M
ATT to macrovasculature	(ms)	(0.5, 10^{-1})	
Arterial blood T_1	(ms)	(1600, 10^{-2})	
Bolus duration	(ms)	600	
Blood-water partition coefficient		0.98	
Inversion efficiency		0.91	

*Values indicate mean and standard deviation of prior; I: Image Prior; M: Markov random field.

ASL difference data and CBF maps using a kernel size of 5×5. In the spatially regularized method, a total of 200 iterations were performed to ensure convergence.

4.3.4 Evaluation Metrics

RMSE values for CBF and ATT were computed for each experiment of simulated PCASL and PASL data using the formulation of Equation 3.5 (previous chapter RMSE equation). For both simulated and healthy cohort data, ROI analysis was conducted to compare the mean GM CBF of each GM ROI using the same method by Asllani et al [14]. The extended ROI analysis was performed to reflect the correlation between estimated GM CBF and GM PV estimates by considering a linear regression of GM CBF and GM PV estimates of the range 10%–90% using a least-square fit (same with the techniques used in Chapter 3), and the estimated slope values were recorded.

4.3.5 Statistical Analysis

In all simulated experiments, a two-tailed paired t-test was conducted to compare the RMSE values of GM CBF between PCASL and PASL of each PVEc methods (including no PVEc). The null hypothesis was that the RMSE value was the same in PCASL and PASL after PVEc (or no PVEc). The alternative hypothesis was that the RMSE or slope value was not equal between the two ASL techniques.

The same test was conducted on the estimated slope values of GM CBF and the RMSE of the estimated GM ATT values.

4.4 Results

4.4.1 Simulated Experiments

Figure 4.1 shows the RMSE between the estimated and simulated GM CBF for PCASL and PASL data. Figure 4.2 shows the estimated slope values from the extended ROI analysis. Figure 4.3 shows the RMSE between the simulated and the estimated GM ATT. For both CBF and ATT estimation of GM, PVEc reduced the estimation errors from the bias of WM. For GM CBF estimation, the PVEc methods provided similar accuracy on both PCASL and PASL. For GM ATT estimation, the spatially regularized method performed poorly on PASL while the accuracy of the LR method was similar for both PCASL and PASL.

The estimated CBF of PCASL and PASL data were similar when there was only one source of uncertainty in the simulated data or PV estimates (comparing the results of each experiment). The accuracy of GM CBF estimation of both PCASL and PASL reduced with the added uncertainty (noise, mismatch of PSF, and PV estimates errors) while the slope value of the spatially regularized method changed most substantially when there was a mismatch of PSF between the ASL data and PV estimates (Figure 4.2C). When the SNR reduced, the slope value for both PCASL and PASL increased. The same observation was found when biased errors were introduced to PV estimates. These results indicated that a positive correlation (about 700ml/100g/min/%) can be found between the GM CBF and GM ROI for both PCASL and PASL if the SNR was low and that there were biased errors in the PV estimates (Figure 4.2B and Figure 4.2E). If there was a mismatch of the PSF between ASL data and the PV estimates, the errors of GM CBF estimation of PCASL was larger than PASL (Figure 4.1C). This is largely due to the underestimation of the GM CBF (about 15%) in high GM ROIs, which translated into a negative slope value of -2500ml/100g/min/% (Figure 4.2C).

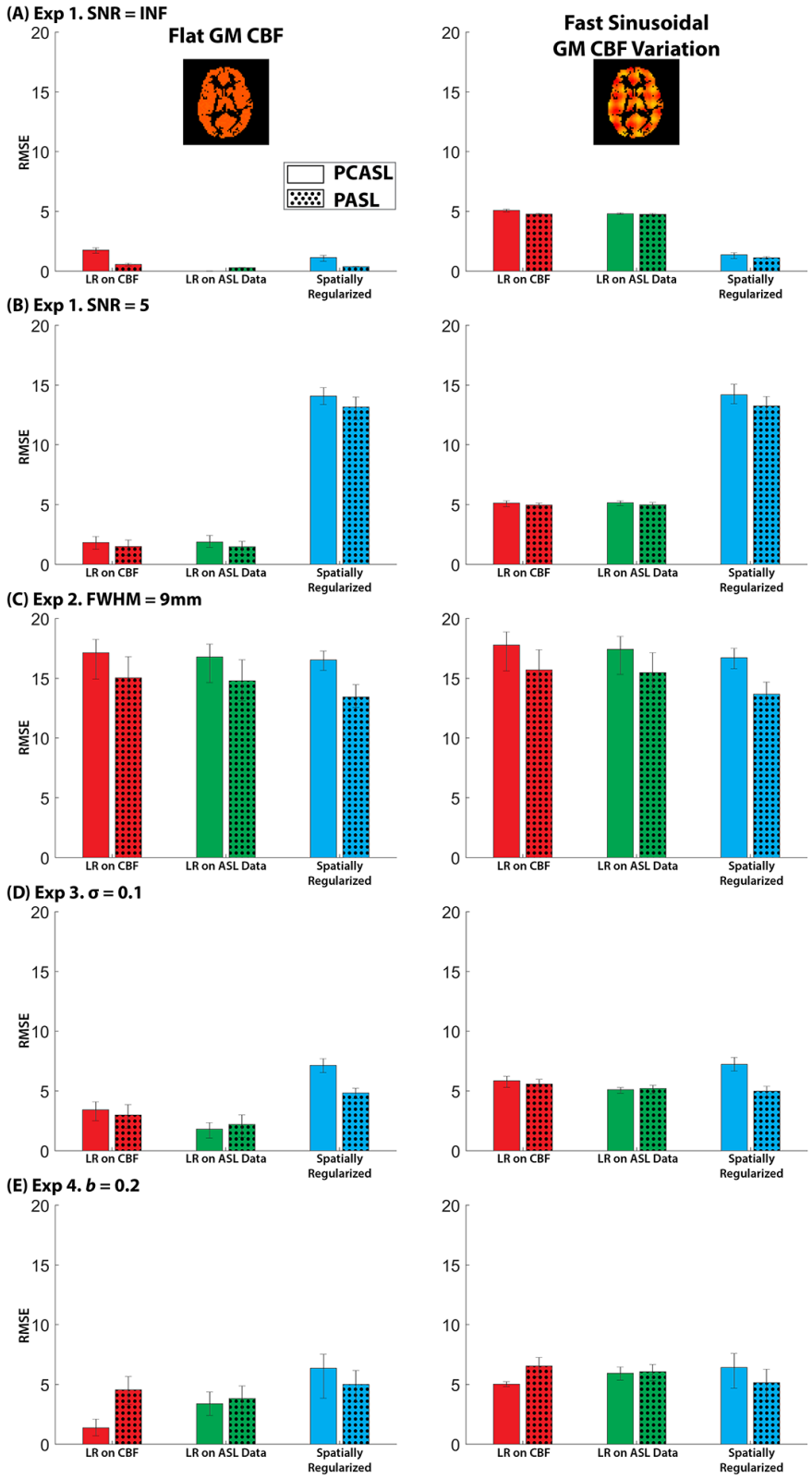

Figure 4.1: RMSE between estimated and simulated CBF in multi-PLD PCASL and PASL. PASL achieved higher accuracy if PVE was corrected by the spatially regularized method (blue dot bars). PCASL showed superiority if the GM CBF was corrected by the LR method and there was biased errors in PV estimates. For each PVEc methods, the RMSE values of PCASL and PASL were all significantly different. For the no PVEc methods, the RMSE was greater than 30 (not shown)

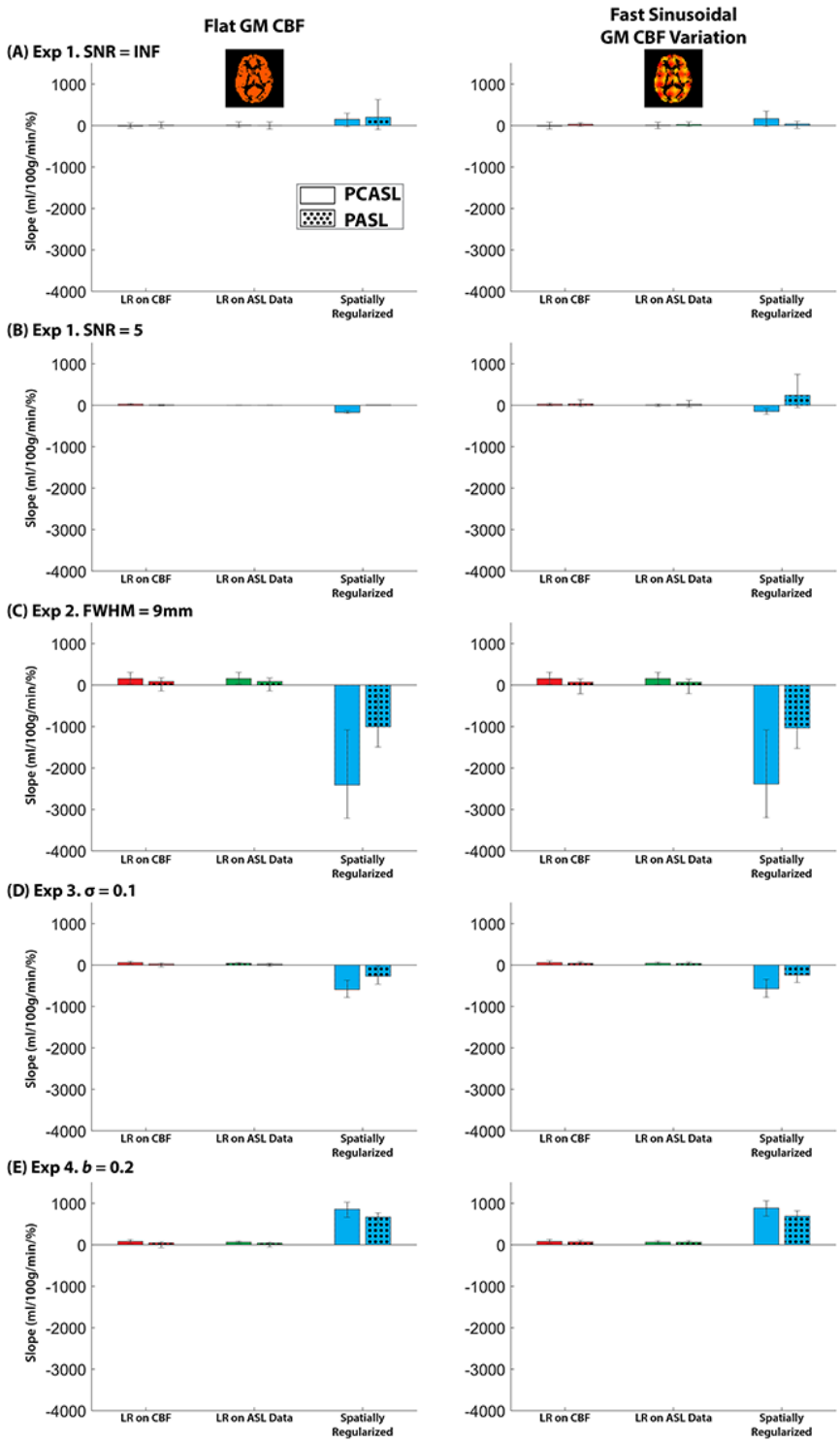

Figure 4.2: Estimated slope values of the extended ROI analysis for the simulated multi-PLD PCASL and PASL data. The slope values of PCASL and PASL were nearly zero in all experiments. GM CBF of PCASL was more correlated (both positively and negatively) to GM ROIs if the spatially regularized PVEc method was chosen.

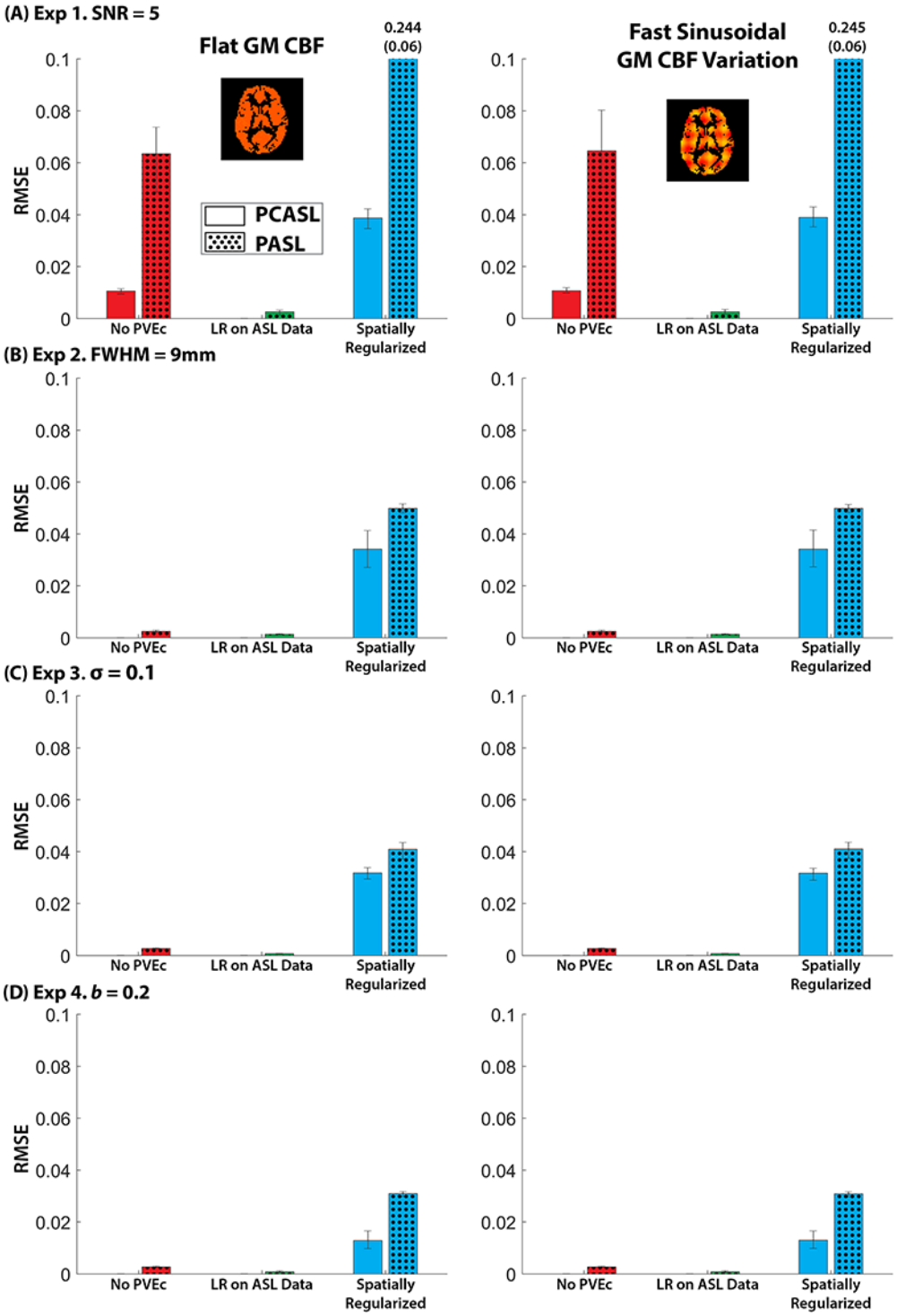

Figure 4.3: RMSE between estimated and simulated GM ATT for the simulated multi-PLD PCASL and PASL data. Overall, applying LR on ASL data produced highest accuracy for GM ATT estimation whereas the spatially regularized method the lowest. The RMSE of the estimated ATT values of PCASL and PASL were all significantly different. In Experiment 1, the mean RMSE values of PASL using the spatially regularized method were 0.244 and 0.245 respectively (higher than the range of the y-axis).

The accuracy of the estimated GM ATT of PCASL and PASL was almost identical using the LR approach on the ASL data but different using the spatially regularized method. For the LR approach on ASL data, the accuracy of the GM ATT for both PCASL and PASL was high in each experiment (RMSE less than 0.01, Figure 4.3). However, the accuracy decreased if the spatially regularized method was used, in particular for PASL data with high noise (Figure 4.3A). For the other experiments (PSF mismatch and errors in PV estimates), the accuracy of the GM ATT estimation by the spatially regularized method was similar for both PCASL and PASL (less than 0.05) while the results of PCASL was always slightly more accurate than PASL. Thus, the LR method had the same effect on the two ASL method and the RMSE of the spatially regularized method was 15% less than the RMSE of the LR method (Figure 4.1A).

Figure 4.4 shows the RMSE between estimated and simulated GM CBF for PCASL and PASL data with SNR = 5. Figure 4.5 shows the estimated slope values from the extended ROI analysis using SNR = 5 simulated data. Figure 4.6 shows the RMSE between the simulated and the estimated GM ATT using SNR = 5 simulated data.

Comparing between the RMSE of CBF using SNR = INF (Figure 4.1) and SNR = 5 (Figure 4.4) simulated data, a common feature was that blurring the ASL data (experiment 2) reduced the accuracy for all the three PVEc methods substantially while the uncertainties on the PV estimates largely affected the spatially regularized method. In experiment 3, where random errors were introduced to the PV estimates, the LR methods were insensitive to the different SNRs used in the simulated data (Figure 4.1D and Figure 4.4B), and the same phenomenon can be found in experiment 4 (Figure 4.1E and Figure 4.4C). On the other hand, the accuracy of the spatially regularized method was further deteriorated when the noisy simulated data were used (Figure 4.4B). Comparing between the results of PCASL and PASL SNR = 5 data, PASL still demonstrated lower errors in most of the experiments, except when biased PV estimates were introduced and the LR method was applied to the ASL data. The slope values of the spatially regularized method using SNR = 5 data

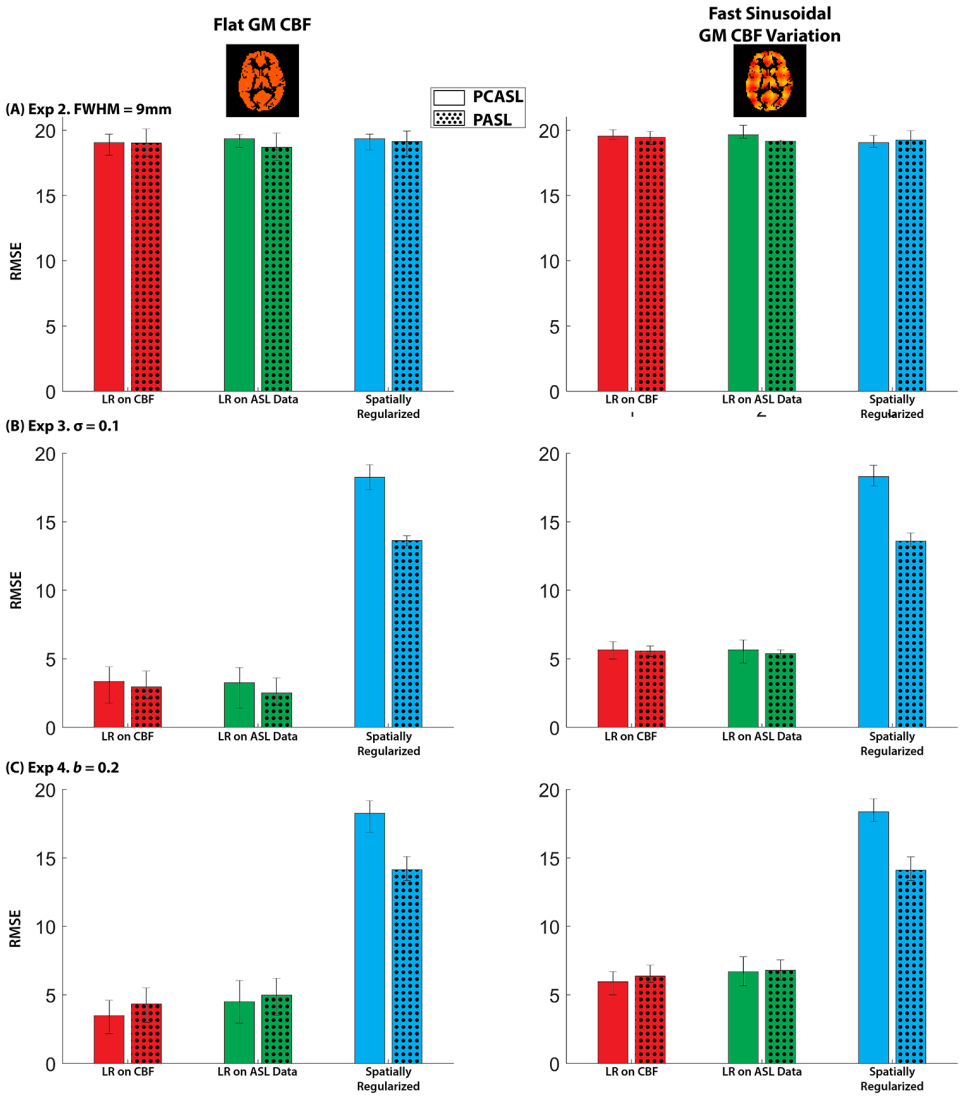

Figure 4.4: RMSE between estimated and simulated GM CBF for the simulated multi-PLD PCASL and PASL data SNR = 5. In experiment 3 and 4, applying LR on ASL data produced highest accuracy for GM ATT estimation whereas the spatially regularized method the lowest. The RMSE for the No PVEc methods were all greater than 30 (not shown).

reduced significantly from using SNR = INF data (nearly 10 times less, Figure 4.2 and Figure 4.5). The slope values of the LR methods, however, remained relatively unchanged after SNR = 5 data was used in the analysis. In terms of the estimation of GM ATT (Figure 4.6), the usage of SNR = 5 data caused the accuracy of all methods to reduce, in particular, the spatially regularized method. For instance, the RMSE of the spatially regularized method increased 110% for the PASL data in experiment 2 (Figure 4.5A). In contrast to the GM CBF estimation, the PCASL technique showed

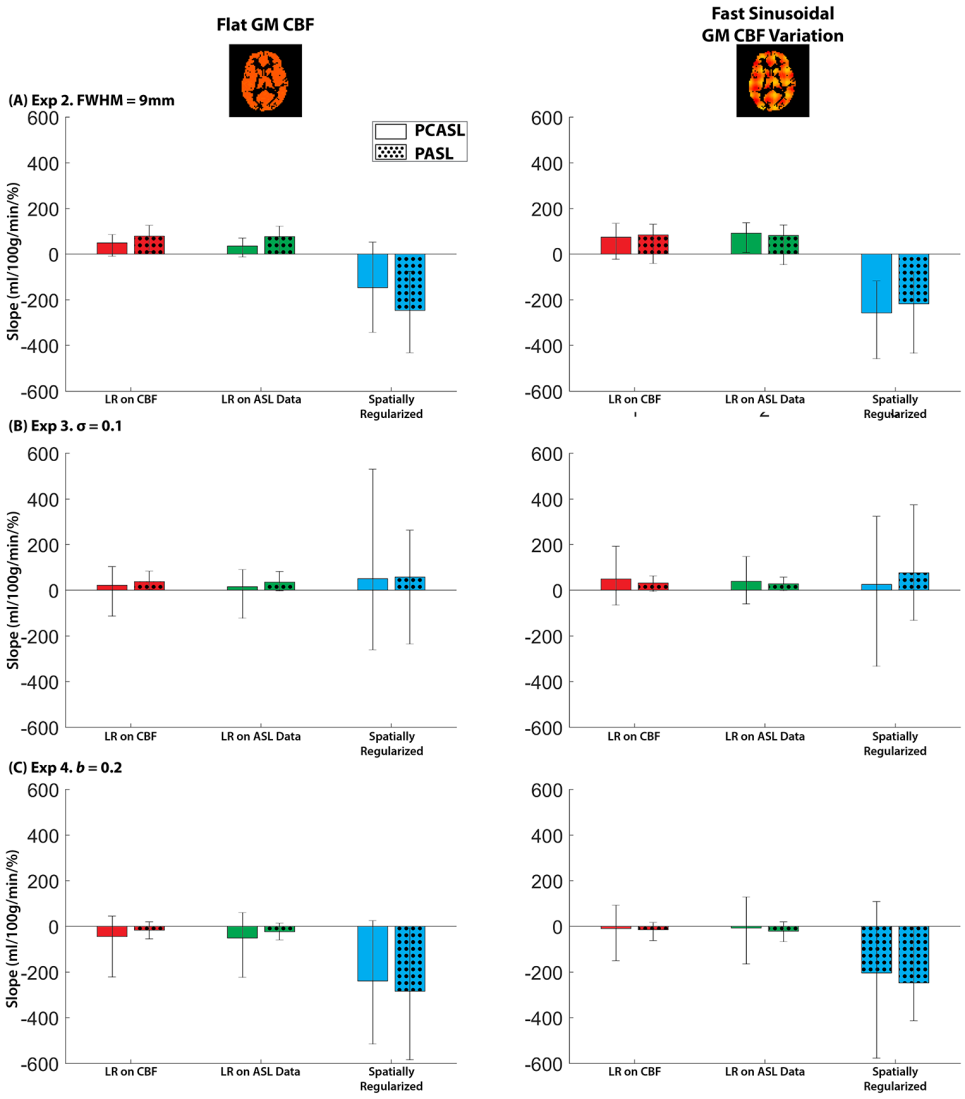

Figure 4.5: Estimated slope values of the extended ROI analysis for the simulated multi-PLD PCASL and PASL data SNR = 5.

higher accuracy than PASL in all experiments using SNR = 5 simulated data.

4.4.2 Healthy Cohort Experiments

Figure 4.7 shows the GM CBF and GM ATT maps (before and after applying the GM mask) of an example subject before and after PVEc. Figure 4.8 shows the mean GM CBF and ATT of the group. In the CBF maps of the example subject, GM CBF increased (brighter) after PVEc using all three methods. The two LR techniques demonstrated similar results in terms of overall GM CBF values. On the other hand, the mean GM CBF of the spatially regularized method was

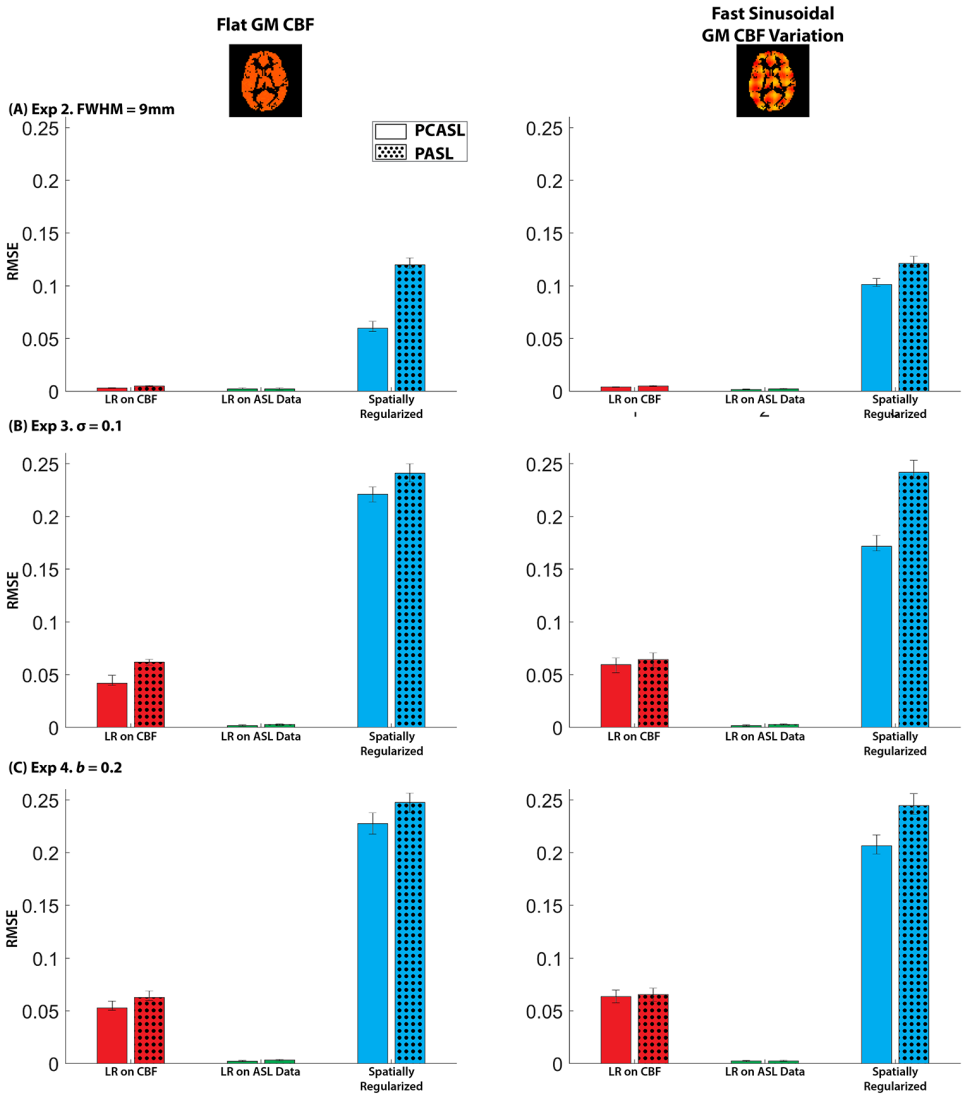

Figure 4.6: RMSE between estimated and simulated GM ATT for the simulated multi-PLD PCASL and PASL data SNR = 5. For all experiments, applying the LR methods on the ASL data resulted in the highest estimation accuracy (lowest RMSE).

higher than the LR methods. Looking at the group level results, the two LR methods increased the mean GM CBF by about 20% (from 58 to 70 ml/100g/min) whereas the mean GM CBF of the spatially regularized method nearly doubled (from 58 to 110 ml/100g/min). The spatially regularized method also expanded the intra-subject variation (broader box length). For the GM ATT measurements, only the results corrected by PVEc on the ASL data were less than the other three methods (Figure 4.8), and this PVEc method showed more smoothness than the spatially regularized method (Figure 4.7).

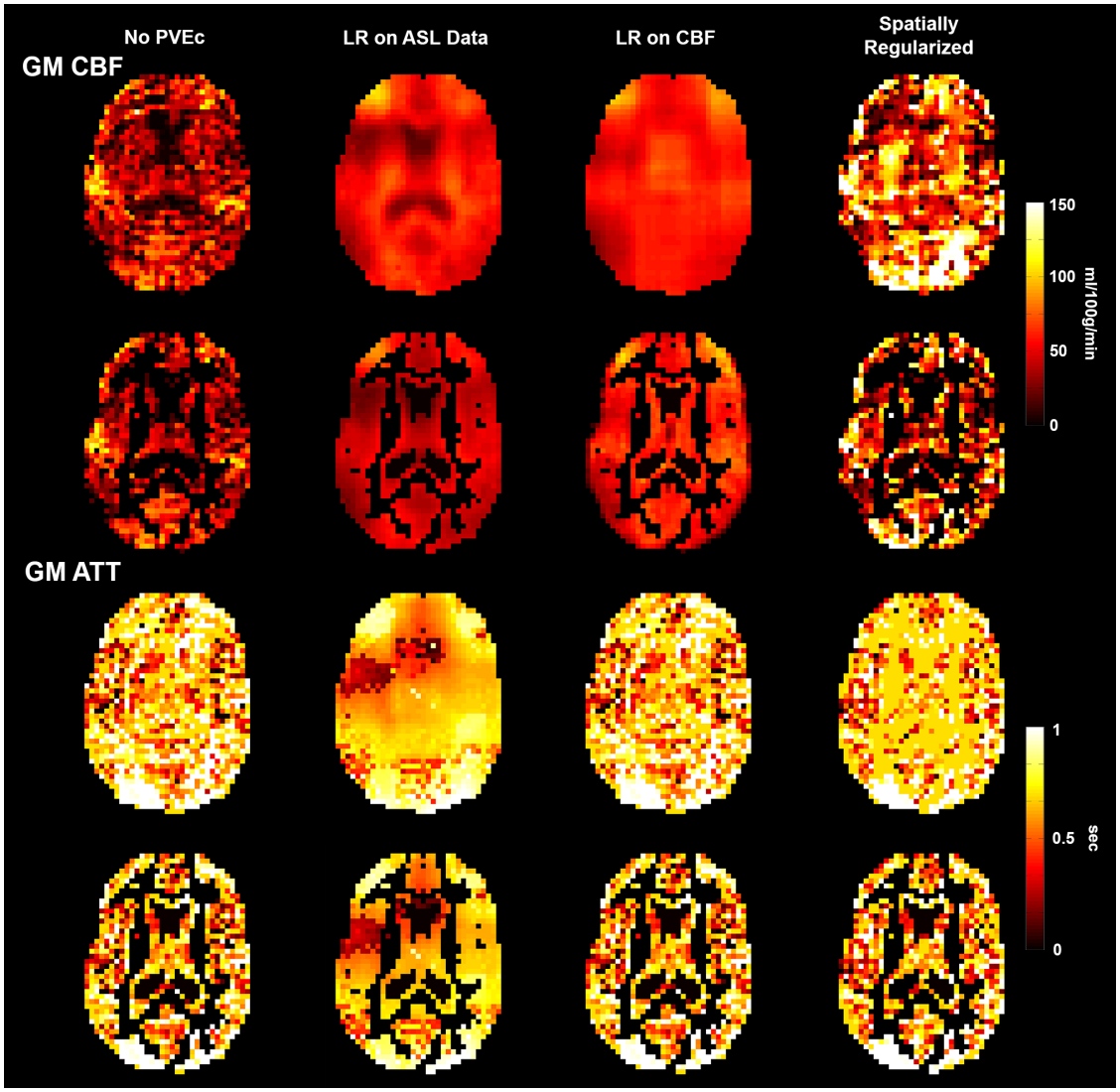

Figure 4.7: Estimated GM CBF and ATT of an example subject before and after PVEc using LR and spatially regularized method. Overall, the GM CBF increased after PVEc. However, the increment after correction by spatially regularized method was higher than the two LR approaches. The GM ATT values were almost identical for the spatially regularized and no PVEc methods, but the values of the LR method applied on data was lower and had greater amount of smoothness. Since the PVEc was applied on the CBF maps, the GM ATT of the LR on CBF method was identical to the No PVEc method.

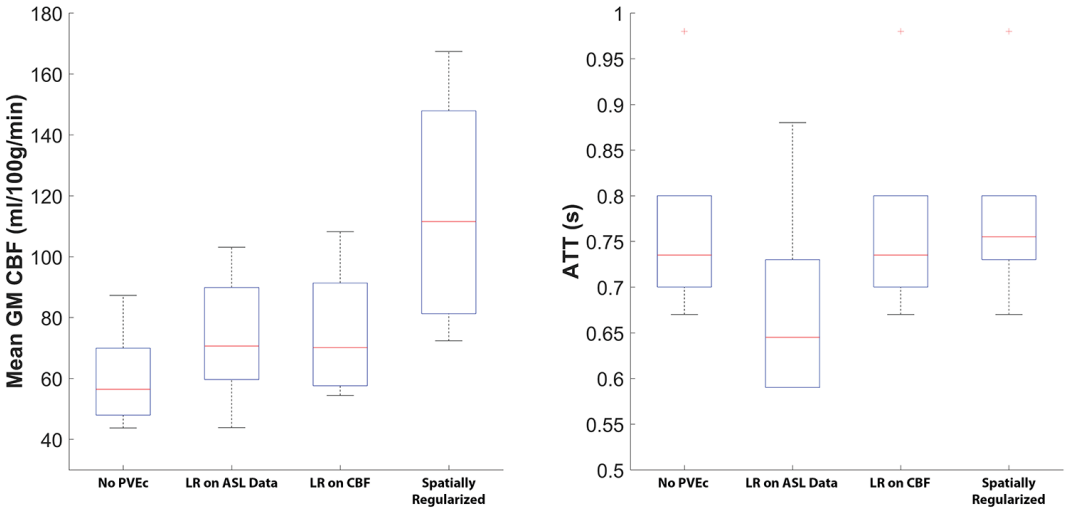

Figure 4.8: Estimated mean GM CBF and ATT of the six subjects before and after PVEc. The mean GM CBF was about 58ml/100g/min before PVEc, it was increased to 70ml/100g/min after applying the LR methods and nearly doubled after using the spatially regularized method. GM ATT estimated by LR on ASL data was lower than the other three methods.

Figure 4.9 shows the ROI plot of an example subject and the estimated slope values from the linear regression fit for each PVEc methods. From the individual ROI plot, it can be seen that the correlation between GM CBF and GM ROI changed little after applying the LR methods (compared with the spatially regularized method), and the corresponding slope values were (270 ml/100g/min/% without PVEc and -520 ml/100g/min/% for LR on the ASL Data). For the spatially regularized method, a negative correlation was found (slope value about -2100 ml/100g/min). The median slope value of the spatially regularized method was about -6000ml/100g/min/% (box plot of Figure 4.9), indicating that the GM CBF of the lowest GM ROI was about 60ml/100g/min higher than the value of the highest GM ROI.

4.5 Discussion

In this work, we have investigated the sensitivity of estimating GM CBF and ATT using different PVEc and multi-PLD ASL techniques. We have simulated multi-PLD PCASL and PASL data under the same conditions and performed PVEc to estimate GM CBF and ATT. In the healthy cohort experiment, GM CBF and ATT values

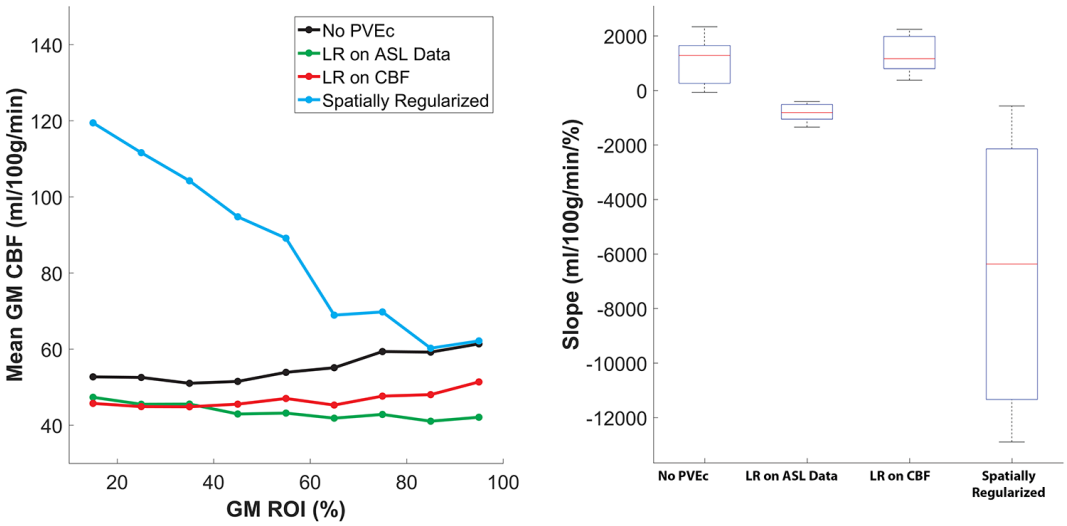

Figure 4.9: ROI plot of an example subject and estimated slope values for all the subjects in the group. A slightly positive correlation was shown between GM CBF and GM ROI before PVEc. After correction by LR methods, the relationship became less correlated and mean slope value decreased. Negative slope values were observed in the spatially regularized methods.

were estimated from a QUASAR ASL dataset to examine the effectiveness of the PVEc methods. The findings of the study are: (1) both the LR and the spatially regularized PVEc methods showed a similar accuracy for GM CBF estimation on simulated multi-PLD PCASL and PASL data with high SNRs; (2) for GM ATT estimation, the LR applied on ASL data was the most accurate method.

4.5.1 Simulated Experiments

The estimated GM CBF demonstrated similar results in both PCASL and PASL data in all of the experiments. Overall, GM CBF estimation accuracy improved after PVEc by either LR or spatially regularized method by at least 35% for both ASL techniques (Figure 4.1). If the spatially regularized method was the chosen PVEc method, PASL demonstrated slightly higher accuracy than PCASL in all experiments (blue bars in Figure 4.1). For PCASL and PASL, the estimation accuracy and the slope values of applying the LR method before or after model-fitting were similar (Figure 4.1 and Figure 4.2), implying consistent underestimation or overestimation in different GM ROIs. Comparing the different slope values between PCASL and

PASL after being corrected by the spatially regularized methods (blue bars in Figure 4.2), only biased errors in the PV estimates caused a positive correlation between GM CBF and GM ROI while the other sources of uncertainties (PSF mismatch, and random errors) resulted in a negative correlation.

Results of GM ATT estimation revealed that the LR method on ASL data were the most accurate method for both PCASL and PASL (Figure 4.3). It should be noted that the simulated GM ATT was homogeneous throughout the brain, which might favor the LR based method over the spatially regularized method. Except for noise, the accuracy of GM ATT estimation was affected little by the variations including mismatch of PSF and errors in the PV estimates (Experiment 2, 3, and 4 of Figure 4.3). If a high noise level was expected in the acquired data, PCASL acquisition seemed to be a better choice than PASL (Figure 4.3A).

The two ASL acquisition methods demonstrated different characteristics when estimating GM CBF and ATT using various PVEc methods. If PVEc was not conducted, PCASL was better when estimating CBF and ATT based on the simulated experiments. If the LR based method was selected, it is best applied on subjects with fairly consistent tissue CBF through the brain using either PCASL or PASL data. However, if there are large discrepancies of the PSF (unmatched PSF) between the ASL and structural data, consistent underestimation of GM CBF and ATT can be found (Figure 4.1C and Figure 4.2C). If the spatially regularized method was the desired choice for PVEc, data should be collected by PCASL sequences to increase SNR and matching the PSF between the ASL and the structural data. Although the accuracy of CBF estimation was similar for the spatially regularized method on PCASL and PASL, results of ATT from PCASL showed lower errors than PASL (blue bars of Figure 4.3). Overall, the spatially regularized approach demonstrated higher sensitivity to detect tissue CBF variations than the LR method. Based on the results of simulated data with noise, accuracy of the spatially regularized method on the GM CBF quantification of the whole brain decreased to lower than the LR method. Thus, the SNR of the data and the expected GM CBF variations should be major factors for the application of the spatially

regularized method to quantify GM CBF. If the SNR of the data is relatively high, such as those acquired by multi-PLD PCASL, and the GM CBF variations is expected to be highly localized, then the spatially regularized method should be the better choice for GM CBF quantification. On the other hand, if the quality of the data was poor (low SNR) and the aim is to compute the mean GM CBF of the whole brain, then the LR method should be considered due to its low sensitivity to noise.

In the simulation experiments, simulated data with two sets of SNR values (5 and INF) were chosen as the input data to compare the performance of the PVEc methods. In general, the RMSE of GM CBF and ATT demonstrated that the spatially regularized methods performed poorly than the LR methods (Figure 4.1 and 4.4) in different noise levels of the simulated data and various sources of uncertainties in the analysis (data blurring and errors in PV estimates). This was not surprising because the spatially regularized approach was in essence a model-based method that tends to be more sensitive to noise and errors. The purpose of using the selected SNR values in the experiments was to compare the two PVEc methods in the ideal situation and evaluate their performances in practice. In the SNR = INF case, the advantage of the spatially regularized method was shown by its ability to retain spatial variations (hyper/hypo perfusion) and rapid changes of GM CBF (sinusoidal variations). Thus, if the ASL data with high SNR and sharp changes in CBF are presented, the spatially regularized method should be the more desirable choice. Nevertheless, if the SNR of the ASL data is low (such as close to SNR = 5 in the simulations), the LR methods may be selected to achieve a fairly accurate estimation of GM CBF and ATT of the whole brain, while compromising the sensitivity to detect hyper/hypo perfusion.

4.5.2 Healthy Cohort Experiments

The LR and spatially regularized methods showed different estimations of GM CBF on the healthy cohort data. Before PVEc, the median slope values of the extended ROI analysis of the group was 1000ml/100g/min/% (Figure 4.9). This implied that the linear relationship between GM CBF and GM ROI before PVEc

was unexpectedly less correlated than the results in the simulated PASL data and the healthy cohort PCASL data (box plot figure in Chapter 3). Since the effect of the LR method is to reduce the correlation between the tissue CBF and the corresponding PV estimates, the ROI plot of the GM CBF obtained by the two LR methods retained the consistent GM CBF levels in each ROI (Figure 4.9). From these results, the effectiveness of the LR methods cannot be justified because the GM CBF in the low PV estimates regions remained the same after PVEc. On the other hand, the slope values of the spatially regularized method were negative, indicating that the GM CBF of the smaller ROIs was higher than the voxels with a higher amount of GM PV estimates.

The difference of the mean slope values between no PVEc and the spatially regularized method was about 6000ml/100g/min/%, which was still higher than the results seen in the simulations (about 5000ml/100g/min/% in Experiment 1 of Figure 4.2). The discrepancy might be due to two factors: a low SNR and a large mismatch of the PSF between the QUASAR ASL data and the PV estimates. As demonstrated in the previous chapter, since the spatially regularized method was particularly sensitive to noise and errors in voxels with a small amount of tissue volume (low ROI values), the estimated GM CBF of this method might not reflect the genuine GM CBF of the subject (Figure 4.9). Another source of error was the different PSF used in the QUASAR ASL data and the PV estimates. Since a Look-locker readout scheme was used in QUASAR ASL, the readout time was fairly long. T_2 related signal modulation at each readout pulse of the Look-locker scheme may result in large amount of blurring [17]. The observed negative correlation between GM CBF and GM ROI (Figure 4.9) was similar to Experiment 2 of the simulated experiment where applying a spatial filter to the ASL image caused negative slope values (Figure 4.2C). The blurring may be corrected by (1) applying deblurring techniques to sharpen the ASL image or (2) alter the signal reconstruction process to reduce the amount of blurring [137].

Applying the LR method to correct PVE reduced the median GM ATT from the value before PVEc by about 13% (Figure 4.8). The results indicated that

the estimated GM ATT was less than the observed ATT without PVEc. The LR method also induced the highest degree of smoothing, which can be found in Figure 4.7. In contrast with tissue CBF patterns, the spatial variation of ATT are generally less. From these results, applying the LR methods on QUASAR ASL might be a favorable approach for its fairly low sensitivity to noise and errors as well as correcting for ATT differences due to PVE.

4.5.3 Limitations

A limitation of the work is the reliance on simulated data in comparing the two ASL techniques. The same GM CBF patterns were adopted as in the previous chapter, which might not necessarily capture the more realistic perfusion variations in the healthy cohort data. This may be one of the factors which caused the discrepancy between the simulation and healthy cohort results. In term of the simulated ATT values, GM and WM ATT values were fixed to be 0.7s and 1.0s respectively in the whole dataset. However, ATT values have been found to increase from the inferior to the superior regions of the brain and vary between different regions of the brain [104]. The current simulation included seven slices to match the parameters of the healthy cohort data, and the simulation results indicated that both PCASL and PASL performed equally well in estimating ATT.

In the simulation experiments, four SNR values were chosen to demonstrate the impacts of noise onto the PVEc methods. It is possible that ASL data with SNR lower than five are acquired in practice, and the present simulation did not capture such cases. Another limitation was the complexity of the impacts from different sources of errors. In practice, it is likely that a combination of uncertainties (such as noise, blurring, and errors in PV estimates) are present simultaneously. Although it is difficult to simulate all the possible effects together, we attempted to investigate the impacts of such uncertainties on data with a high noise level (SNR = 5). The results may be served as a potential benchmark for evaluating the performance of PVEc methods on real data.

In capturing the data variabilities, motion artifact was not considered in the simulations. This might be another factor that caused the discrepancy between simulations and healthy cohort results. As discussed in the Methods section, the healthy cohort data was extracted from a cognitive testing experiment that included several MRI scans. Although the data were collected from healthy volunteers, they were not primed to keep still during the course of an MRI experiment. The QUASAR ASL data acquisition was scheduled at the end of the whole procedure and proceeded by four other MRI experiments (T_1-weighted, T_2-weighted, T2 FLAIR, and PC MRI) that lasted over 15 minutes. Since ASL data was acquired last, the fatigue of the subject might cause motion artifact during the QUASAR ASL data acquisition [136]. For example, the high GM CBF level in Figure 4.8 and Figure 4.9 may be a result of motion artifact, which might have affected CBF estimation without PVEc.

The low SNR of QUASAR ASL limited its CBF estimation and spatial coverage of the brain. Since the bolus duration of QUASAR ASL was only a third of the PCASL bolus duration (1.8s), the signal would become even less due to the T_1 decay between labeling and reaching the tissue region. This is an important factor that the spatial coverage of QUASAR ASL was only about 4.5cm (or about half of the brain). In order to enlarge the spatial coverage and enhance SNR, a new labeling scheme to create longer bolus duration is needed. Turbo QUASAR ASL (to be discussed in the next chapter) may be a solution to this challenge.

4.6 Conclusions

In this work, we have investigated the performance of PCASL and PASL techniques to estimate GM CBF and ATT. In the simulated experiments, the estimation of GM CBF of both ASL techniques improved GM CBF estimation after PVEc (Figure 4.1). GM ATT can be estimated more accurately by the LR method applied to both PCASL and PASL. In the healthy cohort experiment, the GM ATT estimated by the LR method was consistently lower and more smooth than the other methods. The high SNR and mismatch of PSF may be the factors to

the negative correlation observed between the estimated GM CBF and GM ROI for the spatially regularized method.

Ik droom van schilderen en dan schilder ik mijn droom.

I dream of painting and then I paint my dream.

— Vincent Willem van Gogh

5

Investigating Cerebrovascular Reactivity Using PCASL and Turbo QUASAR ASL

Contents

5.1 Introduction 123
5.2 Theory 125
5.2.1 Turbo QUASAR ASL Sequence 125
5.2.2 Tissue Kinetic Model 131
5.3 Methods 135
5.3.1 Simulations 135
5.3.2 Healthy Cohort Data 137
5.3.3 PCASL Perfusion Quantification 140
5.3.4 Turbo QUASAR ASL Perfusion Quantification 140
5.3.5 Absolute Perfusion Quantification 142
5.3.6 Blood Flow Velocity Quantification 143
5.3.7 Statistical Analysis 143
5.4 Results 145
5.4.1 Simulated Experiments 145
5.4.2 Healthy Cohort Experiments 147
5.5 Discussion 155
5.5.1 Turbo QUASAR ASL Sequence 158
5.5.2 Model Based Method and Simulated Experiments . . . 159
5.5.3 Healthy Cohort Experiments 160
5.5.4 CVR Quantification Using PCASL 161
5.5.5 CVR Quantification Using Turbo QUASAR ASL 164
5.5.6 Implications for CVR Studies for SCD Patients 165
5.5.7 Impacts of Resolution and Motion 167
5.5.8 Limitations 167
5.6 Conclusions 169

5.1 Introduction

Cerebrovascular reactivity (CVR) is defined as the ratio between the change in cerebral blood flow (CBF) relative to the baseline CBF in response to a vasoactive stimulus, and it has become an important biomarker to assess cerebrovascular health [138]. From the definition of CVR, the precise estimation of CBF at different flow conditions is crucial to the accurate quantification of CVR. Studies have demonstrated effective CVR measurements in both healthy subjects and patients using BOLD MRI, perfusion weighted MRI, and PET techniques [12][16][139].

ASL is an MRI based technique that allows the quantification of CBF and several other hemodynamic parameters such as ATT and arterial blood volume (ABV). The non-invasive nature of ASL allows repeated measurements of these parameters under different conditions, making ASL MRI a potentially effective tool for CVR measurements. However, changes in CBF are often coupled with subtle variations of several other parameters that affect the ASL signal such as vessel dilation, blood velocity, and the T_1 relaxation time of the blood [133][140]. The influence of these factors need to be addressed for the precise quantification of CBF and CVR using ASL MRI, in particular for studying the hemodynamic of patients with blood disorders.

A consensus paper of the ASL community has recommended using a pseudo-continuous ASL (PCASL) technique and acquiring images after a single PLD as the standard implementation of ASL in clinical applications [17]. The single-PLD PCASL technique has demonstrated high inter-vendor and inter-session repeatability of CBF measurement [85]. However, this technique is sensitive to changes in ATT which varies in different regions of the brain and affects the precise quantification of CBF [104]. Also, the inversion efficiency (the percentage of the spins fully inverted by the RF pulse) of PCASL is known to be sensitive to the changes in velocity of the inflowing arterial blood [2]. In the context of subjects under different

blood flow conditions, both flow velocity and ATT have demonstrated variability and are considered confounding factors to the CBF estimation [133], making the single-PLD PCASL method a potentially less desirable tool for CVR quantification. In contrast to PCASL, Pulsed ASL (PASL) employs a labeling technique that applies the RF pulse to label a volume of blood water in a fixed region, and its inversion efficiency is consequently less sensitive to changes in blood velocity than PCASL [78]. In order to control for the ATT variations, a multi-PLD imaging technique is needed to estimate ATT and correct for it in the CBF estimation. Therefore, an ASL technique that combines the features of PASL and multi-PLD acquisition may be more suitable to study the hemodynamics at varying blood flow conditions and measure CVR accurately.

QUASAR ASL is an advanced ASL sequence that employs a PASL based labeling technique (implemented by PULSAR) and multi-PLD acquisition by applying the Look-locker readout scheme [73]. Studies using QUASAR ASL have demonstrated high reproducibility of CBF measurement [86] as well as a high sensitivity to detect ATT changes during brain activation [96]. The inclusion of the crushing gradients allows QUASAR ASL to separate the ASL signal into tissue and the arterial blood components, not only reducing the associated artifact in the tissue signal, but also allowing both model based and model free methods to be applied for the CBF estimation [101]. Moreover, the signal from the arterial blood component can be used to estimate ABV, which is a measurement of the amount of blood in the macrovasculature in order to understand if higher ABV is the mechanism of the elevated blood flow in some patients with sickle cell disease (SCD) [141]. These advantages may make QUASAR ASL a favorable tool to study hemodynamics under varying blood flow conditions.

QUASAR ASL is limited by the low SNR (compared with PCASL) and the small spatial coverage of the brain. These issues were due to the short bolus duration achieved with the PASL labeling technique, as well as the Look-locker readout scheme that reduced the signal at each excitation [3]. Recently, a new sequence dubbed Turbo QUASAR ASL has been developed to enhance the SNR

of QUASAR ASL by creating multiple boluses in a single ASL experiment while retaining the other characteristics of QUASAR ASL. Preliminary work on a single healthy subject showed comparable SNR with PCASL and CBF estimation of nearly the full brain using a model free quantification approach [142]. The sensitivity of Turbo QUASAR ASL to estimate CBF and CVR at varying flowing conditions remain to be investigated and compared with that of the standard PCASL approach.

In the present study, we compare the sensitivity for estimating CBF and CVR between Turbo QUASAR ASL and PCASL. A model based quantification method was developed for Turbo QUASAR ASL to estimate CBF as well as the auxiliary parameters such as ATT, ABV, and T_1 in order to reflect the changes in these confounding factors that affect the ASL signal. Simulated experiments were conducted to investigate the estimation accuracy and sensitivity of the model based method to explore whether model based or model free method is more suitable for Turbo QUASAR ASL. PCASL and Turbo QUASAR ASL data of a healthy cohort were analyzed retrospectively. The data were collected at baseline and after acetazolamide administration (a vessel dilation drug) to reflect different conditions of blood flow. Three quantification techniques were used in computing the hemodynamic parameters from the healthy cohort data: (1) CBF estimation using PCASL without considering ATT; (2) CBF estimation using PCASL using the ATT estimated by Turbo QUASAR ASL; (3) the newly developed model based method on Turbo QUASAR ASL. CVR was computed and compared on both full brain and regional basis. ATT and blood flow velocity were also computed using the Turbo QUASAR ASL and PC MRI data. Regional CBF differences of PCASL and Turbo QUASAR ASL at the same flowing condition were compared to investigate the differences between the two ASL techniques using paired t-tests.

5.2 Theory

5.2.1 Turbo QUASAR ASL Sequence

In most ASL implementations, one or many (such as in PCASL) RF pulses are used in the label experiment to generate a single bolus of tracer. Multiple images

(multi-TI or multi-PLD) may be acquired to achieve sufficient SNR and account for the different ATT in CBF quantification. In QUASAR ASL, a multi-PLD acquisition scheme is employed using a low FA (35°) Look-locker readout technique [73]. Due to the repeated excitation pulses of the Look-locker readout, the signal intensity decreases after each excitation pulse. Following the conventional inferior to superior sequential readout, the signal reduction and short bolus duration of 0.64s lead to an insufficient amount of signal for the whole brain coverage, causing reduced spatial coverage of the QUASAR ASL technique. Specifically, the signal of the top slice was nearly 60% less than the bottom slice (seven slices or 5cm below) in the data collected in the QUASAR Reproducibility study [86], and the proposed parameters have been widely adopted by several other studies [118][136]. The signal would continue to decline using the same scanning parameters if more slices were added to cover the full brain anatomy. As a result, only seven slices (about 40% of the whole brain coverage) can be acquired in a total scanning time of under six minutes using the parameters in the QUASAR Reproducibility study [86]. Thus, a higher signal is needed to achieve a broader brain coverage.

The newly proposed Turbo QUASAR ASL overcomes the loss of signal due to the rapid decay of the signal by labeling the inflowing blood continuously to create a longer bolus duration. A preliminary study demonstrated that Turbo QUASAR ASL achieved a high SNR (comparable with PCASL) and that CBF and ATT can be estimated using a deconvolution-based model free method [142]. The motivation of Turbo QUASAR ASL was to utilize the time during which images are being acquired to generate more labels. By switching between labeling and imaging, the tracer maintains its magnetization level for a longer period than conventional PASL techniques and thus increasing the overall SNR. Figure 5.1 shows the different labeling techniques in QUASAR and Turbo QUASAR ASL. In QUASAR ASL, the blue lines indicate the readout time point, and half of the readout is replaced by labeling (green lines in Figure 5.1) to create more boluses.

A longer bolus duration was achieved by applying the RF labeling pulses repetitively, each of which was implemented using the PULSAR labeling technique

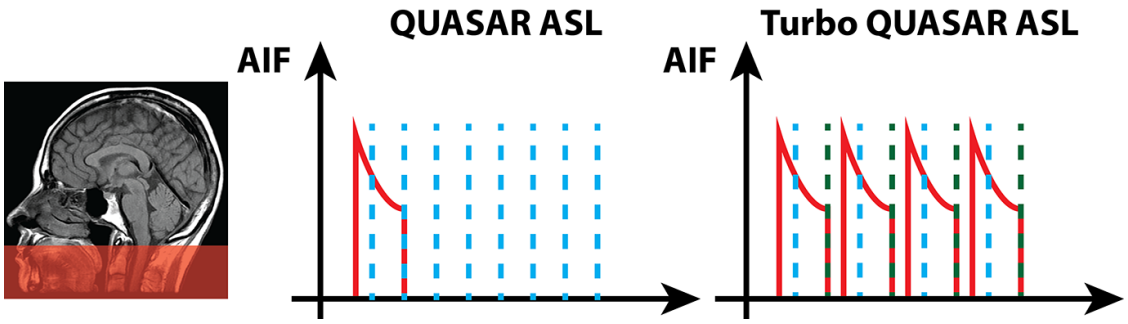

Figure 5.1: QUASAR and Turbo QUASAR ASL labeling and imaging scheme. In QUASAR ASL, only one bolus is created (shown by the AIF curve) and Look-locker readout is performed to acquire multi-PLD (blue dash lines) ASL data. In Turbo QUASAR ASL, labeling (green dash line) and acquisition (blue dash line) are interleaved and multiple boluses are created.

[62]. In essence, the total bolus duration of each Turbo QUASAR ASL experiment was the summation of each bolus duration. Due to the multiple labeling RF pulses and the interleaving of labeling and imaging, the QUIPPS II style bolus saturation pulse used in QUASAR ASL cannot be applied in Turbo QUASAR ASL, which might lead to uncertain bolus duration for each of the individual boluses. However, since each PULSAR labeling pulse is applied exactly between each successive acquisition, the duration of each bolus should be identical to the time between each readout.

Since the average velocity of the inflowing blood in the carotid and vertebral arteries are relatively stable, the amount of arterial blood passing through a fixed region should be relatively consistent. The goal is to invert sufficient spins by each labeling pulse and allow all the labeled spins to move out of the labeling region between each successive pulse. Therefore, the length of the labeling slab has to be designed long enough to fully invert all the inflowing spins but also short enough to ensure that the blood water is not labeled twice. Under such conditions, the bolus duration of Turbo QUASAR ASL can be determined by summing up each individual boluses, whose duration equals to the time between each successive labeling pulse. On the other hand, it may be a potential issue among subjects with blood disorders, such as SCD patients, where the rapid flow of the arterial blood may be too fast to be fully inverted, causing the effective bolus duration to be less than the expected value at normal blood flow velocity. In this case, the

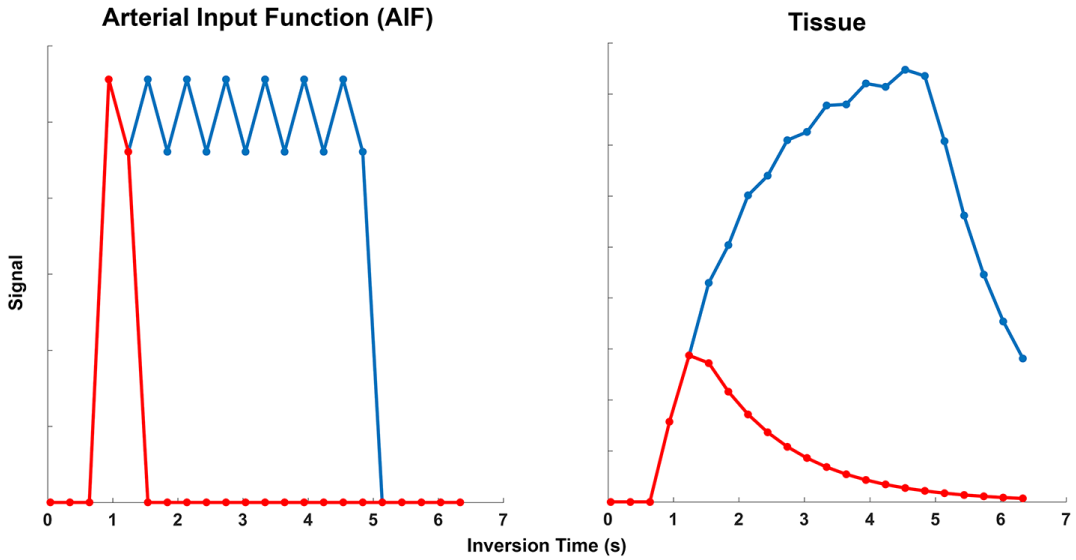

Figure 5.2: QUASAR and Turbo QUASAR ASL. In QUASAR ASL (red), only one bolus is created by the PULSAR labeling pulse. In Turbo QUASAR (blue), multiple boluses are created in a similar manner to QUASAR ASL, resulting in higher SNR as shown in the tissue curve.

velocity of arterial blood may be estimated from a separate phase contrast (PC) MRI to correct the bolus duration of Turbo QUASAR ASL.

The readout scheme of Turbo QUASAR ASL remained a Look-locker readout, but the time between each successive readout (ΔTI or ΔPLD) was chosen to be at 0.6s, longer than QUASAR ASL (0.3s). This not only ensured sufficient time to label each bolus but also avoided rapid signal reduction from the repeated Look-locker excitations. Together with the prolonged bolus duration from multiple labeling pulses, the signal of Turbo QUASAR ASL would be high enough to achieve nearly full brain coverage as demonstrated in the preliminary work [142]. Figure 5.3 shows the AIF and tissue curve of QUASAR and Turbo QUASAR ASL for the same length of the labeling slab. Since Turbo QUASAR ASL included multiple labeling pulses, the total effective bolus duration (and SNR) is much larger than QUASAR ASL.

A high temporal resolution of the ASL data is important for the estimation of the ATT. In this case, a slice shifting technique was developed to increase the effective temporal resolution of Turbo QUASAR ASL to be the same with QUASAR ASL as illustrated in Figure 5.3. In the first repeat, the slices were acquired from the inferior to the superior regions of the brain as in most acquisitions in ASL. In

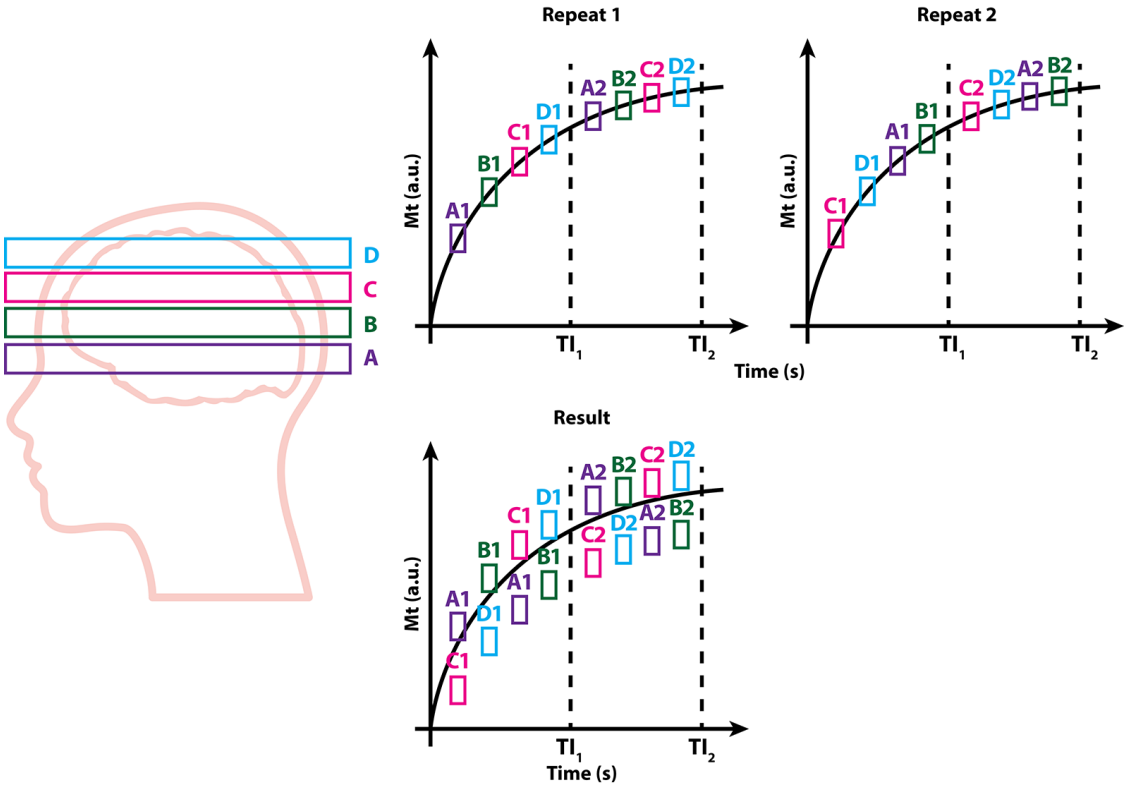

Figure 5.3: Slice shifting strategy in Turbo QUASAR ASL. In Repeat 1, slices were acquired from bottom to top (A to D) in each TI whereas in Repeat 2 slices were acquired from middle to the top then from bottom to the middle (C to D then A to B). This effectively increases the number of slices acquired in each TI – the temporal resolution doubled.

the second repeat, the slices were acquired from the center to the superior regions then from the inferior regions to the center of the brain. Instead of taking the mean across all repeats as in conventional ASL, the signal from each repeat was rearranged such that each TI would contain a particular slice whose signal was acquired at a slightly different time. For example in Figure 5.3, signals from slice A at TI_1 were acquired at a slightly different timing in Repeat 1 and 2 due to the time delay of acquiring signals from each slice. When the data of slice A from the two repeats were rearranged in the Result plot, they appear to be sampled twice in one TI (the two slice A1 in TI_1 of the Result plot). Thus, by interleaving the slices obtained from the two repeats, each TI would contain two acquisitions of the same slice and therefore increase the effective temporal resolution.

The RF pulse applied to label inflowing spins induces MT effects on the slices

that are not near the isocenter. In conventional PASL, such as EPISTAR, the control experiment was done by labeling a region above the imaging area (for single-PLD readout) or inverting the inflowing spins twice (for multi-PLD readout) to cancel the MT effects of a label control subtraction [66]. In QUASAR ASL, a pre-saturation pulse was applied to the imaging region before each readout to remove the MT effects caused by the different label and control RF pulses. Specifically, an adiabatic labeling pulse was applied to invert the inflowing spins. Figure 5.4 shows the different shape of the labeling pulses used in the label and control experiments of QUASAR ASL. The frequency of the pulse sweeps from -700Hz to 700 Hz [62]. Thus the average frequency is zero. The adiabatic pulse induces MT effects on the imaging slice. In the control experiment, the RF pulse of the same frequency inverts the spins and then quickly invert them back again, causing no inversions (equivalent to the yellow block in Figure 2 in reference [73]. However, the averaged frequency is -350Hz and causes different MT effects from the labeling pulse. Since the average frequency of the label and control experiments are different, the induced MT effects are different. In QUASAR ASL, the MT effects were then removed by the pre-saturation pulse in the imaging region before each image acquisition (dark blue block in Figure 2 of reference [73]).

In Turbo QUASAR ASL, due to the continuous labeling of the inflowing blood water, it is not possible to apply the post-saturation pulse in the tissue region to remove the MT effects after each RF pulse in both label and control experiments. As shown in Figure 5.5, two types of adiabatic pulses were used in the control experiment to suppress the MT effects. In the first control experiment, the adiabatic pulse is similar to the original QUASAR ASL experiment, where the frequency goes from -700Hz to zero and then quickly to -700Hz. In the second control experiment, the pulse goes from 700 Hz to zero and then to 700Hz.

Turbo QUASAR ASL adopted a similar implementation of bipolar crushing gradients as in QUASAR ASL to remove the signal from the arterial blood component, but different label/control pulses were used in the different dynamics of data in Turbo QUASAR ASL. Specifically, as shown in Figure 5.6, the odd number

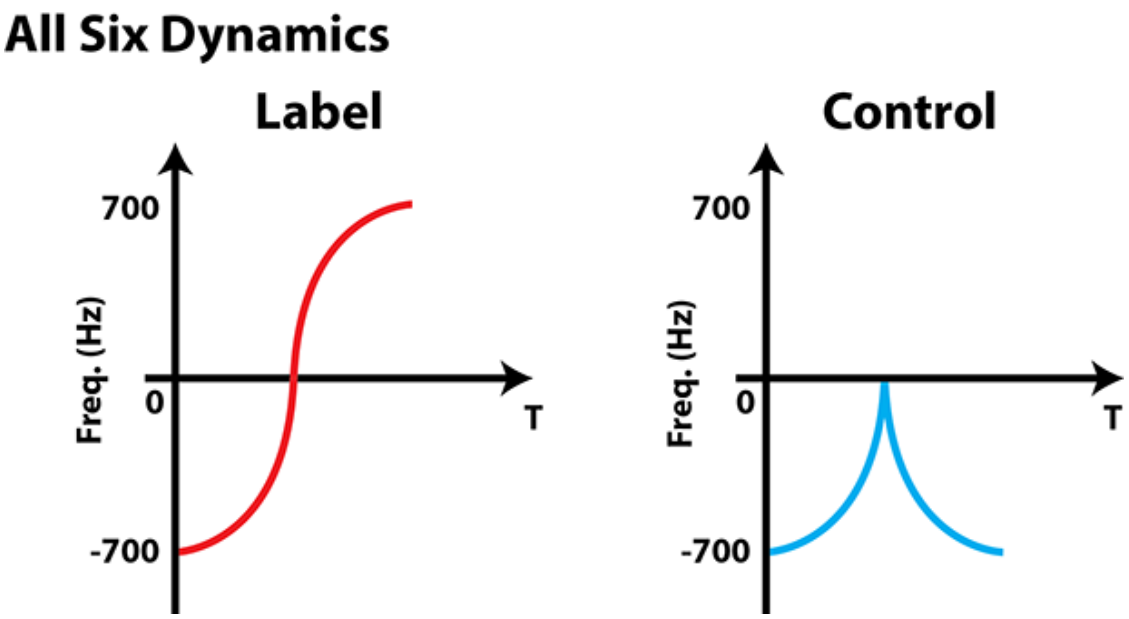

Figure 5.4: Label and control RF pulses in QUASAR ASL. The amount of labeling can be regarded as the area under the curve (or standard integral). In the label experiment, the total area under the curve is zero and the mean frequency is zero. In the control experiment, the total area under the curve is negative and the mean frequency is -350 Hz. The excess frequency causes MT effects in the tissue region which is then suppressed by a post-saturation pulse after the RF pulse and before readout.

dynamics used the first type of label/control pulses and even number dynamics used the second type of label/control pulses. Bipolar crushing gradients were applied in dynamic 1, 2, 4, and 5, and signals from these dynamics were considered to be from the tissue component only. A low flip angle Look-locker acquisition was used in dynamic 7 for estimating the correction factor g for the effective FA [101]. The pulse sequence of each component was implemented in the same way as in the QUASAR ASL Reproducibility study except for the control component [86].

5.2.2 Tissue Kinetic Model

The original general kinetic model proposed by Buxton et al [87] describes the kinetics of one labeled tracer in the tissue ΔM_T and the arterial blood ΔM_A region in the following equation:

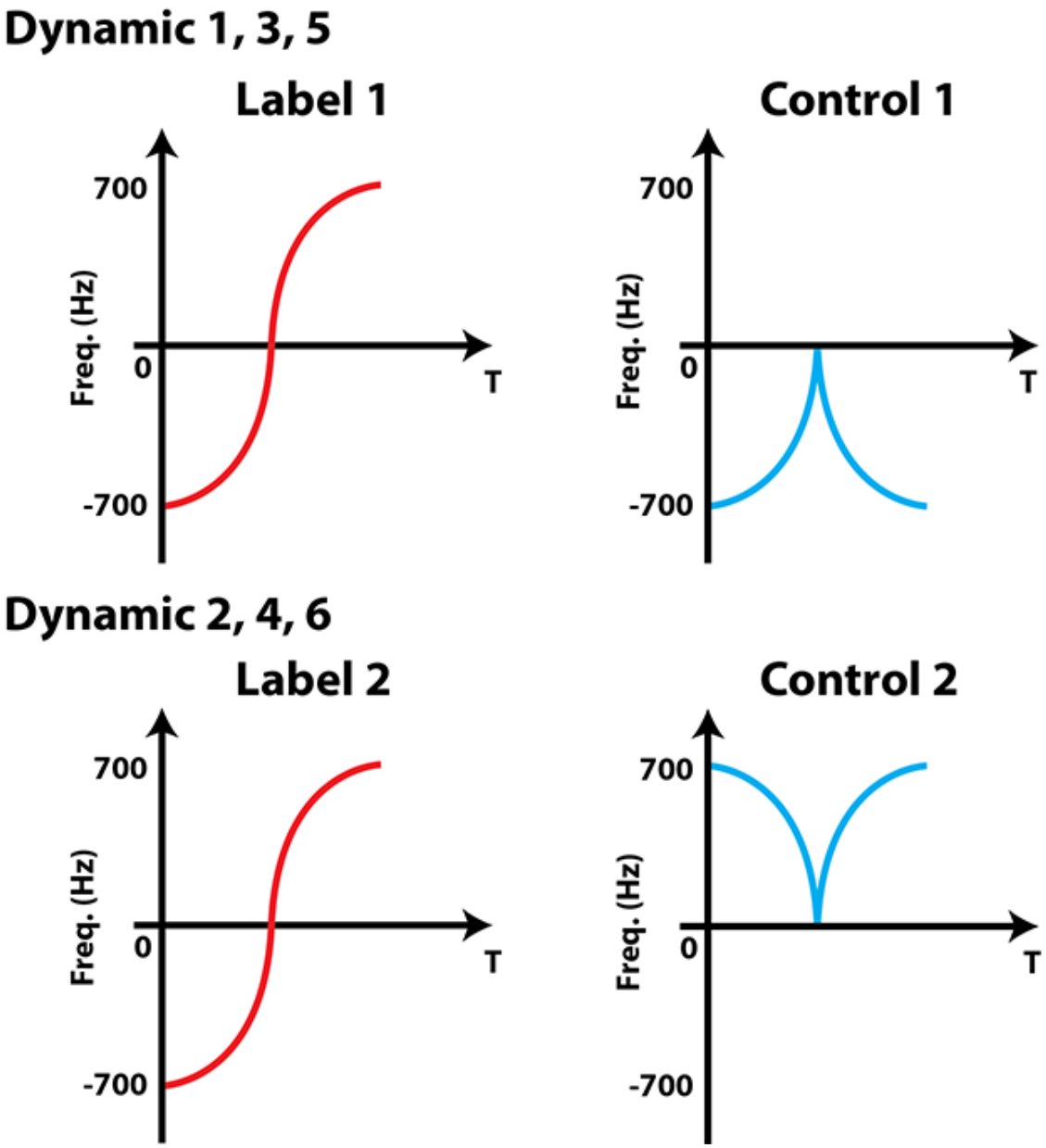

Figure 5.5: Label and control RF pulses in Turbo QUASAR. Due to the continuous application of RF pulses to create multiple boluses, a post-saturation pulse cannot be used to minimize MT effects as in QUASAR ASL. Instead, two sets of label/control pairs are implemented in odd and even number dynamics respectively. In dynamic 1, 3, and 5, the label/control pair is the same with QUASAR ASL, and the average frequency of Control 1 is -350 Hz, causing MT effects. In dynamic 2, 4, and 6, the RF pulse in the control experiment is inverted, which results in an average frequency of +350 Hz. Combining the two sets of label/control pairs, the net MT effects can be canceled.

Figure 5.6: Components of a single repeat of Turbo QUASAR ASL. The implementation follows the same manner as in QUASAR ASL [73] except for the two different control experiments (Label 1 and 2 are the same). Multiple label and control pairs are used in each dynamic to create multiple boluses. Crushing gradients are applied in dynamic 1, 2, 4, and 5. Dynamic 7 (discarded in CBF quantification) uses a low flip angle in the Look-locker readout to facilitate calibration.

$$\begin{aligned} \Delta M_T(t) &= 2 \cdot \alpha \cdot M_{0a} \cdot f \cdot \Big\{ c(t) \otimes [r(t) \cdot m(t)] \Big\} \\ \Delta M_A(t) &= 2 \cdot \alpha \cdot M_{0a} \cdot ABV \cdot c(t) \\ r(t) &= e^{-ft/\lambda} \\ m(t) &= e^{-t/T_{1t}} \end{aligned} \tag{5.1}$$

where t is the time since the start of the RF pulse, M_{0a} is the equilibrium magnetization of the arterial blood, α is the inversion efficiency, f is the perfusion, ABV is the arterial blood volume, $c(t)$ is the AIF, $r(t)$ is the residue function, $m(t)$ is the magnetization decay function, $\otimes$ denotes the convolution operation.

In Turbo QUASAR ASL, multiple boluses are created such that the AIF $c(t)$ becomes the summation of signals generated by each labeled bolus in the following equation:

$$c(t) = \begin{cases} 0 & 0 < t < \Delta t \\ \sum_{i=0}^{n-1} e^{-\frac{i \cdot \Delta TI}{T_{1a}}} & \Delta t \leq t < \Delta t + \tau \\ 0 & \Delta t + \tau \leq t \end{cases} \tag{5.2}$$

Where i is ith bolus that has arrived, n is the total number of boluses, Δt is the arrival time, T_{1a} is the T_1 relaxation time of the arterial blood, T_{1t} is the T_1 relaxation time of tissue, λ is the blood-water partition coefficient, ΔTI is the time between each successive image acquisition, Δt is the ATT, τ is the bolus duration of each RF pulse. The residue function $r(t)$ and magnetization decay function $m(t)$ remained the same in Turbo QUASAR ASL. The magnetization of the spins in the static tissue is modeled by saturation recovery using the following equation:

$$\begin{aligned} M(t) &= M_{0t} \cdot sin(FA) \cdot (1 - A \cdot e^{-t/T_{1t}}) \\ M_{0t} &= M_{0a} \cdot \lambda \end{aligned} \tag{5.3}$$

where $M(t)$ is the signal recorded at each TI, M_{0t} is the equilibrium of tissue, A is the saturation efficiency as pre-saturation is used in Turbo QUASAR ASL, FA is the effective flip angle. Since Turbo QUASAR employs Look-locker readout, the T_1 relaxation is disturbed by the low flip-angle excitation pulses, causing an effective T_1 to be shorter than the real T_1 of tissue [51]. The same correction

method proposed by Chappell et al was used in Turbo QUASAR ASL to account for the shorter T_1 relaxation [101]. Specifically, the effective (observed) T_1 relaxation of tissue can be derived in the following way:

$$\begin{aligned} \frac{1}{T'_{1t}} &= \frac{1}{T_{1t}} - \frac{ln(cos(FA))}{\Delta TI} \\ FA &= (g + \Delta g) \cdot FA_{norm} \end{aligned} \tag{5.4}$$

where T'_{1t} is the effective T_1 relaxation of tissue, FA is the effective flip angle to be estimated, g is the flip angle correction factor and assumed identical in each readout, Δg is set to be 0.023 [143], FA_{norm} is the flip angle set in the MRI sequence. FA and g can be estimated using the data from normal flip angle (first six dynamics in Figure 5.6) and the data from the low flip angle (dynamic seven). The same phenomenon occurs to the T_1 relaxation of arterial blood, and the same correction technique is applied in the following:

$$\frac{1}{T'_{1a}} = \begin{cases} \frac{1}{T_{1a}} & 0 < t < \Delta t_a \\ \frac{1}{T_{1a}} - \frac{ln(cos(FA))}{\Delta TI} & \Delta t_a \leq t \end{cases} \tag{5.5}$$

where T'_{1a} is the effective T_1 relaxation of arterial blood and Δt_a is the transit time to macrovasculature.

5.3 Methods

5.3.1 Simulations

Simulated experiments were conducted to investigate the accuracy of the model based method for Turbo QUASAR ASL under various blood flow conditions. Simulated ASL difference data were created using the kinetic model of Turbo QUASAR ASL in Equation 5.1 and the parameters listed in Table 5.1. For all simulated data, a true signal value was assumed to be the highest signal intensity of the kinetic curve generated by these parameters with one bolus. Noise was added to the simulated data using white noise according to $\mathbb{N}(0, SD)$ where SD = (true signal) / SNR with 1000 realizations. In all experiments, the number of TIs and shifts were chosen to be eleven and two respectively under the assumption that data were collected under

Table 5.1: Parameter Values in Simulations

Parameter		Value
Both Experiments		
CBF	(ml/100g/min)	60
ATT	(ms)	700
PLDs	(ms)	40, 640, ... , 6040
Slice shifting factor		2
FA	(degrees)	90
Tissue T_1	(ms)	1300
Arterial blood T_1	(ms)	1650
Experiment 1		
Number of boluses		1, 2, ... , 7
Effective bolus duration	(ms)	600
SNR		10, INF
Experiment 2		
Number of boluses		7
Effective bolus duration	(ms)	300, 400, 500, 600
SNR		5, 10, 50, 100, INF

five minutes total scanning time. Model based quantification method was used in all simulated experiments. In Experiment 1, the bolus duration was provided and not estimated. In Experiment 2, the bolus duration was estimated. The mean and the standard deviation of the estimated parameters was recorded.

Experiment 1

The aim of this experiment was to compare the accuracy of CBF estimation between model based and model free methods of Turbo QUASAR ASL under different SNRs. The level of SNR was manipulated by (1) varying the number of boluses labeled from one to seven in order to affect the total effective bolus duration and (2) varying the amount of noise by changing the SD. Since the model based technique was shown to be more accurate than the model free technique in QUASAR ASL (only one bolus), the results from this experiment would provide the accuracy of the two methods in well-controlled simulations. CBF was estimated using the model based and model free approaches. In the model based technique, the bolus duration was set to be 0.6s and not estimated.

Experiment 2

The aim of this experiment was to investigate the accuracy of the model based method at various blood flow conditions. As discussed, the effective bolus duration of each bolus in Turbo QUASAR ASL is equal to the time period between each successive RF pulse under normal flow velocity. In conditions where flow becomes more rapid, however, the effective bolus duration would decrease, causing the bolus duration to be uncertain. In this experiment, the simulated bolus duration was set to 0.60 and 0.50 to model the rapid flow and the SNR was chosen to be 5, 10, 50, 100, and infinity. A two-step procedure was implemented for the model based methods to estimate CBF, ATT, and bolus duration: (1) estimate CBF and ATT and setting the bolus duration to be 0.6s; (2) use the results from the first step as initial values to estimate CBF, ATT, and bolus duration and using a prior value of 0.6 for the bolus duration parameter. Results from this experiment would provide the potential errors of the model based method in rapid flow conditions.

5.3.2 Healthy Cohort Data

Eleven healthy volunteers (age: 39±17, hematocrit: 0.40±0.03L/L, genotype: HbAA/HbAS, hemoglobin: 13.6±1.3mmol/L, five female) and ten patients with SCD (age: 37±19, hematocrit: 0.26±0.07L/L, genotype: HbSS/HbSβ^0, hemoglobin: 8.4±2.3mmol/L, four female) were recruited.[1] Each subject underwent one MRI session and acetazolamide administration. All images were acquired at 3.0 Tesla, on a clinical MR system (Philips Ingenia; Philips Healthcare, Best, The Netherlands), and a 32-channel receive head-coil with body-coil transmission was used.

Figure 5.7 shows the process of ASL MRI data collection. Six MR images were collected from each subject at baseline and acetazolamide conditions in the following order: 3D T2-FLAIR, 2D Phase Contrast (PC) MRI (baseline), Turbo QUASAR ASL (baseline), PCASL, Calibration M_0, Turbo QUASAR ASL (acetazolamide), 2D PC MR (acetazolamide). Acetazolamide was administered during the PCASL scan.

[1]Data were collected by Lena Václavů at Academisch Medisch Centrum, Amsterdam, The Netherlands

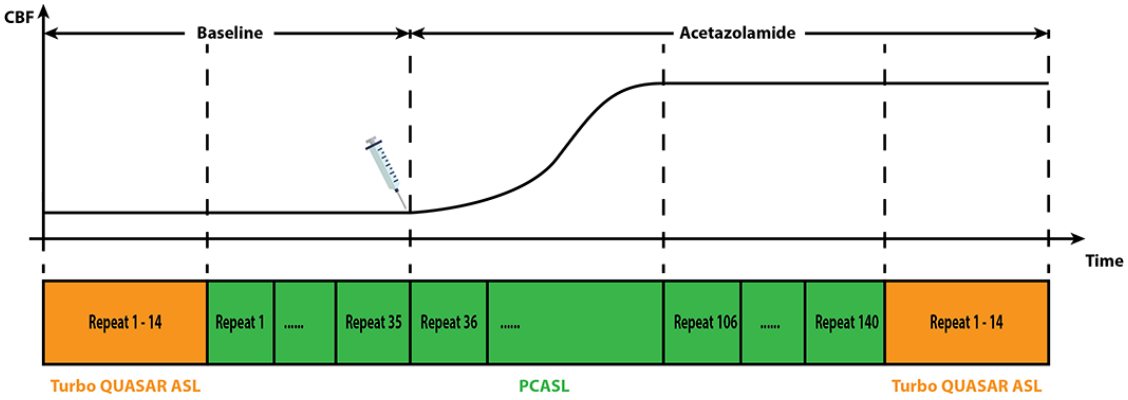

Figure 5.7: Experimental design. A baseline Turbo QUASAR ASL was performed followed by PCASL. At repeat 35 of PCASL, acetazolamide was administered. After repeat 140 of PCASL, a second Turbo QUASAR ASL was performed to measure the CBF after the introduction of acetazolamide.

PCASL and Turbo QUASAR ASL imaging volumes were planned identically such that the middle slice of each volume corresponded to the same slice in both scans.

The PCASL scan of healthy control subject 2 disease subject 1 and 4 were cut short. There were 26 repeats at baseline and 35 repeats post acetazolamide administration for control subject 2; 35 repeats at baseline and 96 repeats post acetazolamide administration for disease subject 1; 35 repeats at baseline and 35 repeats post acetazolamide administration for disease subject 4.

PCASL

Labeling duration = 1800ms, PLD = 1800ms, 2D single shot Gradient Echo EPI readout, 19 slices, slice acquisition time = 42.1ms, voxel size = 3×3×7mm, TR/TE = 4400/14ms, scan duration = 1240s, FOV = 240×240, matrix = 80×80, SENSE = 2.5 in AP direction, no slice gap, two background suppression pulses at 1830ms and 3155ms, SPIR fat suppression, at 130Hz. Each PCASL scan contained 140 dynamics (repeats). The first 35 dynamics were a baseline scan. At dynamic 35, acetazolamide was administered. The last 35 dynamics (from dynamic 106) were used as post-acetazolamide scans, assuming the effect of acetazolamide has reached a plateau.

Calibration M_0 Data

For each subject, a proton density (PD) weighted image with TR = 4400ms, six repeats, and scan duration of 26.4s without background suppression (other parameters the same with PCASL sequence) were acquired to calibrate estimated perfusion into absolute units.

Turbo QUASAR ASL

Multi-phase ASL, FFE single shot EPI (EPI factor 25) Look-locker read out, TE/TR = 16/6000ms, TIs = 40 – 6340ms, ΔTI = 600 ms, 11 TIs, 7 boluses, matrix = 64×64, FOV = 240×240, flip-angle = 35°, voxel-size 3.75×3.75mm, slice thickness = 7mm, 15 slices, slice acquisition time = 36ms, T2 Prep WET1 (ASL scheme NullPulse5) Pulse type HS, no fat suppression, label slab 150mm, vascular crushing all (local) VENC = 4 cm/s, SENSE 2.5 AP, Look-locker readout, 14 dynamics (two repeats of seven dynamics including four crushed, two non-crushed, and a low flip angle), the direction of the crushing gradients were the same as in QUASAR ASL [86], cycle duration 6800 ms, scan duration 204s. Turbo QUASAR scans were performed before and after acetazolamide as shown in Figure 5.7.

3D T2-FLAIR

FOV = 250×250×180, voxel size 0.98×0.98×1.12mm, TR/TE = 4800/356ms, TSE multi-shot 3D flair IR, T2 prep TE 125ms, 4 refocusing pulses, SPAIR fat suppression, IR delay 1650 ms, sagittal plan, scan duration 307s. Due to operational errors, the scan of patient 1, 3, and 4 was done using coronal plan with the same parameters.

2D PC MRI

TR/TE = 15/5.5ms, scan duration = 61.5s, voxel-size = 0.45×0.45×4mm, matrix = 512×512, 1 slice, FOV = 230×4×230mm, VENC = 80cm/s, flip angle = 15°, NSA = 2, no cardiac synchronization. The imaging slice was planned 90mm below the centre of the PCASL and Turbo QUASAR ASL imaging volumes and placed perpendicular to the vessels in the neck at cervical level C1.

Table 5.2: Experimental parameter values for PCASL

Parameter		Value	Spatial Prior
CBF	(ml/100g/min)	(0, 10^{-12})*	M
ATT (without Correction)	(ms)	(0.7, 10^{-1})	
ATT (with Correction)	(ms)	(T, 10^{-1})	
Bolus duration	(ms)	1800	
Tissue T_1	(ms)	1300	
Arterial blood T_1	(ms)	1650	
Blood-water partition coefficient		0.98	
Inversion efficiency		0.85	

*Values indicate mean and standard deviation of prior; T: Values taken from Turbo QUASAR ASL; M: Markov random field spatial prior.

5.3.3 PCASL Perfusion Quantification

For the PCASL data, CBF was estimated using two techniques differed by the priors of ATT: (1) by fitting the ASL difference data to a tissue kinetic curve using the Spatially Regularized Variational Bayesian Inference technique in the FSL tool BASIL [108][113] and a global ATT prior of 0.7s; (2) incorporating the estimated ATT from Turbo QUASAR ASL data as priors to conduct model fitting. The parameters and the priors used in the model fitting process can be found in Table 5.2.

5.3.4 Turbo QUASAR ASL Perfusion Quantification

For Turbo QUASAR ASL, data from the two repeats were re-arranged in each TI of each dynamic to double the temporal resolution using the slice shifting technique described in the Theory section. Dynamic 1, 2, 4, and 5 were used as the tissue component to estimate CBF in both model based and model free methods. Dynamic 3 and 6 were used to estimate the AIF to be used in the model free CBF quantification method. All dynamics (including dynamic 7 of low flip angle) were used to estimate the equilibrium magnetization of the arterial blood for calibration and FA for T_1 value correction.

Model Based Analysis

We used the analytical solution of the tissue kinetic model for PASL proposed by Hrabe et al [88] to implement the convolution operation in Equation 5.1. Incorporating the multiple boluses in Turbo QUASAR ASL and assuming a boxcar input function, the difference of the longitudinal magnetization between label and control experiments of ASL can be represented in the following formulation:

$$\Delta M(t) = \begin{cases} 0 & 0 < t < \Delta t \\ \frac{F}{R} \cdot \sum_{i=0}^{n-1} (e^{R \cdot (t - i \cdot \Delta t)} - e^{R \cdot \Delta t}) & \Delta t \leq t < \Delta t + \tau \\ \frac{F}{R} \cdot \sum_{i=0}^{n-1} (e^{R \cdot (\Delta t + \tau)} - e^{R \cdot \Delta t}) & \Delta t + \tau \leq t \end{cases} \tag{5.6}$$

where $R = \frac{1}{T_{1t}} - \frac{1}{T_{1a}}$, $F = 2 \cdot \alpha \cdot M_{0a} \cdot f \cdot \sum_{i=0}^{n-1} e^{\frac{-(t - i \cdot \Delta TI)}{T_{1t}}}$, f is the CBF, τ is the bolus duration of each label pulse, Δt is the arterial transit time, M_{0a} is the equilibrium magnetization of arterial blood, T_{1a} is the T_1 relaxation of arterial blood, T_{1t} is the T_1 relaxation of tissue, n is the total number of boluses, t is the time since the RF pulse, ΔTI is the time between each Look-locker acquisition, α is the inversion efficiency.

CBF and ATT were estimated by fitting tissue kinetic model to the data of the tissue component in Turbo QUASAR ASL using the Spatially Variational Bayesian Inference technique using Equation 5.1 [108][113]. Since labeling and acquisition were done in an interleaved manner in Turbo QUASAR ASL, the duration of each bolus should be identical to the time between each successive acquisition, and in this case 0.6s. Under normal circumstances, the labeling slab length of 150mm was chosen to be long enough to fully invert the inflowing blood but also short enough to ensure that the inflowing arterial blood was not labeled twice by the two successive RF pulses. In estimating the effective bolus duration, we restricted the variation of the estimated values to be less than the time period between each PLD, in this case 0.6s. The priors and sequence parameters used in model fitting are shown in Table 5.3. CVR (represented in decimal numbers) was computed using relative CBF values by the following equation:

$$CVR = \frac{CBF_{Acetazolamide} - CBF_{Baseline}}{CBF_{Baseline}} \tag{5.7}$$

Table 5.3: Experimental parameter values for Turbo QUASAR ASL

Parameter		Value	Spatial Prior
Model based			
CBF	(ml/100g/min)	(0, 10^{-12})*	M
ATT to tissue	(ms)	(0.7, 10^{-1})	
Tissue T_1	(ms)	1300	
Model free			
ABV	(%)	(0, 10^{-12})	M
ATT to macrovasculature	(ms)	(0.5, 10^{-1})	
Both model based and model free			
Bolus duration of each RF pulse	(ms)	600	
Total number of boluses		7	
Arterial blood T_1	(ms)	1650	
Blood-water partition coefficient		0.98	
Inversion efficiency		0.91	

*Values indicate mean and standard deviation of prior; M: Markov random field spatial prior.

Model Free Analysis

CBF of Turbo QUASAR ASL was estimated by deconvolution using a circular-SVD technique applied to the simulated ASL difference signal and simulated AIF [93]. For each voxel, the maximum signal of the residue function was considered the relative CBF. The oscillatory index of the singular value decomposition was set to be 0.1. The model free analysis was only conducted in simulated Experiments 1, and the parameter values are listed in Table 5.3.

5.3.5 Absolute Perfusion Quantification

For PCASL calibration, since the TR of the M_0 image was shorter than 5s, the signal intensity was corrected by multiplying by a factor of the factor $\frac{1}{1-e^{\frac{-TR}{T_{1t}}}}$, where the T_{1t} value was chosen to be 1.3s for the whole brain. For Turbo QUASAR ASL calibration, the M_0 image was transformed to the resolution of Turbo QUASAR ASL data. Specifically, two transformation matrices from PCASL and Turbo QUASAR ASL resolution to high-resolution space was computed by registering the CBF map to the T2-FLAIR structural image of each subject using the FSL

tool FLIRT [134]. The transformation of Turbo QUASAR ASL was inverted and multiplied with the PCASL matrix using the FSL tool *convert_xfm* to obtain a transformation matrix from PCASL to Turbo QUASAR ASL space. The M_{0a} of PCASL was then transformed to Turbo QUASAR ASL space using this matrix for the absolute CBF quantification. For both PCASL and Turbo QUASAR ASL, the calibration image was corrected using the erosion and extrapolation (kernel size = 5) technique described in Chapter 3. Finally, the estimated CBF images were calibrated voxelwise by the corrected M_{0a} and an assumed inversion efficiency of 0.85 for PCASL [17] and 0.91 for Turbo QUASAR ASL [86].

5.3.6 Blood Flow Velocity Quantification

Phase difference images were corrected for background phase offsets on the scanner console and imported to GTFlow software (Gyrotools, Zurich, Switzerland) for post-processing.[2] Phase unwrapping was performed in cases where velocity values superseded the VENC of 80cm/s, by adding 2x the VENC value to affected voxels. Additional processing steps included manual segmentation of the internal carotid arteries and vertebral arteries on the magnitude images to obtain cross-sectional area, and average flow calculation by taking the product of the cross-sectional area and velocity in each voxel in the phase difference images. The average flow per vessel was quantified in mL/s. The average flow was used to estimate inversion efficiency in the location of the labeling plane, as shown in Figure 5.8.

5.3.7 Statistical Analysis

A Two-tailed Wilcoxon Signed-Rank test was performed in order to compare the mean global CBF (both PCASL and Turbo QUASAR ASL) and ATT (only Turbo QUASAR ASL) values before and after acetazolamide administration. This statistical test was chosen because no assumptions were made about the distribution of the variables and the sample size of this study was small (N=11). The null hypothesis was that CBF or ATT was the same before and after acetazolamide

[2]Blood flow velocity quantification was conducted by Lena Václavů at Academisch Medisch Centrum, Amsterdam, The Netherlands

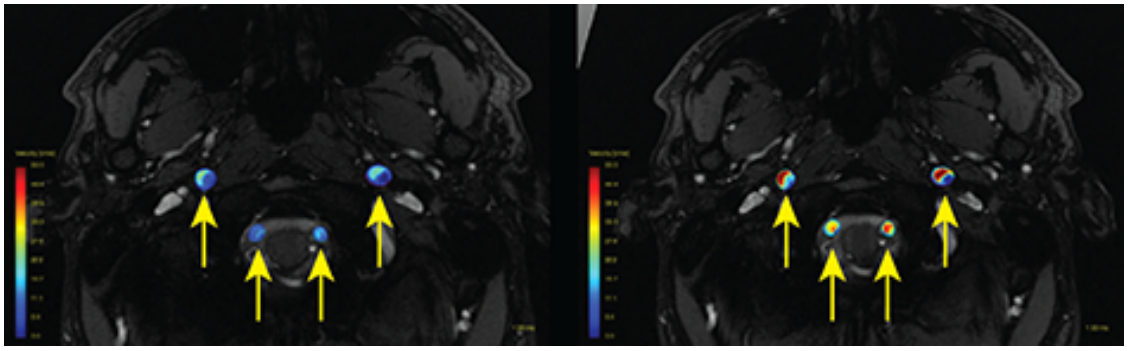

Figure 5.8: 2D PC MRI images in a participant before (left) and after (right) acetazolamide administration. Vessels are pointed by the yellow arrows. The increase in velocity can be appreciated in all vessels depicted in colour. Color bar indicates velocity [ranging from 0 to 50 cm/s].

administration. The alternative hypothesis was that the estimated CBF or ATT after acetazolamide was not equal to the value before. The same test was conducted to compare the mean global CBF between the two ASL techniques.

A two-tailed paired t-test was conducted to compare the voxelwise CBF and ATT before and after acetazolamide administration and between the estimated CBF using the two ASL techniques. All CBF and ATT maps were transformed to the standard MNI 152 space. A transformation matrix (Matrix 1) from ASL image to high-resolution space was computed by registering the CBF map to the T2-FLAIR structural image of each subject using the FSL tool FLIRT [134]. A second transformation matrix (Matrix 2) was obtained by registering the T2-FLAIR image to the standard brain (MNI152_T_1_2 mm) using the FSL tool FLIRT. The transformation matrix (Matrix 3) from ASL space to standard space was obtained by multiplying Matrix 1 by Matrix 2, and Matrix 3 was used to transform CBF and ATT from ASL space to standard space. A T_2-FLAIR image was acquired from each subject. Due to the lack of a standard FLAIR image, the standard T_1 weighted image in MNI 152 (2mm) was used in the group analysis. Since the contrast in the T_2-FLAIR image and the standard T_1 weighted image was different, the registration results using the conventional non-linear registration (FSL tool FNIRT) was less desirable than using linear registration (FSL tool FLIRT). Therefore, linear registration was used to transform the CBF images from the

ASL space to the standard space in this study. Since Turbo QUASAR ASL data had slightly smaller brain coverage than PCASL, a mask for group analysis was created using the coverage of Turbo QUASAR ASL. First, the brain mask of each Turbo QUASAR ASL data was transformed to standard space using Matrix 3. Then the least common space coverage was taken from all the subjects to create the mask for group analysis. Before each t-test, all images were smoothed using a Gaussian spatial filter of 5mm FWHM. Five t-tests were conducted using the FSL tool RANDOMISE with 5000 permutations [144] [145]: (1) PCASL CBF before and after acetazolamide, (2) Turbo QUASAR ASL CBF before and after acetazolamide, (3) Turbo QUASAR ASL ATT before and after acetazolamide, (4) baseline CBF between PCASL and Turbo QUASAR ASL, and (5) acetazolamide CBF between PCASL and Turbo QUASAR ASL. For all permutations, familywise error rate due to multiple testing was corrected using the method developed by Holmes et al [144][146]. Specifically, a reference distribution was constructed from the calculated statistics of each permutation, and the maximum of the statistics was recorded. The corrected p-value can be obtained by computing the portion of the maximum statistics greater than a particular observed value for each test. The corrected p-value was recorded and threshold at 0.05 for significance. For all the t-tests, effect size was computed by taking the voxelwise difference between the CBF or ATT measurement in standard space.

5.4 Results

5.4.1 Simulated Experiments

Figure 5.9 shows the estimated CBF using the model based and model free methods from simulated data with different number of boluses at SNR=INF and 10. Overall, the model based method showed a higher accuracy in both SNR conditions. The underestimation of CBF by the model free method became worse with a longer total bolus duration. With more boluses labeled, which increased the signal, the standard deviation of the estimated CBF of both methods reduced, and it plateaued

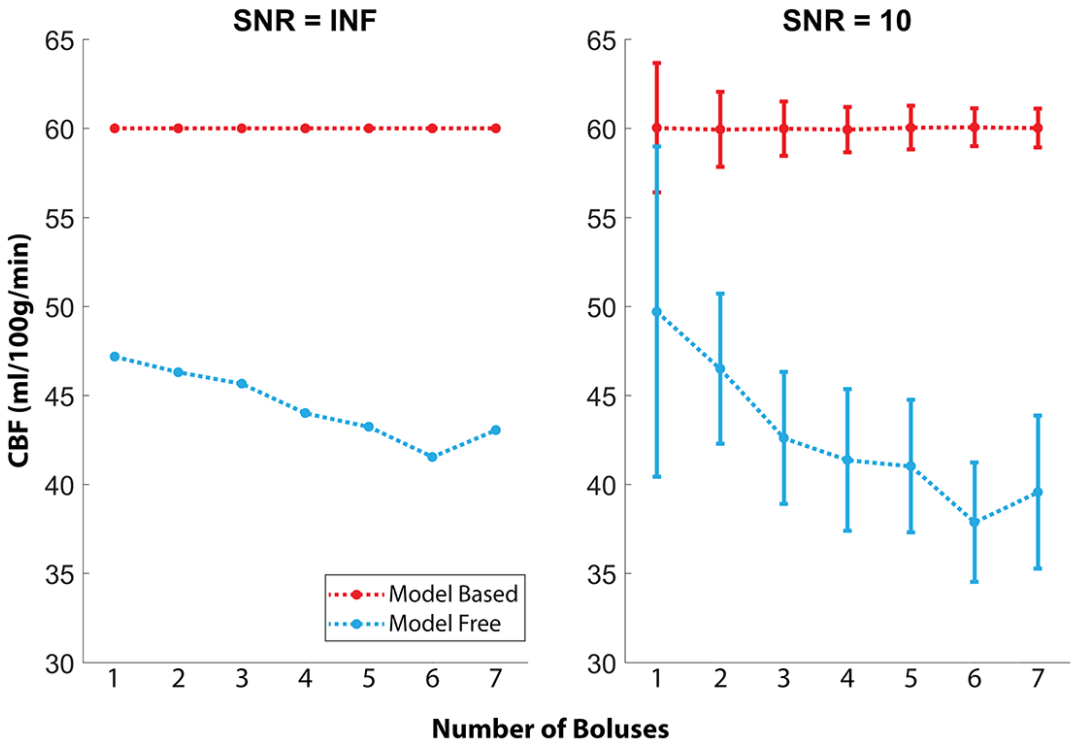

Figure 5.9: Estimated CBF values using model based and model free approach for different total bolus duration at SNR=INF and 10. The model based method was more accurate than the model free approach in all conditions (simulated CBF=60ml/100g/min). The accuracy of model free method decreased as the total bolus duration increased.

after four boluses. This implies that creating more than four boluses for a stronger signal had little effect on the precision of the two methods.

Figure 5.10 shows the estimated CBF, ATT, and bolus duration from simulated data with different bolus duration. When the simulated bolus duration was equal to the bolus duration set in the model-fitting procedure, the accuracy of the estimation improved with higher SNR. As explained, the first step of the process with a fixed bolus duration was sufficient to estimate the correct value (black lines in Step 1). If we attempted to estimate the effective bolus duration in the second step, overestimation of CBF and ATT would occur in low SNR cases (black lines in Step 2 at SNR = 5 and 10), and the effective bolus duration was underestimated (black lines in Step 2). If the simulated effective bolus duration was shorter than the bolus duration set in the model-fitting process or the prior value, all of the three parameters were underestimated in both steps (green, blue and red lines).

However, the estimation accuracy of the three parameters became marginally improved (by 5.5% for CBF estimation) in Step 2 than Step 1. For the most extreme case where simulated bolus duration was 0.3s and SNR was 5, which corresponded to an average blood velocity of 50cm/s under a 15cm labeling slab, the estimation errors of CBF and ATT were around 45% and 18% for Step 1 and 40% and 15% respectively for Step 2.

5.4.2 Healthy Cohort Experiments

Figure 5.11 shows the estimated CBF using PCASL with and without ATT correction and Turbo QUASAR ASL, both before and after acetazolamide administration. Figure 5.12 shows the mean CBF of all subjects at baseline and after acetazolamide administration as well as non-parametric test results (asterisk * indicates significantly different, $p<0.05$). Comparing the results at baseline, the CBF value of PCASL with ATT correction was the lowest (mean CBF of the group at 43.1 ml/100g/min) while the CBF of PCASL without ATT correction and Turbo QUASAR ASL were 49.8 ml/100g/min and 43.6 ml/100g/min and significantly different. After acetazolamide administration, CBF of PCASL without ATT reached to 85.3 ml/100g/min and significantly different from the other two methods whereas the mean CBF of Turbo QUASAR ASL was the lowest (64.1 ml/100g/min). The CBF results of PCASL indicated that taking ATT into account significantly reduced the estimated CBF after the administration of acetazolamide. At baseline, however, no significantly change in CBF of PCASL was observed. This indicated that the recommended single-PLD PCASL was insensitive to variations in ATT in this population. Without considering the impact of ATT, CBF from PCASL data were significantly different from those of Turbo QUASAR ASL. The estimated CBF results of the three methods were all significantly different after acetazolamide administration (not shown), indicating all ASL techniques were sensitive to detect CBF changes in this population. However, the degree of increase detected by the three ASL methods was different. Without ATT correction on PCASL, the CBF values resulted in

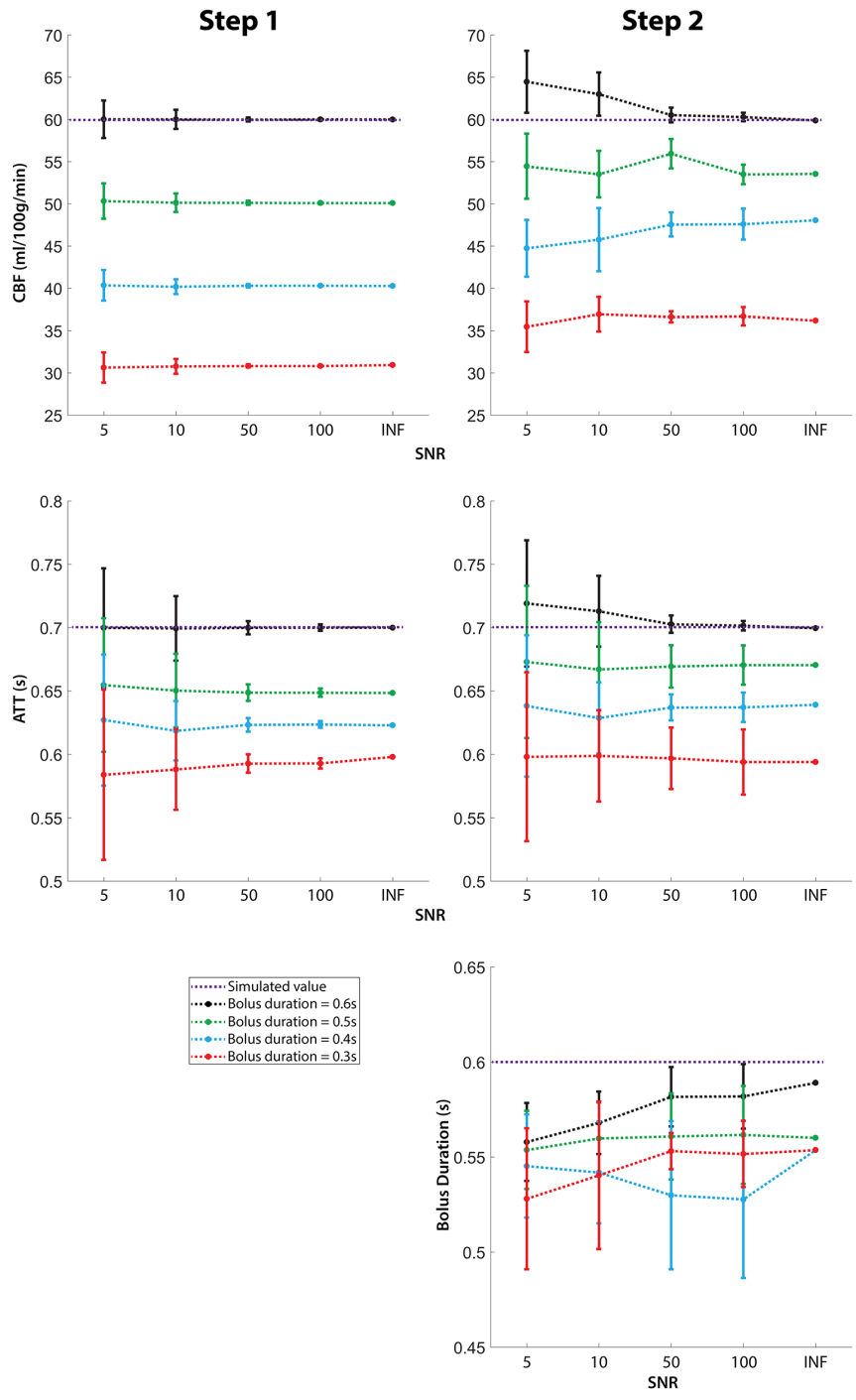

Figure 5.10: Estimated CBF, ATT, and effective bolus duration using the two-step model based approach at different SNRs of simulated data with different true bolus duration. In Step 1 where the bolus duration was assumed to be 0.6s for all cases, both CBF and ATT were underestimated when the bolus duration was shorter and the mean values were nearly the same at different SNR levels. In Step 2 where bolus duration was included in model-fitting, the errors of CBF and ATT estimation reduced from Step 1, but the bolus duration was underestimated.

the largest CBF increase of 68% whereas Turbo QUASAR ASL appeared to show the smallest CBF increase of only 47%.

Figure 5.13 shows the mean voxel-wise CVR of the three ASL methods. Figure 5.14 shows the mean CVR of the three methods from the group. In all three techniques, the CVR in the posterior region of the brain was the highest. After correcting the ATT for PCASL, the CVR of WM reduced and the contrast of CVR between GM and WM became more visible. Cross referencing Figure 5.12, the results in Figure 5.14 indicated that Turbo QUASAR ASL detected smaller CVR than the two PCASL based methods. For the PCASL based method, the correction for ATT increased the observed CVR to about 0.8 while keeping the range similar. CVR from the Turbo QUASAR ASL data were lower than PCASL and the within group variation was also greater.

Figure 5.15 shows the corrected p-value and the effect size of the paired t-test comparing the CBF before and after acetazolamide administration. For the two PCASL based methods, the results were nearly identical where most of the regions in the brain (except corpus callosum) experienced a significant CBF increase and the changes in GM CBF was more than 25 ml/100g/min. For the results of Turbo QUASAR ASL, the regions with a significant increase in CBF were smaller than PCASL, and the corresponding effect size (in the range between 10 and 40 ml/100g/min) was also lower than PCASL. Voxels at the posterior region of the brain demonstrated a higher CBF increase (brighter voxels in effect size maps) than the anterior region.

Figure 5.16 shows the regions of significantly different CBF between the three methods and the corresponding CBF difference at baseline. Figure 5.17 shows the regions of significantly different CBF between PCASL and Turbo QUASAR ASL and the corresponding CBF difference after acetazolamide administration. Overall in both baseline and acetazolamide conditions, CBF estimated by both PCASL based methods demonstrated higher levels than Turbo QUASAR ASL in the superior regions of the brain while the opposite effects in the inferior regions of the brain. Comparing between the two PCASL methods (first row), incorporating ATT

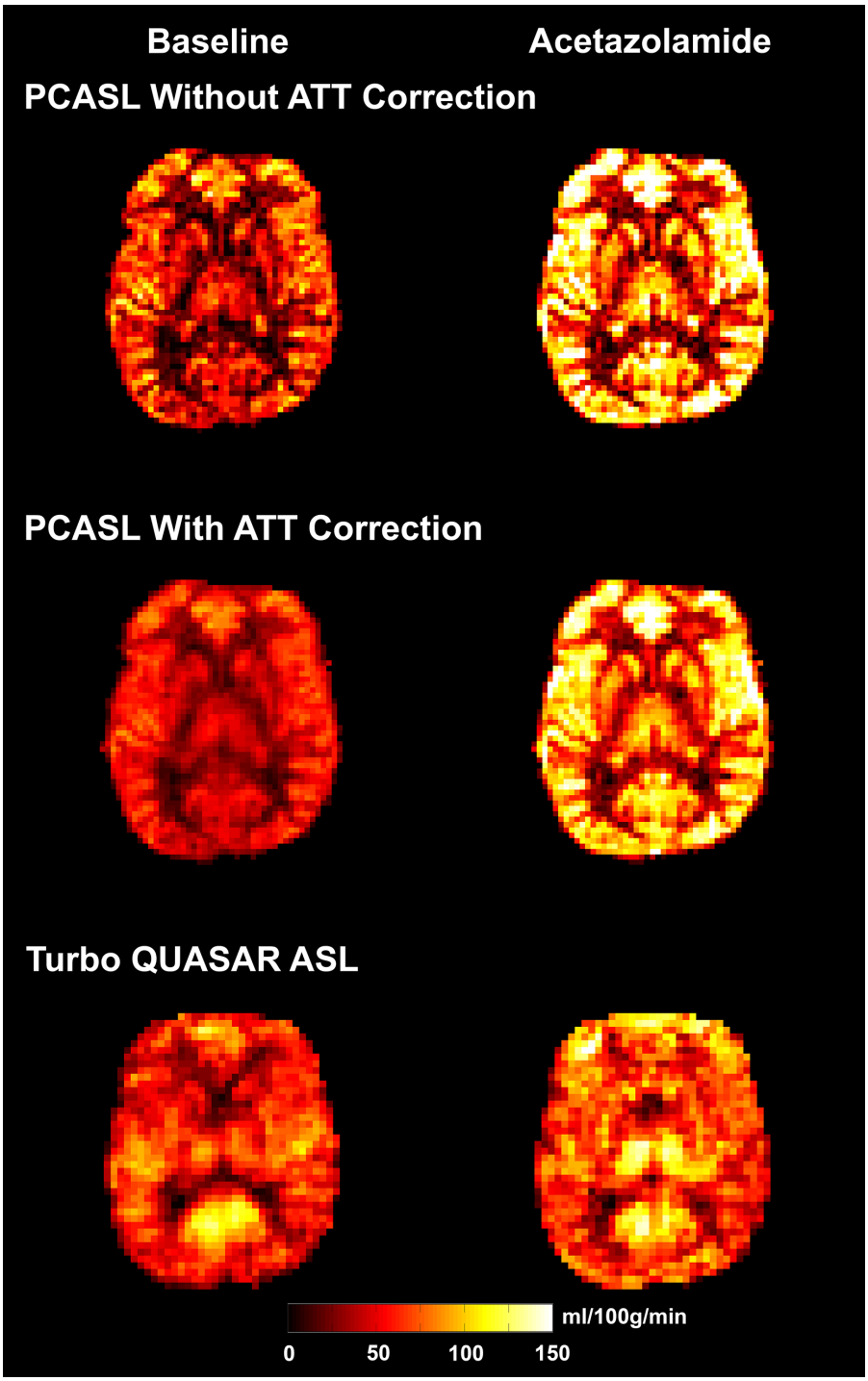

Figure 5.11: Estimated CBF of an example subject using PCASL without and with ATT correction and Turbo QUASAR ASL at both baseline and acetazolamide conditions. In all experiments, CBF increased after acetazolamide administration. At baseline, the estimated CBF using PCASL with ATT correction was the lowest. After acetazolamide administration, the estimated CBF using PCASL without ATT correction was the highest.

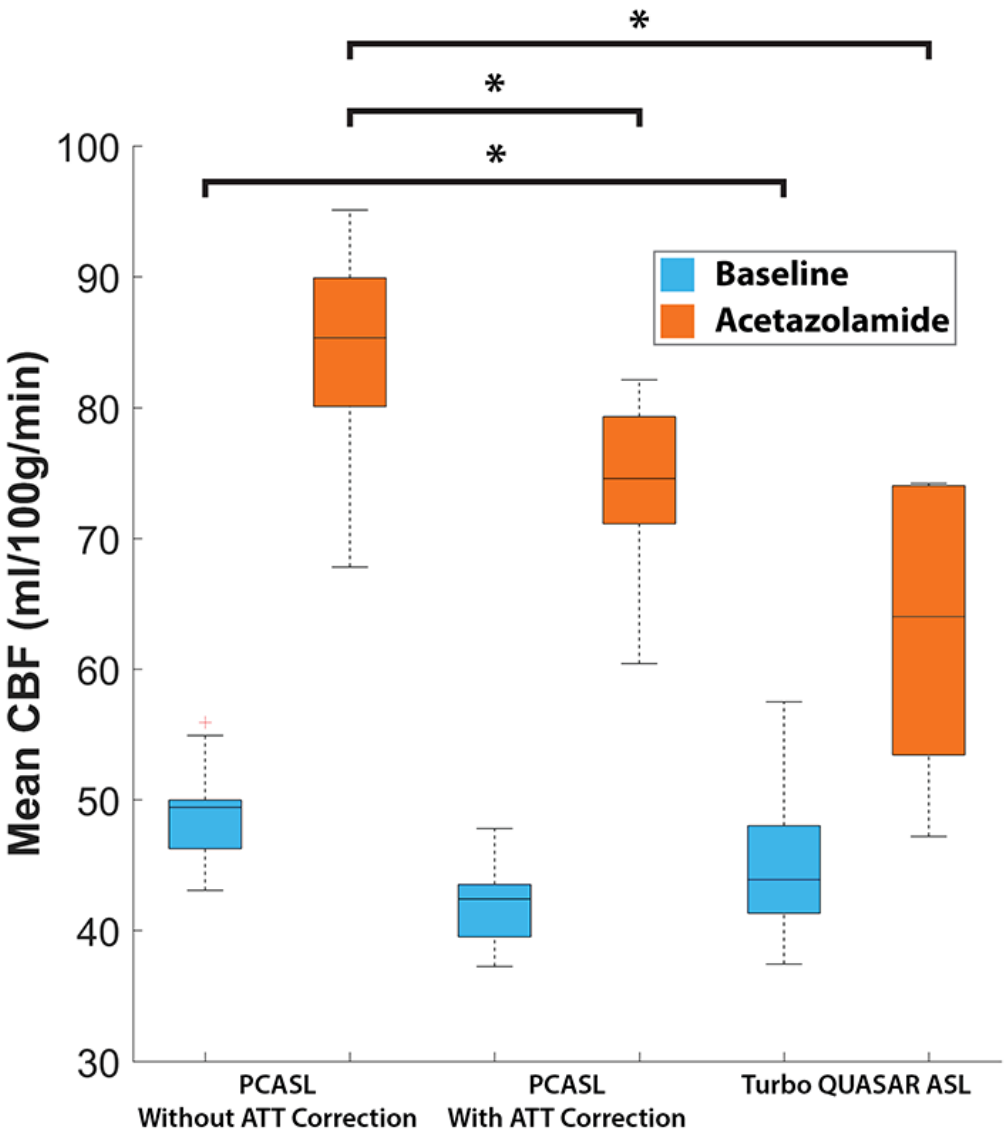

Figure 5.12: Mean CBF of all subjects before and after acetazolamide administration and non-parametric test results. Despite the global increase in CBF detected by each method, changes in the estimated CBF by Turbo QUASAR ASL were the smallest. The asterisk (*) indicates significantly different CBF ($p < 0.05$) after conducting the non-parametric test. In all three methods, CBF was significantly different after acetazolamide administration (not shown).

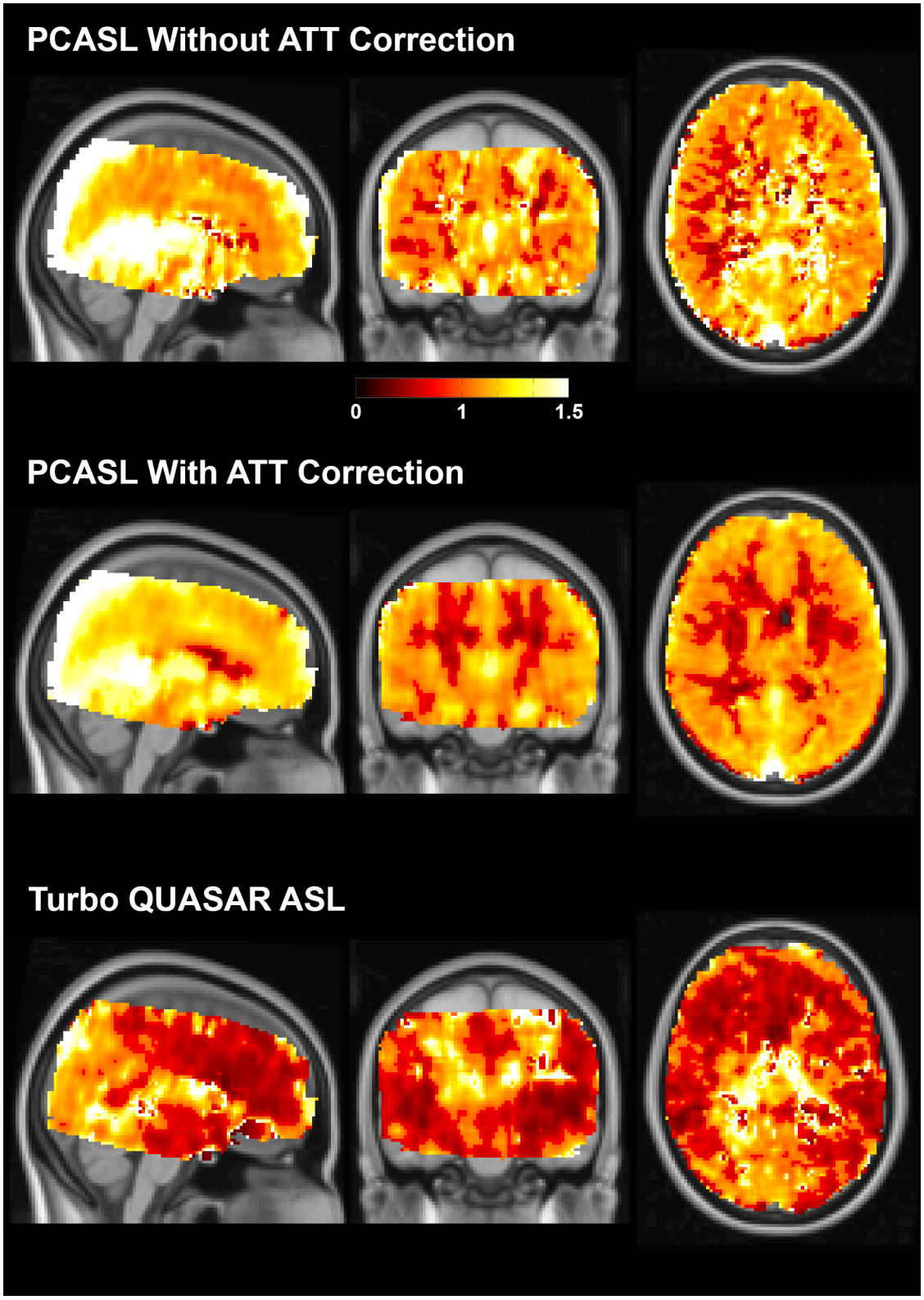

Figure 5.13: Estimated mean CVR of the three methods. In all methods, the GM CVR was larger than WM CVR, and the posterior region appeared to have the largest CVR. Results from Turbo QUASAR ASL method showed lower CVR values globally.

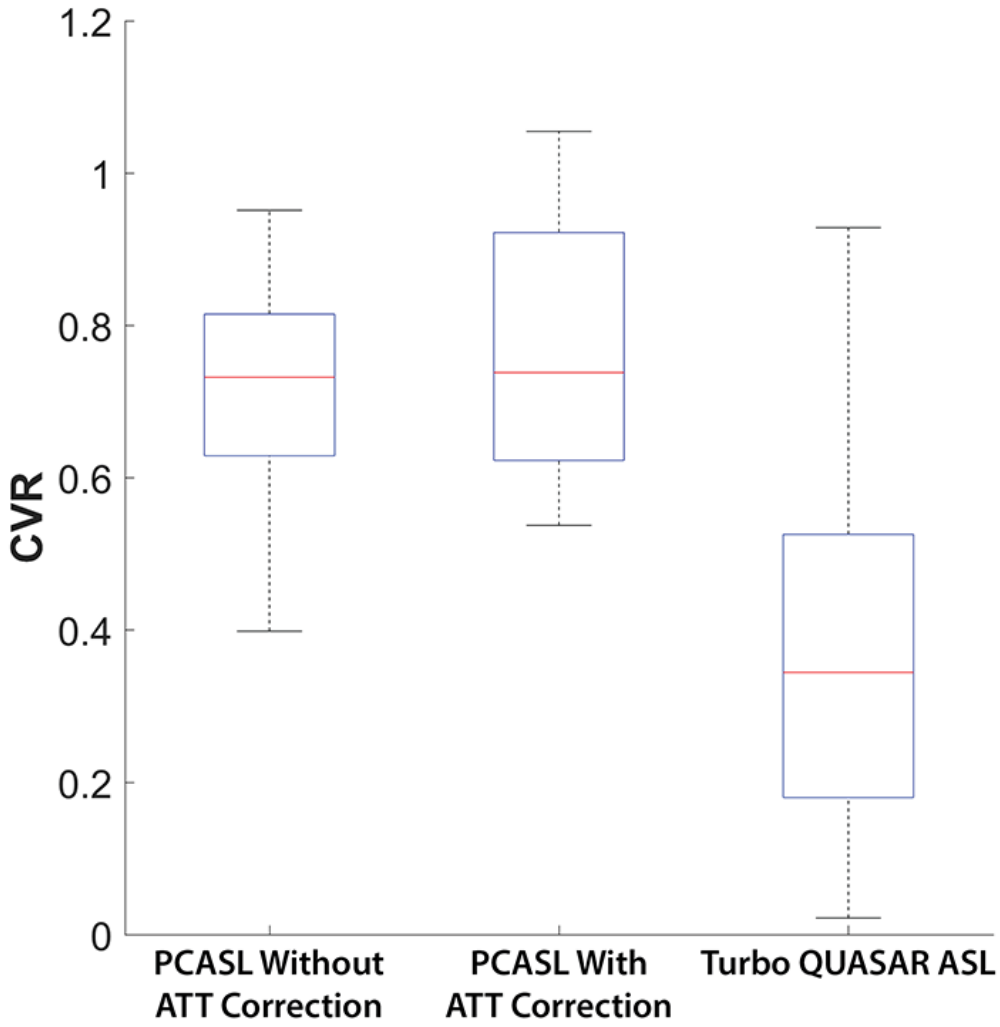

Figure 5.14: Mean CVR of the group using three ASL methods. Correcting for ATT increased the CVR of the PCASL based method slightly while the mean CVR of Turbo QUASAR ASL was the lowest and had the largest range.

reduced estimated CBF in the superior regions, indicated by hot color areas (arrow in Figure 5.16 and Figure 5.17) where the CBF of PCASL after ATT correction was less than the values before ATT correction. Comparing between PCASL and Turbo QUASAR ASL results (second and third rows), CBF of Turbo QUASAR ASL demonstrated higher estimated values in the lower part of the brain whereas CBF of PCASL was higher in the superior regions. After acetazolamide administration, the difference between the two PCASL methods reduced (first row). This indicated that ATT had less impact after acetazolamide administration for the PCASL method.

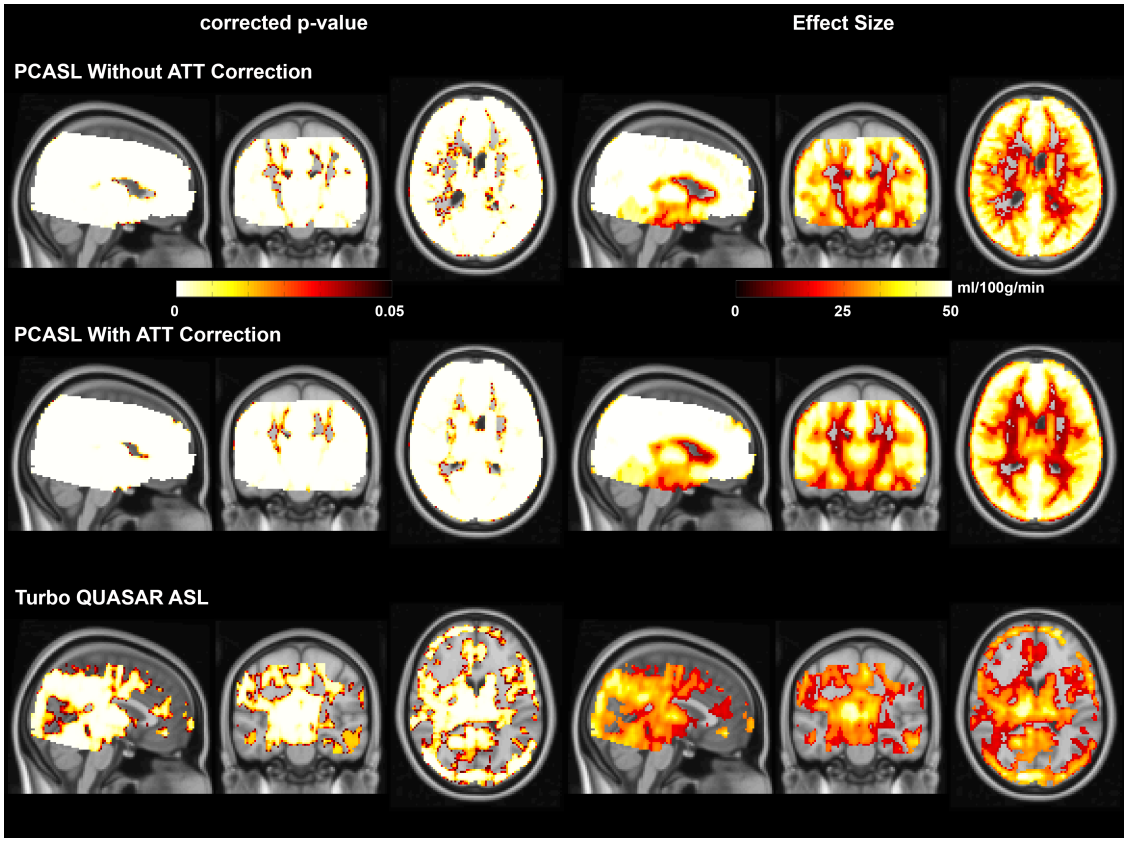

Figure 5.15: Results of paired t-test comparing the CBF before and after acetazolamide administration. The results of the two PCASL based methods were similar where the majority of the regions in the brain underwent significant CBF increase in more than 25 ml/100g/min after acetazolamide administration. In Turbo QUASAR ASL, however, the regions with significant increase and effect size were much less extensive.

CBF of PCASL was higher than Turbo QUASAR ASL globally after acetazolamide administration, confirming the results shown in Figure 5.12.

Figure 5.18 shows the changes in ATT of an example subject estimated by Turbo QUASAR ASL. Figure 5.19 shows the changes in ATT estimated by Turbo QUASAR ASL after acetazolamide administration. Figure 5.20 shows the changes in blood velocity in the carotid artery. Overall, the mean ATT of nearly all subjects decreased significantly (about 15% as shown in Figure 5.19). The ATT map of the example subject showed that ATT decreased in nearly all the regions of the brain (Figure 5.18). In terms of the mean velocity, the value for baseline and acetazolamide conditions were 24.02cm/s and 33.49cm/s respectively (Figure 5.20), which resulted in about 35% increase for this cohort.

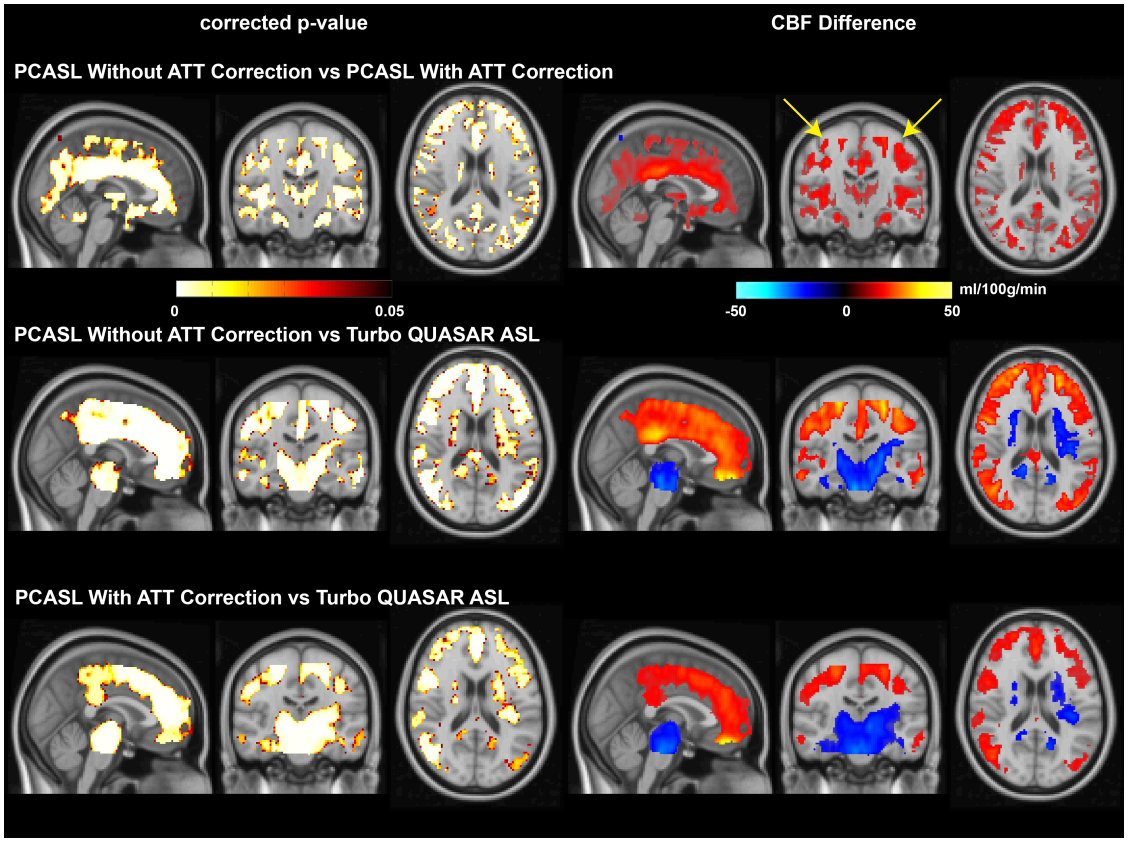

Figure 5.16: Corrected p-value and CBF differences of t-tests comparing CBF estimated by PCASL and Turbo QUASAR ASL in the baseline condition. In the effect size maps, first row: hot color indicates (positive values) CBF of PCASL without ATT correction was greater than PCASL with ATT correction, and cool color (negative values) represents the opposite; second and third row: cool color indicates CBF of Turbo QUASAR ASL was greater than the PCASL based method. The arrows indicate regions with reduced CBF after incorporating ATT into the PCASL analysis.

5.5 Discussion

In this work, we investigated the CVR estimation using PCASL and Turbo QUASAR ASL. A model based quantification method was developed for Turbo QUASAR ASL to estimate the hemodynamic parameters (CBF, CVR, and ATT). In the in vivo experiment, we compared Turbo QUASAR ASL with the standard single-PLD PCASL using data collected from a healthy population before and after acetazolamide administration. The metrics of comparison included the differences of CVR estimation and regional differences of CBF estimation between the two ASL techniques. The primary findings are the following: (1) Turbo QUASAR ASL achieved nearly full brain coverage, and the model based quantification method

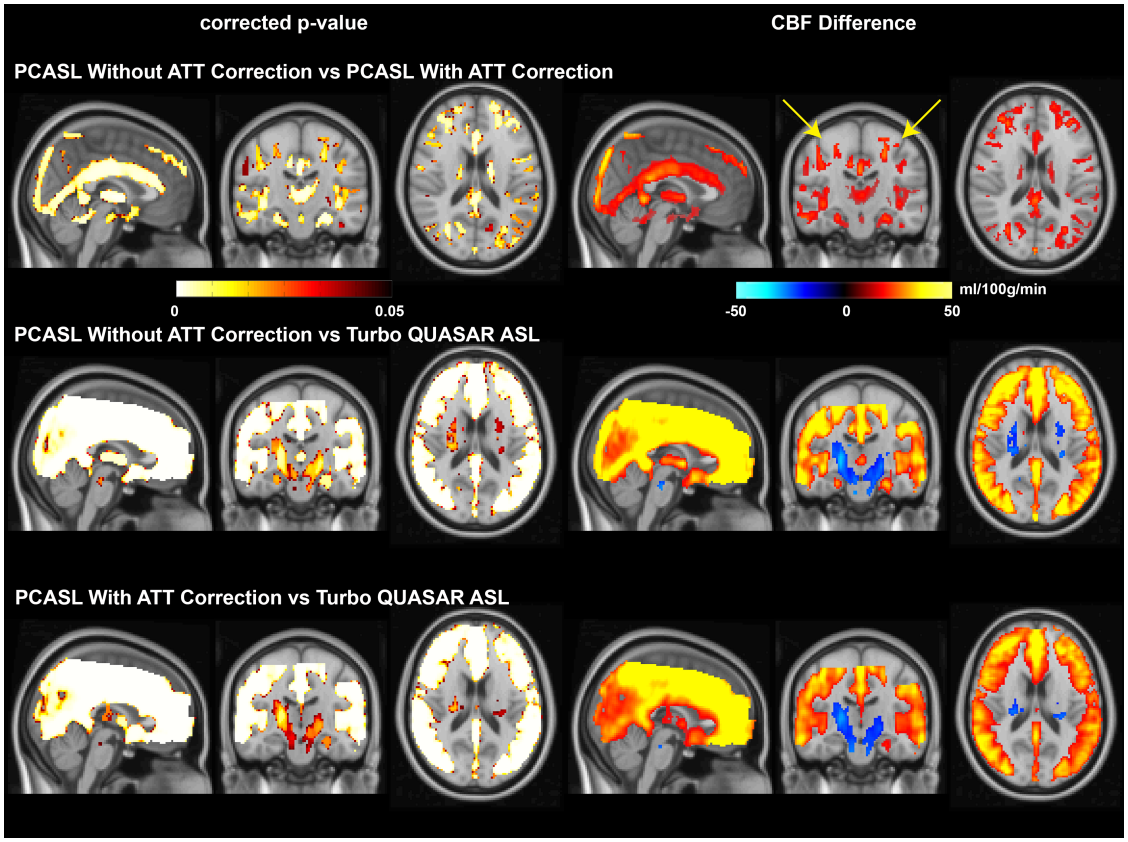

Figure 5.17: Corrected p-value and CBF differences of t-tests on comparing CBF estimated by PCASL and Turbo QUASAR ASL after acetazolamide administration. In the effect size maps, first row: hot color indicates (positive values) CBF of PCASL without ATT correction was greater than PCASL with ATT correction, and cool color (negative values) represents the opposite; second and third row: cool color indicates CBF of Turbo QUASAR ASL was greater than the PCASL based method. The arrows indicate regions with reduced CBF after incorporating ATT into the PCASL analysis.

demonstrated high accuracy and consistency in parameter estimation when the true bolus duration is similar to the time between each successive labeling pulse. However, the accuracy and consistency of the method reduced if the bolus duration became uncertain, causing a consistent bias in the estimation of CBF and ATT. (2) Both Turbo QUASAR ASL and PCASL were sensitive to CVR and a significant increase in CBF was detected after acetazolamide administration, but the two techniques were limited by the confounding factors induced by the acetazolamide administration (Turbo QUASAR ASL sensitive to flow velocity and PCASL sensitive to ATT and inversion efficiency. (3) There were significant regional differences of CBF between the Turbo QUASAR ASL and PCASL and the differences reduced

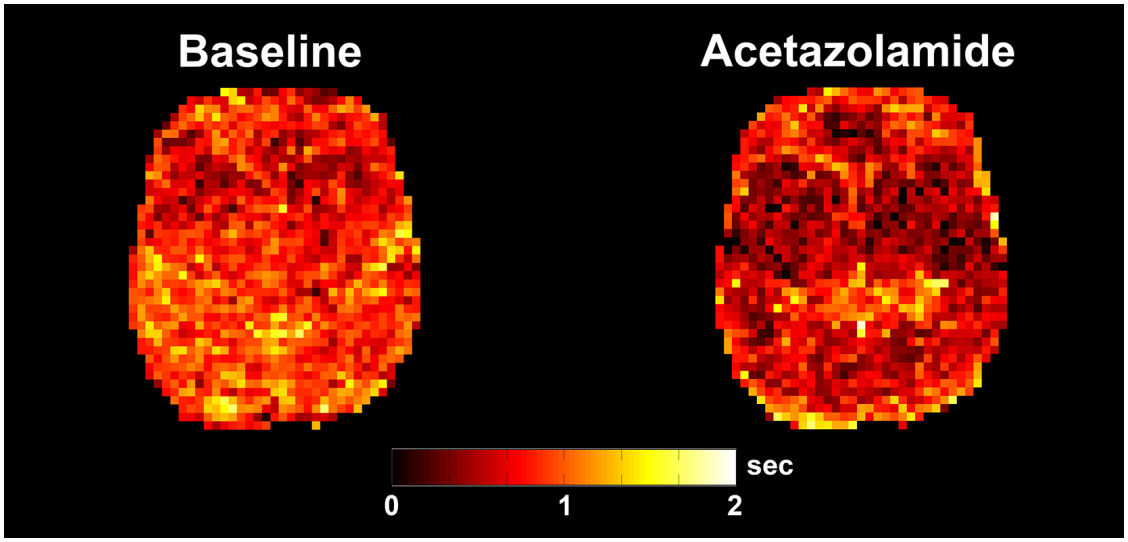

Figure 5.18: Estimated ATT of an example subject using Turbo QUASAR ASL after acetazolamide administration. For this subject, a global reduction of ATT can be identified after acetazolamide administration.

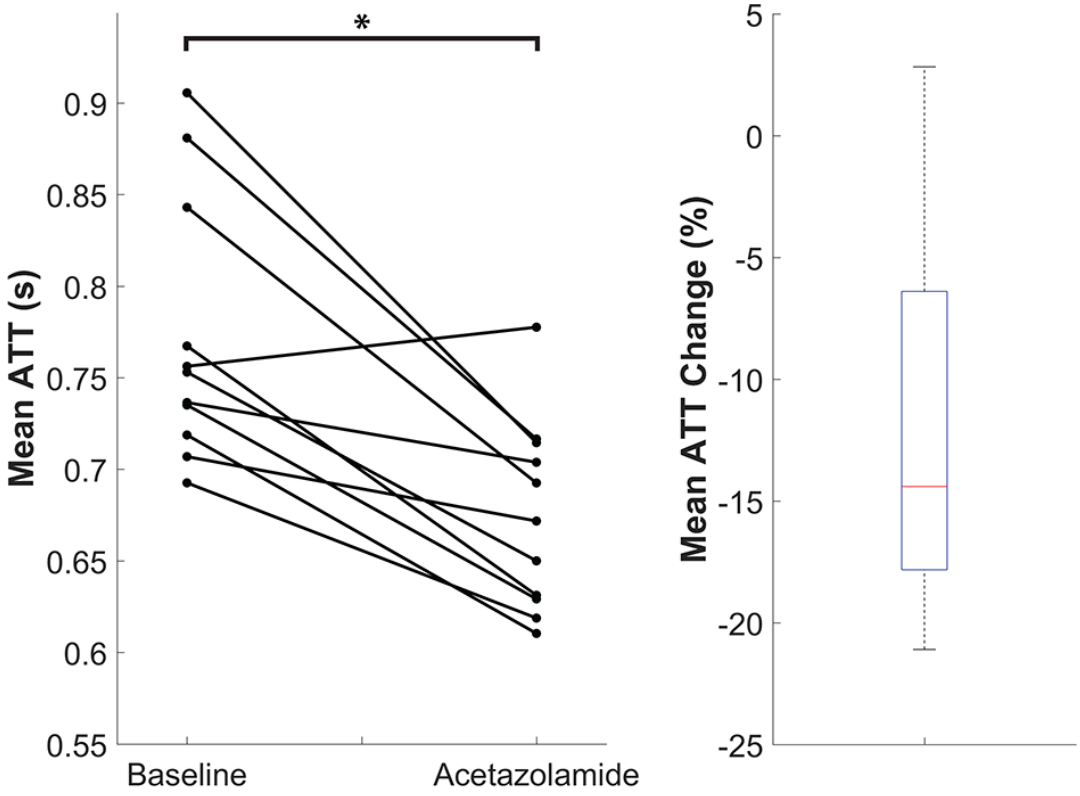

Figure 5.19: Changes in mean ATT of the group after acetazolamide administration and non-parametric test results. Except in one subject, ATT reduced significantly after acetazolamide administration. The median decrease was about 15% in this population.

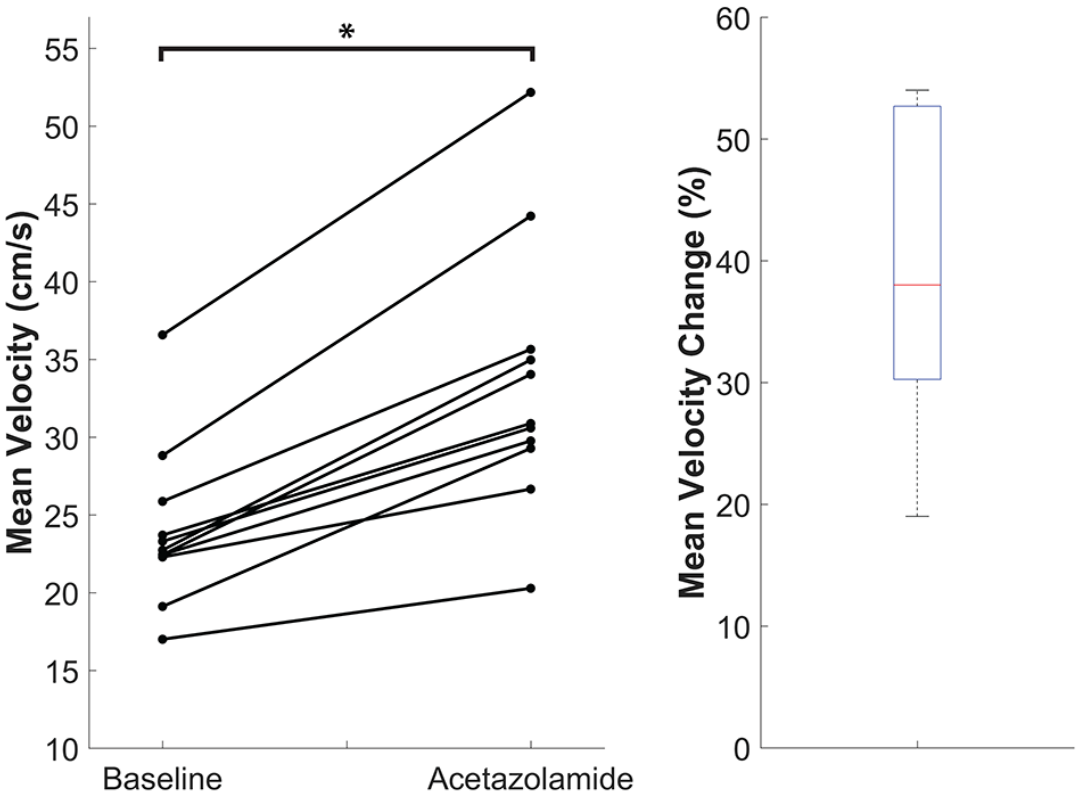

Figure 5.20: Changes in the mean arterial blood velocity in the carotid artery. A significant increase in the blood velocity was found after acetazolamide administration.

when ATT was accounted for in the PCASL data analysis.

5.5.1 Turbo QUASAR ASL Sequence

The objective of the newly developed Turbo QUASAR ASL technique was to combine the advantage continuous labeling scheme and multi-PLD image acquisition. The number of boluses was important to the SNR of the data while the number of PLDs was crucial to determine the ATT. In Turbo QUASAR ASL, the continuous labeling of the inflowing blood water created a PCASL-like bolus consisting of a train of small boluses. Each labeling pulse and acquisition were implemented in an interleaved manner to maintain a balance between stronger a SNR and a sufficient number of PLDs. Compared with QUASAR ASL, Turbo QUASAR ASL replaced half of the acquisition time by applying the RF pulse to create another bolus,

which reduced the signal reduction due to the frequent excitation of the Look-locker readout scheme. Together with a higher SNR, Turbo QUASAR ASL resolved the spatial coverage issue of QUASAR ASL and achieved nearly full brain coverage.

5.5.2 Model Based Method and Simulated Experiments

A new kinetic model was developed for the data collected using Turbo QUASAR ASL, and it was compared with the model free approach using simulated data. The model was based on the same tissue kinetic principle proposed by Buxton et al [87], but the formulation of the effective AIF was implemented by the summation of the AIF of each bolus. Similar to QUASAR ASL, the model based technique demonstrated a consistently higher accuracy of CBF estimation and was less sensitive to noise than the model free approach. When the two methods were compared under the condition of different number of boluses labeled (or total bolus duration), the model free approach became less accurate with more boluses whilst the accuracy of the model based technique was retained in all cases (Figure 5.9), making the model based method a better choice. Another benefit of using the model based approach was its lower sensitivity to noise than the model free method, which was demonstrated by the low standard deviation of the estimated CBF by the model based method in Figure 5.9.

A potential issue for Turbo QUASAR ASL is the unknown effective bolus duration at abnormal flowing conditions. The impact of shortened bolus duration due to more rapid blood velocity was investigated by comparing the estimation accuracy in cases where there is a mismatch between simulated effective bolus duration and the prior of bolus duration (assumed value) in the model based method. In the first step of the analysis, where bolus duration was fixed to 0.6s, both CBF and ATT were underestimated (Step 1 of Figure 5.10), except when the bolus duration provided matched with the value simulated. For the results from data using simulated bolus duration of 0.3, 0.4, and 0.5s, a consistent bias can be observed between the estimated CBF and the simulated CBF (also for estimated ATT and simulated ATT). For example, an underestimation of 17% for CBF was

found in the case where the simulated bolus duration was 0.5s (green plot in Step 1 of Figure 5.10). The errors increased with more mismatch between the effective and the assumed bolus duration. In Step 2, where we attempted to estimate the bolus duration together with CBF and ATT by incorporating the results from Step 1, an overall trend was that the accuracy of the parameter estimation improved (Step 2 of Figure 5.10). However, the accuracy was still affected by the choice of bolus duration prior. For example, in simulated data without noise, the CBF was underestimated by 8% for the data with simulated bolus duration of 0.5s while an underestimation of 40% for the data with simulated bolus duration of 0.3s. The results implied that the choice of bolus duration prior is important for the accurate estimation of the hemodynamic parameters from Turbo QUASAR ASL using the two-step approach. A potential issue is the decreased sensitivity to measure CBF and ATT when the bolus duration becomes uncertain, such as in subjects with abnormal blood flow conditions. Therefore, the reliable quantification of the bolus duration, such as derived from the flow velocity measurement, is beneficial for analysis of Turbo QUASAR ASL data.

5.5.3 Healthy Cohort Experiments

The estimation of several hemodynamic parameters was investigated at different flow conditions using Turbo QUASAR ASL and PCASL data from a healthy cohort. The non-parametric test results (Figure 5.12) and CVR maps (Figure 5.13) indicated that PCASL demonstrated a higher sensitivity of CVR of the whole brain than Turbo QUASAR ASL. The mean CVR value (0.73) from the PCASL data was within the range of the CVR results from a separate study using PET techniques and acetazolamide administration [147]. This implied that the PCASL technique can be employed as an alternative to PET to measure CVR of the whole brain.

In a recent review paper, Liu et al highlighted the issues of ATT variations in quantifying CVR using ASL based techniques [148]. In the present study, we also demonstrated that Turbo QUASAR ASL detected a significant reduction in ATT on healthy subjects after acetazolamide administration (Figure 5.19). Since single-PLD

PCASL is unable to account for the variations of ATT in CBF estimation, we attempted to incorporate the ATT from Turbo QUASAR ASL to correct in the PCASL data analysis. Although the mean CBF of PCASL reduced significantly after the administration of acetazolamide (Figure5.12), there was no significant change in the mean CVR of PCASL of the group (Figure 5.13). From these results, we can conclude that ATT is not an influential factor for measuring the CVR of the whole brain in healthy subjects.

The ASL methods were compared by conducting a paired t-test to examine the regional CBF differences at baseline and acetazolamide conditions. For the comparison between the two PCASL based methods at baseline, CBF estimation without considering ATT was always higher than the results of taking ATT into account, and the difference was less than 25 ml/100g/min (first row of Figure 5.16). Comparing between Turbo QUASAR ASL and PCASL based methods (second and third row of Figure 5.16), a common feature was that the CBF from Turbo QUASAR ASL was always significantly higher than PCASL methods at the inferior region of the brain and vice versa at the superior region of the brain. A possible explanation to this was the impact of ATT in the CBF estimations because ATT tends to be longer in the superior region than the inferior region of the brain. After incorporating ATT into PCASL data analysis, the effect size (absolute CBF difference between PCASL and Turbo QUASAR ASL) reduced (third row of Figure 5.16). For the results after acetazolamide administration (Figure 5.17), CBF estimated by PCASL was larger than Turbo QUASAR ASL by over 25ml/100g/min, which reflected the larger mean CBF differences of the whole brain in Figure 5.12. The CBF of nearly all cortical gray matter demonstrated differences between PCASL and Turbo QUASAR ASL (second and third row of Figure 5.17), including the posterior region of the brain where CBF was not significantly different at baseline.

5.5.4 CVR Quantification Using PCASL

The estimated CVR from the single-PLD PCASL data was biased by variations of ATT and inversion efficiency. The observed mean CVR value (about 0.75 in Figure

5.14) was caused by three varying factors after the administration of acetazolamide: ATT, inversion efficiency, and CBF. Since the chosen PCASL technique was sensitive to the changes in ATT, we incorporated the ATT estimation from Turbo QUASAR ASL to correct the CBF estimation of PCASL. As a result, the CBF estimation reduced by about 10% for both before and after acetazolamide administration (middle box in Figure 5.12). From analyzing the Turbo QUASAR ASL, it was found that the ATT reduced by about 15% (Figure 5.19). Suppose the observed median CBF values (or ASL difference signal) before acetazolamide administration were 49 ml/100g/min (Figure 5.12) and ATT reduced by 15% after acetazolamide administration (Figure 5.19), then the effective CBF variation caused by both the reduction of ATT should be about 2% decrease based on the tissue kinetic model. This implied that if ATT was not corrected for the PCASL results in this cohort, the estimated CVR would include a 2% bias due to changes in ATT, which might explain the subtle differences of median CVR values of the PCASL methods in Figure 5.14. Although the impact of ATT might be minor (only 2% less), it should be noted that the ATT values used in the above calculation were taken from the estimated results from Turbo QUASAR ASL. Specifically, the ATT values used to correct PCASL was lower than the results reported in a study using multi-PLD PCASL [84]. Thus, care should be taken when interpreting the corrected CVR values of PCASL.

The CVR maps of PCASL in Figure 5.13 revealed that CVR was higher in cortical gray matter than white matter both before and after ATT correction. These results in differences in tissue CVR were consistent with the findings of a previous study using BOLD MRI to measure CVR [16]. After correcting for ATT variations, the CVR of white matter reduced (second row in Figure 5.11). This was due to the reduction of CBF in white matter after ATT correction (by 9%, second row in Figure 5.11), while the CBF of gray matter showed little changes after ATT correction. The variations in CBF of white matter contributed to results that CBF of the whole brain reduced significantly after ATT correction (Figure 5.12). Another feature was that before correcting for ATT for PCASL, the CVR of the posterior region of the brain was higher than other areas (by 20%, first row in Figure 5.13).

Since the ATT in the posterior region is typically longer than other regions, the observed CBF of this region would be higher without correcting for ATT variations, according to the general kinetic model [87]. This resulted in the relatively higher CVR in the posterior regions of the brain. After ATT correction (second row in Figure 5.13), the CVR of the posterior regions reduced, suggesting that ATT was an influential factor to the regional CVR differences.

The voxel-wise CBF and CVR values demonstrated different spatial distributions between PCASL and Turbo QUASAR ASL. Looking at the baseline PCASL results shown in Figure 5.11, the CBF in cortical GM reduced by 12% after incorporating ATT correction. This can be explained by the general kinetic model that a longer ATT after correction would result in a lower CBF [87]. However, the reduction was not a significant factor in the mean CBF reduction of the whole brain. Comparing the baseline CBF maps (Figure 5.11) between PCASL and Turbo QUASAR ASL, a unique feature was that the CBF of Turbo QUASAR ASL was higher than PCASL in the posterior regions, and the CBF of these regions showed little increase after acetazolamide administration. Since the perfusion of the posterior region of the brain is supplied by the posterior cerebral artery with the longest ATT, it is possible that there may be some dispersion effects that affected the profile of the bolus and caused the CBF to be overestimated at baseline. In terms of the regional CVR differences, a common feature for both PCASL and Turbo QUASAR ASL results was that the CVR of the posterior regions was higher than the rest of the brain (Figure 5.13). Additionally, the CVR of PCASL was higher than that of Turbo QUASAR ASL in the posterior regions. Such observation can be explained by CBF maps in Figure 5.11 in which the CBF of the posterior regions in Turbo QUASAR ASL showed a much less increase than PCASL after the administration of acetazolamide. Apart from the CVR differences in the posterior regions of the brain, the CVR of cortical GM of Turbo QUASAR ASL was also significantly lower than the GM CVR of PCASL. This was due to the underestimation of Turbo QUASAR CBF after the administration of acetazolamide by assuming the bolus duration unchanged (explained in the previous paragraph).

The changes in flow velocity will affect the inversion efficiency of the PCASL technique [17]. In our analysis, we assume the same inversion efficiency before and after acetazolamide administration. Since a higher blood flow velocity reduces the actual inversion efficiency [149], the CBF after acetazolamide administration will have been underestimated. Aslan et al reported a linear relationship between inversion efficiency and flow velocity higher than 30cm/s [150]. If this relationship can be assumed, the actual inversion efficiency of PCASL would be about 0.68 after acetazolamide administration, which would make the observed mean CBF (75ml/100g/min, Figure 5.12) in the current analysis 20% underestimated. Consequently, CVR results would be affected by the different inversion efficiency before and after the administration of acetazolamide. Together with the CBF variations caused by ATT, the observed CVR of PCASL contained a 20% bias due to inversion efficiency and a 2% bias due to ATT.

5.5.5 CVR Quantification Using Turbo QUASAR ASL

Estimating the CVR using Turbo QUASAR ASL was limited by the change in flow velocity after acetazolamide administration. Both ATT and the mean velocity of the blood in carotid artery changed significantly after the administration of acetazolamide. At baseline, the group mean velocity of 24.02cm/s (Figure 5.20) should translate into an effective bolus duration of 0.62s for each of the 15cm labeling slab and only 3% different from the assumed bolus duration (0.6s) in the Turbo QUASAR ASL analysis. After acetazolamide administration, the mean velocity increased to 33.49cm/s, and the estimated effective bolus duration became 0.45s (25% less) for each RF pulse. Since the bolus duration of 0.6s was used in analyzing the data after acetazolamide administration, both CBF and ATT might be underestimated according to simulation results (Figure 5.10). Suppose the actual bolus duration was 0.45s and SNR was 5 after acetazolamide administration, the CBF and ATT were likely to be underestimated by 25% and 8% respectively (green and blue lines of Step 1 in Figure 5.10). For an underestimation of 25% of CBF and an observed mean CBF of 65ml/100g/min (Figure 5.12), the actual mean CBF

would be about 80 ml/100g/min and actual CVR would become 0.75 (Figure 5.14), which reduces the discrepancy with the PCASL results. Although it is possible to include a second step in the model-fitting process to estimate the actual bolus duration, the improvement to the accuracy of CBF and ATT is marginal (less than 5% more accurate according to simulations in Figure 5.10). The underestimation of the ATT (8%) after acetazolamide administration also implied that the PCASL results needed to be further corrected. Therefore, the observed CVR of Turbo QUASAR ASL should include a 25% bias due to the underestimation of CBF.

The simulation results and the observed increase in blood velocity suggested that a more realistic bolus duration prior should be used to reduce underestimation of CBF and ATT in Turbo QUASAR ASL in high blood flow conditions. The sequence parameter of 15cm labeling slab should be effective for the baseline condition. However, in high flow conditions without adjusting the prior values of bolus duration, both CBF and ATT would be underestimated. A possible solution would be using the mean velocity to set the prior value to improve estimation accuracy.

5.5.6 Implications for CVR Studies for SCD Patients

The present work is part of a study to investigate the CVR of SCD patients. MRI experiments using the same parameters have been conducted on patients. One of the challenges of estimating the CVR of these patients was the abnormally high CBF and flow velocity at the baseline condition. Specifically, The estimated flow velocity of the blood in carotid artery of patients increased from 33 to 41cm/s as shown in Figure 5.21. The current analysis on the healthy control cohort has been applied to patients data to estimate the hemodynamic parameters (CVR, CBF, and ATT). [3] For the single-PLD PCASL data, the mean GM CBF increased from about 75 ml/100g/min to 100 ml/100g/min without ATT correction, and a corresponding CVR value of 0.33. For the Turbo QUASAR ASL data, the mean CBF changed from 90 ml/100g/min to 110 ml/100g/min (0.22 CVR) and the mean ATT reduced from 0.7s to 0.68s (about 3% decrease). Following the same rational, the observed CVR of

[3]The Turbo QUASAR ASL analysis of patient data was performed by Lena Václavů at Academisch Medisch Centrum, Amsterdam

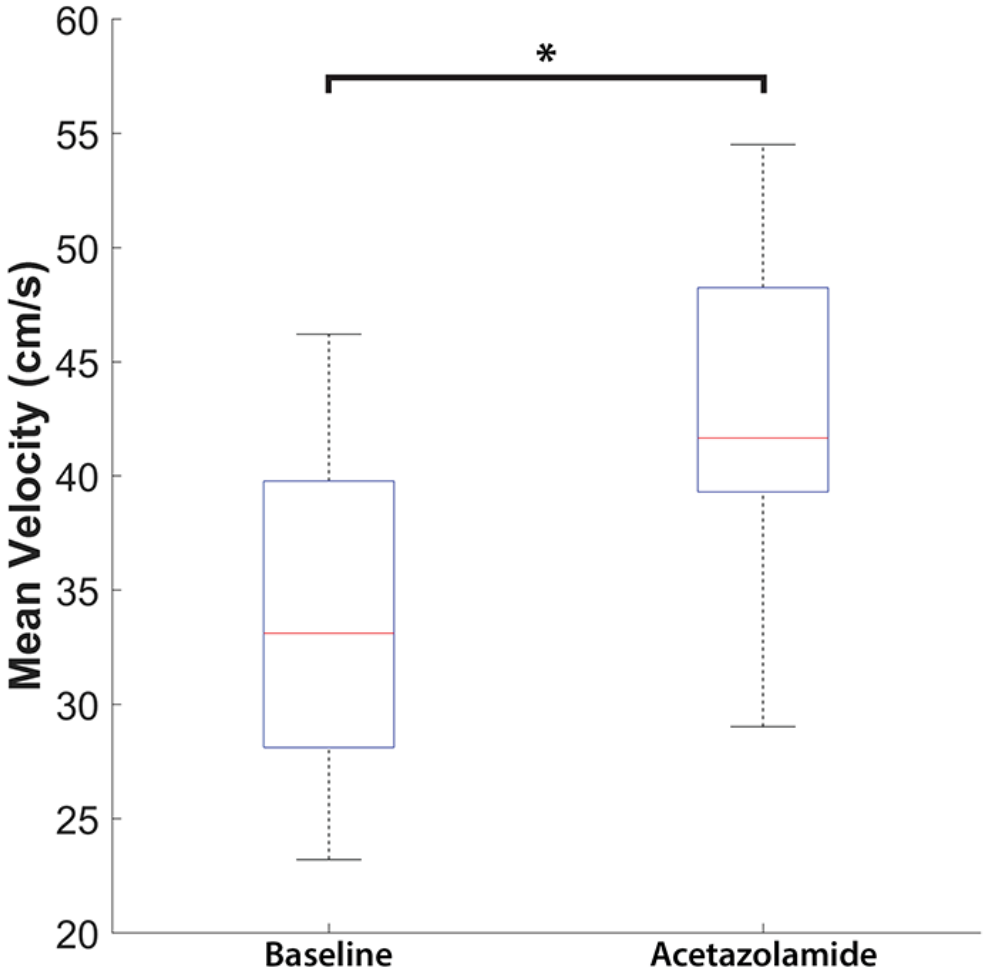

Figure 5.21: Mean velocity of SCD patients. The estimated median velocity of the patients increased from 33 to 41cm/s or by 24%.

PCASL would include a less than 1% bias due to changes in ATT and a 24% bias due to changes in inversion efficiency. For Turbo QUASAR ASL, if the blood velocity increased from 33cm/s to 41cm/s, the effective bolus duration would be 0.45s and 0.37s respectively. As a consequence, the observe CVR of Turbo QUASAR ASL would include a 18% bias. Therefore, the abnormal ATT and inversion efficiency must be taken into account to reduce the bias in CVR estimation for patients.

5.5.7 Impacts of Resolution and Motion

The different CVR maps between PCASL and Turbo QUASAR ASL may also due to the different resolutions of the data (PCASL: 3×3mm; Turbo QUASAR ASL: 3.75×3.75mm). The low resolution of the data caused partial volume effects that affected the tissue CBF quantification, and partial volume correction could be considered to correct the bias. Since the structural image was collected using a T2-FLAIR sequence instead of the commonly used T_1-weighted technique, segmenting this image may introduce bias to the partial volume estimates. The impact of biased partial volume estimates was investigated in Chapter 3 where both the accuracy and consistency of the GM CBF decreased.

Motion was likely to be another factor that caused the disagreement between PCASL and Turbo QUASAR ASL. For example, the PCASL and Turbo QUASAR ASL data used to for acetazolamide condition were collected nearly forty minutes after the start of the MRI experiments, making it difficult for the subject to stay in the same position during scanning. In principle, motion correction can be included in post processing to reduce the impact of motion artifact. For PCASL, this is possible where the data from all the dynamics are aligned to a specific reference point using the FSL tool FLIRT [134]. However, it is more challenging to perform motion correction for Turbo QUASAR ASL using the same technique due to the slice shifting procedure. As discussed in the methods section, half of the data were acquired such that the middle slice had the lowest signal because it was acquired first. This made motion correction difficult because the first and second half of the data had highly different signal intensities to be registered to the same reference point.

5.5.8 Limitations

MT effects limited the independent use of Turbo QUASAR ASL data for absolute CBF quantification. In the present study, we attempted to estimate voxel-wise M_0 values from the control data of Turbo QUASAR ASL by fitting it to a saturation recovery model [101]. Comparing with the M_0 results used in the healthy cohort experiments, the M_0 values estimated from the Turbo QUASAR ASL control data

was consistently lower by 20% both before and after acetazolamide administrations. As a consequence, the estimated CBF values in absolute units would be 20% higher than the results reported in the healthy cohort experiments (shown in Figure 5.22), causing further inconsistency with the PCASL CBF results. MT effects may be the main factor that caused the differences between the two M_0. As discussed in the Method section, Turbo QUASAR ASL employed two types of label/control RF pulses to minimize the MT effects. However, this technique was demonstrated effective when only one RF pulse was applied in conventional ASL [151]. Since multiple RF pulses were used in Turbo QUASAR ASL, the MT effects caused by each RF pulse may accumulate to affect the acquired signals. Therefore, the independent use of Turbo QUASAR ASL data for absolute CBF quantification was not used in this work. Another limitation was the use of linear registration in group analysis. In general, non-linear registration is applied to transform the CBF data from ASL space to standard space. Due to the lack of T_1-weighted structural images for each subject and the less desirable results from using a particular non-linear registration (FNIRT), however, linear registration was adopted in the group analysis. Possible solutions include replacing the T_1-weighted standard image in this study with a T_2-FLAIR standard image and using alternative registration tools capable of performing non-linear registration between different modalities.

In the simulated experiments, we sought to investigate the accuracy of CBF and ATT estimation with different bolus duration to simulate the effects of changing blood velocity and vessel diameter. Although we demonstrated overestimation of CBF and consistency of ATT at low bolus duration values, changes in flowing condition might also cause variations of arterial blood T_1 apart from a reduced bolus duration, where the T_1 of blood largely depends on hematocrit [152]. As a consequence, changes in blood T_1 would alter the signal decay in AIF. However, the numerous boluses of Turbo QUASAR ASL are able to create enough signal that the changes in blood T_1 may be ignored. Ideally, the length of the labeling slab of Turbo QUASAR ASL should be adjusted according to the estimated velocity of the inflow blood to ensure an optimal bolus duration. However, this is difficult to implement

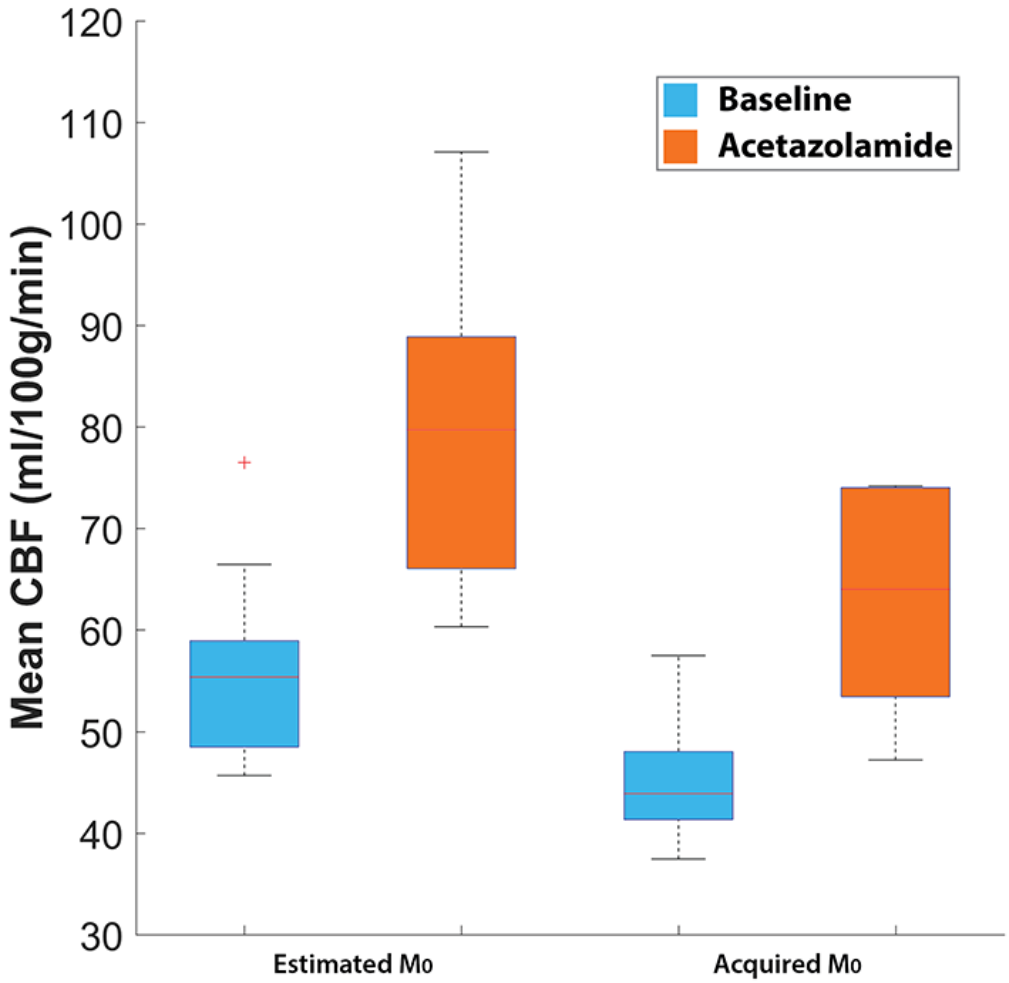

Figure 5.22: Estimated CBF from Turbo QUASAR ASL data using different calibration techniques. CBF estimated using the M_0 from fitting a saturation recovery model were consistently higher than using the acquired M_0 image for both conditions.

in practice because (1) blood velocity estimation is sensitive to the ROI selection of PC MRI and (2) the scanning plane needs to be re-planned for each case.

5.6 Conclusions

In this work, we investigated the CVR on a healthy cohort using single-PLD PCASL and Turbo QUASAR ASL. In simulated experiments, we demonstrated that the model based quantification method achieved higher accuracy and consistency

than the model free approach. The superiority of the model based technique was more obvious when the bolus duration became less certain, which could resemble a population with blood disorders. In the in vivo experiment that compared Turbo QUASAR ASL with PCASL, the two ASL methods demonstrated different sensitivities for CVR measurements of the whole brain in a healthy control population due to the significantly different CBF measurement after the administration of acetazolamide, despite the CBF estimation was similar at baseline. The regional differences of CBF estimated by the two ASL methods were largely due to ATT differences. Both ASL techniques demonstrated limitations in CVR measurements: the single-PLD PCASL technique was more biased by the variations of inversion efficiency at different flow conditions than variations of ATT; the Turbo QUASAR ASL method was biased by the uncertainties of effective bolus duration caused by the changing flow velocity at different conditions. The analysis suggested that the inclusion of PC MRI for flow velocity estimation should be essential to reduce the bias in both PCASL and Turbo QUASAR ASL.

The last stretch of a journey marks the halfway point.

— Chinese proverb

6 Conclusions and Future Work

Contents

6.1 Conclusions 171
6.1.1 Sensitivity of PVEc Methods on Single-PLD ASL 172
6.1.2 Impact of PVEc on Repeatability of GM CBF Estimation 172
6.1.3 Sensitivity of PVEc Methods on Multi-PLD ASL 173
6.1.4 Impact of PVEc Methods on QUASAR ASL 173
6.1.5 Turbo QUASAR ASL and Model Based Quantification Method 174
6.1.6 Investigating CVR Measurements Using PCASL and Turbo QUASAR ASL 174
6.2 Future Work 175
6.2.1 Partial Volume Correction For ASL Data of Brain Activation 175
6.2.2 Partial Volume Correction For ASL Data of Patients . . 175
6.2.3 Improving Turbo QUASAR ASL 175
6.2.4 Investigating CVR In Patients 176

6.1 Conclusions

In this thesis, we have investigated the impact of PVEc methods for GM CBF quantification from single and multi-PLD ASL as well as examined the CVR estimation using single-PLD PCASL and Turbo QUASAR ASL techniques. The PVEc methods were evaluated by the ability to preserve spatial variations and the accuracy of estimating GM CBF and ATT using simulated PCASL and PASL

data. Results indicated that the spatially regularized method was more suitable for preserving spatial variations and that the LR method was less sensitive to variations in the data. In order to improve the repeatability of GM CBF estimation using ASL, performing PVEc was effective in reducing the within subject variations of repeated measurements due to PVE. From the results of the study that compared the PVEc methods on multi-PLD ASL, it can be concluded that both multi-PLD PCASL and PASL are suitable for GM CBF estimation. However, multi-PLD PCASL is superior to PASL in GM ATT estimation using the spatially regularized method. In the quantification of hemodynamic parameters using Turbo QUASAR ASL, the model based method demonstrated higher estimation accuracy than the model free technique. In the CVR study, both single-PLD PCASL and Turbo QUASAR ASL were sensitive to the changes in CBF for CVR estimation, but they were limited by different confounding factors: PCASL by the variations of ATT and inversion efficiency and Turbo QUASAR ASL by the variations of blood flow velocity.

6.1.1 Sensitivity of PVEc Methods on Single-PLD ASL

In the simulated experiments that investigated the sensitivity of PVEc methods on single-PLD PCASL, the spatially regularized method demonstrated consistently greater ability to preserve spatial details in GM CBF maps, but it was also shown to be sensitive to noise in ASL data and errors in the PV estimates. The LR method was consistently less sensitive to noise and errors, but this appeared to be largely due to the smoothing effect of the kernel employed. Thus, the estimated GM CBF was less accurate than the spatially regularized method whenever there were features in the data represented over short length scales.

6.1.2 Impact of PVEc on Repeatability of GM CBF Estimation

The results from the analysis of the multi-PLD PCASL data of healthy volunteers indicated that both the LR and the spatially regularized PVEc methods improved the repeatability of GM CBF measurement. Although the estimated GM CBF by

the spatially regularized method showed higher discrepancies than the LR method in low GM PV estimates regions, the two PVEc techniques achieved similar (high) repeatability in GM PV estimates larger than 40%. It appears to be important to correct for PVE (using either LR or spatially regularized method) in order to enhance the reliability of GM CBF estimation of ASL.

6.1.3 Sensitivity of PVEc Methods on Multi-PLD ASL

In the simulated experiments using multi-PLD ASL, both the LR and the spatially regularized PVEc methods improved the accuracy of estimation GM CBF on both PCASL and PASL. Applying the spatially regularized method on PASL data was slightly more accurate than PCASL data under the same experimental conditions. The LR methods demonstrated similar results on both PCASL and PASL. The GM ATT results indicated that applying the PVEc methods achieved more accurate results on PCASL than PASL and that the LR method was the most accurate. Therefore, the simulations implied that using multi-PLD PCASL data collection method should be the favorable choice for quantifying GM CBF and ATT.

6.1.4 Impact of PVEc Methods on QUASAR ASL

A new kinetic model was developed to incorporate the arterial blood signal and the tissue signal from both GM and WM for QUASAR ASL. The separation of the tissue component into GM and WM contributions allowed the independent estimation of GM CBF and ATT. The corrected GM CBF results showed different characteristics from simulations: the GM CBF changed very little after applying the LR PVEc method, but the values increased after the spatially regularized method was applied. These results were likely due to the mismatch of the PSF between the QUASAR ASL data and the estimated PV estimates, which was observed in the simulations. More work is needed to investigate the effective PSF in the QUASAR ASL data acquisition. From the GM ATT results after PVEc, a lower GM ATT values may be expected if the ASL data were collected using the QUASAR approach and if the PVE were corrected by the LR method.

6.1.5 Turbo QUASAR ASL and Model Based Quantification Method

The newly developed model based method allowed the estimation of CBF, ATT, and bolus duration for Turbo QUASAR ASL. In cases where the effective bolus duration matches the assumed value set by the sequence, the model based method was more accurate and robust than the model free technique. Thus, it was chosen as a favorable tool for the analysis of Turbo QUASAR ASL. If the effective bolus duration was uncertain, the model based method became less accurate, but estimating the bolus duration as an extra step reduced the errors for all parameter estimations. However, the correlation between ATT and effective bolus duration cannot be separated by the current model based technique.

6.1.6 Investigating CVR Measurements Using PCASL and Turbo QUASAR ASL

Single-PLD PCASL and Turbo QUASAR ASL demonstrated distinct CVR estimations in terms of regional variations as well as mean CVR values of the whole brain. Although both methods were sensitive to detect the significant changes in CBF, they were limited by particular factors: the single-PLD PCASL technique was limited by the variations of ATT and inversion efficiency at different flow conditions, while Turbo QUASAR ASL was hindered by the uncertainties of effective bolus duration due to different blood flow velocities. The bias in the Turbo QUASAR ASL was reduced by incorporating the velocity estimation from PC MRI data, which also benefited the correction the inversion efficiency of single-PLD PCASL. However, the velocity information must be handled carefully because only the blood flow in the carotid arteries were included. Thus, more work is needed to control the confounding factors for CVR estimation using ASL. For Turbo QUASAR ASL, the issue MT effects need to be addressed before this ASL technique can be used for the absolute CBF quantification.

6.2 Future Work

6.2.1 Partial Volume Correction For ASL Data of Brain Activation

We have not sought to investigate the impact of PVEc on tissue CBF during task activities in single and repeated sessions. Previous studies have identified significant CBF and ATT changes during brain activation using multi-PLD PCASL and QUASAR ASL without PVEc [84][96]. Since PVEc alters the CBF values by reducing the bias of PVE, it remains unknown whether the same significant changes in tissue CBF and ATT can be observed. In addition, since the LR and spatially regularized PVEc methods demonstrated different characteristics on detecting subtle changes of CBF, the effects of applying these PVEc methods on activation data needs to be investigated.

6.2.2 Partial Volume Correction For ASL Data of Patients

An open question is the degree to which PVEc might be useful for GM CBF estimation of dementia patients in group studies. Since one of the motivations of this thesis was to investigate the feasibility of ASL to detect the early onset of dementia, it is important to address the issues of PVE in patients already diagnosed with dementia as well as those with early symptoms. The simulations in Chapter 3 and 4 have partially explored the potential challenges of applying PVEc on this population such as the subtle spatial variations of GM CBF and uncertainties of PV estimates. Further work using different PVEc methods within ASL groups studies would still be valuable to address these questions.

6.2.3 Improving Turbo QUASAR ASL

The current Turbo QUASAR ASL technique needs improvement on the calibration process and the validation of the estimated CBF values. The calibration issue can be resolved by either (1) adding an independent M_0 scan for Turbo QUASAR ASL or (2) modeling the MT effects to correct the estimation of M_0. The former approach is easier to implement and only involves an additional 30s time to acquire

the calibration data after each Turbo QUASAR ASL scan. The latter approach is more complicated because the MT effects are different at each PLD.

The issue of uncertain bolus duration may be addressed by an auxiliary measurement of flow velocity from PC MRI or adjusting the sequence parameters. The impact of adjusting the effective bolus duration using the velocity estimation of PC MRI was partially explored in Chapter 5. A linear relationship was assumed between the effective bolus duration and flow velocity. However, this may have oversimplified the geometry of the arteries and caused systematic errors. Thus, more work is needed to validate the relationship between flow velocity and effective bolus duration in both carotid and vertebral arteries. An alternative approach is by modifying the time between each labeling pulse. Since the effective bolus duration can be controlled by the time difference between each successive readout (0.6s in the current implementation) or labeling pulse, it is possible to reduce this period of time to accommodate the more rapid flow after acetazolamide administration or in SCD patients. Simulated experiments are needed to determine the optimal time for these conditions as well as the impact to the Look-locker readout.

6.2.4 Investigating CVR In Patients

The feasibility of applying PCASL and Turbo QUASAR ASL to CVR estimation on SCD patients needs to be investigated. Data have already been collected along with the healthy cohort. As discussed in Chapter 5, since the baseline flow velocity and CBF of SCD patients are higher than normal subjects, it is important to use the velocity estimation from PC MRI as a reference to enhance the CBF estimation of Turbo QUASAR ASL.

The current study used the recommended implementation of PCASL (single-PLD) to quantify CVR due to the availability of the ASL sequence. An open question is the effect of using multi-PLD PCASL, which is less sensitive to ATT. Since the results of Chapter 4 indicated that the quantification of ATT and CBF are independent, the estimated CBF of multi-PLD PCASL would be less affected by ATT under different flow conditions. The issue of inversion efficiency also

needs to be addressed for PCASL when the blood velocity changes and its impact on the CVR estimation.

Appendices

Non enim te celavi sermonem.

In fact, I did not hide the speech.

— Marcus Tullius Cicero

A

Supplementary Data For Investigating Partial Volume Correction Using PCASL

Contents

A.1 Simulation Study: Multi-PLD Data (Kernel Size 5×5 for the LR Methods) 179
A.2 Simulation Study: Single-PLD Data (Kernel Size 3×3 for the LR Methods) 179
A.3 Simulation Study: Multi-PLD Data (Kernel Size 3×3 for the LR Methods) 179

A.1 Simulation Study: Multi-PLD Data (Kernel Size 5×5 for the LR Methods)

A.2 Simulation Study: Single-PLD Data (Kernel Size 3×3 for the LR Methods)

A.3 Simulation Study: Multi-PLD Data (Kernel Size 3×3 for the LR Methods)

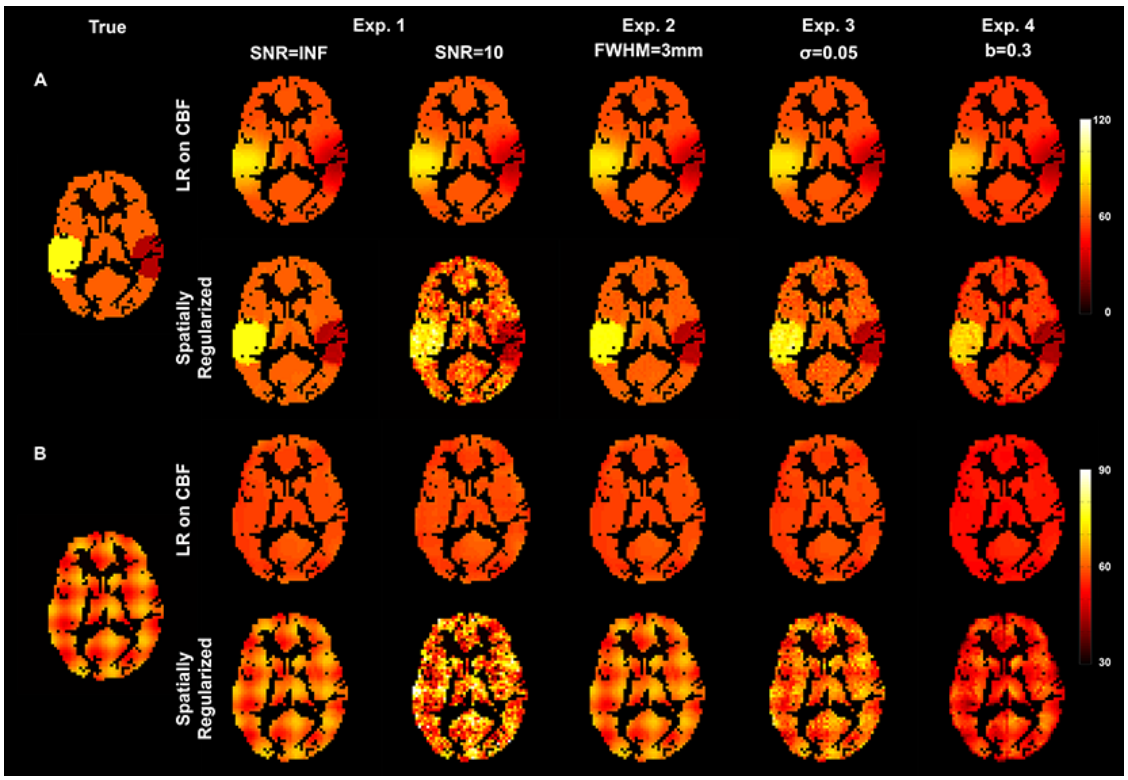

Figure A.1: Estimated GM CBF map for multi-PLD simulated data using PV estimates of subject 1 as the reference PV estimates (kernel size 5×5 for the LR methods). (A) Hyper/hypo GM CBF; (B) Fast sinusoidal GM CBF variation.

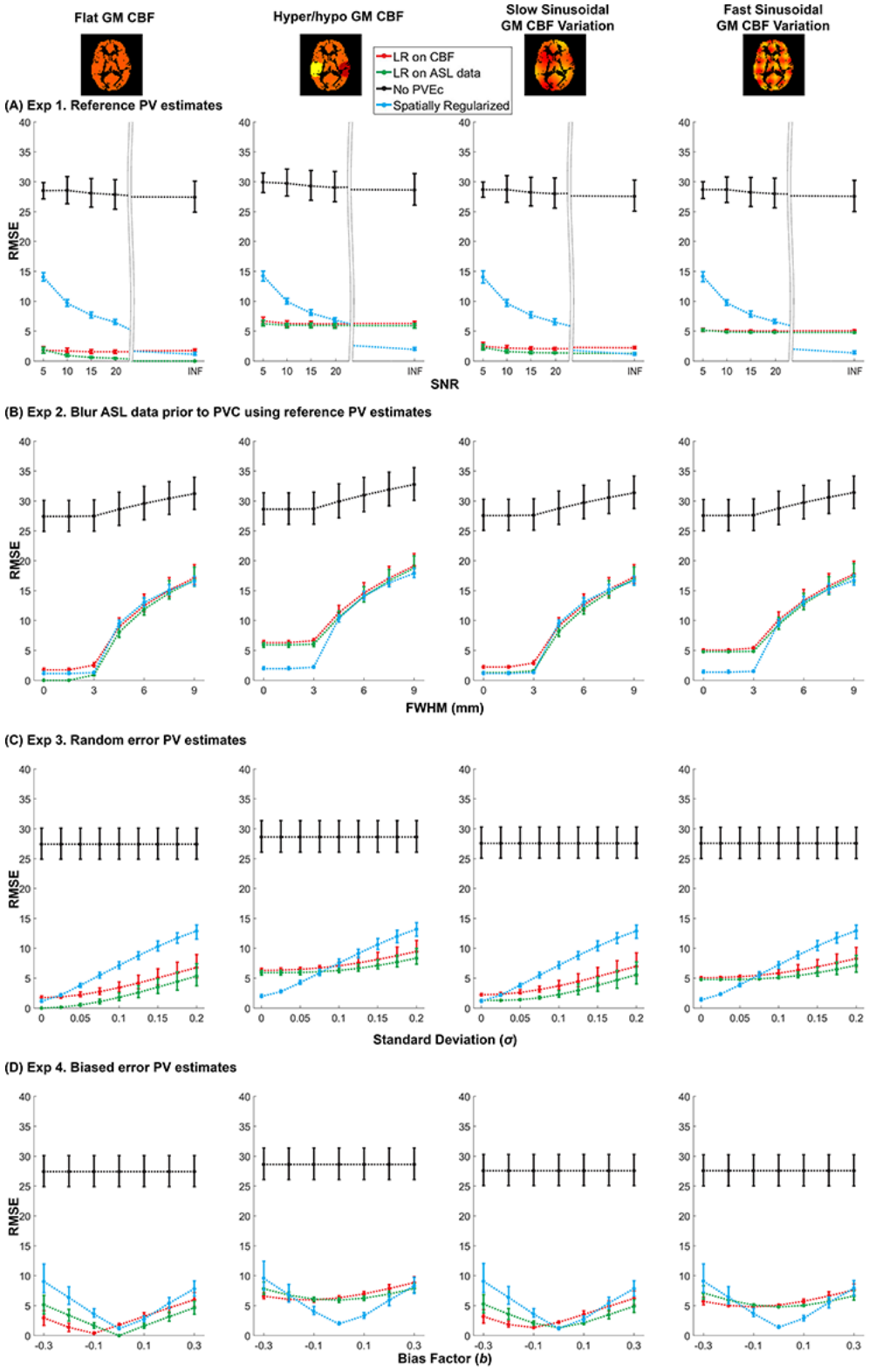

Figure A.2: RMSE between estimated and simulated GM CBF using noise-free simulated multi-PLD data (kernel size 5×5 for the LR methods).

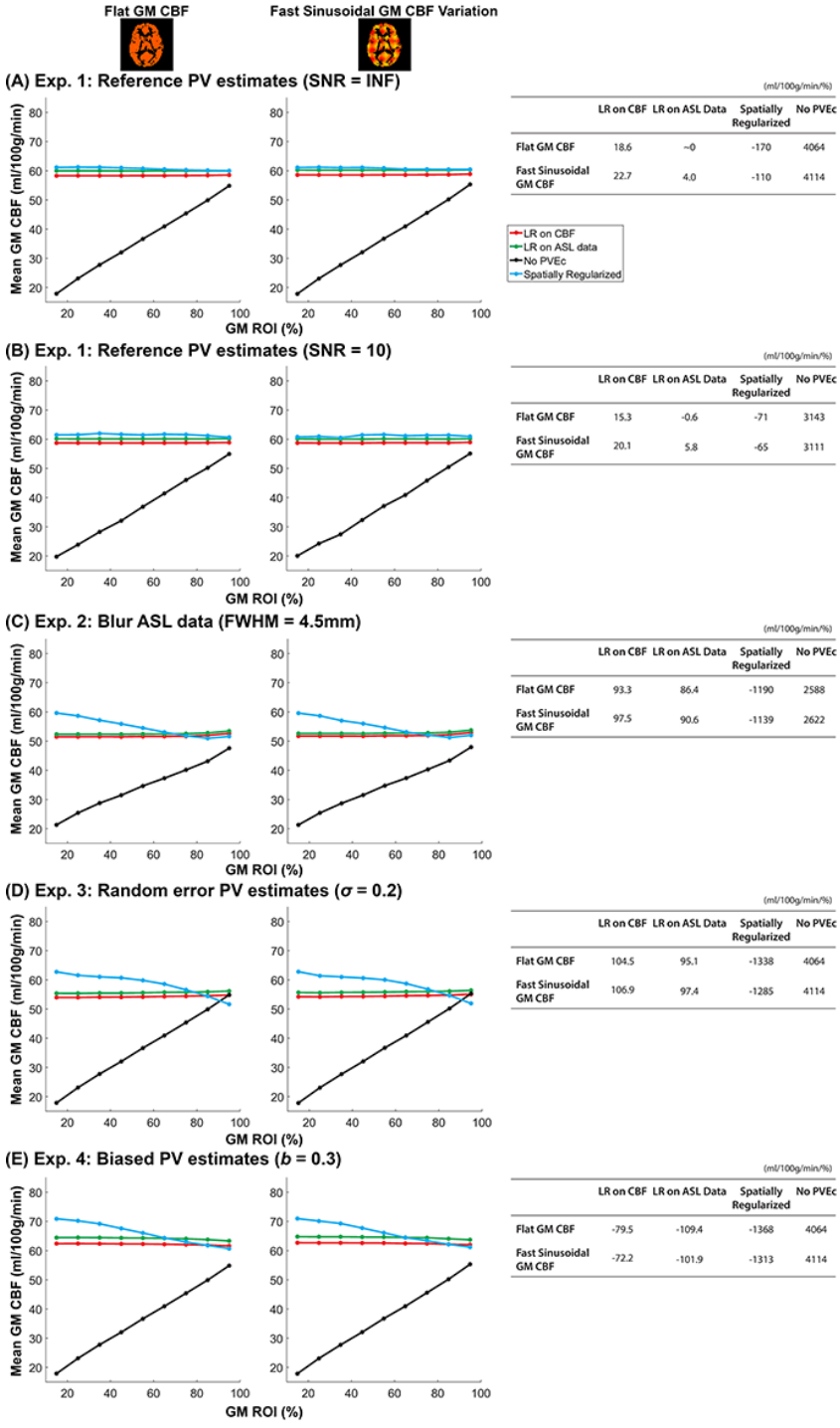

Figure A.3: ROI curve for all experiments using multi-PLD data (kernel size 5×5 for the LR methods). The first row of curves shows the ROI analysis in a perfect situation (SNR=INF and reference PV estimates). Subsequent plots reveal the changes of mean GM CBF in each experiment. Each adjacent table shows the estimated slope values for the linear regression fitting between estimated GM CBF and GM ROI.

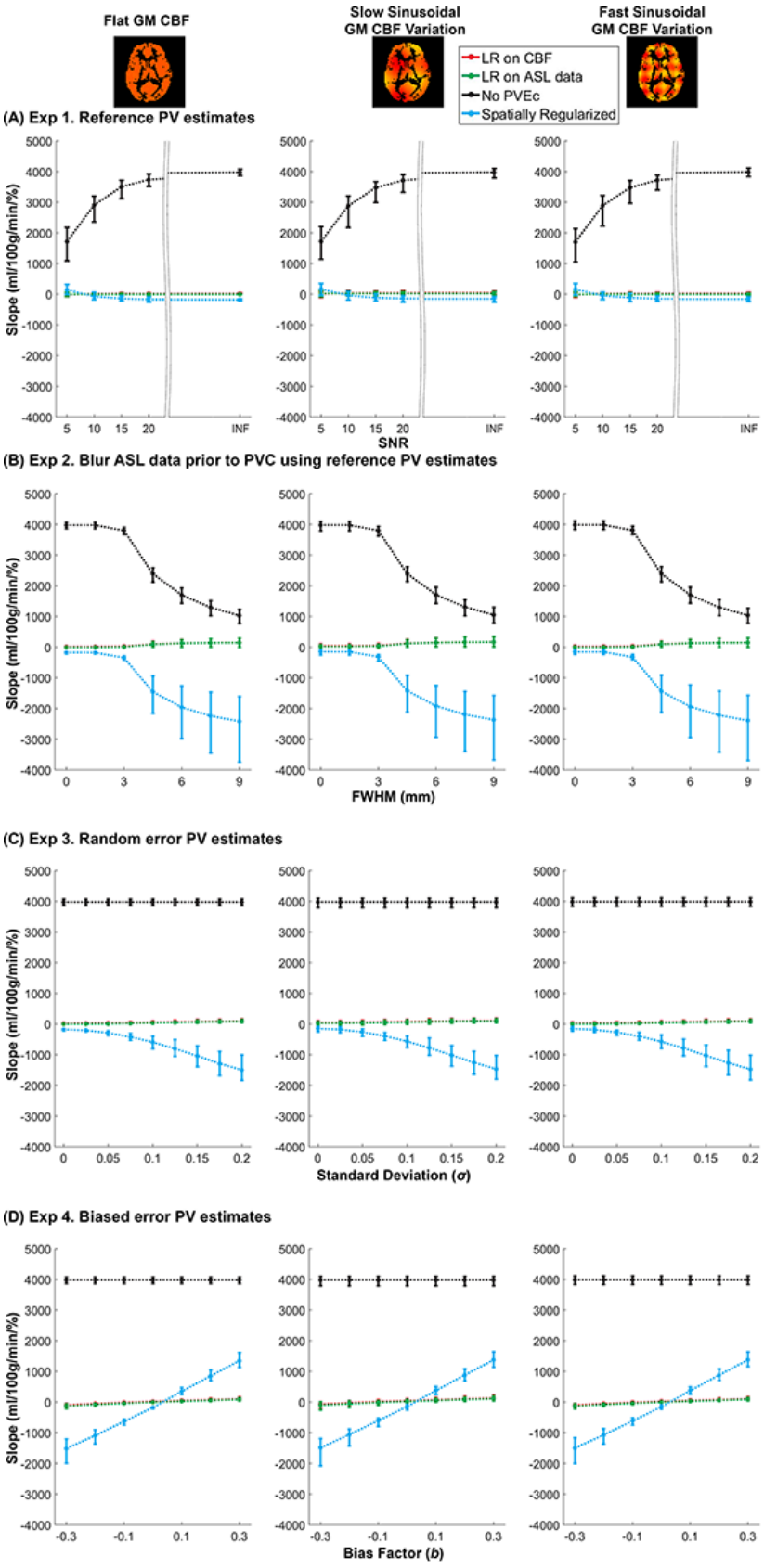

Figure A.4: Estimated slope values of the extended ROI analysis using multi-PLD data (kernel size 5×5 for the LR methods).

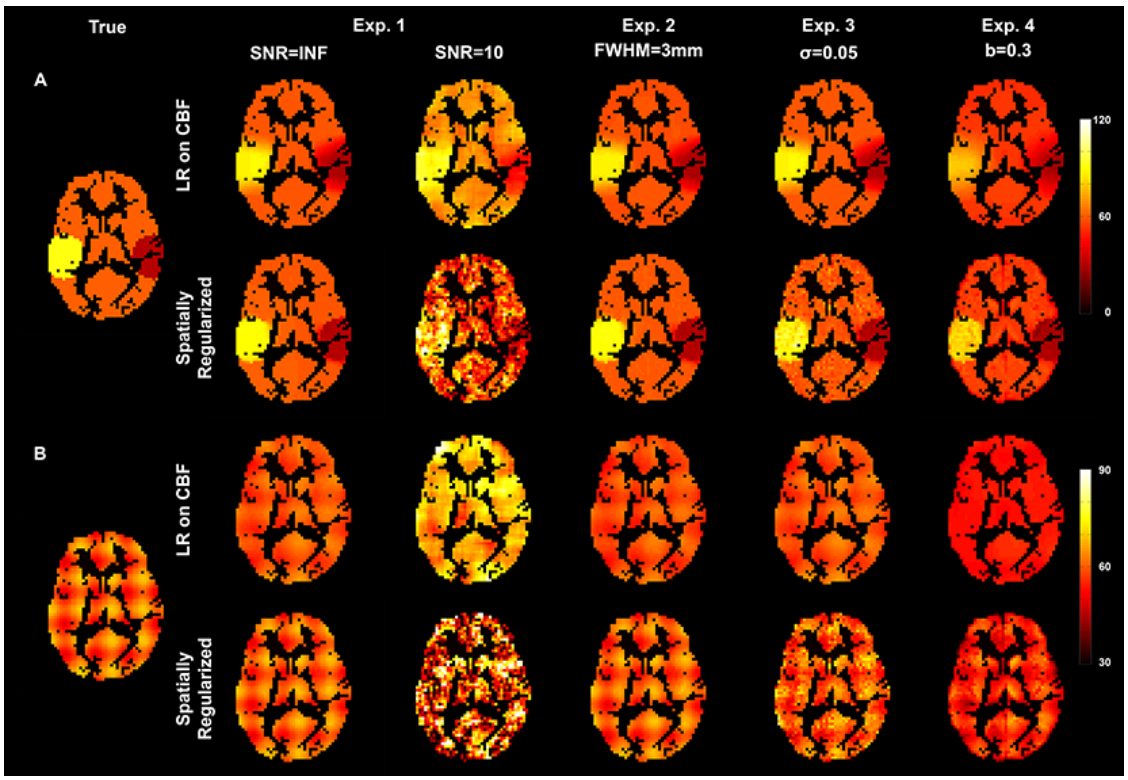

Figure A.5: Estimated GM CBF map for single-PLD simulated data using PV estimates of subject 1 as the reference PV estimates (kernel size 3×3 for the LR methods). (A) Hyper/hypo GM CBF; (B) Fast sinusoidal GM CBF variation.

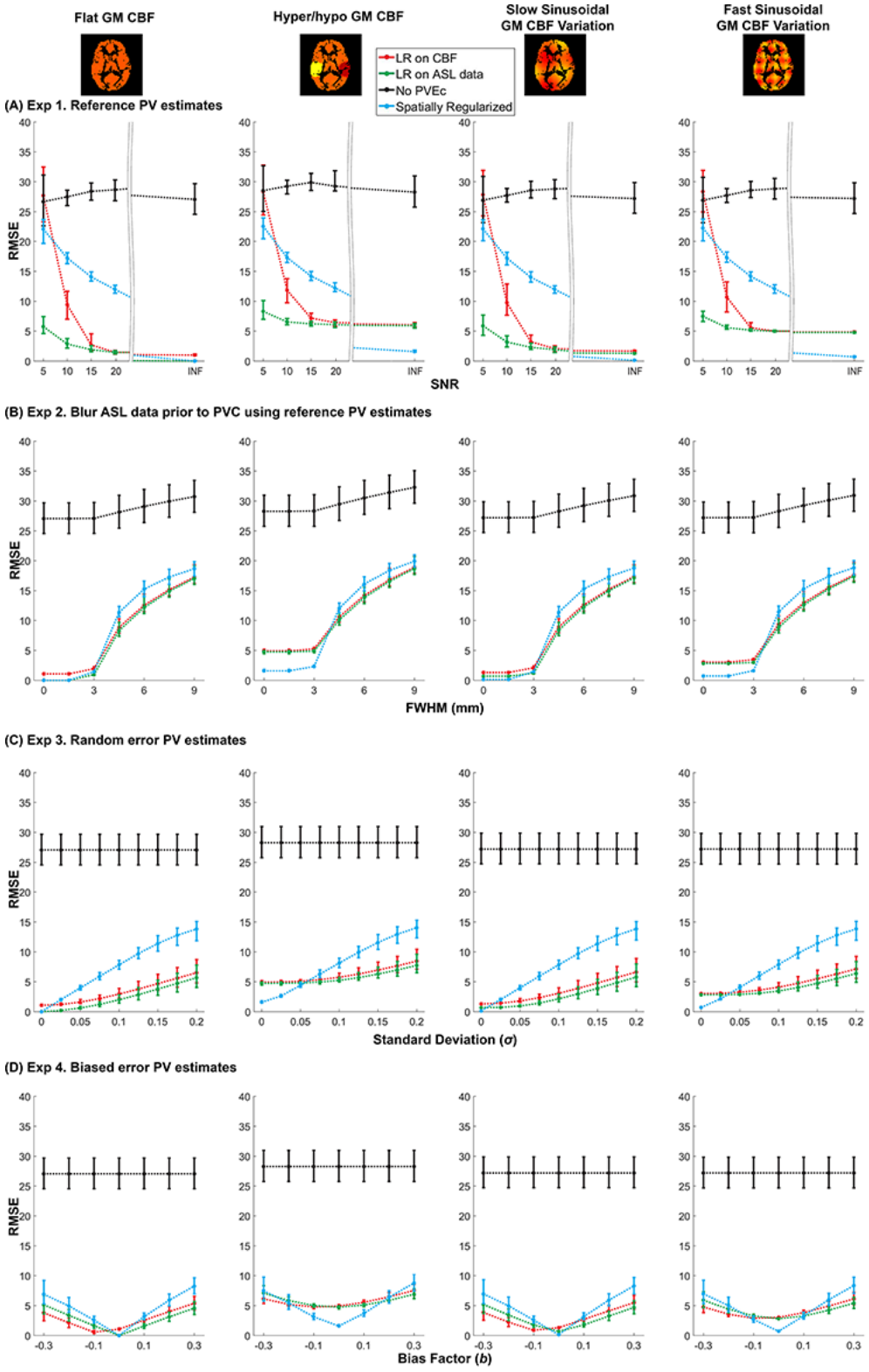

Figure A.6: RMSE between estimated and simulated GM CBF using noise-free simulated single-PLD data (kernel size 3×3 for the LR methods).

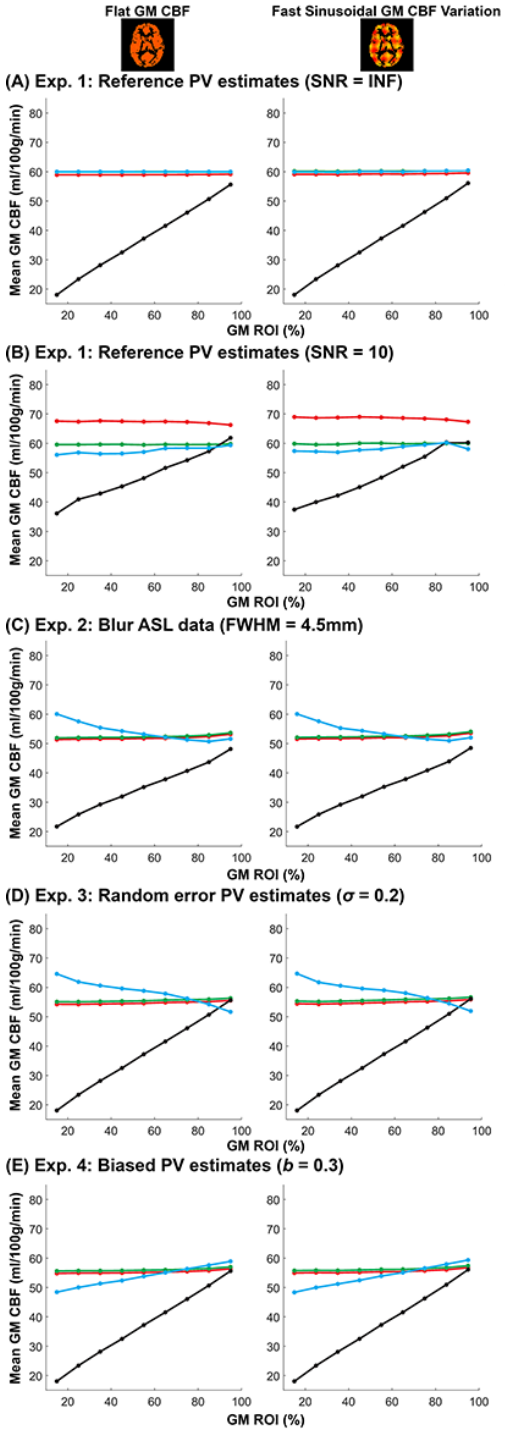

(ml/100g/min/%)

	LR on CBF	LR on ASL Data	Spatially Regularized	No PVEc
Flat GM CBF	20.8	~0	~0	4072
Fast Sinusoidal GM CBF	50.1	29.8	61	4118

(ml/100g/min/%)

	LR on CBF	LR on ASL Data	Spatially Regularized	No PVEc
Flat GM CBF	-110.28	10.7	525	1429
Fast Sinusoidal GM CBF	-140.25	41.0	492	1559

(ml/100g/min/%)

	LR on CBF	LR on ASL Data	Spatially Regularized	No PVEc
Flat GM CBF	169.2	161.2	-1142	2590
Fast Sinusoidal GM CBF	192.7	185.0	-1093	2630

(ml/100g/min/%)

	LR on CBF	LR on ASL Data	Spatially Regularized	No PVEc
Flat GM CBF	168.5	158.3	-1134	4072
Fast Sinusoidal GM CBF	191.0	181.3	-1066	4118

(ml/100g/min/%)

	LR on CBF	LR on ASL Data	Spatially Regularized	No PVEc
Flat GM CBF	169.9	153.7	1441	4072
Fast Sinusoidal GM CBF	201.0	185.3	1508	4118

Figure A.7: ROI curve for all experiments using single-PLD data (kernel size 3×3 for the LR methods). The first row of curves shows the ROI analysis in a perfect situation (SNR=INF and reference PV estimates). Subsequent plots reveal the changes of mean GM CBF in each experiment. Each adjacent table shows the estimated slope values for the linear regression fitting between estimated GM CBF and GM ROI.

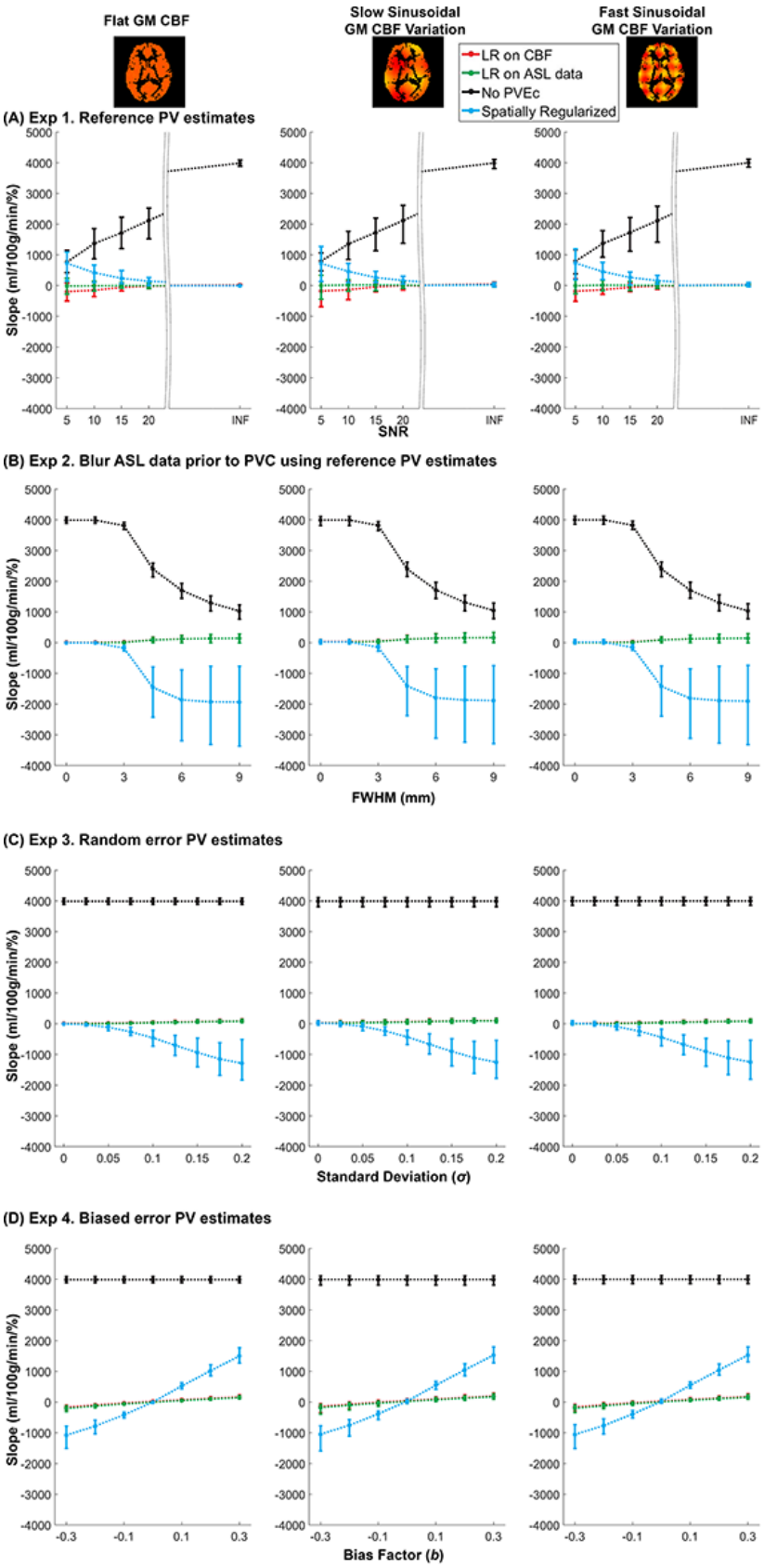

Figure A.8: Estimated slope values of the extended ROI analysis using single-PLD data (kernel size 3×3 for the LR methods).

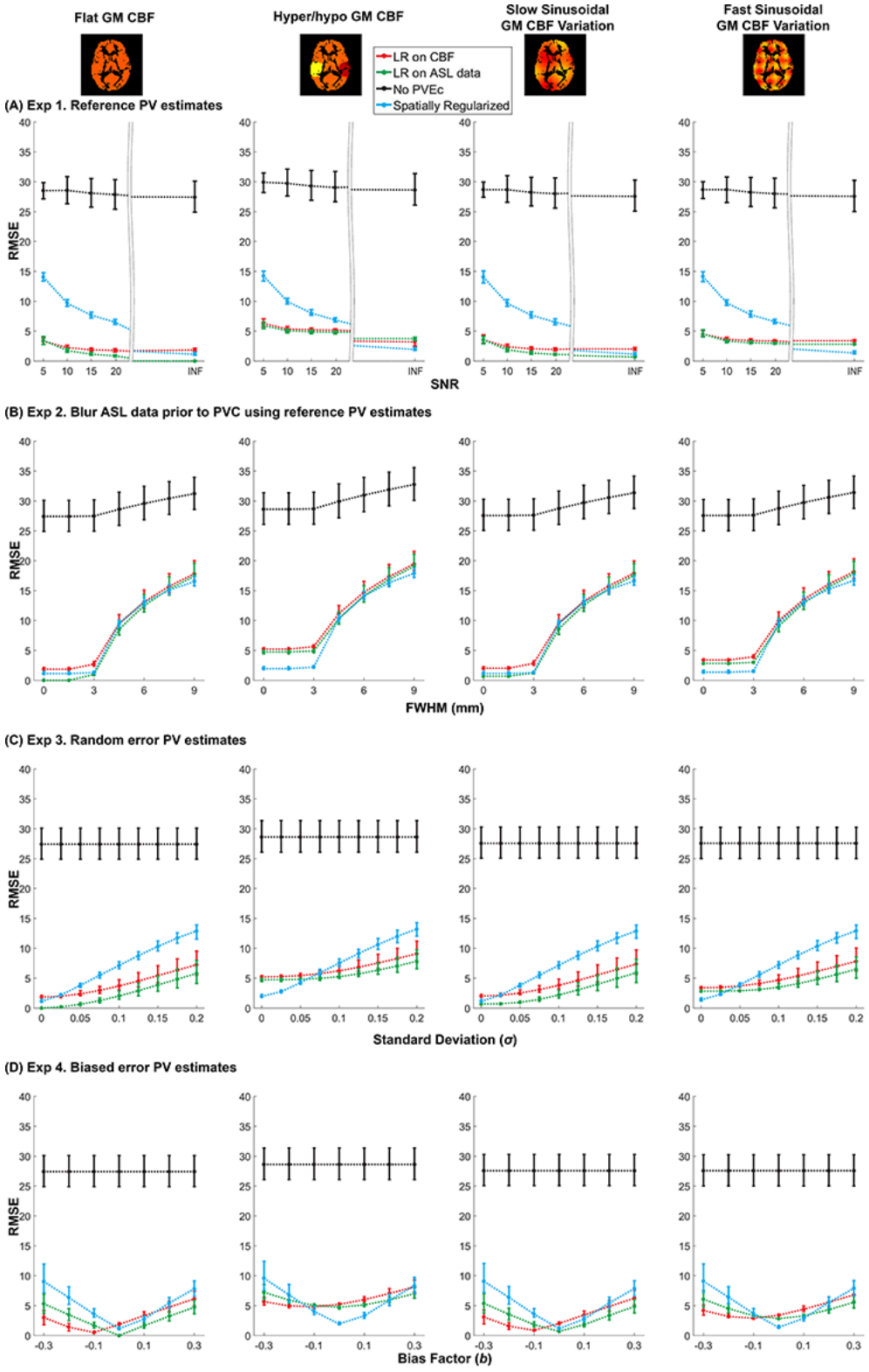

Figure A.9: RMSE between estimated and simulated GM CBF using noise-free simulated multi-PLD data (kernel size 3×3 for the LR methods).

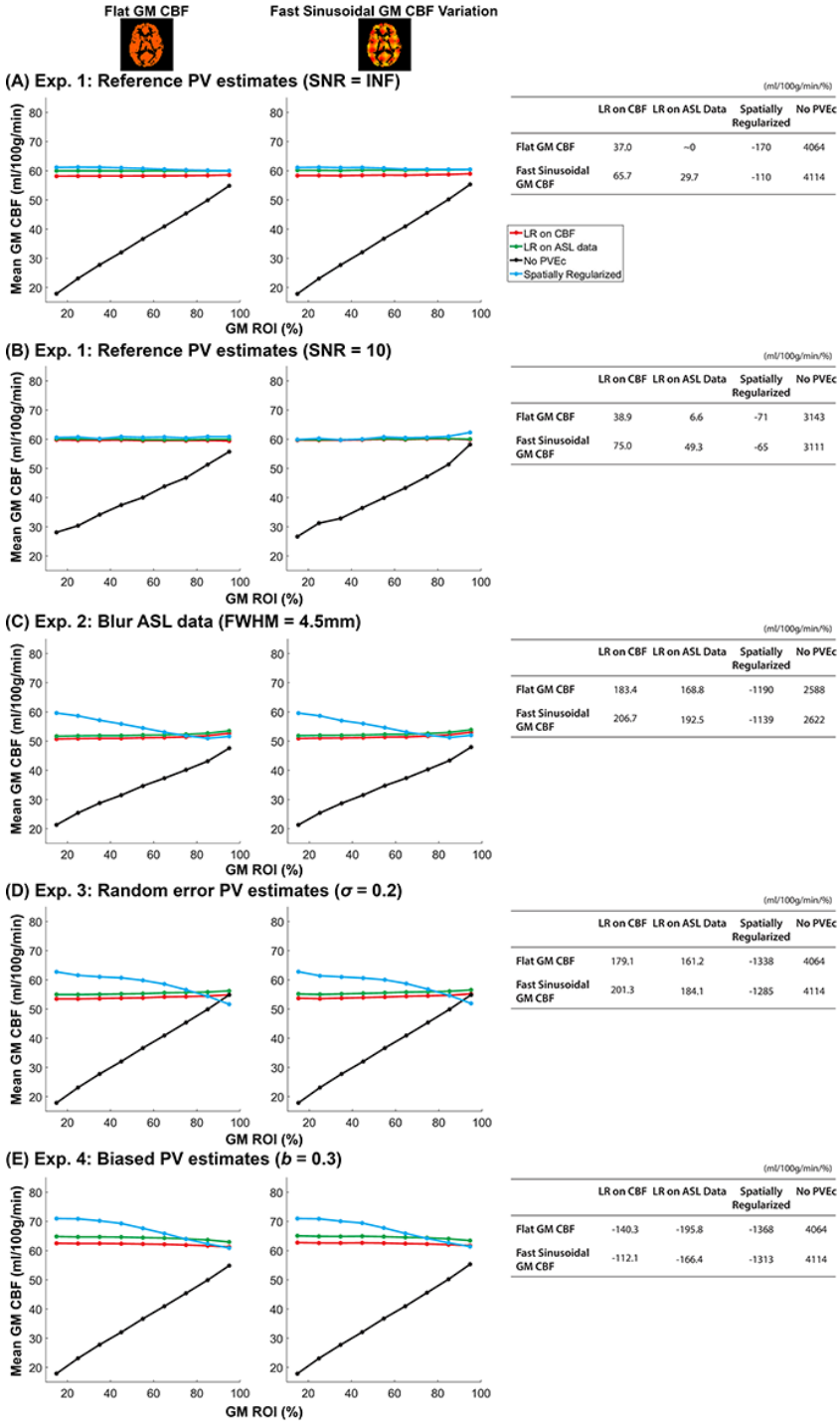

Figure A.10: ROI curve for all experiments using multi-PLD data (kernel size 3×3 for the LR methods). The first row of curves shows the ROI analysis in a perfect situation (SNR=INF and reference PV estimates). Subsequent plots reveal the changes of mean GM CBF in each experiment. Each adjacent table shows the estimated slope values for the linear regression fitting between estimated GM CBF and GM ROI.

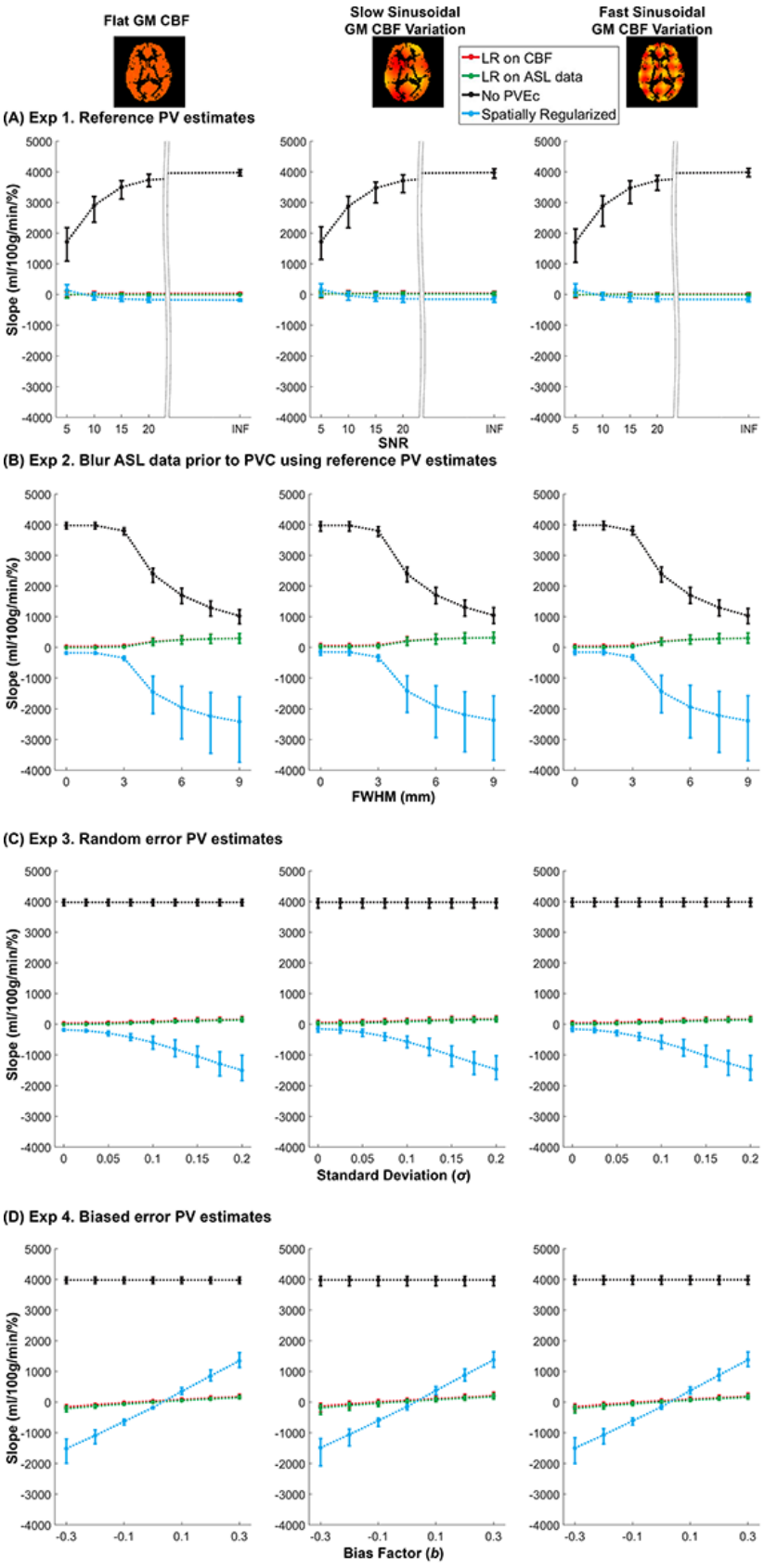

Figure A.11: Estimated slope values of the extended ROI analysis using multi-PLD data (kernel size 3×3 for the LR methods).

Sometimes a scream is better than a thesis.

— Ralph Waldo Emerson

References

[1] World Health Organization. *Dementia: a public health priority*. Tech. rep. 2012, p. 112. arXiv: 9789241564458. URL: http://whqlibdoc.who.int/publications/2012/9789241564458%7B%5C_%7Deng.pdf.

[2] M. Grade et al. *A neuroradiologist's guide to arterial spin labeling MRI in clinical practice*. 2015.

[3] Matthias J P van Osch et al. "Advances in arterial spin labelling MRI methods for measuring perfusion and collateral flow". In: *Journal of Cerebral Blood Flow & Metabolism* (June 2017), p. 0271678X17713434. URL: http://dx.doi.org/10.1177/0271678X17713434.

[4] Heinz Gerd Zimmer. "August Krogh." In: *Clinical cardiology* 29.5 (2006), pp. 231–233.

[5] S. S. Kety and C. F. Schmidt. "THE NITROUS OXIDE METHOD FOR THE QUANTITATIVE DETERMINATION OF CEREBRAL BLOOD FLOW IN MAN: THEORY, PROCEDURE AND NORMAL VALUES". In: *The Journal of clinical investigation* 27.4 (1948), pp. 476–483.

[6] L Ostergaard et al. "Absolute cerebral blood flow and blood volume measured by magnetic resonance imaging bolus tracking: comparison with positron emission tomography values." In: *Journal of cerebral blood flow and metabolism : official journal of the International Society of Cerebral Blood Flow and Metabolism* (1998).

[7] Weili Lin et al. "Quantitative measurements of cerebral blood flow in patients with unilateral carotid artery occlusion: A PET and MR study". In: *Journal of Magnetic Resonance Imaging* (2001).

[8] J. J. Lee et al. "The Kety-Schmidt technique for quantitative perfusion and oxygen metabolism measurements in the MR imaging environment". In: *American Journal of Neuroradiology* (2013).

[9] W D Obrist et al. "Determination of regional cerebral blood flow by inhalation of 133-Xenon." In: *Circulation research* 20.1 (1967), pp. 124–135.

[10] P. Pantano et al. *Regional cerebral blood flow and oxygen consumption in human aging*. 1984.

[11] D S Williams et al. "Magnetic resonance imaging of perfusion using spin inversion of arterial water." In: *Proceedings of the National Academy of Sciences of the United States of America* 89.1 (1992), pp. 212–6. URL: http://www.pubmedcentral.nih.gov/articlerender.fcgi?artid=48206%7B%5C&%7Dtool=pmcentrez%7B%5C&%7Drendertype=abstract.

[12] Christian Federau et al. “Cerebral blood flow, transit time, and apparent diffusion coefficient in moyamoya disease before and after acetazolamide”. In: *Neuroradiology* 59.1 (2017), pp. 5–12. URL: http://link.springer.com/10.1007/s00234-016-1766-y.

[13] Esther E. Bron et al. “Diagnostic classification of arterial spin labeling and structural MRI in presenile early stage dementia”. In: *Human Brain Mapping* 35.9 (2014), pp. 4916–4931.

[14] Iris Asllani, Ajna Borogovac, and Truman R. Brown. “Regression algorithm correcting for partial volume effects in arterial spin labeling MRI”. In: *Magnetic Resonance in Medicine* 60 (2008), pp. 1362–1371.

[15] M. A. Chappell et al. “Partial volume correction of multiple inversion time arterial spin labeling MRI data”. In: *Magnetic Resonance in Medicine* 65 (2011), pp. 1173–1183.

[16] Joana Pinto et al. “Fourier modeling of the BOLD response to a breath-hold task: Optimization and reproducibility”. In: *NeuroImage* 135 (2016), pp. 223–231.

[17] David C. Alsop et al. “Recommended implementation of arterial spin-labeled Perfusion mri for clinical applications: A consensus of the ISMRM Perfusion Study group and the European consortium for ASL in dementia”. In: *Magnetic Resonance in Medicine* (2015). arXiv: NIHMS150003.

[18] Hiroshi Ito et al. “Changes in human cerebral blood flow and cerebral blood volume during hypercapnia and hypocapnia measured by positron emission tomography.” In: *Journal of cerebral blood flow and metabolism : official journal of the International Society of Cerebral Blood Flow and Metabolism* 23.6 (2003), pp. 665–670.

[19] Erfan Nur et al. “Cerebrovascular reserve capacity is impaired in patients with sickle cell disease.” In: *Blood* 114.16 (2009), pp. 3473–8. URL: http://www.ncbi.nlm.nih.gov/pubmed/19700663.

[20] CS Roy and CS Sherrington. “On the Regulation of the Blood-Supply of the Brain”. In: *The Journal of physiology* 11.1-2 (1890), pp. 85–158.

[21] David Attwell and Costantino Iadecola. *The neural basis of functional brain imaging signals*. 2002.

[22] Claire M. Peppiatt et al. “Bidirectional control of CNS capillary diameter by pericytes”. In: *Nature* 443.7112 (2006), pp. 700–704. URL: http://www.nature.com/doifinder/10.1038/nature05193.

[23] Y. Iturria-Medina et al. “Early role of vascular dysregulation on late-onset Alzheimer’s disease based on multifactorial data-driven analysis”. In: *Nature Communications* 7 (2016), p. 11934. arXiv: arXiv:1011.1669v3. URL: http://www.nature.com/doifinder/10.1038/ncomms11934.

[24] Junseok A. Kim et al. “Reduced cerebrovascular reserve is regionally associated with cortical thickness reductions in children with sickle cell disease”. In: *Brain Research* 1642 (2016), pp. 263–269.

[25] Mark S Shiroishi et al. "Principles of T2 *-weighted dynamic susceptibility contrast MRI technique in brain tumor imaging." In: *Journal of Magnetic Resonance Imaging* 00.2 (2014), pp. 296–313. URL: http://www.ncbi.nlm.nih.gov/pubmed/24817252.

[26] Meng Law et al. "Glioma grading: sensitivity, specificity, and predictive values of perfusion MR imaging and proton MR spectroscopic imaging compared with conventional MR imaging". In: *AJNR American journal of neuroradiology* 24.10 (2003), pp. 1989–1998. URL: papers3://publication/uuid/C58DFDF1-444E-440B-BD8E-55C3C32585DE.

[27] Olaf B Paulson et al. "History of International Society for Cerebral Blood Flow and Metabolism." In: *Journal of cerebral blood flow and metabolism : official journal of the International Society of Cerebral Blood Flow and Metabolism* 32.7 (2012), pp. 1099–106. URL: http://www.pubmedcentral.nih.gov/articlerender.fcgi?artid=3390811%7B%5C&%7Dtool=pmcentrez%7B%5C&%7Drendertype=abstract.

[28] S P Yang and J A Krasney. "Cerebral blood flow and metabolic responses to sustained hypercapnia in awake sheep." In: *Journal of cerebral blood flow and metabolism : official journal of the International Society of Cerebral Blood Flow and Metabolism* 15.1 (1995), pp. 115–123.

[29] W Jagust et al. "SPECT perfusion imaging in the diagnosis of Alzheimer's disease: a clinical-pathologic study." In: *Neurology* 56.7 (2001), pp. 950–956.

[30] Hiroshi Matsuda. *Cerebral blood flow and metabolic abnormalities in Alzheimer's disease*. 2001.

[31] Ronald Boellaard et al. "Evaluation of basis function and linear least squares methods for generating parametric blood flow images using 15O-water and positron emission tomography". In: *Molecular Imaging and Biology* 7.4 (2006), pp. 273–285.

[32] Audrey P Fan et al. "Comparison of cerebral blood flow measurement with [15O]-water positron emission tomography and arterial spin labeling magnetic resonance imaging: A systematic review." In: *Journal of cerebral blood flow and metabolism : official journal of the International Society of Cerebral Blood Flow and Metabolism* (2016), p. 0271678X16636393. URL: http://jcb.sagepub.com/content/early/2016/03/03/0271678X16636393.full.

[33] A Villringer et al. "Dynamic imaging with lanthanide chelates in normal brain: contrast due to magnetic susceptibility effects." In: *Magnetic resonance in medicine : official journal of the Society of Magnetic Resonance in Medicine / Society of Magnetic Resonance in Medicine* 6.2 (1988), pp. 164–174.

[34] Em Purcell, Hc Torrey, and Rv Pound. "Resonance Absorption by Nuclear Magnetic Moments in a Solid". In: *Physical Review* 69.1-2 (1946), pp. 37–38. URL: http://journals.aps.org/pr/abstract/10.1103/PhysRev.69.37%7B%5C%%7D5Cnhttp://link.aps.org/doi/10.1103/PhysRev.69.37.

[35] F. Bloch, W. W. Hansen, and M. Packard. "The nuclear induction experiment". In: *Physical Review* 70.7-8 (1946), pp. 474–485. arXiv: arXiv:1011.1669v3.

[36] Govind B Chavhan et al. “Principles, techniques, and applications of T2*-based MR imaging and its special applications.” In: *Radiographics : a review publication of the Radiological Society of North America, Inc* (2009).

[37] E. L. Hahn. “Spin echoes”. In: *Physical Review* 80.4 (1950), pp. 580–594.

[38] A D Elster. “Gradient-echo MR imaging: techniques and acronyms.” In: *Radiology* 186.1 (1993), pp. 1–8. URL: http://pubs.rsna.org/doi/10.1148/radiology.186.1.8416546.

[39] F. Bloch. “Nuclear induction”. In: *Physical Review* 70.7-8 (1946), pp. 460–474.

[40] Donald W. McRobbie et al. *MRI from picture to proton*. 2006. arXiv: arXiv:1011.1669v3.

[41] P Mansfield. “Multi-planar image formation using NMR spin echoes”. In: *Journal of Physics C: Solid State Physics* 10.3 (1977), pp. L55–L58. URL: http://stacks.iop.org/0022-3719/10/i=3/a=004?key=crossref.f48893f3d8bf21cb4a102c6293b5ce83.

[42] D a Feinberg and K Oshio. “GRASE (gradient- and spin-echo) MR imaging: a new fast clinical imaging technique.” In: *Radiology* 181.2 (1991), pp. 597–602.

[43] Matthias Günther, Koichi Oshio, and David A. Feinberg. “Single-shot 3D imaging techniques improve arterial spin labeling perfusion measurements”. In: *Magnetic Resonance in Medicine* 54.2 (2005), pp. 491–498.

[44] David a Feinberg and Matthias Günther. “Cerebral Blood Flow Imaging with 3D GRASE ASL Sequence Increases SNR and Shortens Acquisition Time”. In: *MAGNETOM Flash* 3.3 (2009), pp. 62–69.

[45] Sd Caruthers, H Jara, and Er Melhem. “MR imaging: some applications of GRASE”. In: *Medicamundi* 42.3 (1998), pp. 23–28. URL: http://www.healthcare.philips.com/pwc%7B%5C_%7Dhc/main/about/assets/docs/medicamundi/mm%7B%5C_%7Dvol42%7B%5C_%7Dno3/mm%7B%5C_%7Dvol42%7B%5C_%7Dno3%7B%5C_%7Darticle%7B%5C_%7Dmr%7B%5C_%7Dimaging%7B%5C_%7Dsome%7B%5C_%7Dapplications.pdf.

[46] M Brant-Zawadzki, G D Gillan, and W R Nitz. “MP RAGE: a three-dimensional, T1-weighted, gradient-echo sequence–initial experience in the brain”. In: *Radiology* 182.3 (1992), pp. 769–775. URL: papers3://publication/uuid/1CE1EF99-AA66-4455-9067-000738AE0B4A.

[47] Joseph V Hajnal et al. “High signal regions in normal white matter shown by heavily T2-weighted CSF nulled IR sequences”. In: *J Comput Assist Tomogr* 16.4 (1992), pp. 506–513. URL: http://www.ncbi.nlm.nih.gov/pubmed/1629405.

[48] Joseph V. Hajnal et al. “Use of Fluid Attenuated Inversion Recovery (FLAIR) Pulse Sequences in MRI of the Brain”. In: *Journal of Computer Assisted Tomography* 16.6 (1992), pp. 841–844. URL: http://content.wkhealth.com/linkback/openurl?sid=WKPTLP:landingpage%7B%5C&%7Dan=00004728-199211000-00001.

[49] Elias R. Melhem et al. “MR of the spine with a fast T1-weighted fluid-attenuated inversion recovery sequence”. In: *American Journal of Neuroradiology* (1997).

[50] D. C. Look and D. R. Locker. “Time saving in measurement of NMR and EPR relaxation times”. In: *Review of Scientific Instruments* 41.2 (1970), pp. 250–251.

[51] Matthias Gunther, Michael Bock, and Lothar R. Schad. "Arterial spin labeling in combination with a look-locker sampling strategy: Inflow turbo-sampling EPI-FAIR (ITS-FAIR)". In: *Magnetic Resonance in Medicine* 46 (2001), pp. 974–984.

[52] Peter Kellman and Michael S. Hansen. "T1-mapping in the heart: Accuracy and precision". In: *Journal of Cardiovascular Magnetic Resonance* (2014). arXiv: NIHMS150003.

[53] Steven D. Wolff and Robert S. Balaban. "Magnetization transfer contrast (MTC) and tissue water proton relaxation in vivo". In: *Magnetic Resonance in Medicine* 10.1 (1989), pp. 135–144.

[54] R. M. Henkelman, G. J. Stanisz, and S. J. Graham. *Magnetization transfer in MRI: A review*. 2001.

[55] J A Detre et al. "Perfusion imaging." In: *Magnetic resonance in medicine : official journal of the Society of Magnetic Resonance in Medicine / Society of Magnetic Resonance in Medicine* 23.1 (1992), pp. 37–45.

[56] Matthias A. Mutke et al. "Clinical evaluation of an arterial-spin-labeling product sequence in steno-occlusive disease of the brain". In: *PLoS ONE* 9.2 (2014).

[57] David C. Alsop and John A. Detre. "Reduced transit-time sensitivity in noninvasive magnetic resonance imaging of human cerebral blood flow". In: *Journal of cerebral blood flow and metabolism : official journal of the International Society of Cerebral Blood Flow and Metabolism* 16.6 (1996), pp. 1236–1249. URL: http://www.ncbi.nlm.nih.gov/pubmed/8898697.

[58] J a Detre et al. "Tissue specific perfusion imaging using arterial spin labeling." In: *NMR in biomedicine* 7.1-2 (1994), pp. 75–82.

[59] D C Alsop and J a Detre. "Multisection cerebral blood flow MR imaging with continuous arterial spin labeling." In: *Radiology* 208.2 (1998), pp. 410–416.

[60] E Matthew et al. "Reproducibility of resting cerebral blood flow measurements with H2(15)O positron emission tomography in humans". In: *J Cereb Blood Flow Metab* 13.5 (1993), pp. 748–754.

[61] Weiying Dai et al. "Continuous flow-driven inversion for arterial spin labeling using pulsed radio frequency and gradient fields". In: *Magnetic Resonance in Medicine* 60.6 (2008), pp. 1488–1497.

[62] Xavier Golay, Esben T. Petersen, and Francis Hui. "Pulsed Star Labeling of Arterial Regions (PULSAR): A robust regional perfusion technique for high field imaging". In: *Magnetic Resonance in Medicine* 53 (2005), pp. 15–21.

[63] Greg Zaharchuk et al. "Multislice perfusion and perfusion territory imaging in humans with separate label and image coils". In: *Magnetic Resonance in Medicine* 41.6 (1999), pp. 1093–1098.

[64] R R Edelman et al. "Qualitative Mapping of Cerebral Blood-Flow and Functional Localization With Echo-Planar Mr-Imaging and Signal Targeting With Alternating Radio-Frequency". In: *Radiology* 192.2 (1994), pp. 513–520.

[65] Robert R. Edelman et al. *Signal targeting with alternating radiofrequency (STAR) sequences: Application to MR angiography*. 1994.

[66] R R Edelman and Q Chen. "EPISTAR MRI: multislice mapping of cerebral blood flow." In: *Magnetic resonance in medicine : official journal of the Society of Magnetic Resonance in Medicine / Society of Magnetic Resonance in Medicine* 40.6 (1998), pp. 800–805.

[67] K K Kwong et al. "MR perfusion studies with T1-weighted echo planar imaging." In: *Magnetic resonance in medicine : official journal of the Society of Magnetic Resonance in Medicine / Society of Magnetic Resonance in Medicine* 34.6 (1995), pp. 878–887.

[68] S. G. Kim. "Quantification of relative cerebral blood flow change by flow-sensitive alternating inversion recovery (FAIR) technique: Application to functional mapping". In: *Magnetic Resonance in Medicine* 34 (1995), pp. 293–301.

[69] R J Ogg, P B Kingsley, and J S Taylor. "WET, a T1- and B1-insensitive water-suppression method for in vivo localized 1H NMR spectroscopy." In: *Journal of magnetic resonance. Series B* 104.1 (1994), pp. 1–10.

[70] Eric C. Wong, Richard B. Buxton, and Lawrence R. Frank. "Quantitative imaging of perfusion using a single subtraction (QUIPSS and QUIPSS II)". In: *Magnetic Resonance in Medicine* 39 (1998), pp. 702–708.

[71] Xavier Golay, Jeroen Hendrikse, and Tchoyoson C C Lim. "Perfusion imaging using arterial spin labeling". In: *Topics in magnetic resonance imaging : TMRI* 15.1 (2004), pp. 10–27. URL: papers3://publication/uuid/3B1D5756-24CD-4DD4-903D-0E7FAD62542D.

[72] Jane F. Utting et al. "Velocity-driven adiabatic fast passage for arterial spin labeling: Results from a computer model". In: *Magnetic Resonance in Medicine* (2003).

[73] Esben Thade Petersen, Tchoyoson Lim, and Xavier Golay. "Model-free arterial spin labeling quantification approach for perfusion MRI". In: *Magnetic Resonance in Medicine* 55.2 (2006), pp. 219–232.

[74] Janneke Schepers, Matthias J.P. Van Osch, and Klaas Nicolay. "Effect of vascular crushing on FAIR perfusion kinetics, using a BIR-4 pulse in a magnetization prepared FLASH sequence". In: *Magnetic Resonance in Medicine* 50.3 (2003), pp. 608–613.

[75] Frank Q. Ye et al. "Correction for vascular artifacts in cerebral blood flow values measured by using arterial spin tagging techniques". In: *Magnetic Resonance in Medicine* 37 (1997), pp. 226–235.

[76] Dairon M. Garcia, Guillaume Duhamel, and David C. Alsop. "Efficiency of inversion pulses for background suppressed arterial spin labeling". In: *Magnetic Resonance in Medicine* (2005).

[77] Jiongjiong Wang et al. "Comparison of quantitative perfusion imaging using arterial spin labeling at 1.5 and 4.0 Tesla". In: *Magnetic Resonance in Medicine* (2002).

[78] Yufen Chen, Danny J J Wang, and John A. Detre. "Test-retest reliability of arterial spin labeling with common labeling strategies". In: *Journal of Magnetic Resonance Imaging* 33.4 (2011), pp. 940–949.

[79] W. Thomas Dixon et al. “Multiple inversion recovery reduces static tissue signal in angiograms”. In: *Magnetic Resonance in Medicine* (1991).

[80] Sanjay Mani et al. “Background suppression with multiple inversion recovery nulling: Applications to projective angiography”. In: *Magnetic Resonance in Medicine* (1997).

[81] Jeff H. Duyn et al. “High-sensitivity single-shot perfusion-weighted fMRI”. In: *Magnetic Resonance in Medicine* (2001).

[82] Frank Q. Ye et al. “Noise reduction in 3D perfusion imaging by attenuating the static signal in arterial spin tagging (ASSIST)”. In: *Magnetic Resonance in Medicine* (2000).

[83] Varsha Jain et al. “Longitudinal reproducibility and accuracy of pseudo-continuous arterial spin-labeled perfusion MR imaging in typically developing children.” In: *Radiology* 263.2 (2012), pp. 527–36. URL: http://www.pubmedcentral.nih.gov/articlerender.fcgi?artid=3329270%7B%5C&%7Dtool=pmcentrez%7B%5C&%7Drendertype=abstract.

[84] M. Mezue et al. “Optimization and reliability of multiple postlabeling delay pseudo-continuous arterial spin labeling during rest and stimulus-induced functional task activation.” In: *Journal of cerebral blood flow and metabolism : official journal of the International Society of Cerebral Blood Flow and Metabolism* 34.12 (2014), pp. 1919–27. URL: http://www.pubmedcentral.nih.gov/articlerender.fcgi?artid=4269746%7B%5C&%7Dtool=pmcentrez%7B%5C&%7Drendertype=abstract.

[85] Henri J M M Mutsaerts et al. “Multi-vendor reliability of arterial spin labeling perfusion MRI using a near-identical sequence: Implications for multi-center studies”. In: *NeuroImage* 113 (2015), pp. 143–152.

[86] Esben Thade Petersen, Kim Mouridsen, and Xavier Golay. “The QUASAR reproducibility study, Part II: Results from a multi-center Arterial Spin Labeling test-retest study”. In: *NeuroImage* 49.1 (2010), pp. 104–113.

[87] R B Buxton et al. “A general kinetic model for quantitative perfusion imaging with arterial spin labeling.” In: *Magnetic resonance in medicine : official journal of the Society of Magnetic Resonance in Medicine / Society of Magnetic Resonance in Medicine* 40 (1998), pp. 383–396.

[88] J. Hrabe and D. P. Lewis. “Two analytical solutions for a model of pulsed arterial spin labeling with randomized blood arrival times”. In: *Journal of Magnetic Resonance* 167 (2004), pp. 49–55.

[89] J Zhou et al. “Two-compartment exchange model for perfusion quantification using arterial spin tagging.” In: *Journal of cerebral blood flow and metabolism : official journal of the International Society of Cerebral Blood Flow and Metabolism* 21 (2001), pp. 440–455.

[90] Amit Mehndiratta et al. “A control point interpolation method for the non-parametric quantification of cerebral haemodynamics from dynamic susceptibility contrast MRI”. In: *NeuroImage* 64.1 (2013), pp. 560–570.

[91] Marco Pizzolato, Timothé Boutelier, and Rachid Deriche. “Perfusion deconvolution in DSC-MRI with dispersion-compliant bases”. In: *Medical Image Analysis* 36 (2017), pp. 197–215.

[92] M.E. Valentinuzzi and E.M. Montaldo Volachec. “Discrete Deconvolution”. In: *Medical and biological engineering* 13.January (1975), pp. 123–125.

[93] Ona Wu et al. “Tracer arrival timing-insensitive technique for estimating flow in MR perfusion-weighted imaging using singular value decomposition with a block-circulant deconvolution matrix”. In: *Magnetic Resonance in Medicine* 50 (2003), pp. 164–174.

[94] E. T. Petersen et al. “Non-invasive measurement of perfusion: A critical review of arterial spin labelling techniques”. In: *British Journal of Radiology* 79.944 (2006), pp. 688–701.

[95] B J MacIntosh et al. “Regional Cerebral Arterial Transit Time Hemodynamics Correlate with Vascular Risk Factors and Cognitive Function in Men with Coronary Artery Disease.” In: *AJNR* (2014), pp. 1–7. URL: `http://www.ncbi.nlm.nih.gov/pubmed/25147198`.

[96] Yi-Ching Lynn Ho, Esben Thade Petersen, and Xavier Golay. “Measuring arterial and tissue responses to functional challenges using arterial spin labeling”. In: *NeuroImage* 49 (2010), pp. 478–487.

[97] Henri J.M.M. Mutsaerts et al. *Comparison of arterial spin labeling registration strategies in the multi-center GENetic frontotemporal dementia initiative (GENFI)*. 2017.

[98] L. Vaclavu et al. “In vivo T1 of blood measurements in children with sickle cell disease improve cerebral blood flow quantification from arterial spin-labeling MRI”. In: *American Journal of Neuroradiology*. Vol. 37. 9. 2016, pp. 1727–1732.

[99] Philips. “DICOM Conformance Statement”. In: *BMJ (Clinical research ed.)* 339 (2010), b2700. URL: `http://www.ncbi.nlm.nih.gov/pubmed/19622552`.

[100] William D. Rooney et al. “Magnetic field and tissue dependencies of human brain longitudinal 1H2O relaxation in vivo”. In: *Magnetic Resonance in Medicine* 57.2 (2007), pp. 308–318.

[101] Michael A. Chappell et al. “Comparing model-based and model-free analysis methods for QUASAR arterial spin labeling perfusion quantification”. In: *Magnetic Resonance in Medicine* 69 (2013), pp. 1466–1475.

[102] Jiongjiong Wang et al. “Arterial transit time imaging with flow encoding arterial spin tagging (FEAST)”. In: *Magnetic Resonance in Medicine* 50.3 (2003), pp. 599–607.

[103] Tetsuya Tsujikawa et al. “Arterial transit time mapping obtained by pulsed continuous 3D ASL imaging with multiple post-label delay acquisitions: Comparative study with PET-CBF in patients with chronic occlusive cerebrovascular disease”. In: *PLoS ONE* 11.6 (2016).

[104] Bradley J. MacIntosh et al. “Assessment of arterial arrival times derived from multiple inversion time pulsed arterial spin labeling MRI”. In: *Magnetic Resonance in Medicine* 63 (2010), pp. 641–647.

[105] Mark W. Woolrich et al. “Bayesian analysis of neuroimaging data in FSL.” In: *NeuroImage* 45.1 Suppl (2009).

[106] Virginia Mato Abad et al. "ASAP (Automatic Software for ASL Processing): A toolbox for processing Arterial Spin Labeling images". In: *Magnetic Resonance Imaging* 34.3 (2016), pp. 334–344.

[107] T Bayes. "Essay towards solving a problem in the doctrine of chances". In: *Biometrika* 45.7 April 2010 (1958), pp. 293–315. URL: http://blog.sina.com.cn/s/blog%7B%5C_%7D4701280b0100ht1x.html.

[108] M A Chappell et al. "Variational Bayesian Inference for a Nonlinear Forward Model". In: *IEEE Transactions on Signal Processing* 57.1 (2009), pp. 223–236. URL: http://ieeexplore.ieee.org/lpdocs/epic03/wrapper.htm?arnumber=4625948%7B%5C%%7D5Cnpapers3://publication/doi/10.1109/TSP.2008.2005752.

[109] Charles Geyer. "Practical Markov Chain Monte Carlo". In: *Statistical Science* 7.4 (1992), pp. 473–483. URL: http://www.jstor.org/stable/2246094%7B%5C%%7D5Cnpapers3://publication/uuid/1CA942D7-4558-492D-976B-45E29C41C49E.

[110] S. Stigler. "Laplace's 1774 Memoir on Inverse Probability." In: *Statistical Science* 1.3 (1986), pp. 359–363.

[111] Hagai Attias. "A variational Bayesian framework for graphical models". In: *Advances in neural information processing systems* 12.1-2 (2000), pp. 209–215.

[112] William D. Penny, Nelson J. Trujillo-Barreto, and Karl J. Friston. "Bayesian fMRI time series analysis with spatial priors". In: *NeuroImage* 24.2 (2005), pp. 350–362.

[113] Adrian R. Groves, Michael A. Chappell, and Mark W. Woolrich. "Combined spatial and non-spatial prior for inference on MRI time-series". In: *NeuroImage* 45.3 (2009), pp. 795–809.

[114] C C Henery and T M Mayhew. "The cerebrum and cerebellum of the fixed human brain: efficient and unbiased estimates of volumes and cortical surface areas." In: *Journal of anatomy* 167 (1989), pp. 167–180.

[115] Rebecca M. E. Steketee et al. "Early-stage differentiation between presenile Alzheimer's disease and frontotemporal dementia using arterial spin labeling MRI". In: *European Radiology* (2015). URL: http://link.springer.com/10.1007/s00330-015-3789-x.

[116] Nathan A Johnson et al. "Pattern of Cerebral Hypoperfusion in Alzheimer Disease and Mild Cognitive Impairment Measured with Arterial Spin-labeling MR Imaging: Initial Experience1". In: *Radiology* 234.3 (2005), pp. 851–859. arXiv: NIHMS150003. URL: http://radiology.rsna.org/content/234/3/851.abstract.

[117] Jan Petr et al. "Partial volume correction in arterial spin labeling using a Look-Locker sequence". In: *Magnetic Resonance in Medicine* 70.6 (2013), pp. 1535–1543.

[118] André Ahlgren et al. "Partial volume correction of brain perfusion estimates using the inherent signal data of time-resolved arterial spin labeling". In: *NMR in Biomedicine* 27 (2014), pp. 1112–1122.

[119] André Ahlgren et al. “A linear mixed perfusion model for tissue partial volume correction of perfusion estimates in dynamic susceptibility contrast MRI: Impact on absolute quantification, repeatability, and agreement with pseudo-continuous arterial spin labeling”. In: *Magnetic Resonance in Medicine* C (2016), pp. 1–12.

[120] Xiaoyun Liang, Alan Connelly, and Fernando Calamante. “Improved partial volume correction for single inversion time arterial spin labeling data”. In: *Magnetic Resonance in Medicine* 69.2 (2013), pp. 531–537.

[121] Jan Petr et al. “Comparison of two methods for atrophy-correction in perfusion imaging: Partial-volume correction versus graymatter volume covariate”. In: *ESMRMB Congress 2017*. Vol. c. Figure 2. 2017, pp. 70–72.

[122] C. J. Lueck et al. “The colour centre in the cerebral cortex of man”. In: *Nature* 340.6232 (1989), pp. 386–389. arXiv: `nature.vol.342.30nov1989`. URL: `http://www.nature.com/doifinder/10.1038/340386a0`.

[123] Wanyong Shin et al. “Automated brain tissue segmentation based on fractional signal mapping from inversion recovery Look-Locker acquisition”. In: *NeuroImage* 52.4 (2010), pp. 1347–1354.

[124] Y Zhang, M Brady, and S Smith. “Segmentation of brain MR images through a hidden Markov random field model and the expectation-maximization algorithm.” In: *IEEE transactions on medical imaging* 20.1 (2001), pp. 45–57.

[125] Mark Jenkinson et al. “Improved optimization for the robust and accurate linear registration and motion correction of brain images”. In: *NeuroImage* 17.2 (2002), pp. 825–841. arXiv: `arXiv:1011.1669v3`.

[126] Douglas N. Greve and Bruce Fischl. “Accurate and robust brain image alignment using boundary-based registration”. In: *NeuroImage* 48.1 (2009), pp. 63–72.

[127] Campbell J Le Heron et al. “Comparing cerebral perfusion in Alzheimer’s disease and Parkinson’s disease dementia: an ASL-MRI study.” In: *Journal of cerebral blood flow and metabolism : official journal of the International Society of Cerebral Blood Flow and Metabolism* 34.October 2013 (2014), pp. 1–7. URL: `http://www.ncbi.nlm.nih.gov/pubmed/24619276`.

[128] Henri J M M Mutsaerts et al. “Gray matter contamination in arterial spin labeling white matter perfusion measurements in patients with dementia”. In: *NeuroImage: Clinical* 4 (2014), pp. 139–144.

[129] Moss Y Zhao et al. “Partial Volume Effects Correction for QUASAR ASL: A Spatially Regularised Approach”. In: *Proceedings of International Society for Magnetic Resonance In Medicine* (2016).

[130] Karla L Miller et al. “Multimodal population brain imaging in the UK Biobank prospective epidemiological study”. In: *Nature Neuroscience* 19.11 (2016). URL: `http://www.nature.com/doifinder/10.1038/nn.4393`.

[131] Wen Chau Wu et al. “Pseudocontinuous arterial spin labeling perfusion magnetic resonance imaging-A normative study of reproducibility in the human brain”. In: *NeuroImage* 56.3 (2011), pp. 1244–1250.

[132] Thomas W. Okell et al. "Cerebral blood flow quantification using vessel-encoded arterial spin labeling". In: *J Cereb Blood Flow Metab* 33.11 (2013), pp. 1716–24. URL: http://dx.doi.org/10.1038/jcbfm.2013.129%7B%5C%%7D5Cn10.1038/jcbfm.2013.129%20http://www.ncbi.nlm.nih.gov/pubmed/23921895%7B%5C%%7D5Cnhttp://www.pubmedcentral.nih.gov/articlerender.fcgi?artid=PMC3824178.

[133] Patricia Clement et al. "Variability of physiological brain perfusion in healthy subjects – A systematic review of modifiers. Considerations for multi-center ASL studies". In: *Journal of Cerebral Blood Flow & Metabolism* (Apr. 2017), p. 0271678X17702156. URL: http://dx.doi.org/10.1177/0271678X17702156.

[134] Mark Jenkinson and Stephen Smith. "A global optimisation method for robust affine registration of brain images". In: *Medical Image Analysis* 5.2 (2001), pp. 143–156.

[135] Matthias J P Van Osch, Jeroen Hendrikse, and Jeroen Van Der Grond. "Sensitivity comparison of multiple vs. single inversion time pulsed arterial spin labeling fMRI". In: *Journal of Magnetic Resonance Imaging* 25.1 (2007), pp. 215–221.

[136] O M Henriksen et al. "Sub-Clinical Cognitive Decline and Resting Cerebral Blood Flow in Middle Aged Men". In: *PLoS One* 12.1 (2017), e0169912. URL: http://www.ncbi.nlm.nih.gov/pubmed/28095458.

[137] Marta Vidorreta et al. "Comparison of 2D and 3D single-shot ASL perfusion fMRI sequences". In: *NeuroImage* 66 (2013), pp. 662–671. arXiv: NIHMS150003.

[138] Sheliza Halani et al. "Comparing cerebrovascular reactivity measured using BOLD and cerebral blood flow MRI: The effect of basal vascular tension on vasodilatory and vasoconstrictive reactivity". In: *NeuroImage* 110 (2015), pp. 110–123.

[139] Peiying Liu et al. "Cerebrovascular reactivity mapping without gas challenges". In: *NeuroImage* 146 (2017), pp. 320–326.

[140] Merideth A. Addicott et al. "The effect of daily caffeine use on cerebral blood flow: How much caffeine can we tolerate?" In: *Human Brain Mapping* 30.10 (2009), pp. 3102–3114.

[141] Robert P. Hebbel, Raymond Osarogiagbon, and Dhananjay Kaul. *The endothelial biology of sickle cell disease: Inflammation and a chronic vasculopathy*. 2004.

[142] E. Thade Petersen et al. "Turbo-QUASAR: a signal-to-noise optimal arterial spin labeling and sampling strategy". In: *Proc. Intl. Soc. Mag. Reson. Med. 21 (2013) 2146.* 60.6 (2013), p. 2146.

[143] Michael A. Chappell et al. "Modeling dispersion in arterial spin labeling: Validation using dynamic angiographic measurements". In: *Magnetic Resonance in Medicine* 69 (2013), pp. 563–570.

[144] Thomas E. Nichols and Andrew P. Holmes. "Nonparametric permutation tests for functional neuroimaging: A primer with examples". In: *Human Brain Mapping* 15.1 (2002), pp. 1–25.

[145] Anderson M. Winkler et al. "Permutation inference for the general linear model". In: *NeuroImage* 92 (2014), pp. 381–397.

[146] A. P. Holmes et al. "Nonparametric Analysis of Statistic Images from Functional Mapping Experiments". In: *Journal of Cerebral Blood Flow & Metabolism* 16.1 (1996), pp. 7–22. URL: http://journals.sagepub.com/doi/10.1097/00004647-199601000-00002.

[147] Laura L. Boles Ponto et al. "Technical issues in the determination of cerebrovascular reserve in elderly subjects using 15O-water PET imaging". In: *NeuroImage* 21.1 (2004), pp. 201–210.

[148] Peiying Liu, Jill B. De Vis, and Hanzhang Lu. *Cerebrovascular reactivity (CVR) MRI with CO2 challenge: A technical review*. 2018.

[149] Wen Chau Wu et al. "A theoretical and experimental investigation of the tagging efficiency of pseudocontinuous arterial spin labeling". In: *Magnetic Resonance in Medicine* 58.5 (2007), pp. 1020–1027.

[150] Sina Aslan et al. "Estimation of labeling efficiency in pseudocontinuous arterial spin labeling". In: *Magnetic Resonance in Medicine* 63.3 (2010), pp. 765–771.

[151] Esben T. Petersen et al. "An Improved QUASAR sequence for User-Independent Quantitative and Reproducible Perfusion Measurements". In: *ISMRM Proceedings* 15.376 (2007), p. 376.

[152] Patrick W Hales, Fenella J Kirkham, and Christopher A Clark. "A general model to calculate the spin-lattice (T 1) relaxation time of blood , accounting for haematocrit , oxygen saturation and magnetic field strength". In: *Journal of Cerebral Blood Flow & Metabolism* 00 (2015), p. 0271678X15.